Ion Transportation and Adsorption in Two-Dimensional Materials

A thesis submitted in partial fulfilment of the requirements for the degree of Doctor of Philosophy

University of Technology Sydney
Faculty of Science
School of Mathematical and Physical Science

By

Javad Safaei

Supervisor

Prof. Guoxiu Wang

February 2023

CERTIFICATE OF ORIGINAL AUTHORSHIP

I, Javad Safaei, declare that this thesis, is submitted in fulfilment of the requirements for the award of Doctor of Philosophy, in the School of Mathematical and Physical Sciences at the University of Technology Sydney. This thesis is wholly my own work unless otherwise referenced or acknowledged. In addition, I certify that all information sources and literature used are indicated in the thesis. This document has not been submitted for qualifications at any other academic institution. This research is supported by the Australian Government Research Training Program.

Signature: Production Note: Signature removed prior to publication.

Date: 01.12.2023

Abstract

Ion transportation and adsorption shape several of the modern technologies from batteries, supercapacitors and fuel cells, to water desalination, ion capture and storage, and salinity gradient energy harvesting. Most of the ionic devices function based on the transportation or adsorption of ions. Hence, it is of critical importance to study the fundamentals and applications of ion transportation and adsorption. 2D materials stand out as one of the promising candidates in this field, due to their ease of fabrication into membranes and electrodes, abundant surface functional groups, ordered galleries, and mechanical flexibility. Hence, it is important to do research on the fundamental and applications of 2D materials for ion transportation and absorption applications. In this thesis, we firstly provide a literature review on the fundamentals and applications of ionic transport and adsorption. Next, we present two chapters on the application of 2D materials for salinity gradient energy harvesting where the cation permselectivity results in the generation of electricity from the interface of river water/seawater. Moreover, we present a chapter on capacitive water desalination governing the principle of ion adsorption. Lastly, we end this thesis by a conclusion and future research direction in this area. It is envisioned that further research into the ion transportation and adsorption properties of 2D materials can not only advance the current technologies, but also help develop the future of ionic devices.

Acknowledgements

I would like to sincerely thank my supervisor Prof. Guoxiu Wang for his great mentorship and support. I would like to thank Dr. Jane Yao and Dr. Dong Zhou for their kind help. I am grateful to my friends and colleagues in CCET. I am thankful to UTS for providing scholarships. Lastly, I am thankful to my family.

Table of Contents

List of Figures

Abbreviations

1D	one-dimensional
2D	two-dimensional
AFM	atomic force microscopy
ALD	atomic layer deposition
ANF	aramid nanofiber
BET	Brunauer-Emmett-Teller
BN	boron nitride
BP	black phosphorous
CDI	capacitive deionization
CNF	cellulose nanofibers
CNT	carbon nanotube
COF	covalent organic framework
CTAB	cetyltrimethylammonium bromide
CTF	covalent triazine frameworks
CV	cyclic voltammetry
CVD	chemical vapor deposition
DFT	density functional theory
DI	deionized
DMF	N-dimethyl formamide
DMSO	dimethyl sulfoxide
EDA	ethylenediamine
EDL	electrical double layer
EDS	energy dispersive spectroscopy
EIS	electrochemical impedance spectroscopy
FO	forward osmosis
GO	graphene oxide
HAADF	high angle annular dark field
HRTEM	high resolution TEM
ISE	ion selective electrode
LMHB	Litre m^{-2} h^{-2} bar^{-1}
MD	molecular dynamics

MESP	molecular electrostatic potential
MOF	metal organic frameworks
MPD	m-phenylenediame
NMP	N-methyl-2-pyrrolidone
PAN	polyacrylonitrile
PDDA	polydiallyl dimethylammonium chloride
PRO	pressure-retarded osmosis
PSS	polystyrene sulfonate
PVDF	polyvinylidene difluoride
RED	reverse electrodialysis
rGO	reduced graphene oxide
RO	reverse osmosis
SAC	salt adsorption capacity
SAED	selective area electron diffraction
SANF	sulfonated aramid nanofibers
SEC	salt electrosorption capacity
SEM	scanning electron microscope
SER	salt electrosoption rate
SSNa	styrene sulfonic sodium
STEM	scanning transmission electron microscope
SWNT	single-walled carbon nanotube
TEM	transmission electron microscope
TFPPY	tetrakis (p-formylphenyl) pyrene
TGA	thermogravimetric analysis
THF	tetrahydrofuran
TMD	transition metal dichalcogenides
XPS	X-ray photoelectron spectroscopy
XRD	X-ray diffraction

List of Publications

[1] **J. Safaei**†, Y. Gao†, M. Hosseinpour, X. Zhang, Y. Sun, X. Tang, Z. Zhang, S. Wang, X. Guo, Y. Wang, Vacancy Engineering for High-Efficiency Nanofluidic Osmotic Energy Generation, *Journal of the American Chemical Society*, 2023, 145, 4, 2669–2678.

[2] Z. Man†, **J. Safaei**†, Z. Zhang, Y. Wang, D. Zhou, P. Li, X. Zhang, L. Jiang, G. Wang, Serosa-Mimetic Nanoarchitecture Membranes for Highly Efficient Osmotic Energy Generation, *Journal of the American Chemical Society*, 2021, 143, 16206–16216.

[3] **J. Safaei**, S.M.H. Mashkani, H. Tian, C. Ye, P. Xiong, G. Wang, Self-Assembled NbOPO4 Nanosheet/Reduced Graphene Oxide Heterostructure for Capacitive Desalination, *ACS Applied Nano Materials*, 2021, 4, 12629-12639.

[4] **J. Safaei**, G. Wang, Progress and prospects of two-dimensional materials for membrane-based osmotic power generation, *Nano Research Energy*, 2022, 1, e9120008.

[5] **J. Safaei**, P. Xiong, G. Wang, Progress and prospects of two-dimensional materials for membrane-based water desalination, *Materials Today Advances*, 2020, 8, 100108.

† These authors contributed equally.

Chapter 1: Introduction

This thesis is the collection of works on the ion transportation and ion adsorption and in two-dimensional (2D) materials. Nowadays, ionic devices work based on the principles of ion transportation and adsorption. Several devices such as batteries, fuel cells, sensors, and etc. functions based on ion transportation and adsorption. Further understanding of this field helps to develop new devices to purify the water by capacitive ion adsorption or to harness the electrical energy between the interface of seawater/riverwater by selective ion transportation. Two-dimensional materials have demonstrated the merit of high surface area, abundant nanochannels, and ease of fabrication rendering them highly suitable to adsorb and transport ions. Hence, research in this area can not only expand our understanding in this field, but it will pave the way to develop devices from water purification to energy harvesting.

In Chapter 2, we start by firstly reviewing the background of ion transportation and ion adsorption in 2D membranes. In order to understand the ion transportation in 2D materials, it is important to firstly study the ionic sieving mechanism in 2D materials. Having the knowledge on the size exclusion and electrostatic repulsion properties of 2D membranes helps to understand the properties of 2D membranes for several applications. Moreover, tailoring the properties of 2D membranes for selective transportation of cation/anions is further reviewed in this chapter. The selective transportation of ions can render possible the electrical energy harvesting at the interface of seawater/river water. Lastly, the progress and advances of capacitive ion adsorption in 2D materials with particular focus on capacitive water desalination are further reviewed in this chapter.

Chapter 3, is the first application of ion transportation through a two-dimensional serosa-mimetic nanoarchitecture membrane for salinity gradient energy harvesting. In this chapter, a special type of 2D covalent organic framework (COF) is developed with nanometre-sized pores that can accelerate ion diffusion

in the vertical diffusion direction. Moreover, the 2D COF are intertwined with one-dimensional (1D) nanofibers mimicking the properties of the bio-inspired serosa structure. Experimental and DFT+MD computational details are discussed in this chapter, highlighting the role of functional groups in the cation permselectivity and ion transportation dynamics.

Chapter 4, is the second application of ion transportation through vacancy-engineered niobium oxyphosphate nanosheets for osmotic energy conversion applications. In this chapter, we discuss the role of phosphrous vacancies on increasing the surface charge of 2D metal oxide nanosheets via experimental and computational (DFT/MD) techniques. Several characterisation techniques prove the atomic vacancy engineering is an effective strategy in increasing the surface charge of metal oxides, that enhances both the cation permselectivity and ion transportation dynamics.

Chapter 5, we discuss the application of ion adsorption in a self-assembled heterostructure with the focus for capacitive water desalination. In this chapter, the crucial role of interface engineering is highlighted where strong and weak 2D/2D coupling can tailor the electronic and ion adsorption properties of the heterostructure. Characterisation techniques together with DFT computations further elucidate the role of interface engineering on the electrochemical performance of the heterostructure.

Chapter 6, we discuss the overall conclusion on and future research directions for the fundamentals and applications of ion transportation and adsorption through 2D materials. All in all, it is hoped that further understanding of the fundamental and application merits of 2D materials and 2D membranes can accelerate the progress in the field of ion transportation and adsorption.

Chapter 2: Background

2.1. Progress and Prospects of 2D Materials for Membrane-based Water Desalination

2.1.1. Abstract

Water scarcity is one of the most critical issues of this century. Currently, water desalination is performed using polymeric membranes. However, the polymers suffer from low water permeability and degradation, both of which increase energy consumption and the cost of water desalination. There have been several breakthroughs by deploying 2D materials with the merits of excellent water permeability and chemical resistance, rendering them highly promising as alternative materials of choice for water desalination. Herein, the research progress on 2D materials for membrane-based water desalination is summarized. Several nanoporous and stacked membranes of 2D materials are discussed. Design strategies to maintain the stability of the membranes are elucidated, including pore size optimization and interlayer spacing engineering. The current challenges and future research directions are also provided.

2.1.1 Introduction

One of the unrelenting issues of global concern in the 21st century is the inadequate availability of potable water. Rapid urbanization, population growth, and climate disruption directly account for freshwater scarcity on our planet [1]. Half of the world‘s population live in the close vicinity of oceans that cover 80% of earth water supply. Hence, seawater desalination could solve the world‘s water shortages problems, especially in areas where ground or spring water is not available [2]. Water desalination based on membranes is one of the most energy-efficient approaches currently implemented in the industry [3].

Membranes generally act like sieves where water molecules are permeated while dissolved ions are blocked. The first step in designing membranes is to

realize the types of impurities that we want to filter out. sodium (Na^+) and chloride (Cl^-) ions (i.e monovalent ions) form 85% of seawater minerals, with magnesium (Mg^{2+}), calcium (Ca^{2+}) and sulphate (SO_4^{2-}) ions (i.e divalent ions), together forming 12% [4]. Hence, the separation of monovalent ions removes the majority of the impurities from seawater and makes it drinkable. However, monovalent ions are significantly more challenging to filter out than divalent ions due to their smaller size [5]. The separation of monovalent ions via membrane-based technique requires materials that have pores/channels with sizes of less than 1 nm (i.e., subnanometer scales).

Currently, the principle filtration technique in the market is based on thin-film composites membranes, where the dense polyamide layer with its subnanometer pores is responsible for blocking monovalent ions [6]. However, polyamide has several drawbacks, such as low water permeability and degradation [7]. Generally, the polymeric membranes suffer from weak chemical resistance, limited lifetime, and membrane fouling [8]. This issue promoted scientists to pursue inorganic materials with the merits of outstanding water permeability, thermal stability, solvent resistance, and durability [9-11]. Several inorganic materials such as zeolites [12, 13], and carbon nanotubes [14], can desalinate water due to their subnanometer pores/channels. Traditionally, scientists targeted zeolites and carbon nanotubes for this application due to their excellent water permeability and mechanical robustness. However, the high-cost and time-consuming process in growing perfectly ordered subnanometer arrays of zeolites and carbon nanotubes hinder their commercialization for water desalination [15].

As another alternative to polymeric membranes, 2D materials are actively sought after since they can achieve ions-sieving either via in-plane pores or channels of stacked nanosheets, both of which can be economically produced at large-scales [15-17]. 2D materials are well-known for nanofiltration membrane applications (i.e., molecular and divalent ions sieving with sizes above 1 nm) [18, 19]. Several review articles have summarized 2D materials for molecular sieving and nanofiltration applications [20-23]. However, most of them lack the implementation of 2D materials, specifically for monovalent ion-sieving. This is because controlling and maintaining the pore/channel sizes of 2D-based membranes down to the subnanometer level is a challenging process. There

have been several profound scientific breakthroughs in tuning the pores and interlayer distances of 2D materials down to the subnanometer scale [24-26]. Furthermore, new 2D materials and novel techniques have enabled electrostatic exclusion capabilities that enable monovalent ion sieving without the need for subnanometer scale size-tuning [27, 28]. Thus, at this point, it is consequential to review the materials and techniques for obtaining monovalent ion-sieving via pores, nanochannels, and electrostatic repulsion effects for water desalination.

In this review, we summarized the recent progress on 2D material-based membranes for water desalination. We first discussed the mechanism of water desalination across 2D materials. We summarized two types of nanoporous and stacked membranes together with the underlying challenges of optimizing pore/channels down to the subnanometer scale. We then proposed future research directions for the implementation of 2D materials for water desalination. It is envisioned that membrane-based water desalination could be made significantly energy-efficient and low-cost upon discovering the potentials of 2D materials.

2.1.2 Mechanism of water desalination in 2D materials

The understanding of the diffusion of water molecules or solutes and solvents is crucial for designing water desalination membranes. For any membrane, regardless of its type, the transportation of water is governed by the solution-diffusion model, Equation (1):

$$J_W = A(\Delta P - \Delta \pi_m) \quad (1)$$

where J_W is the volumetric water flux, A is water permeability coefficient (permeance), ΔP is the applied hydraulic pressure, and $\Delta \pi_m$ is the osmotic pressure difference between feed and permeate side. In reverse osmosis (RO), the water flow is driven by hydraulic pressure, whereas in forward osmosis (FO), the osmotic pressure drives the stream via a highly concentrated draw solution. Hence, increasing either external pressure on the feed solution in RO mode, or raising the concentration of draw solution in FO mode accelerates the diffusion of solute molecules across the membrane.

The solute flux can be modeled using Fick's law of diffusion, Equation (2):

$$J_s = B\Delta c_m \quad (2)$$

where J_s is the solute flux, B is solute permeability coefficient, and Δc_m is the solute concentration difference across the membrane. From Fick's law, it is concluded that regardless of FO or RO operation, increasing the concentration of feed solution accelerates solvent diffusion across membranes. Equations (1) and (2) clearly shows the contribution of the membrane's active layer towards solvent/solute permeability via A and B coefficients. For commercial membranes, these coefficients can be tailored via changing the thickness of the polyamide layer. Usually, commercial polyamide layers have a thickness of ~150 nm. Reducing the width of the selective layer results in higher water permeability, but it comes at the expense of higher salt permeability (i.e., low salt rejection). Hence, control over compactness, thickness, and chemistry of polyamide layers considerably changes desalination performance [7].

For 2D materials, the mechanisms are identical, except instead of dense polyamide layers, the nanosheets perform the selective mass transportation. Ion sieving can be achieved either via drilling subnanometer pores on the surfaces of nanosheets, or nanochannels from the stacked membranes (Figure 2.1.1 a,d). Selective mass transport through the 2D materials-based membranes for water desalination is mainly achieved via two principle mechanisms of size exclusion and Donnan electrostatic exclusion. Via size-exclusion mechanism, the water molecules of smaller sizes are permeated while hydrated ions are blocked. In 2D materials, water desalination via size exclusion can be achieved either via the in-plane nanopores on single monolayers (Figure 2.1.1 b) or as stacked nanosheets on top of one another with the nanochannels in between (Figure 2.1.1 e) [17]. The second principle mechanism is due to the electrostatic Donnan exclusion effect, where electrically-charged surfaces block the hydrated ions [29]. Regardless of having stacked or nanoporous membranes, the Donnan effect plays a crucial role in selective transportation. In this case, surface electrostatic charges block ions either on the pore edges of the nanopores (Figure 2.1.1 c) or on the line edges and surfaces of nanosheets (Figure 2.1.1 f).

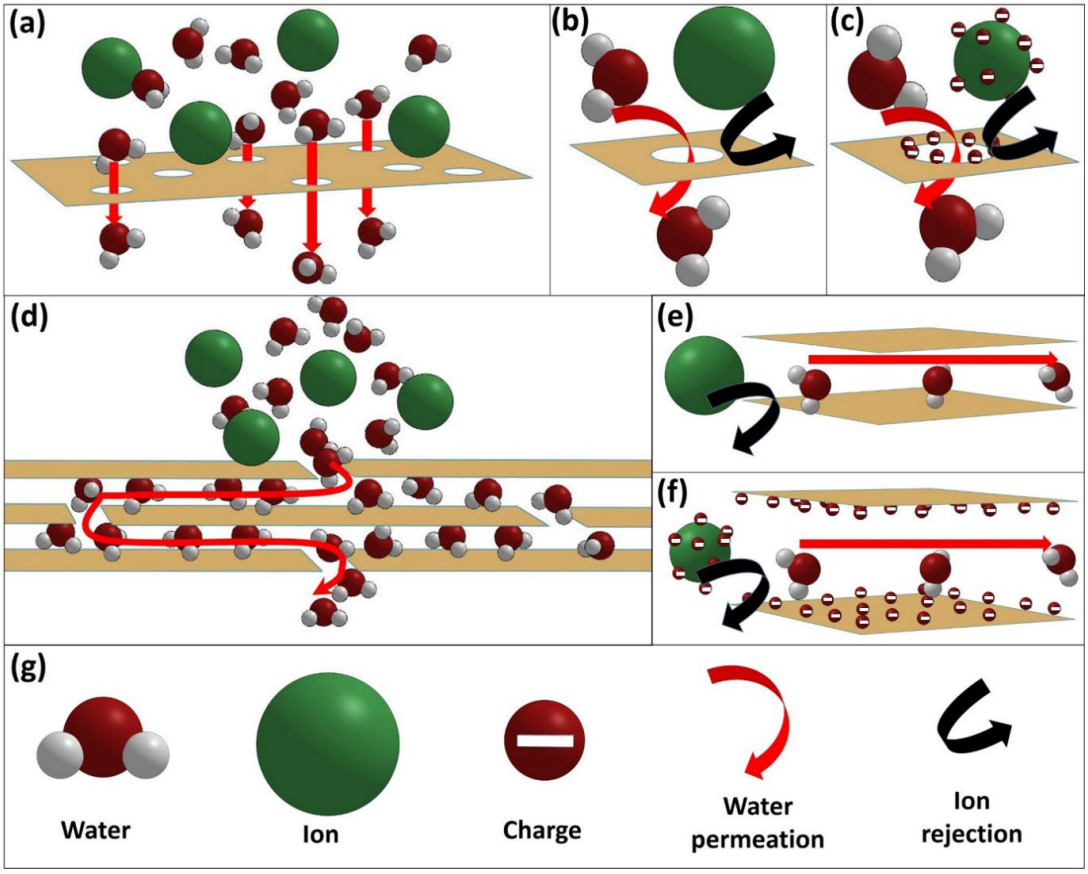

Figure 2.1.1. Mechanism of water desalination in 2D materials. *(a) Water desalination across in-plane nanopores of monolayers, showing the ion blocking effect via (b) size exclusion, and (c) electrostatic exclusion effect. (d) Water desalination across interlayer spacings of nanochannels of stacked nanosheets, showing the ion blocking effect via (e) size exclusion, and (f) electrostatic exclusion effect. (g) The symbols of water molecule, ion, electrostatic charge, water permeation, and ion rejection.*

For stacked membranes, increasing the interlayer distances also increases J_W followed by the increase in salt diffusion J_s. Whereas for nanoporous membranes, J_W and J_s is directly proportional to the pore sizes. Hence, to achieve selective mass transfer and to obtain the optimum selectivity (J_s) /permeability (J_W) tradeoff, one should optimize the pore size of the nanoporous membranes or tune the interlayer distances of the stacked nanosheets. The surface chemistry and polarity of the nanopores and nanosheets could also alter salt rejection performance. Although we mainly focus on the techniques for tuning interlayer distances of stacked membranes in this paper, we also briefly discuss the effect of surface chemistry and Donnan exclusion in the last section of this review.

2.1.3. Nanoporous membranes

Nanoporous membranes are highly promising due to their atomic thickness, which decreases solute diffusion friction dramatically, resulting in impressive water permeability. Tuning pore sizes below the sizes of the hydrated ions would enable the use of these membranes for monovalent ion removal [10, 30, 31]. In this section, 2D materials with externally drilled pores (extrinsic pores) and ingenious/intrinsic pores for water desalination applications are discussed.

2.1.3.1. Extrinsic pores

Developing nanopores on monolayers of 2D materials is a unique technique to produce membranes with ultra-high water permeability. Parameters such as defects [24, 32, 33], pore size [24, 33], pore surface chemistry [34, 35], and mechanical strength of nanoporous monolayers [36, 37] are critical to consider for practical applications.

O'Hern et al. grew defective graphene via CVD and bombarded it with gallium ions. Before gallium ion bombardment, the defects were sealed using polymers and ALD-coated hafnium oxide. This membrane, however, showed relatively low water permeability and salt rejection rates, especially for NaCl. The low salt rejection and low water permeability could be correspondingly pertinent to undesired defects, which could not be perfectly sealed and the nature of the nanopore chemistry, respectively [33]. However, growing defect-free graphene facilitate the use of monolayer membranes for water desalination. [24, 37].

To produce pores on graphene, O'Hern et al. utilized the Gallium ions bombardment technique. This technique yielded subnanometer pores with a mean diameter of 0.152 nm with no holes larger than 0.5 nm. These pore sizes could theoretically permeate water molecules while blocking salt ions (van der Waals diameter of the water molecule and hydrated salt ions are approximately 0.275 nm and 0.7 nm, respectively). The membrane demonstrated 1.51 L m^{-2} h^{-1} bar^{-1} (LMHB) flux with 70 % rejection of $MgSO_4$. There is no report on tuning pore sizes via the traditional Gallium ions bombardment technique [33]. Deploying oxygen plasma technique, however, could solve this issue, rendering the

possibility of pores of various sizes [24, 37]. In one study, Surwade et al. grew defect-free graphene and deployed oxygen plasma as a method to generate subnanometer pores. This strategy yielded ultra-high water flux as high as 70 g m^{-2} s^{-1} atm^{-1} (254 LMH) that is significantly higher than the previous research by a considerable degree and also among the highest ever reported (Table 2.1.1). The pore formation could be studied using Raman plot via the ratio I_D to I_G, which is a widely recognized technique to measure defects in graphene [38]. Increasing plasma etching time increased the I_D/I_G ratio, and also reduced the length of neighboring pores. However, excess of plasma exposure eliminated the 2D nature of carbon, producing amorphous carbon due to the elimination of the 2D peak (Figure 2.1.2 a) [24].

The nature of pore chemistry either depends on the external factor such as pore fabrication technique [24, 33, 37], or ingenuine properties of the materials [15, 35]. Although having the same sizes, the pores developed by oxygen plasma demonstrated higher water permeability compared to those produced by Gallium Ions bombardment [24, 37]. It is stated that the surface chemistry of the pores dominates the water structure in the nanopores [39]. In a theoretical simulation by Cohen et al., the hydroxyl functional groups on the edges of nanopores could roughly double the water flux due to their hydrophilic character [34]. Hence, it is arguable that oxygen plasma could have hydroxylated the pores, dramatically enhancing the water flux. Deployment of other nanopore fabrication techniques such as chemical etching [40], electrochemical reactions [41], annealing under oxygen [42], and chemical oxidations [43] could also alter pore chemistry, demanding further investigations.

As another factor that alters the nature of pore chemistry is the intrinsic elemental features of 2D materials [15, 35]. As an alternative to graphene monolayers, transition metal dichalcogenides (TMD) could also be promising for this application due to their both surfaces being exposed to sulfur atoms, rendering them highly hydrophilic with high affinity for water molecules [15]. Heiranian et al. theoretically simulated water desalination through nanoporous MoS_2. The results proved that the membranes could obtain 70% higher water flux compared with graphene nanopores while maintaining 88% ions rejection rate. More specifically, of the three pore configurations of molybdenum only, sulfur

only, and mixed, the molybdenum-only pores showed the highest water velocity and also water density. This performance ascribed to be due to the hydrophilic nature of molybdenum as it attracts water to the pore interior (Figure 2.1.2 b-d) [35].

One of the most important problems to tackle with these membranes is the mechanical fragility due to atomic-layer thickness of the nanosheets. In one insightful study by Ferrari et al. In-situ Atomic Force Microscopy (AFM) technique demonstrated that monolayers of graphene could completely swell and soften upon introducing and removing water in a microfluidic system. The swelling of graphene could be up to (~tens of nanometres), and graphene could also still retain its intrinsic elastic properties upon contact with water [36]. This study demonstrates the excellent mechanical properties of the monolayer graphene for various membrane applications. Although monolayer graphene is strong, the formation of defects and nano-sized pores could deteriorate its mechanical properties for membrane applications [17]. This issue, however, can be solved by incorporation into the interconnected matrix of nanotubes [37]. Considering all the mentioned strategies, Yang et al. grew defect-free graphene, developed nanopore via oxygen plasma etching, followed by incorporation with single-walled carbon nanotube (SWNT) backbone, simultaneously solving the issues faced by defects, pore sizes, pore chemistry and also mechanical stability. Inspired by the structures of plant leaves, nanoporous graphene monolayer was incorporated into SWNT as mechanical support. They first integrated monolayer CVD-grown defect-free graphene into SWNT, followed by oxygen plasma etching under various times. Tuneable pore sizes of ~0.55 nm, ~0.63 nm, and ~1.41 nm were achieved proportional to plasma etching time. Furthermore, 80% of the pores had sizes ranging from ~0.5-0.75 nm, representative of their uniform distribution [37]. In fact, pore homogeneity is a crucial parameter since uniform pore distribution would reduce pressure difference due to lessened frictional loss and pressure drop across the membrane [44]. Interestingly, the tensile strength of the SWNT was also enhanced via incorporation with the monolayer graphene (Figure 2.1.2 e-h). Water and salt permeance increased proportionally to the plasma etching time. The 10 seconds of plasma etching resulted in water permeance of 20.6 LMHB and NaCl rejection of 98.1%, which was stable for 24 h of the test. The

membranes were also tested under reverse osmosis cross-flow filtration system, demonstrating an outstanding water flux of 97.6 LMHB and a reasonable salt rejection rate of more than 85 % [37].

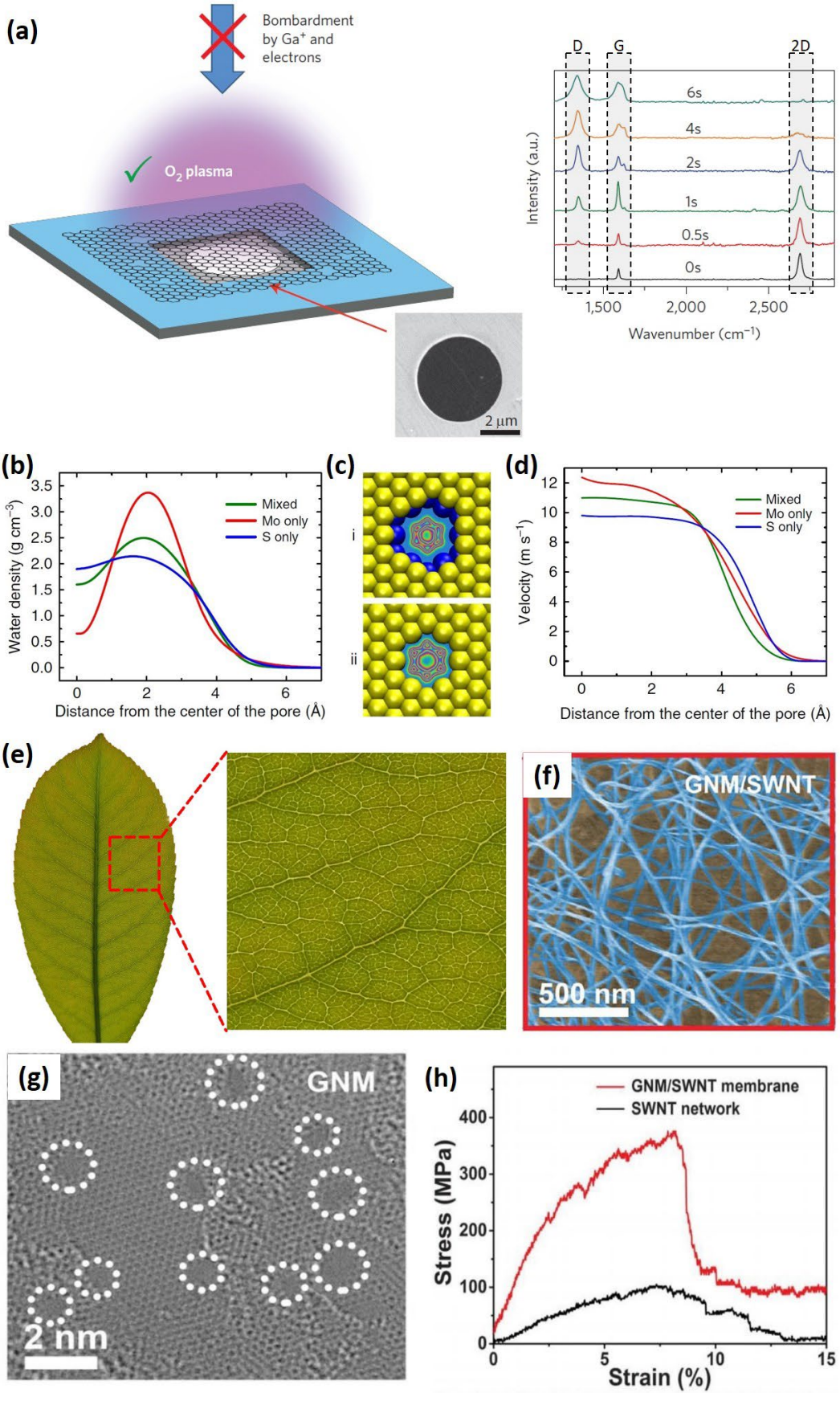
(a)
Bombardment by Ga+ and electrons
O2 plasma
2 μm
D
G
2D
6s
4s
2s
1s
0.5s
0s
Intensity (a.u.)
1,500
2,000
2,500
Wavenumber (cm−1)
(b)
Water density (g cm−3)
Mixed
Mo only
S only
Distance from the center of the pore (Å)
(c)
i
ii
(d)
Velocity (m s−1)
Mixed
Mo only
S only
Distance from the center of the pore (Å)
(e)
(f)
GNM/SWNT
500 nm
(g)
GNM
2 nm
(h)
GNM/SWNT membrane
SWNT network
Stress (MPa)
Strain (%)

Figure 2.1.2. Extrinsic Nanoporous membranes. *a) Oxygen plasma etching of graphene monolayer as an effective nanopore fabrication technique, together with the Raman spectra under different plasma etching time. Reproduced with permission [24]. Copyright 2015, Nature Publishing Group. The effect of pore chemistry for nanoporous MoS_2 membrane, depicting: b) Water distribution in the radial direction with different pore chemistry. c) Density map of water distribution for (i) Mo only and (ii) S only pores. d) The velocity of water molecules as a function of distance from the center of the nanopore. Reproduced with permission [35]. Copyright 2015, Nature Publishing Group. Nature-mimicking fabrication of graphene incorporated with SWNT depicting: e) The structure of the plant leaves, f) SEM image, g) Aberration-corrected STEM image of graphene-nanomesh (GNM), h) Stress-strain of SWNT and its composite with graphene under uniaxial tensile strength. Reproduced with permission [37]. Copyright 2019, American Association for the Advancement of Science (AAAS).*

From the studies mentioned above, we can infer that the fabrication of uniform and defect-free graphene is the first step to block the movement of unwanted ions. What's more, the technique of nanopore formation could alter the nature of pore chemistry, which has a consequential effect on water permeability. And lastly, the mechanical fragility of the monolayers can be solved via the incorporation of carbon nanotubes backbone. Although theoretical studies demonstrate excellent potentials of TMD's, no experimental research has been performed on these types of membranes until now. Recently Thiruraman et al. and Ryu et al. demonstrated the fabrication of atomic vacancies fabricated in MoS_2 and WS_2 [45, 46]. These experiments could lay the foundation for deploying TMD monolayers with subnanometer pores for water desalination applications.

2.1.3.2. Intrinsic pores

Although most of the researches are devoted to developing extrinsic pores on monolayers, less focus is put forward on materials with intrinsic pores. Materials with built-in pores not only eliminate the tedious pore fabrication process but also results in higher mechanical strength and filtration performance. In this regard, scientists studied various materials such as the family of covalent triazine frameworks [47, 48], metal organic frameworks [49, 50], and graphynes [51-54] for water desalination.

Some materials, such as the family of covalent triazine frameworks (CTF), more widely known as graphitic carbon nitride (g-C_3N_4), have the intrinsic in-plane nanopores that theoretically enable the sieving of monovalent ions [47, 48]. Favored by the high chemical and structural stability of g-C_3N_4, Lin et al.

theoretically simulated water desalination across CTF with various configurations (Figure 2.1.3 a). In order to reduce the effective pore size, two types of chemical functional groups of –Cl and $–CH_3$ were further added. Due to the negative charges of –Cl functionalized CTF (CTF-Cl) that attracts the positive sodium ions, this membrane showed lower salt rejection of 96 % compared with the non-polar $–CH_3$ functionalized CTF (CTF-CH_3) with 100 % salt rejection. The water permeability of CTF-Cl was, however, higher than that of CTF-CH_3 (Figure 2.1.3 b) [47]. This phenomenon was identical to hydroxylated and hydrogenated graphene nanopores, where the latter showed a significantly higher water permeability compared with the former due to the presence of negative charges on the oxygen atoms of the hydroxyl functional groups [34].

Metal organic frameworks (MOF) have been popular for water purification. However, their pore sizes are not suitable for monovalent ion sieving. This issue limited their application only to divalent ion sieving and capacitive deionization [55, 56]. Recent studies, however, demonstrated that by stacking 2D MOF, the effective radius of the in-plane nanopore could be reduced, rendering them operational for monovalent ion sieving [49, 50]. In one study by Zhou et al., the effect of MOF stacking orientations was investigated on its desalination performance. Although MOF has intrinsic pore sizes of 1.58 nm, unsuitable for monovalent ions blocking, their stacking in multilayer offset fashion can reduce the pore size down to 0.89 nm. Using molecular dynamics simulation, they demonstrated 100% $MgCl_2$ rejection with two orders of magnitude higher water permeance compared with commercial nanofiltration membranes. MOF in fully-eclipsed configuration shows higher water permeance but lower $MgCl_2$ rejection compared with MOF in offset-eclipsed fashion (Figure 2.1.3 c,d) [49]. Other classes of MOF with pore sizes of 0.8 nm could also be employed for desalination with water fluxes that are nine times higher than that of MoS_2 or graphene and salt rejection of nearly 90 %. The salt rejection could reach approximately 100 % with stacking two layers only [50].

The family of graphynes could also be promising for water desalination due to their tunable pore sizes relative to their structural configurations [51-54]. Via molecular dynamics simulations, Lin et al. investigated the effect of acetylenic linkage lengths (*N*) of graphyne on its desalination performance. Upon increasing

this linkage number, the pore diameters were also correspondingly increased with the values of 3.8, 5.4, 7.0, and 8.6 Å (Figure 2.1.3 e,f). The water permeability was directly proportional to the linkage number, and it could be increased from 2.9 to 4.5 × 10^{-9} m Pa^{-1} s^{-1}. The 100% salt rejection, however, could only be achieved for *N*=3 (i.e., graphtriyne) with an effective pore diameter of 3.8 Å (Figure 2.1.3 g) [52].

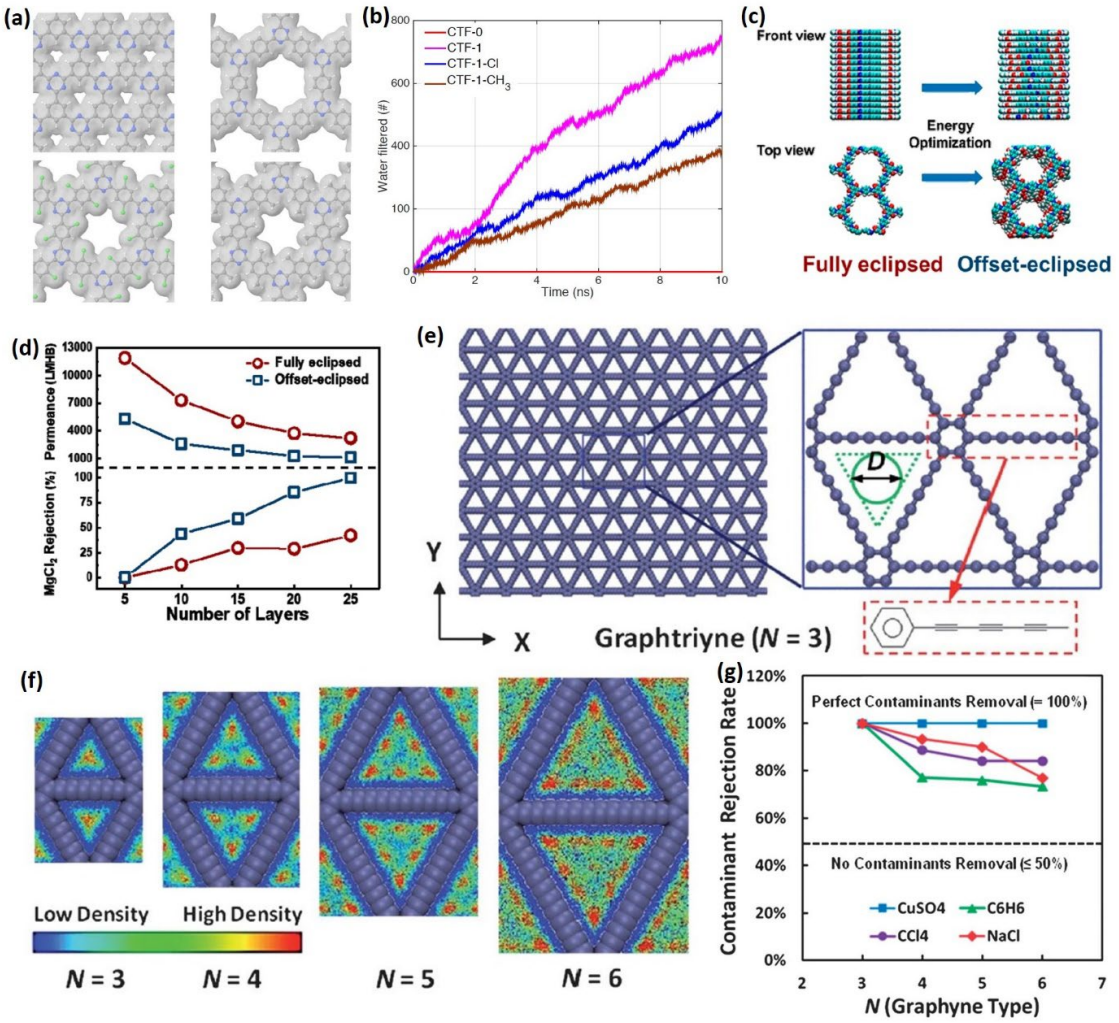

Figure 2.1.3. Intrinsic Nanoporous Membranes. *a) Covalent triazine frameworks (CTF) with various configurations and chemical functional groups, CTF-0 (top left), CTF-1 (top right), CTF-1-Cl (bottom left), CTF-1-CH_3 (bottom right). b) Theoretical simulation of water permeance for CTF. Reproduced with permission [47]. Copyright 2015, Royal Society of Chemistry. c) Multilayer MOF stacked in two styles of fully eclipsed and offset-eclipsed. d) Water permeance and $MgCl_2$ rejection as a function of the number of stacked MOF layers. Reproduced with permission [49]. Copyright 2019, American Chemical Society. e) Atomic structure of the graphyne showing the effective pore diameter d) of the triangular nanopore. f) Increasing the number of acetylene linkage also increase the effective pore diameter and water density. g) The rejection rate of different contaminants ($CuSO_4$, C_6H_6, CCl_6, and NaCl) as a function of the acetylene linkage number (N). Reproduced with permission [52]. Copyright 2013, Royal Society of Chemistry.*

Up until now, there is no experimental research on deploying these materials for water desalination. Fabrication of defect-free monolayers with intrinsic nanopores may be the first step in realizing these materials for water desalination applications.

2.1.4. Stacked membranes

The other alternative to the 2D nanoporous monolayer membranes is the 2D stacked membranes where the solute passes via nanochannels between nanosheets. These membranes can be produced via facile techniques such as vacuum filtration, which eliminates the costly CVD process, rendering them highly cheap and scalable to produce in commercial scales. This section is mainly devoted to the challenges associated with these types of membranes.

2D materials that are dispersed in liquid environments can be stacked on top of one another using the vacuum filtration technique. However, the stacked nanosheets often re-disperse when tested under actual water purification. The re-dispersion of these nanosheets is referred to as “swelling” in the membrane community. The swelling often results in membrane disintegration, especially when deployed under cross-flow conditions [16]. Also, the swelling widens the interlayer spacing and results in membrane failure due to the permeation of monovalent ions. It was found that when graphene oxide (GO) membrane is immersed in aqueous solutions, hydration occurs, developing negative charge on GO and resulting in membrane disintegration due to electrostatic repulsion effects [57]. Finding a way to bind these nanosheets together would ultimately solve this issue. In addition to fixing the interlayers distances, tuning these distances is also consequential for achieving an optimum selectivity/permeability tradeoff (i.e., larger interlayer spacing yields higher water permeability but lower salt rejection rate and vice versa) [26].

In this section, our primary focus is to discuss the techniques to tune and fix interlayer spacing of 2D materials yielding robust, stable, and high-performance membranes. The first section elaborates tuning and adjusting interlayer distances without any external component placed within interlayers, while the second section deals with inserting a foreign agent between nanoflakes. In the third

section, we discuss anti-swelling 2D materials (i.e., 2D materials that show diminished degree of swelling when immersed in water) and the effect of salt rejection via Donnan exclusion, making un-necessary the tuning or fixing of interlayer distances.

2.1.4.1. Tuning interlayer distances without external component

There are several techniques to tune and fix the interlayer distances of 2D materials such as controlled-reduction [58-61], dihydroxylation [28], and application of external pressure [25, 62, 63]. We will review these strategies in this part.

Controlled-reduction of GO could be a promising alternative to tune its interlayer spacing and restrict its swelling [58-61]. Molecular dynamics simulation showed that swelling of GO could be controlled by optimizing both the flake oxygen content and membrane water content [59]. This study implies that controlled-reduction of GO to reduced graphene oxide (rGO), where oxygen functional groups are partially reduced, could yield 2D stacked membranes of various interlayer sizes [60]. The tuning of interlayer distances for the graphene-based membrane can be achieved by the degree of GO reduction from large interlayer spacing for GO (~10 Å) to short interlayer spacing for rGO (~ 3.5 Å). In one study by Liu et al. complete reduction of GO to rGO was achieved via reducing GO with hydrogen iodide vapor. The free-standing graphene showed excellent water permeability but modest salt rejection due to the loss of polar groups [61].

Dehydroxylation of chemical bonds, followed by covalent bond formation induced by thermal annealing, could be a simple technique to cross-link the 2D nanosheets together [28]. In fact, the thermal annealing of GO renders possible the partial and controllable reduction of GO with interlaying spacing tunability. However, this comes at the expense of losing polar groups, yielding moderate salt rejection performance [43, 64]. Lu et al., however, found that the mild annealing of MXene resulted in covalent bonds formation between laminates in a self-crosslinking fashion. This cross-linking occurred via dehydroxylation of MXene sheets where Ti–OH functional groups tend to dehydrate and form stable Ti-O-Ti bonds with fixed interlayer spacing (Figure 2.1.4 a). Increasing annealing

temperature up to 80 °C resulted in almost 100% salt rejection (Figure 2.1.4 b). Interestingly, MXene had an interlayer spacing of ~13 Å, that is much larger than the hydrated radius of Sodium (7.5Å), suggesting surface polarities and hence, Donnan exclusion effect to remain even after annealing. However, the water permeability of this stacked membrane is rather low, which may be due to surface-induced hydrophobicity via dehydration of MXene [28]. This issue promotes scientists to quest for other interlayer tuning techniques without surface chemistry modification of nanosheets such as the application of external pressure [25, 62, 63].

Scientists expressed different opinions on the impact of external pressure on the performance of stacked membranes. Talyzin et al. suggested that increasing filtration pressure would increase the permeation of water molecules in the interlayers, leading to layers expansion [62]. Furthermore, Sun et al. suggested that applied pressure lessened water-ion interaction and yielded lower ionic selectivity [63]. Given these contradicting ideas, Li et al. developed a technique where water molecules did not play a role in compressing GO membranes. Instead, the external pressure was the main factor in the size-controlling of interlayers (Figure 2.1.4 c). In this technique, two face-to-face GO membranes were pressed together by two punched steel plates. Multiple ultrafiltration membranes were required to weaken the indentation on GO membrane and also to uniformly distribute the external pressure. The filtration performance was performed under cross-flow filtration while external pressure was maintained vertically (Figure 2.1.4 d). The application of 6.0 MPa resulted in the NaCl rejection rate as high as 96.1 % with water permeability of 22 LMHB (Figure 2.1.4 e). Since the X-ray diffraction (XRD) technique is challenging to characterize GO under external pressure, the interlayer distances of GO was instead obtained by measuring the thickness of GO membrane via a contact thickness gauge with high accuracy. The interlayer distances were successfully tuned relative to the external pressure (Figure 2.1.4 f). The XRD tests demonstrated that after removing external pressure, the interlayer distances of GO nanosheets went back to their original value. There are two main drawbacks associated with this technique that is first, the necessity of applying continuous external pressure

during filtration and second, the presence of multiple ultrafiltration membranes, which reduces water permeability [25].

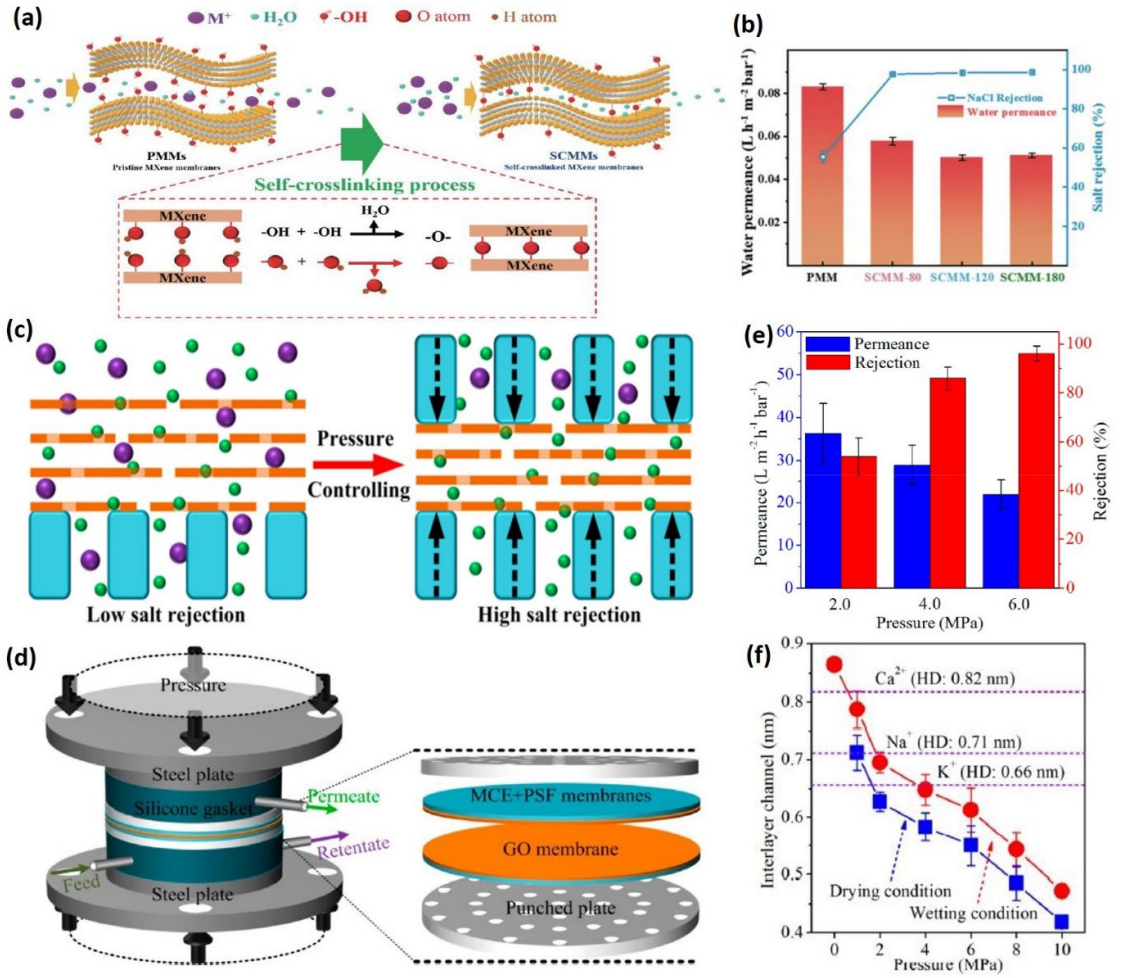

Figure 2.1.4. Tuning interlayer spacing without external components. *a) Self cross-linking of MXene via dehydroxylation effect. b) Water permeance and salt rejection for the MXene membrane annealed at different temperatures. Reprinted with permission [28]. Copyright 2019, American Chemical Society. c) Application of external pressure as a technique for regulating interlayer distances. d) The steel plates maintain external pressure, and water is desalinated under cross-flow filtration. e) Water permeability and NaCl rejection as a function of external applied pressure. f) The interlayer distances can be controlled as a function of applied external pressure. The hydrated radii of cations are also shown for comparison. Reproduced with permission [25]. Copyright 2018, American Chemical Society.*

2.1.4.2. Tuning interlayer distances with an external component

In the above section, tuning of interlayer spacing was achieved intrinsically without the need for a foreign/third-party agent. However, we inferred that the intrinsic functional groups of 2D materials are often not sufficient to develop robust membranes with stable and high performances. Besides, chemical

functional groups of 2D materials could also degrade upon self cross-linking. In this section, four methods of interlayer distance tuning and fixation via external components are elaborated. These components can be water molecules [26], metal ions [65-67], monomers [68-74], and polymers [75, 76] that we correspondingly discuss in the sections below.

2.1.4.2.1. Water molecules

Abraham et al. reported the fabrication of interlayer-tuned GO membrane via relative humidity control, where water molecules intercalated within GO interlayers. The interlayer spacing could be tuned from 6.4 Å to 9.8 Å by controlling the atmospheric humidity. Also, epoxy was applied between GO laminates to prevent swelling of GO layers (Figure 2.1.5 a-c). This strategy hindered swelling of GO successfully and yielded NaCl rejection of nearly 97% [26]. Although this study reports a novel membrane with filtration across vertical nanochannels, the fabrication is rather tedious. This is because interlayer distance tuning (i.e., relative humidity control) and interlayer distance fixing (i.e., epoxy binding) are two separate processes. In the following sections, cross-linking via external components will be discussed as a method that not only retains chemical functional groups intact but also adjusts the interlayer distances and also fixes the interlayer spacing, killing three birds with one stone.

2.1.4.2.2. Metal ions cross-linkers

2D materials with abundant functional groups such as GO [65, 66, 77], and MXene [67] can be cross-linked via intercalating metal ions. Modification of GO with small percentages of metal ions such as Mg^{2+} and Ca^{2+} was deemed as an effective strategy to enhance the mechanical stiffness of GO paper significantly. This enhancement was mainly due to electrostatic bonding between metal ions and the carboxylate groups on the edges of GO [77]. To shed further insight into this mechanism, Chen et al. performed a detailed study via hydrated Na^{+} ions. They found the hydrated ion to adsorb via hydrogen bonds at the regions where oxidized groups and aromatic rings co-exist (Figure 2.1.5 d-f). Further, DFT

calculations demonstrated additional pi bonding between hydrated cations and the aromatic rings. Deploying ions of varying hydrated diameter could effectively tune and fix the interlayer distances. The interlayer distances were directly proportional to the hydrated radius of ions in the corresponding Li^+>Na^+>K^+ order (Figure 2.1.5 g) [65]. Specifically, the hydrated radius is directly proportional to the hydration energy in the ionic shell [5]. GO membranes modified by KCl showed negligible swelling when immersed in different ionic solutions (Figure 2.1.5 h).

Amongst the three alkali anions, K^+ displayed the highest interaction energy and an enormous van der Waals volume (Figure 2.1.5 e), demonstrating the fact that potassium ion is the most stable within GO interlayers. Ghaffar et al. obtained identical results where GO cross-linked by Li^+ and Na^+ was not stable in the water while those intercalated by K^+ were stable [66]. The KCl-controlled membranes demonstrated negligible ion permeation rates for Na^+, $Mg^{+,}$ and Ca^+ ions, with cross-linked GO showing ions rejection rate of more than 99% relative to the pristine GO. However, leaking of ions could partially occur from GO interlayers that are probably due to the weak nature of these hydrogen bondings [65].

In another research by Ding et al. the Al^{3+} could intercalate within $Ti_3C_2T_x$ MXene membrane, binding the nanosheets together (Figure 2.1.5 i). The abundant surface terminations such as =O, -OH and –F functional groups enable the tuning and controlling of its d-spacing. The d-spacing change could be successfully reduced from 3.2 Å to 0.6 Å after Al^{3+} intercalation. Moreover, this strategy proved effective when modified MXene showed significant reduction in the permeation rate of monovalent and divalent ions compared with unmodified MXene (Figure 2.1.5 j). The covalent binding between Al^3 and –O functional groups on MXene was so robust that no leaking was observed [67].

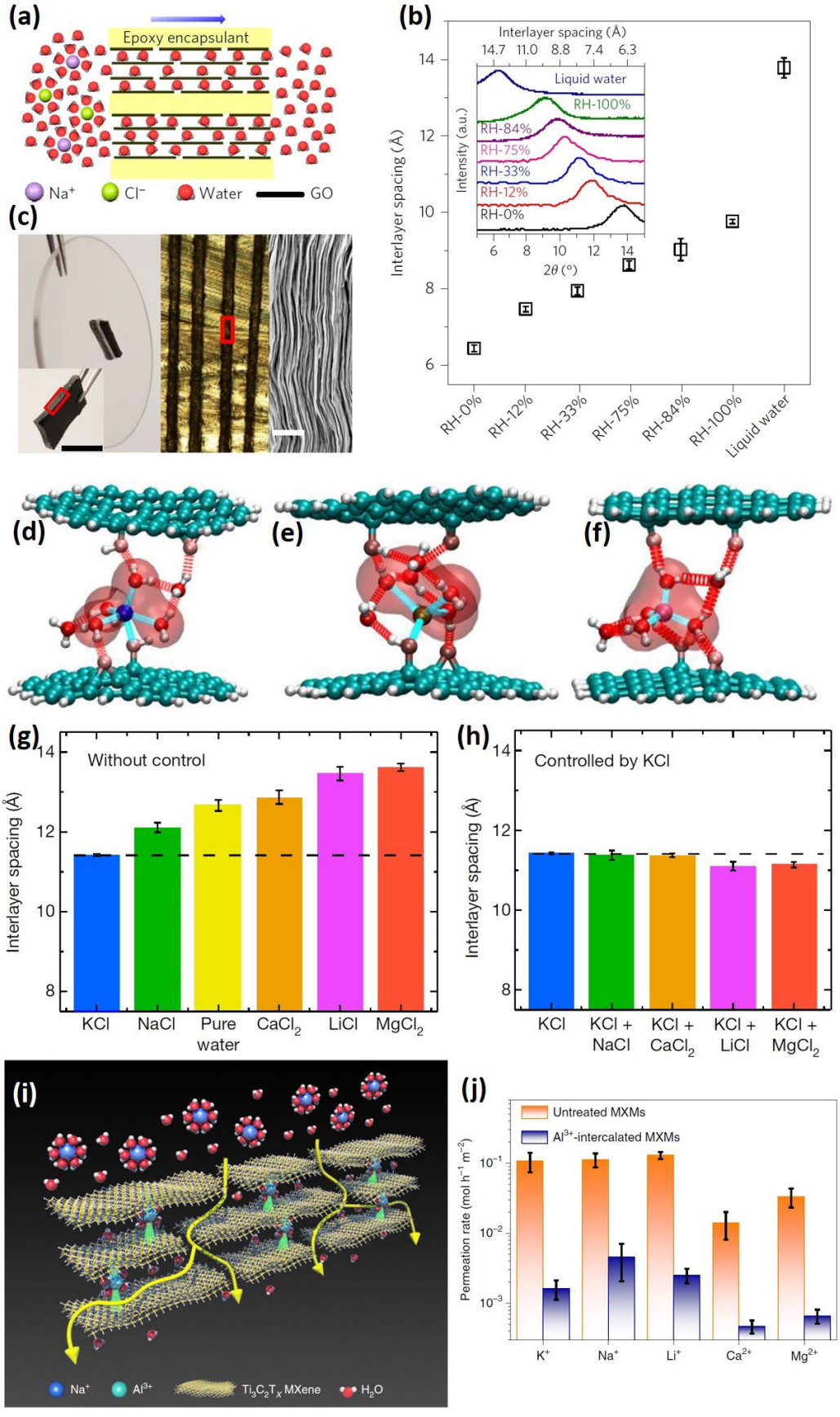
(a)
Epoxy encapsulant
Na+
Cl−
Water
GO
(b)
Interlayer spacing (Å)
14.7 11.0 8.8 7.4 6.3
Liquid water
RH-100%
RH-84%
RH-75%
RH-33%
RH-12%
RH-0%
Intensity (a.u.)
2θ (°)
Interlayer spacing (Å)
RH-0%
RH-12%
RH-33%
RH-75%
RH-84%
RH-100%
Liquid water
(c)
(d)
(e)
(f)
(g)
Without control
Interlayer spacing (Å)
KCl
NaCl
Pure water
CaCl2
LiCl
MgCl2
(h)
Controlled by KCl
Interlayer spacing (Å)
KCl
KCl + NaCl
KCl + CaCl2
KCl + LiCl
KCl + MgCl2
(i)
Na+
Al3+
Ti3C2Tx MXene
H2O
(j)
Untreated MXMs
Al3+-intercalated MXMs
Permeation rate (mol h−1 m−2)
K+
Na+
Li+
Ca2+
Mg2+

Figure 2.1.5. Tuning Interlayer spacing with water and ions. *a) Tuning GO interlayer spacings via inserting a different number of water molecules into GO interlayers by changing the relative humidity. Epoxy can be utilized to fix interlayer spacings. b) interlayer spacing as a function of relative humidity. c) Digital photograph and SEM image of the membrane with exposed vertical nanochannels. Reproduced with permission [26]. Copyright 2017, Nature Publishing Group. The most stable geometries of the hydrated cation and GO cluster depicting: d) Na^+, e) K^+, f) Li^+. The transparent red area is the van der Waals volume of the hydration water molecule. g) Interlayer space tuning via different ionic solutions, including pure water. h) The effect of ionic solutions on interlayer spaces of KCl-controlled GO. Every ionic solution is added with an identical amount of KCl to prevent leaking of potassium ions from GO interlayers. Reproduced with permission [65]. Copyright 2017, Nature Publishing Group. i) Inserting Al^{3+} within $Ti_3C_2T_x$ MXene layers as a technique to tune its interlayer distances. j) Ion permeation rate through un-treated and Al^{3+} MXene. Reproduced with permission [67]. Copyright 2020, Nature Publishing Group.*

2.1.4.2.3. Monomer cross-linkers

Cross-linking of 2D materials via organic molecules is another effective strategy in tuning and fixing the interlayer distances. Covalent cross-linking of GO with organic monomers could be achieved via esterification [68], and nucleophilic substitution reaction [69-74] with the latter being more popular due to not deploying highly oxidizing acids. Nucleophilic substitution reaction is usually performed via reactions between aliphatic/aromatic diamines and oxygen-containing groups of 2D materials [69]. The reason for choosing diamine molecules over single amines is that two adjacent nanosheets could react with each amine group, yielding cross-linking between two neighboring nanosheets. In one study by Hung et al., GO was cross-linked by three diamine monomers, namely ethylenediamine (EDA), butylenediamine (BDA) and p-phenylenediamine (PDA). The tuning of interlayer distances was directly proportional to the monomer chain length. Furthermore, upon immersion of GO in water the interlayer stretching was significantly suppressed compared with unmodified GO (Figure 2.1.6 a-c). FTIR result demonstrated total attenuation of hydroxyl groups due to condensation and nucleophilic substitution reactions between amines and oxygen-containing groups of GO, forming C-N covalent bonds [69]. Besides the aforementioned symmetric monomers, asymmetric molecules such as polyvinyl alcohol (PVA), m-phenylenediamine (MPD), 1,3,5-benzenetricarbonyl (TMC), and the mixture of MPD/TMC could also tune interlayer distances of GO (Figure 2.1.6 d) [72].

Apart from the nature of cross-linkers, the ratio between GO and monomers is also very crucial. Hung et al. and Qian et al. utilized an almost identical ratio of GO and diamine monomer and could successfully tune interlayer distances with stable performance for separating water/alcohol mixture [69, 70]. To apply this strategy for water desalination, Meng et al. developed EDA monomer cross-linked with GO but deployed a significantly lower amount of monomer, resulting in low salt rejection performance of 36 %. The lack of pressure during the filtration process may be another reason for this unsatisfactory performance [71]. To solve this issue, Hung et al. also utilized a small amount of monomer to GO ratio but instead deployed external pressure during membrane fabrication. Consequently, they could adjust interlayer spacing and attained negligible salt permeability of ~1.5 g h^{-1} m^{-2} that was several orders of magnitude lower compared with pristine GO (Figure 2.1.6 e). The smallest possible interlayer distance they could obtain was nearly 10 Å, via MPD/TMC (Figure 2.1.6 f) [72]. Surprisingly, the interlayer distances via MPD alone in this work (~11 Å) is 1Å smaller than that previously reported [69]. This fact demonstrates the importance of GO and monomer ratio to tune interlayer distances, where extensive monomer/GO loading could compress GO nanosheets further. Nicolai et al. theoretically simulated the effect of monomer density on the performance of cross-linked GO and found a very consequential relation between monomer density and water desalination performance [78]. Hence, utilization of optimum monomer to GO ratio and also the pressure during filtration are important parameters to consider for effective adjustments and fixation of GO layers for water desalination applications.

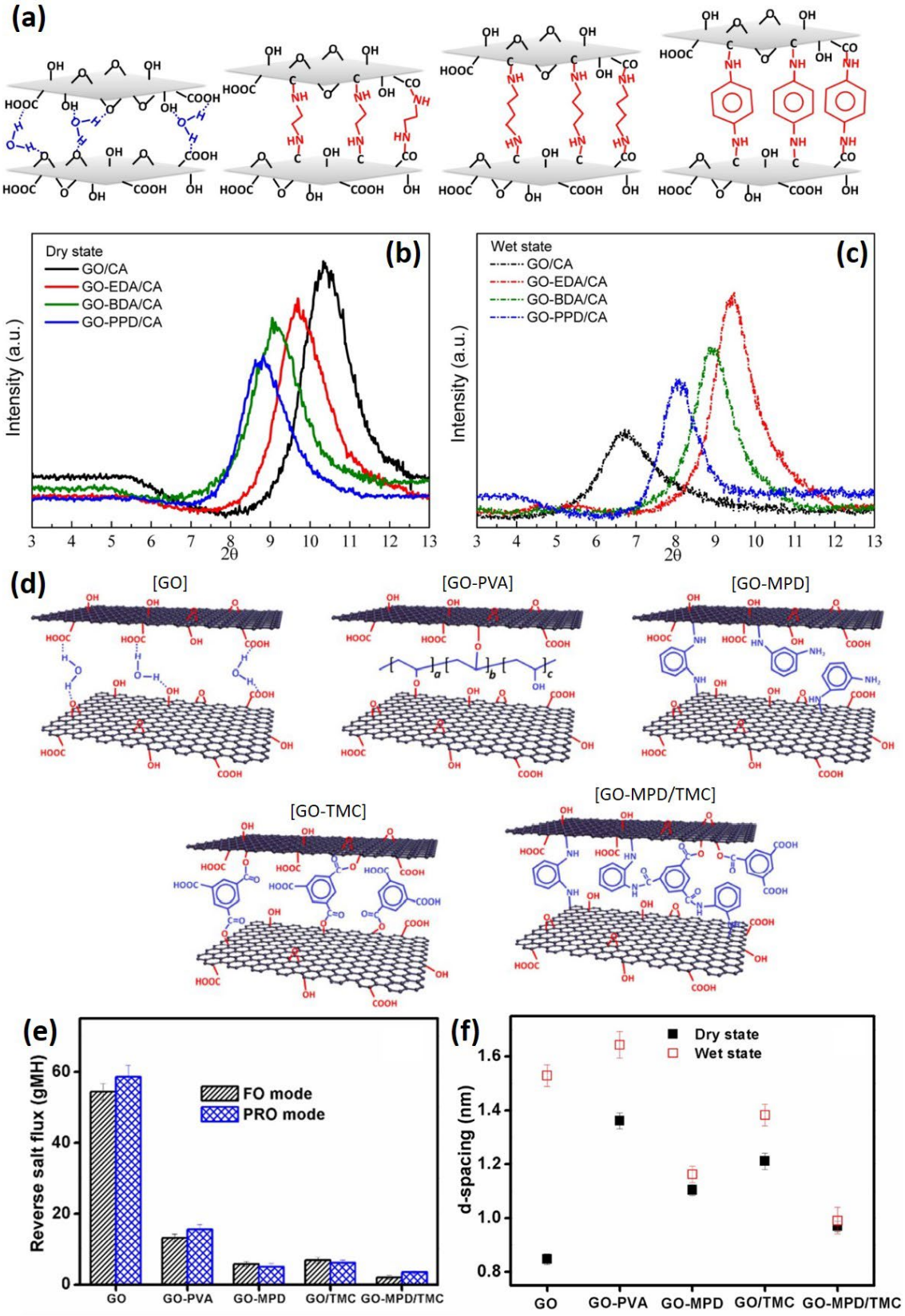

Figure 2.1.6. Tuning interlayer spacing with monomers. *a) Controlling interlayer distances of GO with symmetric diamine monomers of different chain lengths. Low angle XRD to measure d-spacing and interlayer distances of pristine and diamine-functionalized GO in b) dry state, and c) wet state. Diamine functionalization of GO results in a negligible change in d-spacing, whereas*

pristine GO swells significantly. Reproduced with permission [69]. Copyright 2014, American Chemical Society. d) Asymmetric molecules as another strategy to tune interlayer spacing of GO. e) reverse salt flux, and f) corresponding d-spacing in the wet and dry state. Reproduced with permission [72]. Copyright 2019, Elsevier.

We have seen from the previous works that apart from monomer chain length, the ratio of monomer/active material and also the application of external pressure during filtration are essential parameters to consider for these classes of membranes. Although the above-mentioned works tunes and fixes the interlayers successfully, the interlayer distances are significantly larger than the hydrated radii of cations. This fact renders the monomer cross-linked membranes, not an option currently for practical water desalination. Applying a smaller chain molecular bridge could probably resolve this issue.

However, the lack of nucleophilic sites and oxygen functional groups on other types of 2D materials renders impossible the cross-linking reactions, prompting researchers to quest for alternative cross-linking strategies such as polymers. In-situ polymerization of 2D materials can physically bind and cross-link them together, irrespective of the nature of 2D materials' functional groups. We discuss these classes of cross-linkings in the subsequent section.

2.1.4.2.4. Polymer cross-linkers

Several studies reported the incorporation of GO and its composites into polymers, either in the membrane support layer [79, 80], or in the active layer [81-83]. In these studies, the incorporation of 2D materials enhanced not only the mechanical rigidity of the polymers but also its hydrophilicity and, consequently, its water permeability [6]. These studies, however, do not report the tuning or fixation of GO layers. It is by Wang et al. group where GO is cross-linked and twinned together via free-radical polymerization [75]. What's more, the vacuum filtration pressure could adjust the GO interlayer distances [76]. In their group, they invented a free radical polymerization technique where *N, N'-methylene-bis-acrylamide* (MBA) functions as cross-linker, *N-Isopropylacrylamide* (NIPAM) as monomer followed by *Ammonium Persulfate* (APS) as initiator. These precursors are then in-situ polymerized with GO to developed a highly cross-linked network of GO@polymers (Figure 2.1.7 a,b). The prepared membranes demonstrated

outstanding anti-swelling behavior with unique desalination capability [75, 76]. Altering the vacuum level could tune the thickness as well as the crystallinity of membranes (Figure 2.1.7 c,d). Membranes prepared under low vacuum showed amorphous structure, while high vacuum resulted in enhanced membrane crystallinity. Although membranes showed reduced thickness upon increasing vacuum pressure, this did not alter interlayer distances as the changes were merely from amorphous to crystalline, with the latter slightly outperforming the former (Figure 2.1.7 e). The cross-linking of GO was so robust that membranes demonstrated anti-compaction properties where the structure remained stable under high pressure, whereas commercial polyamide membrane compacted and displayed reduced water flux (Figure 2.1.7 f) [76].

The study mentioned above showed that interlayer fixation could be achieved together with the controllability over membrane crystallinity. The interlayer spacing of the GO was found to be ~1 nm under 0.1 MPa of applied pressure [76]. The same group also prepared GO@polymer composite via the identical free radical polymerization technique but varied polymer precursors ratio. The spin-coated membrane achieved an interlayer spacing of 0.47 nm instead [75]. These different values may arise due to the varying amount of polymer precursors used. This mechanism, however, is not thoroughly investigated in these works and demands further studies. Hence, to tune the interlayer spacing of stacked sheets via polymer chains, one should consider the degree of polymerization and also the applied pressure.

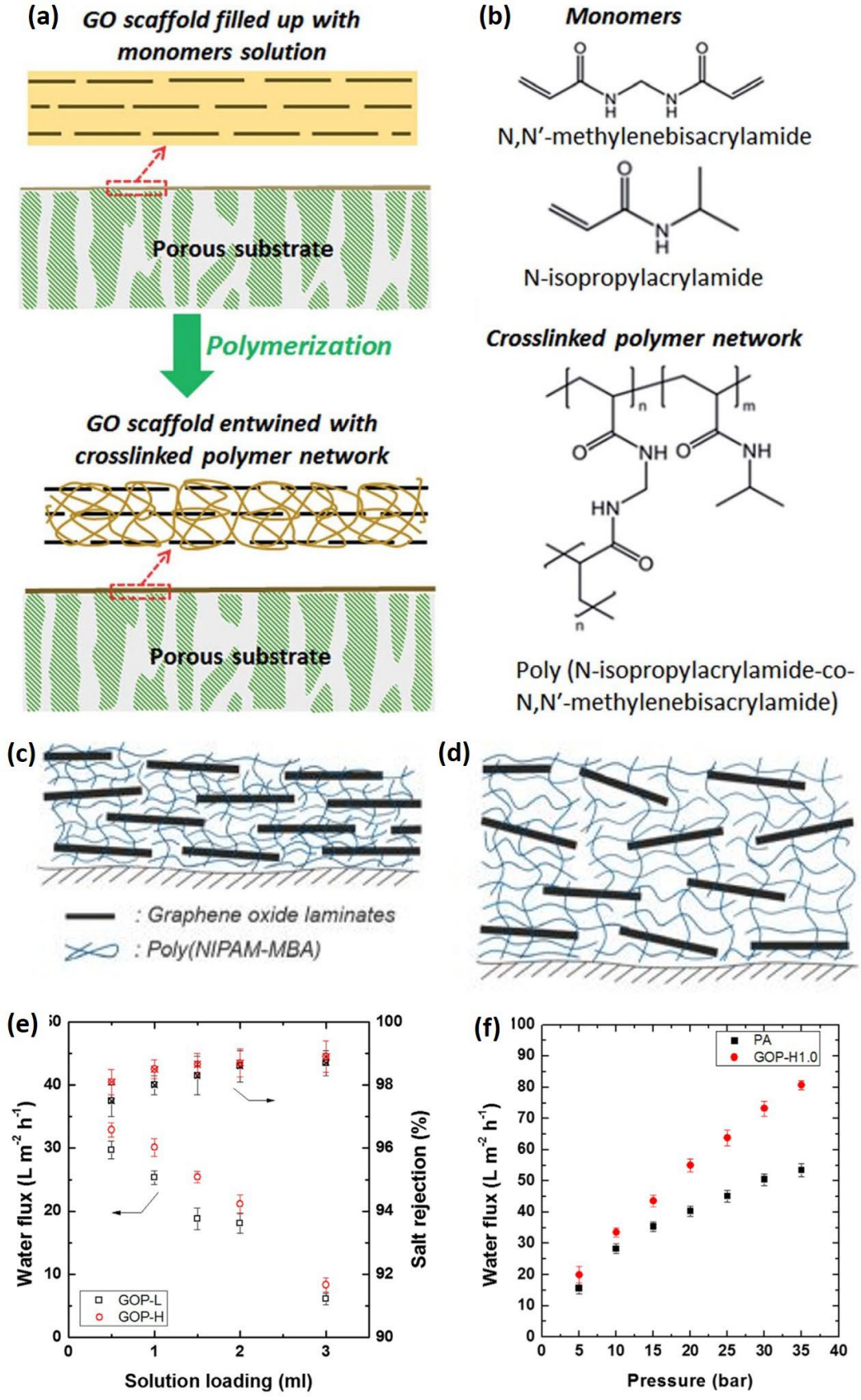

Figure 2.1.7. Polymer cross-linkers. *a) Schematic for in-situ free-radical polymerization of GO. b) Molecular structures of monomers MBA and NIPAM. Reproduced with permission [75].*

Copyright 2017, Royal Society of Chemistry. Fabrication of GO@polymer cross-linked membrane where the vacuum filtration pressure can tune the thickness and crystallinity of the membrane. The schematic of membranes prepared under c) high vacuum and d) Low vacuum. e) Water flux and salt rejection properties of GO@polymer membrane as a function of solution loading where GOP-L and GOP-H show membranes developed under low and high vacuum, respectively. The GOP-L shows lower membrane performance due to its amorphous structure. f) Comparison of water flux for GO-polymer membrane (GOP-H1.0) vs. commercial polyamide (PA) membrane as a function of applied pressure. Reproduced with permission [76]. Copyright 2018, Elsevier.

2.1.4.3. The issues beyond tuning interlayer distances

Besides the importance of tuning interlayer distances, we need to consider four significant issues for realizing practical applications of stacked membranes. These issues are first, the 2D materials with anti-swelling properties [84-86], the role of surface chemistry in 2D materials [27, 87], the function of a separate salt-blocking layer on top stacked membranes [29, 84], and lastly the binding between 2D materials and the substrate [29, 73, 88-90].

It is noteworthy to mention some of the 2D stacked membranes that are developed, such as MoS_2, demonstrates some intrinsic anti-swelling properties. More research devotion to these types of materials could greatly simplify the membrane fabrication process and increase their filtration stabilities. Interestingly, stacked MoS_2 nanoflakes demonstrated an identical interlayer spacing of (~0.65 nm) with that of the bulk MoS_2. This fact suggests that the electrostatic field on the surface of MoS_2 nanosheets is not high enough, probably rendering the re-stacking of nanosheets with interlayer spacing down to the size of its bulk structure. Moreover, due to these electrostatic field deficiencies and also the lack of hydrophilicity on the surface layers, fewer water molecules will be intercalated within the nanosheets, and hence swelling can be prevented [84, 85]. For the multilayer MoS_2 stacked membrane that is fabricated via CVD, this spacing was suitable to permeate water molecules and reject NaCl with 98% rates up to 24h [85]. However, for the vacuum-filter deposited membrane that was fabricated via solvent exfoliation of MoS_2, the rejection of NaCl was not satisfactory unless functionalized by organic dyes [84]. On the other hand, the MoS_2 membrane prepared via lithium exfoliation technique yielded negligible NaCl permeation on the order of 10^{-12} m^{-2} s^{-1} [86]. These studies emphasize that

although some materials may demonstrate anti-swelling properties, the role of the functional group and surface chemistry cannot be neglected. Hence, membranes with anti-swelling properties but without proper surface polarity are still un-operational [87].

To elucidate the role of surface chemistry, Song et al. incorporated pyridinic nitrogen sites on GO as polar groups to reject salts via the Donan effect. Increasing the nitrogen doping amount impeded the permeability of ions, specifically the monovalent K^+ and Na^+ (Figure 2.1.8 a,b). Interestingly, they observed no correlation for other nitrogen-bonding configurations such as pyrrolic-N and graphitic-N. This is due to the strong polarization effects and high adsorption energy of pyridinic nitrogen, rendering possible the significant electrostatic interactions with ions [27]. In another work, Ries et al. grafted different functional groups with varying degrees of polarity on MoS_2 nanosheets. They found that a small degree of functionalization can maintain salt rejection rates, but it can dramatically enhance water permeability due to interlayer expansion [87]. These two studies demonstrate that doping or chemical functionalization could optimize the surface polarity of 2D materials, making them useful for water desalination.

Apart from modifying the surface chemistry of nanosheets, functionalizing the top surface layers in the stacked membrane, via coating separate ionic or organic molecules, could also effectually reject salts via the Donnan effect [29, 84]. The coating of electrostatically-charged polymers on top of GO could dramatically enhance its $MgCl_2$ rejection rate by a factor of more than two times, reaching 96%. Besides, this additional layer did not reduce water permeability due to its hydrophilic nature. The surface charge of GO could be tuned from highly positive via polydiallyl dimethyl ammonium (PDDA) to highly negative via polystyrene sulfonate (PSS). The permeability of $MgCl_2$ increased upon altering membrane surface charge from positive to negative, while Na_2SO_4 displayed a reverse trend. This revealed that high valent anions $(SO_4)^{2-}$ and cations $(Mg)^{2+}$ are repelled by negatively-charged and positively-charged GO, respectively (Figure 2.1.8 c-f). For NaCl, however, the transport behavior remained approximately unchanged due to the electrostatic balance between monovalent co-ions and counter-ions [29].

Lastly, it is essential to state the effect of substrate chemical functional groups on the binding properties of the 2D stacked materials with its underlying support. Pre-treating the substrate in organic [73, 88, 89], or alkaline media [29, 90] could form abundant functional groups, yielding an enhanced interfacial adhesion between the substrate and 2D materials. In one study, Zhang et al. found that pretreating the ceramic tube in aldehyde-modified chitosan could develop plenty of O=CS groups that are beneficial for chemical binding with amine-functionalized GO. The AFM nano-scratch technique was utilized to measure the interfacial binding force of GO with the substrate. The pre-treated membrane showed the critical load at failure of 46.3 mN that is more than twice compared with the unmodified membrane (Figure 2.1.8 g-k) [73]. Their group also found that GO deposited on polyacrylonitrile (PAN) develops small cracks under cross-flow filtration. However, after treating PAN in NaOH no detachment was observed. This was attributed to the abundant oxygen functional groups on the surface of PAN after hydrolysis that could bind well with GO [90].

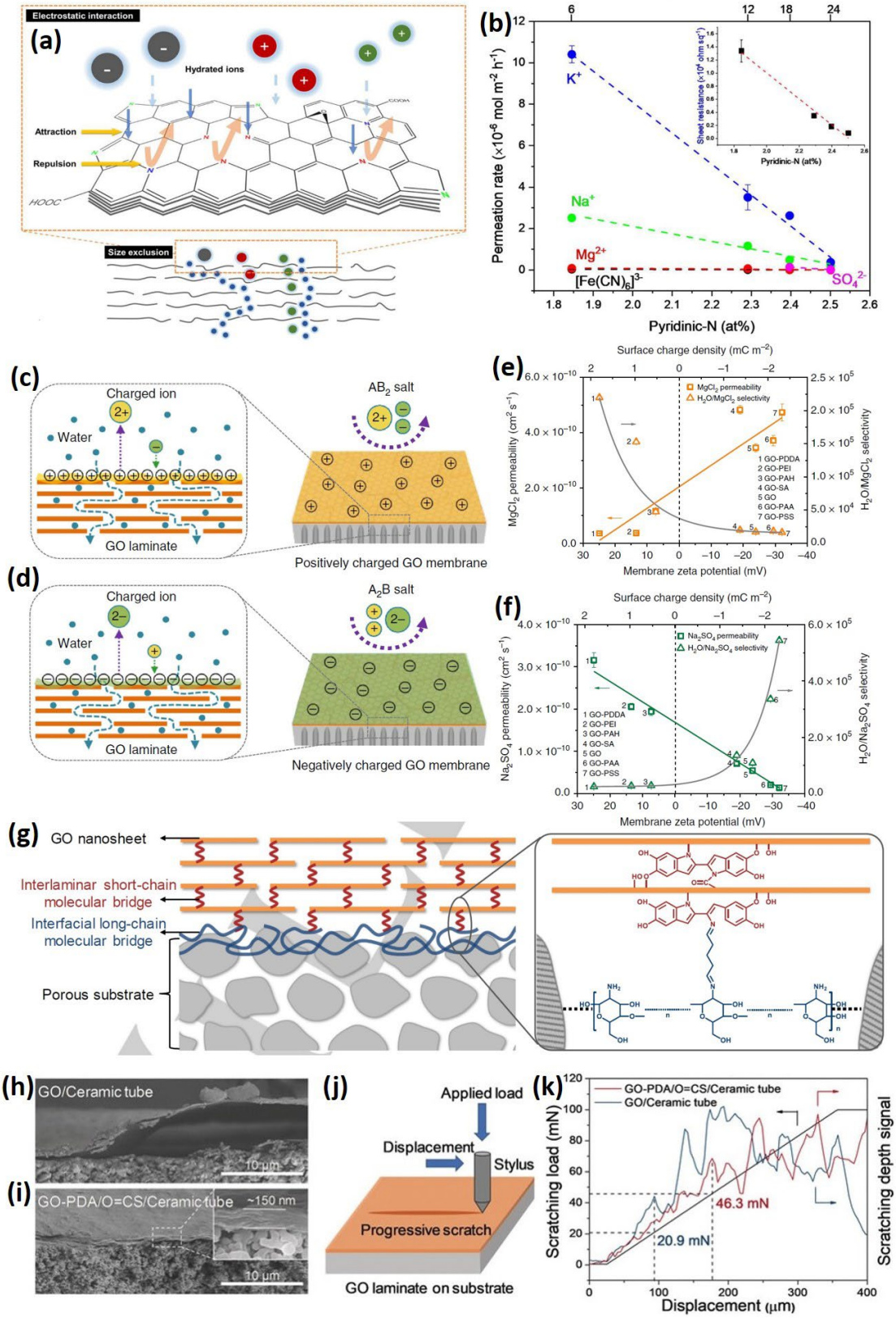

Figure 2.1.8. Issues beyond tuning interlayer spacings. *a) ion sieving via the combined effect of electrostatic repulsion and size exclusion. b) The relationship between pyridinic-N content of GO and permeation rate for various ions. Reproduced with permission [27]. Copyright 2018, American Chemical Society. Depositing positively and negatively-charged polyelectrolyte on GO*

to repel high-valent c) cations and d) anions. Permeability of e) $MgCl_2$ and f) Na_2SO_4 as a function of membrane zeta potential. Reproduced with permission [29]. Copyright 2019, Nature Publishing Group. g) The interfacial long-chain molecular bridge as a strategy to chemically bind GO with its substrate. The long-chain bridge (shown in blue) bind with amine-functionalized GO via O=CS groups. h) SEM image of GO and unmodified ceramic tube and i) modified with long-chain bridges. Molecular bridges prevent peeling-off from the substrate and also reduces the air gap between GO and its substrate, representative of its intimate contact. j) The setup for the AFM nano-scratch technique. k) Results of nano-scratch measurements with molecular bridges outperforming unmodified membrane in terms of the value of the critical load. Reproduced with permission [73]. Copyright 2019, John Wiley and Sons.

These studies suggest that the Donnan exclusion effect (where electrostatic fields are either in the surface of nanosheets or as a separate coated layer on the top surface of membranes) can be the principle filtration mechanism both for swelling and anti-swelling materials. Furthermore, membrane swelling, water permeability, and salt rejection rates are proportional to the surface polarities of 2D stacked membranes. Hence, the electrostatic charges on nanosheets that yield these trade-offs need to be delicately optimized and taken into consideration. Lastly, pre-treatment of the substrate to form chemical bonding with 2D materials and avoid its detachment is necessary for long-term and steady operation.

Table 2.1.1. Performance comparison of 2D material membranes for water desalination.

Membrane Classification		Membrane Materials	Preparation Technique	Salt rejection rate[a)]	Water flux[a)]	Stability	Test condition[a,b)]	Ref.
Nanoporous		Single-layer nano-porous graphene@ single-walled carbon nanotubes	CVD followed by oxygen plasma etching for subnanometer pore generation	87 %	97.6 LMHB	24 h	2000 ppm NaCl (cross-flow reverse osmosis)	[22b]
		Subnanometer porous monolayered graphene	CVD followed by Gallium ion bombardment	~10 % for [16.6 mM NaCl/glycerol ethoxylate]	~33 LMH	N/A	[glycerol ethoxylate/DI water] FO (~25 atm)	[20b]
		Single-layer nano-porous graphene	CVD followed by oxygen plasma etching for subnanometer pore generation	100 %	254 LMHB	25 h	[DI water/1M KCl] (FO)	[16a]
Stacked	Unmodified	Few-layered MoS_2	Chemical vapour deposition	99.5 % [DI water/0.1M NaCl] (FO)	322 LMHB	1.78% salt rejection degredation after 24 h	DI water (dead-end) under 1 bar	[46b]
		MXene	Vacuum filtration (self-cross-linked by heating)	99 %	0.06 LHMB	70 h	[DI water/0.2 M NaCl] (FO)	[17b]
		rGO and reduced by HI (Free-standing)	Vacuum filtration	0.2 $mol^{-1}\ h^{-1}\ m^{-2}$ [0.1 M NaCl/0.5M NH_4HCO_3] (FO)	57.0 LMH	N/A	[DI water/2M NaCl] (FO)	[36c]
		rGO laminates Interlayer spacing control using humidity control	Physical binding using epoxy (free-standing)	97 %	0.5 LMH	20 h	0.1M NaCl/3M sucrose (FO)	[16c]
		MoS_2 modified by organic dyes	Vacuum filtration	99 % [0.1mM/1M NaCl] (FO)	262 LMHB	8% salt rejection degradation after 3 h	1M NaCl under 1 bar (dead-end)	[46a]
		PDDA-functionalized GO	Pressure Filtration (~3 bar)	96%	14 LMH	120 h	50 ppm Na_2SO_4 (dead-end)	[18]
		Methyl-functionalized MoS_2	Vacuum filtration	87 %	80 LMH (dead-end) under 4 bar	15 h (20% water flux reduction)	[0.1M NaCl/3M KCl] (FO)	[47]

	Modified	Metal ions	GO cross-linked by K^+ ion	Drop casting (free-standing)	2.7 × 10^{-2} mol^{-1} h^{-1} m^{-2}	0.1 LMH	5 h	[0.25M KCL/0.25M KCL + 0.25M NaCl] (FO)	[39a]
			K^+ ion-modified GO	Doctor blade casting (free-standing)	82 %	100 LMH	80 min (37% water flux reduction)	100 mgL^{-1} NaCl (dead-end) under 1 bar	[39b]
		Monomers	GO cross-linked by EDA	Vacuum filtration	36.3 %	4.1 LMH	N/A	1000 ppm NaCl (dead-end) under 1 bar	[40c]
			MPD-TMC cross-linked GO	Pressure Filtration (5 bar)	~1.5 g h^{-1} m^{-2}	~18 LMH	350 min (1.3% water flux reduction)	[DI water/2M NaCl] (FO)	[40d]
		Polymers	GO cross-linked with polymer	Spin coating (Free radical polymerization)	99.9 %	25.8 LHM	Few weeks	[DI water/1M NaCl] (FO)	[41a]
			GO cross-linked with polymer	Vacuum filtration (Free radical polymerization)	98.5 %	35.6 LHM	N/A	[2000 ppm NaCl/DI water] (RO under 10 bar)	[41b]

[a)] ("Salt rejection rate" and "Water flux" are tested under identical conditions (i.e., "Test condition" column) unless stated otherwise. In that case, "Test condition" is pertinent to "Water flux".); [b)] (The forward osmosis (FO) is represented as [A/B], where A is the feed solution, and B is the draw solution.)

2.1.5. Summary and outlook

In this manuscript, we have reviewed the progress and challenges of developing 2D materials for membrane-based water desalination. Water desalination and ion sieving across 2D materials can be achieved either via physical size exclusion or electrostatic Donnan exclusion effect. Two classes of membranes can be developed based on 2D materials, which are monolayers with in-plane nanopores or the stacked nanosheets with nanochannels in between.

Water desalination can be achieved via monolayers with in-plane externally drilled nanopore. Several issues, such as defects, pore sizes, and pore surface chemistry, need considerations. Drilling an external pore on the surface of monolayers was traditionally done via the ion bombardment technique. However, new oxygen plasma etching has shown higher promise on graphene as it produces significantly higher water flux due to surface chemistry modifications, together with size tunability features. Due to the atomic layer thickness of these membranes, the mechanical properties also need to be improved via incorporation with nanowire backbone, such as carbon nanotubes. Several 2D materials, such as covalent triazine frameworks, metal organic frameworks, and graphynes, have subnanometer pore sizes for water desalination, where altering the phases or stacking configurations could optimize their pore sizes.

Compared with nanoporous monolayer membranes, 2D stacked membranes have better scalability and mechanical properties, but often re-disperse in liquid media and are thus required to be stabilized and fixed by some techniques. The interlayer distances of 2D stacked membranes can be optimized via controlled-reduction, dehydroxylation and, changing external pressure. Certain materials and applications demand inserting an external component in between the interlayers to cross-link and bind adjacent layers together. These components can be water molecules, metal ions, and organic monomers. The combined strategy of vacuum pressure and polymers can also be utilized to tune and fix interlayers, respectively. Apart from tuning and adjusting interlayer distances, some issues need to be considered. These issues are salt rejection via Donnan exclusion by modifying the surface polarities of the stacked nanosheets, and the chemical treatment of the substrate to increase its binding force with the stacked 2D materials.

Regarding nanoporous membranes, though researchers performed numerous theoretical and experimental studies on ions sieving via graphene nanopores, this area is still to be discovered for other types of 2D materials. Furthermore, the nature of pore chemistry that relies on pore fabrication technique should be given further attention in future works. Lastly, there should be more focus on the practical application of 2D materials with intrinsic pores.
Considering stacked membranes, apart from developing innovative and scalable techniques to tune and fix interlayer distances of 2D nanosheets, future works should consider the development of 2D materials with anti-swelling properties with interlayer sizes below hydration radius of cations. This achievement could eliminate the tedious interlayer tuning process, which could greatly simplify the fabrication challenges and also enhance the stability of desalination membranes. Moreover, altering the surface chemistry of 2D materials could also streamline the membrane fabrication process since Donnan electrostatic exclusion effect comes into play instead of the physical size exclusion. This technique could be applied either on a diverse range of anti-swelling or swelling 2D materials with various interlayer sizes. Fabrication of 2D stacked membranes with in-plane nanopores requires more attention. In this scenario, water permeates not only via nanochannels of 2D stacked membranes but also through the in-plane pores of the nanosheets.

2.2. Progress and prospects of two-dimensional materials for membrane-based osmotic power generation

The electrical energy that can be harnessed from the salinity difference across the sea water and river water interface can be one of the sustainable and clean energy resources of the future. This energy can be harnessed via the nanofluidic channels that selectively permeates ions. The selective diffusion of cations and anions can produce electricity through reverse electrodialysis. Two-dimensional (2D) materials are a class of nanomaterials that hold great promise in this field. Several breakthrough works have been previously published which demonstrate the high electrical power densities of 2D membranes. The Ion transportation can be either through the nano-sized in-plane pores or interlayer spacings of 2D

materials. This review article highlights the progress in 2D materials for salinity gradient power generation. Several types of 2D membranes with various nano-architectures are discussed in this review article. These include atom-thick 2D membranes with nanopores, 2D lamellar membranes, 2D lamellar membranes with nanopores, 2D/1D, and 2D/2D hybrid membranes. The fabrication techniques, physical characteristics, ion transportation properties, and the osmotic power generation of these 2D membranes are elaborated in this review article. Finally, we overview the future research direction in this area. It is envisioned that the research on 2D materials can make practical salinity gradient power generation one step closer to reality.

2.2.1. Introduction

The energy that can be harvested from the interface between sea water and river water can reach up to 0.8 KW m^{-3} based on theoretical entropy change calculations [91]. This amount of energy density is much lower compared with fossil fuels. However, several advantages could render this blue energy a promising alternative clean energy source in the future [92]. These benefits include the enormous availability of saline water on earth and the lack of intermittency issue that exists in wind and solar energy [93]. Scientists have found several estuaries on the planet where the river water and saline water are naturally mixed. If all this energy could be harvested, that would amount to an enormous power of ~ 1 TW [94]. To obtain a vivid understanding of how enormous this value could be, this power is substantially higher than the global solar (~710 GW) and wind energy (~730 GW), as of 2020 [95]. The research on osmotic power generation is ongoing at a tremendous pace, with over 160 publications and 10,000 citations in the year 2021, according to the data from ISI web of science (Figure 2.2.1 a). This attests to the expanding popularity of this field among the community of materials scientists.

Several techniques have so far been developed to harness blue energy [96, 97]. Among the available options, pressure-retarded osmosis (PRO) and reverse electrodialysis (RED) are the two most promising approaches [98-101]. PRO utilizes a membrane permeable to water and transports water between high/low

concentrated reservoirs. The generated kinetics from the water stream is deployed to drive a turbine and generate power [98, 99]. Several pilot plants were installed to harvest the blue energy via PRO technique, but the profit margins were insufficient, yielding a maximum output power density of ~5 W m^{-2} [100, 101]. The second more promising approach for power generation is RED that functions based on the selective transportation of co-ions/counterions [102]. The advantage of RED over PRO is that it functions based on the kinetics of ions, as opposed to PRO which utilizes the kinetics of water molecules. This renders the RED systems easier to be commercialized and industrially applied [103]. Several studies have shown the membranes with high power density for RED-based osmotic energy generation. However, the research is still ongoing to further increase the output power density of RED membranes [104].

Two-dimensional (2D) materials are in the frontiers of nanofluidic applications owing to their simplicity and scalability in the membrane fabrication process [105-107]. Furthermore, 2D materials could be engineered into ultra-thin membranes, which renders them superior in terms of ionic conductivities compared with other classes of membranes [108]. Several classes of 2D materials and their nanocomposites were applied for osmotic energy generation, and satisfying power densities have been obtained [109]. However, there is still room to further optimize the parameters of 2D membranes to achieve higher power densities. The 2D membranes for osmotic power generation can be developed based on monolayer 2D materials with an atomic thickness or multilayered stacks of 2D materials forming a lamellar structure. Essentially, there are two principal ionic pathways in 2D membranes that are through the vertical pathways via the in-plane pores and the horizontal pathways via the interlayer channels [110, 111]. Optimizing the sizes of the nanopores/nanochannels to the nanoscale results in the surface-charged governed ion transport behaviors that enhance the ionic conductance and the permselectivity of the membranes [112]. Additionally, the hybrid of 2D materials with other 2D materials or with 1D nanofibers further tunes the physical/chemical properties of the membranes that can enhance the ion transportation and the permselectivity of the membranes [113].

This review article is principally focused on the application of 2D materials for RED membranes for osmotic energy generation. Firstly, we overview the

fundamentals and ion transportation mechanism of reverse electrodialysis. Then, we highlight several 2D materials-based membranes for osmotic power generation. The reviewed articles are classified based on the nano-engineering and nano-structural aspects of the 2D membranes. These include Atom-thick 2D membranes with nanopores, 2D lamellar membranes, porous 2D membranes, 2D/1D, and 2D/2D hybrid membranes (Figure 2.2.1 b). Several essential properties such as the fabrication procedures, physical characteristics, ionic transportation properties, and osmotic energy conversion behavior of these membranes are particularly elaborated in this article. Lastly, we proposed a future research direction for the application of 2D materials for osmotic energy generation.

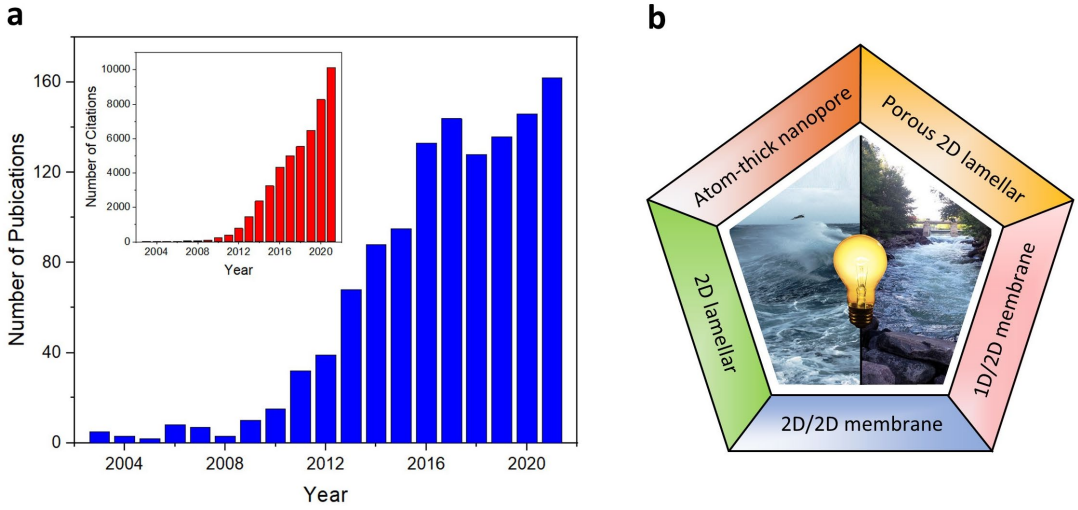

Figure 2.2.1. Publication numbers on osmotic power generation. *The number of publications and citations (inset) in the field of osmotic power generation from 2003 till 2021. The topic keywords were set to ["osmotic power generation" OR "salinity gradient power generation"], obtained from ISI Web of Science, March 2022 (a). Several types of two-dimensional membranes for salinity gradient power generation are reviewed in this paper (b).*

2.2.2. Fundamentals and Mechanisms

When two solutions with different salinities are separated by a semipermeable membrane, water tends to move from the high-salinity to the low-salinity regions. This flow of water occurs to equilibrate the differences in the chemical potentials of the two reservoirs. This osmotic pressure can be expressed according to Vant' Hoff equation:

$$\Pi = \Delta cRT \qquad (1)$$

Where Π is the osmotic pressure, Δc is the concentration ratio between high/low-salinity reservoir, R is the ideal gas constant, and T is the temperature. Increasing the temperature of the reservoir or the concentration difference increases the osmotic pressure and the potential for output work.

Another underlying mechanism is Gibb's free energy of mixing. When two ideal solutions with different salinities are combined, energy is released due to the movement of ions. Gibb's free energy of mixing is calculated from the differences between Gibbs's free energy of mixed (G1) and that of the unmixed solutions of varied salinities (G_2 and G_3).

$$\Delta G_{mix} = G_1 - (G_2 + G_3) = \Sigma_i\left(c_{i,1}V_1 RTlna_{i,1}\right) - (c_{i,2}V_2 RTlna_{i,2} + c_{i,3}V_1 RTlna_{i,3}) \quad (2)$$

Where subscript 1 refers to the final mixed solution and subscripts 2, 3 refer to the initial solutions of different salinities, V is the volume of solution, and a is the activity coefficient of the i^{th} component. When two solutions of different salinities are separated by a semipermeable membrane, the salt ions (cations and anions) permeate from the high concentration side to the low concentration side according to Fick's law of diffusion [114]. However, if the semipermeable membrane is replaced by an ion-exchange membrane, only counterions can diffuse due to the permselectivity of the pore/channels of the membrane [115]. The ion concentration difference across the high/low-salinity sides develops an internal electromotive force across the membrane that is called the osmotic potential (ε_{osm}). In the presence of suitable redox couple electrodes, this driving force generates the osmotic current (I_{osm}). The values of ε_{osm} and I_{osm} can be obtained from the I-V characteristics (Figure 2.2.2 a-c). The osmotic potential is the sum of the Nernst potentials over each cell [116]. For cation-permselective membranes, the ε_{osm} is expressed by:

$$\varepsilon_m \sim (2t_+ - 1)\frac{RT}{F}\ln\left(\frac{a_H}{a_L}\right) \quad (3)$$

Where t_+ is the cation transference number, R is the ideal gas constant, T is the temperature, F is the Faraday constant, a_H is the salt activity in the high-concentrated region, and a_L is the salt activity in the low-concentrated region. The cation transference number (t_+) is expressed as the ratio of cation flux to the sum of cation and anions flux [117], that is expressed as follows:

$$t_+ = \frac{I_+}{I_+ + I_-} \quad (4)$$

Where $I_+$is the cation flux and I_- is the anion flux. If the diffusion flux of cations and anions are identical across the membrane, a membrane with zero permselectivity and $t_+ = 0.5$, there will be no driving force for the osmotic power, and all of Gibb's free energy of mixing dissipates into heat [118]. However, if the channel is ion-selective and one charged species has higher flux compared with the other, a non-zero short circuit current will be developed, hence converting some of Gibb's free energy of mixing into electrical power [119]. The ion selectivity of the pore/channels is related to the Debye length (λ_B) and the surface charge. As the physical dimension of the pore/channels is reduced to the nanoscale level, the Debye length of the charged species overlaps with the surface charge of the membrane (Figure 2.2.2 d). At this scale, the ions are diffused with respect to the surface charge of the pore/channel. In this regard, the charged pore/channel walls attract ions of the opposite charge (counterions) while repelling ions of the same charge (co-ions). Hence, membrane permselectivity can be achieved by the delicate balance between the surface charge and pore/channel sizes [120, 121].

For permselective membranes, the ionic flux can be transformed into electric current via the appropriate redox couples electrodes, and the electric work is produced at an external load resistance [122]. The power that can be generated in this process is expressed by:

$$P = \frac{{\varepsilon_m}^2 R_{load}}{(R_{load}+R_c)^2} \quad (5)$$

Where ε_m, R_c and R_{load} are the osmotic potential, channel resistance, and external load, respectively. In the condition when the channel resistance and the load resistance are equal (R_{load}=R_c), the maximum power can be harvested [123, 124], that is expressed as:

$$P_{max} = \frac{{\varepsilon_m}^2}{4R_c} \quad (6)$$

This equation demonstrates that to achieve maximum power, one needs to balance between the osmotic potential and the channel resistance. The osmotic potential is dependent on ion selectivity and concentration gradients. Hence, the adequate balance between the concentration gradient, channel resistance, and ion selectivity of the nanofluidic channel is a necessity in harvesting the maximum power [125].

To circumvent the limitations of PRO and RED, several properties of nanochannels need to be optimized at the nanoscale. One of the essential phenomena that occurs within the nanofluidic channels is the diffusio-osmotic process. The diffusio-osmotic transport is developed within a Debye layer of finite thickness that is generated via the interactions of the ions with the surface of the nanofluidic channel (Figure 2.2.2 e) [126, 127]. This osmotic pressure gradient in the nanochannels forms a fluid flow inside the channel which contributes to the ions flux. This fluid flow is called the diffusio-osmotic flow that induces a plug-like velocity profile. The diffusio-osmotic velocity (V_{DO}) can be expressed as:

$$V_{DO} \approx \frac{RT}{8\pi l_B \eta} \times \frac{\Delta \log c}{L} \quad (7)$$

Where R, T, l_B, η, L and c are the ideal gas constant, absolute temperature, Bjerrum length, water viscosity, channel length, and concentration ratio, respectively. The Bjerrum length is the distance at which electrostatic interactions are not dominant, which is ~0.7 nm for water at room temperature [128]. Diffusio-osmotic transport occurs due to the electrostatic interactions of the ions with the surface of the nanochannels, within the nanometric Debye Layer, close to the surface. The diffusio-osmotic fluid flow goes in the same direction as the charged species, which is in the reverse direction of osmotic water flow. This phenomenon can reduce the controlled mixing of water, thereby maintaining the salt concentration at the high-salinity and low-salinity sides [129]. If the surface of the nanochannel has a net surface charge, the ions can be carried by this flow. The diffusio-osmotic current (I_{DO}) obeys the following expression:

$$I_{DO} \approx N \times 2\pi R \Sigma V_{DO} \quad (8)$$

Where N, R, Σ and V_{DO} are the number of channels, radius of the channels, surface charge density, and the diffusio-osmotic velocity, respectively. This expression is valid if the surface of the nanochannel is highly charged. For low-charged surfaces, the diffusio-osmotic current can be approximated as $I_{DO} \propto \Sigma^3$. In this case, the diffusio-osmotic current solely depends on the surface area of nanochannels [130].

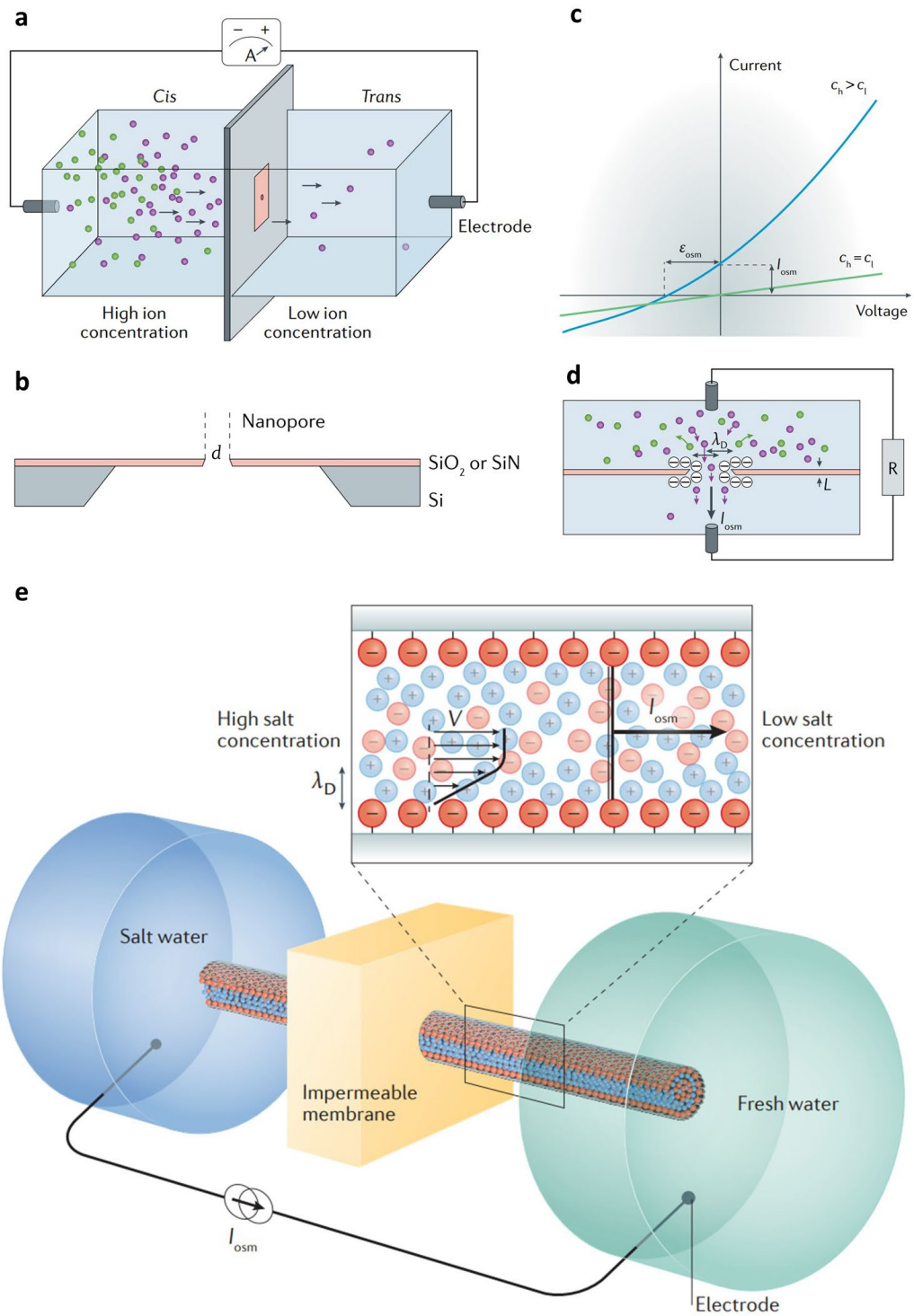

Figure 2.2.2. Fundamentals and mechanism. *A Thin membrane is placed across two reservoirs with a salinity gradient that is connected via Ag/AgCl electrodes (a). The schematic diagram of a nanofluidic channel which is comprised of thin atomic layers with nanopores, placed on a supporting window (b). Typical I-V curves under an osmotic gradient (blue curve) and no osmotic gradient (green curve) (c). A thin 2D membrane with a nanopore that shows selective ion transportation (d). Reproduced with permission from [121]. Copyright 2019, Nature Publishing Group. The diffusio-osmotic mechanism in a charged nanofluidic channel (e). Reproduced with permission from [130]. Copyright 2017, Nature Publishing Group.*

2.2.3. Atom-thick 2D membranes with nanopores

The ionic conductivity has an inverse relationship with the membrane thickness. Hence, reducing the membrane thickness to the atomic level can significantly improve the power generation performance [108, 131-133]. Developing pores in the range of nanoscale for atom-thick 2D materials have been reported in several previous studies for various membrane applications [37, 134]. Single-layer MoS_2 sheet is a three-atom thick film consisting of molybdenum atoms that are sandwiched by two sulfur atoms [135]. In one study by Feng et al., the salinity gradient power is harnessed across a nanopore of a single MoS_2 nanosheet with a thickness of 0.65 nm (Figure 2.2.3 a) [136]. MD simulations showed that the cations are localized around the center of the pore, which can affirm the cation-permselectivity of the nanopore (Figure 2.2.3 b). The pores on the surface of MoS_2 were created either by electrochemical oxidation or by TEM irradiation (Figure 2.2.3 c). The pores on the surface of MoS_2 could be tuned from 2-20 nm. I-V curves showed that the ionic conductance has a direct relationship with the pore sizes (Figure 2.2.3 d). As the pore size is increased, the osmotic current is increased as well. However, this comes at the expense of reduced ion selectivity from 0.62 to 0.23 [136]. The total current increases more rapidly within small pores due to the electrical double-layer overlap in nanoconfined regions [118]. In addition, the total current decreases in the larger pores that might be attributed to the reduced local concentration gradient effects (Figure 2.2.3 e). The maximum power was achieved at a pore size of ~10 nm. Considering a porosity of 30 %, the pore size density could reach 10^{12} pores cm^{-2}, amounting to the power density of 10^6 W $m^{-2,}$ which is the highest compared with other 2D membranes (Table 1) [136].

Another candidate for osmotic power generation based on 2D nanopore is graphene. Several reports have demonstrated the feasibility of graphene in water desalination applications owing to its excellent mechanical properties [37, 134, 137]. Previous reports have displayed the tunable cationic/anionic conductivity through graphene and boron nitride nanopores by modifying the concentration of multivalent ions [138]. In addition, theoretical calculations have demonstrated that

the power generation of single-pore graphene could reach up to ~700 W m^{-2} [139]. In an important study by Liu et al., a centimeter-sized nanoporous atom-thick carbon membrane was developed via the bottom-up synthesis route (Figure 2.2.3 f) [140]. The membrane was fabricated by thermal cross-linking of polycyclic aromatic hydrocarbon. In the first step, the core-rim monomer of hexa(2,2'-dipyridylamino) hexabenzocoronene (HPAHBC) was synthesized. HPAHBC consists of six flexible dipyridylamino groups as the rim and one hexabenzocoronene (HBC) as the core (Figure 2.2.3 g). Due to the hydrophilicity of the dipyridylamino rim, the HPAHBC could form a monolayer at the air/water interface. The membrane was subsequently transferred onto the Si/SiO_2 substrate using Langmuir–Blodgett technique. After annealing the HPAHBC, the dipyridylamino rim is decomposed while the HBC core is being thermally cross-linked to form an atom-thick membrane with a pore size of 3.6 ± 1.8 nm. Although the membrane had an atomic thickness of 2.0 ± 0.5 nm, it was robust enough to be free-standing over open apertures of as large as 2 μm in diameter (Figure 2.2.3 h-i). The ionic-conductance measurements showed that the membranes had a pore density of 1.5×10^{10} cm^{-2} that matched well with the pore density obtained from HAADF-STEM images (Figure 2.2.3 j). The power density reached 67 W m^{-2} at a load resistance of 15 MΩ (Figure 2.2.3 k) [140].

Recently, Yang et al. synthesized a centimeter-scale monolayer covalent organic framework (COF) via the interfacial polymerization reaction of zinc tetraphenylporphyrin and 2,5-dihydroxyterephthalaldehyde, denoted as ZnTPP–COF [141]. The synthesized COF membrane showed a thickness of 1.1 nm and pore sizes of 2.4 nm, coordinating well with the theoretical model (Figure 2.2.3 l-p). In contrast to numerous materials in this field, the ZnTPP–COF showed a positive surface charge, rendering it anion-selective. In the presence of 0.5 M / 0.01 M NaCl, the membrane showed an astonishing power density of 135.8 W m^{-2}. Interestingly, the power density could dramatically increase in the presence of divalent salts, yielding a power density of 203.8 W m^{-2} for the natural sea water | river water mixtures (Figure 2.2.3 q). Increasing the testing area by 2025 times substantially reduced the power density to 14.6 W m^{-2} [141]. This phenomenon has also been observed in previous research, where the power density of polyelectrolyte hydrogel membrane dramatically decreased with the testing area

of membranes increasing [142]. This issue may not be related to the membrane materials but be ascribed to the engineering aspects such as the reservoir geometry [141], or the errors from the testing apparatus [142], which demands additional research.

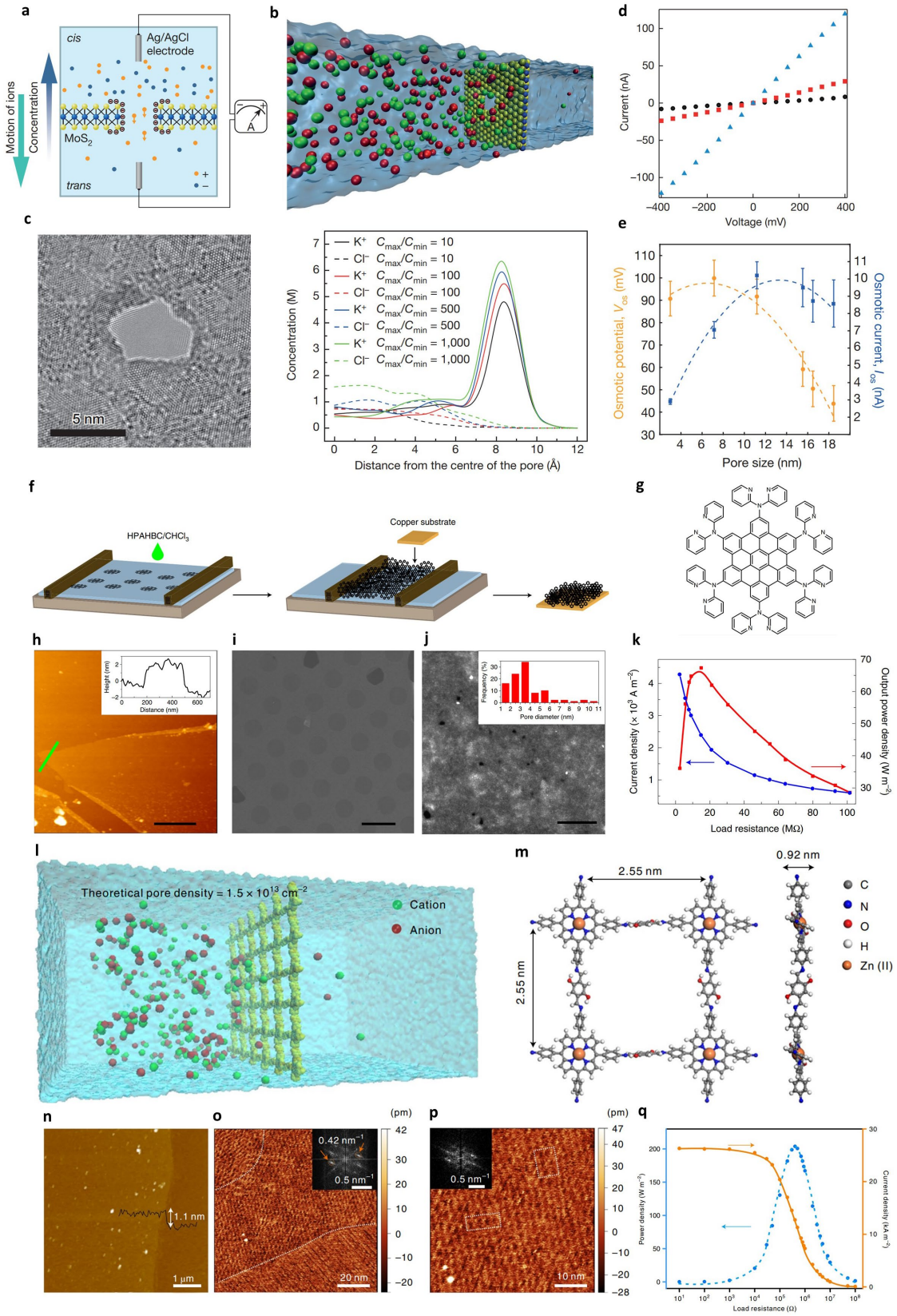

Figure 2.2.3. Atom-thick 2D membranes with nanopores. *Cation-permselectivity of a 0.65 nm-thick MoS_2 nanopore membrane (a). Top panel, Simulation box for MD simulations showing MoS_2 nanopore and the salts. Bottom panel, MD simulation results for potassium and chloride ions of different concentration gradients as a function of radial distance from the pore center (b). TEM-drilled MoS_2 nanopore with a diameter of 5 nm (c). I-V curves of MoS_2 nanopores with different*

pore sizes (black, 2 nm; red, 6 nm; blue, 25 nm) (d). The osmotic current and osmotic potential as a function of pore sizes (e). Reproduced with permission from [136]. Copyright 2016, Nature Publishing Group. Schematic demonstration of the fabrication process for a nanoporous 2D carbon membrane using bottom-up synthesis route (f). Chemical structure of HPAHBC monomer (g). AFM image of the membrane (inset, height profile of the membrane). Scale bar, 1 μm (h). SEM image of the membrane on a perforated substrate with an array of 2 μm diameter holes. Scale bar, 4 μm (i). HAADF-STEM image of the membrane showing the nanopores as dark regions on a bright background. (inset, pore size distribution) (j). Current density and power density profiles in 0.5 M/0.01 M NaCl (k). Reproduced with permission from [140]. Copyright 2020, Nature Publishing Group. Schematic of ion transport through COF monolayer membrane (l). Simulated structure of ZnTPP-COF using DFT calculations (m). AFM image and height profile of ZnTPP-COF monolayer membrane (n). Large-scale (o) and high-resolution STM image of ZnTPP-COF membrane (p). Inset: corresponding fast Fourier transform images. The white dotted lines in (o) denote the grain boundaries and the white dotted rectangles in (p) represent nanopores. Current and power density profiles vs. external load resistance measured using artificial sea water and river water (q). Reproduced with permission from [141]. Copyright 2022, Nature Publishing Group.

2.2.4. 2D lamellar membranes

Other classes of 2D membranes are the lamellar re-stacked membranes, in which the nanochannels are formed between the nanosheets. The effective ion exclusion in these membranes is either through the spacing between the nanochannels or the slits between the nanosheets [113]. These membranes have the advantages of lower fabrication costs compared with atom-thick membranes, and they can be produced via the facile, scalable, and cost-effective techniques of vacuum filtration or coating method. Furthermore, these membranes are of higher mechanical stiffness compared with atom-thick membranes. Several 2D lamellar membranes have been fabricated and applied for osmotic power generation. These include nano-clays [143, 144], graphitic carbon nitride [145], graphene oxide [146, 147], and MXene [148-150]. In this section, several pristine 2D lamellar membranes will be reviewed. This section will also outline the 2D lamellar membranes modified with organic molecules.

Inspired by the microscopic structure of nacre, clay-like materials can be structured into membranes where the inorganic layers serve as the backbone to give its hardness, and the organic layers serve as glue to give its flexibility [143, 144]. In one study, Chen et al. developed a reconstructed kaolinite membrane. The kaolinite consists of silicon tetrahedral sheets (STS) and aluminum octahedral sheets (AOS). The membrane showed channel sizes of 6.8 Å and

13.8 Å that corresponded to AOS-to-AOS and STS-to-STS assemblies. The kaolinite was first exfoliated and then modified with bis-(γ-triethoxysilylpropyl)-tetrasulfide (Si-69). The Si-69 is solely attached to the Al-OH groups, forming a Janus-like structure. The Janus membrane showed surface-charged governed ionic transport properties and a power density of 0.18 W m^{-2} at 100-fold concentration gradients [143]. In another research, the montmorillonite nanosheets were modified by cetyltrimethylammonium bromide (CTAB), and the power density could reach up to 0.18 W m^{-2} at 1000-fold concentration gradients [144]. Although the organic modification increases the mechanical stability of the clay-like materials, it renders the nanosheets more hydrophobic and also decreases the surface charge, diminishing the power density of these membranes.

In another research, Xia et al. developed an ultrathin polymeric carbon nitride membrane using the CVD technique [145]. Carbon nitride is a conjugated polymer with repeated tri-azine units with in-plane pore sizes of 3.11 Å, making it suitable for nanofluidic applications [151-153]. In their research, the melamine is thermally polymerized on a glass surface that can be delaminated by soaking in water. The membrane shows smoothness and no apparent defects. As a result, the ions can only diffuse through the membrane by the intrinsic carbon nitride pores and the interlayer spacings. The physical characterizations illustrate the crystallinity of the carbon nitride membrane (Figure 2.2.4 a-g). The thickness of the membrane can be tuned from 140 nm to 1 μm by changing the amount of melamine. As the thickness increases, both the open circuit potential and short circuit currents decreased. The values of open circuit potential and short circuit currents scale inversely and directly with the thickness and concentration gradients, respectively. For the 250 nm thick membrane, the maximum power density of 0.21 W m^{-2} was achieved in 0.1 mM / 0.1 M KCl (Figure 2.2.4 h-j) [145]. The 2D lamellar membranes can also be applied in the full reverse electrodialysis cells with cation- and anion-exchange membrane-pairs [147, 148]. In one study by Ji et al. the surface charge of graphene oxide could be tuned from negative -123 mC m^{-2} to positive +147 mC m^{-2}, yielding cation- and anion-selective membranes, respectively. The power density of the membrane-pairs in full cell reached 0.77 W m^{-2} for 0.5 M/ 0.01 M NaCl [147]. In another research by Ding et

al., the surface charge of MXene was made positive via poly-diallyl dimethylammonium chloride, and the zeta potentials could be altered from negative -41 mV to positive 48 mV. The membrane-pairs could generate power density of up to 4.6 W m^{-2} under sea water | river water. Additionally, the tandem of ten membrane-pairs stacks could produce a voltage of up to 1.66 V that could directly power electronic devices (Figure 2.2.4 k-o) [148].

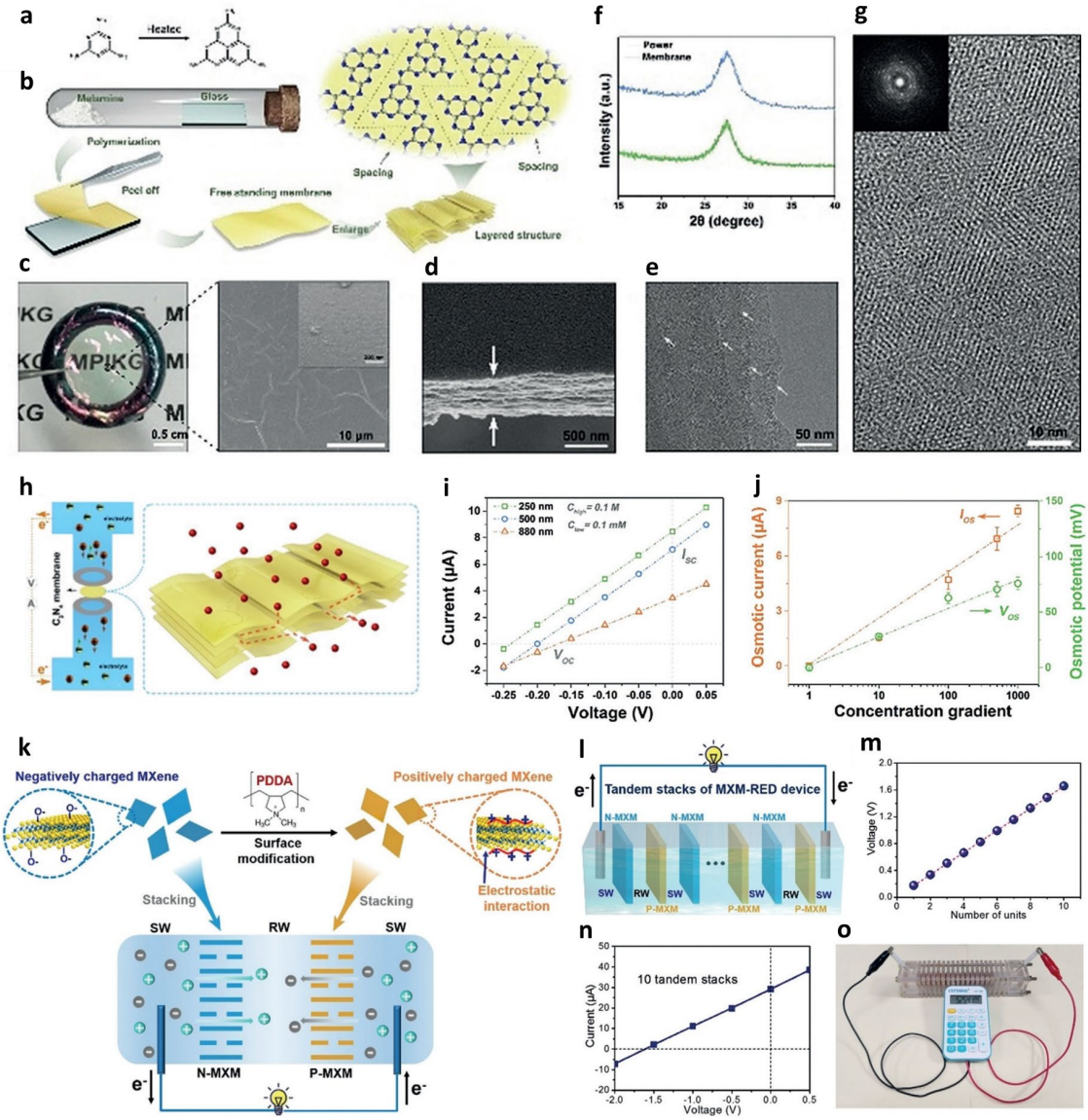

Figure 2.2.4. 2D lamellar membranes. *The synthesis procedure of carbon nitride membrane (a). Vapor-deposition polymerization and the molecular structure of carbon nitride (b). Optical and SEM image of the free-standing membrane (c). Cross-section image (d). TEM of the layered structure (e). XRD of the carbon nitride powder and membrane (f). HRTEM and electron diffraction images which indicate the crystallinity of the carbon nitride membrane (g). Schematic of the ion transport across the membrane (h). I-V curves of the membrane with different thicknesses under 0.1 M / 0.1 mM NaCl (i). The osmotic current and osmotic potential for carbon nitride membrane with the thickness of 250 nm as a function of concentration gradients (j). Reproduced with permission from [145]. Copyright 2018, John Wiley and Sons. Scheme of the full reverse*

electrodialysis cell using MXene membrane-pairs. The surface charge of MXene can be tuned from negative to positive, acting as cation- and anion-exchange membranes, respectively (k). Schematic of the tandem of membrane-pair stacks (l). The output voltage of 10 MXene RED cells stacked in series (m). I-V curves of 10 tandem membrane-pairs stacks (n). The tandem cells can power a calculator with a working voltage of 1.5 V (o). Reproduced with permission from [148]. Copyright 2020, John Wiley and Sons.

2.2.5. 2D lamellar membranes with nanopores

Generally, for 2D lamellar membranes, the in-plane diffusion is more sluggish compared with the out-of-plane diffusion [154]. For nonporous nanosheets, the ion flows only around the edges or the junctions of the sheets. However, ion diffusion length can substantially decrease if the ions diffuse directly through the nanopores in the basal plane of the nanosheets [155]. In this regard, developing pores on the basal planes of 2D materials can improve the ionic conductance in 2D lamellar membranes [154, 156, 157]. Development of nanopores on the surface of nanosheets in 2D lamellar membranes for osmotic power generation application have been reported for graphene [156], vermiculite nano-clays [157], and MXene [154].

According to the report by Wan et al., the pores were created on the surface of graphene via the catalytic oxidation using metal nanoparticles (Figure 2.2.5 a). The pore sizes could be tuned from ~5 nm up to ~100 nm via adjusting the concentration of metal nanoparticles and the microwave treatment times (Figure 2.2.5 b-d). The corresponding I-V curves demonstrated that both open circuit voltage and short circuit current dropped as the pore sizes increased due to the reduced ion selectivity (Figure 2.2.5 e). The highest power density was achieved for ~5 nm pores, reaching 1.15 W m^{-2} for 1 M/10^{-6} M NaCl (Figure 2.2.5 f) [156]. In another research by Cao et al., the pores were created on the surface of vermiculite nanosheets using hydrochloric acid (HCl) treatments. The pore sizes could be tuned from ~5 to 30 nm via altering the concentration of HCl solutions. The maximum power density of 4.1 W m^{-2} under 0.5 M / 0.01 M NaCl was achieved for membranes with a pore size of ~20 nm. Although increasing the pore size enhanced the ionic conductance and the short circuit current, it came at the expense of reduced cation-permselectivity and transmembrane potential [157]. The numerical studies have shown that excessively high pore densities

render the pore-pore interactions more dominant, thereby inducing strong concentration polarization effects and sacrificing the membrane selectivity [158, 159]. Hence, tuning the pore sizes and pore densities are essential in achieving the optimum power density for large-area 2D nanoporous membranes.

In another research, Hong et al. introduced pores into the $Ti_3C_2T_x$ MXene sheets via H_2SO_4 as an oxidizing agent (Figure 2.2.5 g) [154]. The H_2SO_4 treatment neither altered the crystallinity nor changed the surface functionality of the unetched parts of the $Ti_3C_2T_x$ sheets. The generated pores were in the range of 5-15 nm with the estimated pore density of 10^{10} cm^{-2} (Figure 2.2.5 h-i). The nanoporous MXene showed a higher osmotic voltage and osmotic current compared with the pristine MXene. The osmotic current reached the maximum value at a concentration gradient of 100, followed by an unusual decline at higher concentration gradients. Such a drop was attributed to the strong concentration polarization at the permeate side (Figure 2.2.5 j). The nanoporous $Ti_3C_2T_x$ membrane exhibited a maximum power density of 17.5 W m^{-2} under a 100-fold KCl gradient, which is 38% higher than that of the pristine membrane (Figure 2.2.5 k). The nanoporous $Ti_3C_2T_x$ membrane showed a higher packing density than the unmodified membrane (Figure 2.2.5 l) [154]. The vacuum-filtration of 2D lamellar membrane results in the trapping of water inside the nanosheets. The drying procedure results in the evaporation of these water molecules, which causes the formation of several unwanted voids, lowering the packing density. Nanopores on the surface of 2D sheets, however, offer pathways for trapped water to escape during the drying process, yielding tightly packed morphology while preventing the formation of undesired voids [160]. Generally, higher packing density renders membranes to retain their structure without being re-stacked, which is highly beneficial for long-time operation [154].

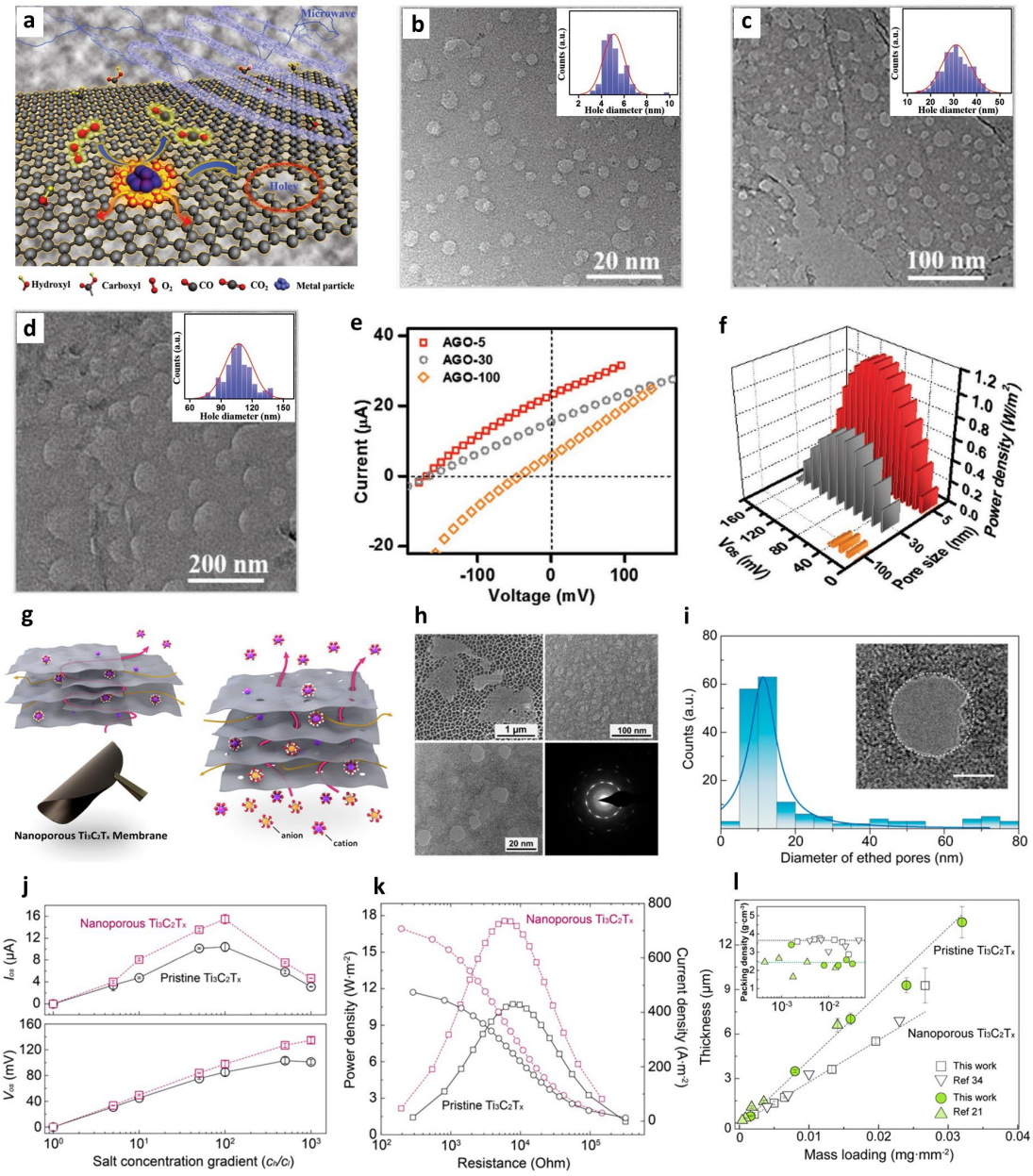

Figure 2.2.5. 2D lamellar membranes with nanopores. *Mechanism of the fabrication process for porous graphene (a). HRTEM images of porous graphene with various sizes and the corresponding hole diameter distribution statistics (inset) for ~5 nm (b), ~30 nm (c), and ~100 nm (d). I-V curves for porous graphene membrane with a pore size of 5, 30, and 100 nm under 1 M / 10^{-6} M NaCl gradient (e). Power generation from porous graphene with different pore sizes (f). Reproduced with permission from [156]. Copyright 2018, John Wiley and Sons. Schematic of the ion transport through 2D slit channels and nanopores of the chemically etched MXene (g). SEM, TEM, and SAED of nanoporous $Ti_3C_2T_x$ MXene sheets (h). Size distribution of the etched hole on MXene sheets. Inset: well-retained crystal structure around the single-etched hole (scale bar: 5 nm) (i). The osmotic potential and current as a function of concentration gradient (j). Power density and current density profiles vs. external load resistance for pristine and nanoporous MXene (k). The mass loading vs. membrane thickness for pristine and nanoporous MXene. Inset: packing density of both membranes was derived from the areal mass loading over thickness (l). Reproduced with permission from [154]. Copyright 2022, American Chemical Society.*

2.2.6. 2D lamellar membranes with 1D nanofibers

Stacked 2D membranes typically exhibit low strength and mechanical fragility that could easily fail in harsh reverse electrodialysis conditions. Besides, the re-stacking of 2D materials results in the 2D-2D interlayer spacings being in the subnanometer ranges, which significantly deteriorates the ionic conductance. Introduction of 1D nanofibers enhances the mechanical properties of the 2D lamellar membranes [161, 162]. Additionally, the 1D nanofibers can intercalate between the 2D nanosheets, thereby increasing the interlayer distances and the ionic conductivity [163-168]. Previous studies have shown that the surface charge of nanosheets and space charge of 1D nanofibers synergistically enhance the output power density due to the overlap of electric double layers in the confined channel [165]. However, the excessive incorporation of nanofibers is detrimental to the power generation performance due to the physical steric hindrances of charged nanofibers [163-166]. Moreover, replacing the charged nanofibers with neutral poly(vinyl alcohol) decreases the power density due to the absence of the space charge effects [164-166].

Inspired by the biological structure of the serosa, Man et al. prepared a 2D covalent organic framework (COF), denoted as PyPa, that was intertwined by aramid nanofibers (ANF) [163]. The membrane possessed abundant 1D and 2D nanochannels that were vertical and parallel to the lamination direction, respectively (Figure 2.2.6 a-b). The PyPa/ANF membrane demonstrated an osmotic power generation of up to 6.4 W m^{-2} for 0.5 M/0.01 M NaCl. Sulfonation of PyPa and ANF further improved the cation-permselectivity due to the enhanced surface charge of the nanosheets and nanofibers (Figure 2.2.6 c). Additionally, the sulfonation rendered the membrane more hydrophilic by reducing the surface contact angle from 51.8 ° to 38.4 °. The PyPa-SO_3H/ANF-SO_3H membrane showed an enhanced power density of up to 8.7 W m^{-2} for 0.5 M/0.01 M NaCl. The sulfonation of PyPa altered the crystallinity from A-A packing arrangement to A-B, resulting in a reduced pore size of 11.5 Å. The MD simulation manifested that upon sulfonation of PyPa, the sodium transportation and the cation-permselectivity are improved both in the horizontal and vertical diffusion directions (Figure 2.2.6 d-g). The enhanced selectivity is primarily attributed to

the negative charges of the sulfonate functional groups. Furthermore, the enhanced transportation of Na^+ in the vertical and horizontal directions is attributed to the electrostatic charges of the SO_3H and the enlarged interlayer spacings brought by nanofibers, respectively [163]. Under natural sea water | river water conditions, the maximum output power density could reach up to 9.6 W m^{-2} that is one of the highest among 2D membranes (Table 1). Furthermore, the output power density increased with the concentration gradients, reaching 73.5 W m^{-2} in the case of 614-fold (artificial Dead-sea water | river water) concentration gradients (Figure 2.2.6 h-i).

In another research, Zhu et al. developed the hybrid of MoS_2 and 1D cellulose nanofibers (CNF) as shown in Figure 2.2.6 j-l [164]. MoS_2 principally exists in two common structures that are trigonal prismatic or octahedral coordination of Mo atoms, to generate the semiconducting 2H phase or metallic 1T phase, respectively [169-173]. In their study, both phase structures of MoS_2 corresponding to metallic (M-MoS_2) and semiconducting (S-MoS_2) were examined. The M-MoS_2 phase was synthesized via the ultrasonication exfoliation of the lithium-intercalated S-MoS_2. As a comparison, the S-MoS_2 with similar lateral sizes were prepared by the mechanical exfoliation technique. The Nyquist plots demonstrated a higher ionic resistance of 150 % for S-MoS_2 compared with M-MoS_2. Additionally, the S-MoS_2 showed a power density of ~2.5 W m^{-2} and energy conversion efficiency of 10%, which are considerably lower compared with M-MoS_2 of 5.2 W m^{-2} and efficiency of ~32 % (Figure 2.2.6 m). The zeta potential of S-MoS_2 is ~-18 mV which is also significantly lower compared with M-MoS_2 (~-36 mV). Besides, S-MoS_2 shows hydrophobic properties with a surface contact angle of 101°, while M-MoS_2 demonstrated hydrophilic properties with a surface contact angle of about 28° (Figure 2.2.6 n). The DFT results attested that the hydrated cations preferentially adsorb onto the surface of M-MoS_2, with much lower adsorption energy (-3.34 eV) compared with S-MoS_2 (-1.86 eV) (Figure 2.2.6 o-q) [164]. Basically, the M-MoS_2 is developed via the filling of electrons in the d orbitals of the Mo atom in S-MoS_2, which occurs due to the electron transfer between the lithium and S-MoS_2 during the intercalation procedure [174, 175]. As a result, this electron-rich phase of M-MoS_2 exhibits a higher surface charge,

hydrophilicity, affinity to cations, and consequently a higher power generation performance [164].

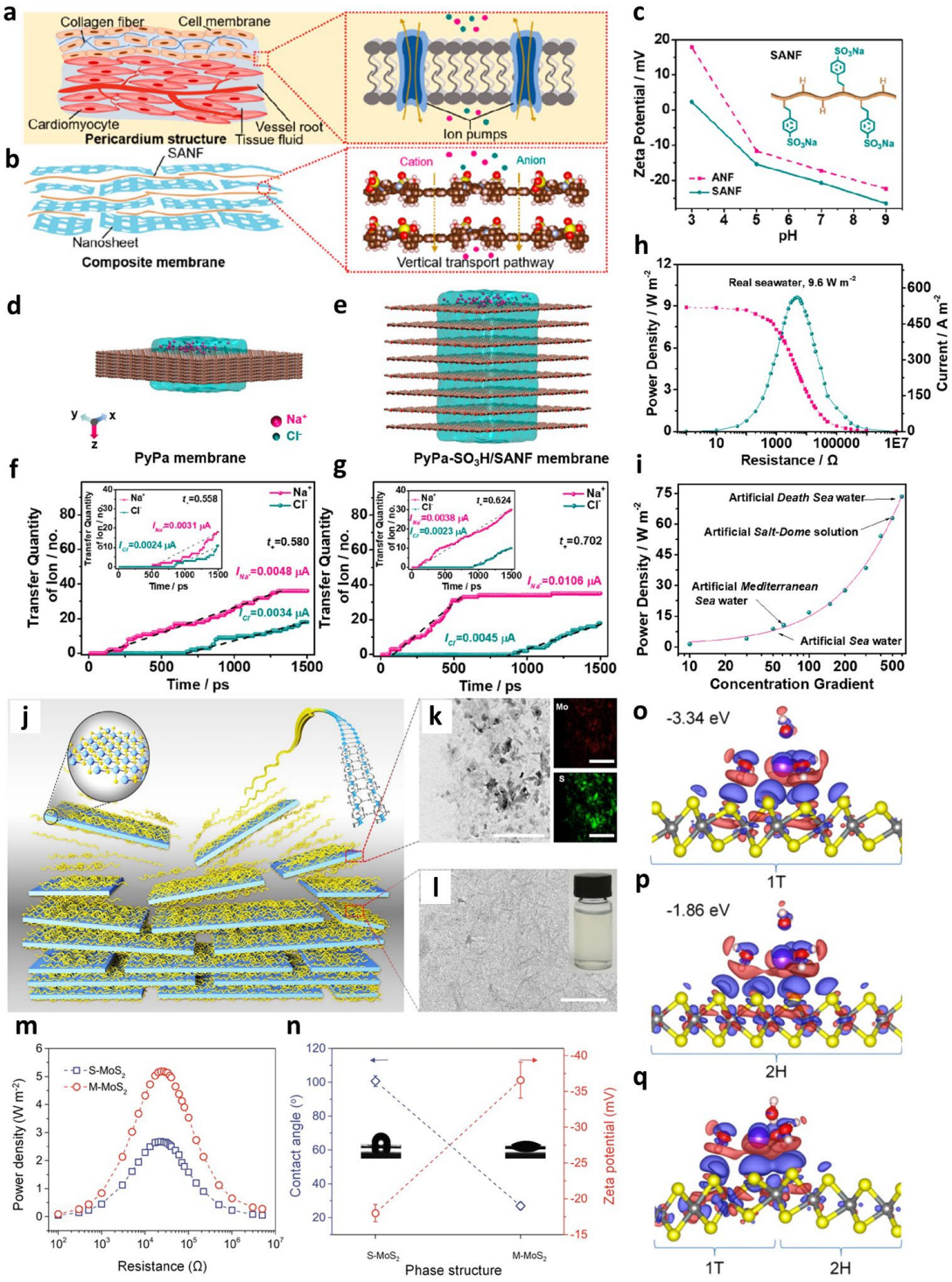

Figure 2.2.6. 2D lamellar membranes with 1D nanofibers. *Schematic illustration of the pericardium structure (left) and the ion pumps on the cell membrane (right) (a). Schematic of PyPa-SO₃H/SANF membrane (b). Zeta potentials of ANF and SANF (c). MD simulations for ion diffusion across PyPa (d) and PyPa-SO₃H/SANF (e). Transfer quantity of Na^+ and Cl^- ions in the vertical direction for PyPa (inset, horizontal directions) (f). Transfer quantity of Na^+ and Cl^- ions in the vertical direction for PyPa-SO₃H/SANF (inset, horizontal directions) (g). Power density of PyPa-SO₃H/SANF (natural sea water | river water) (h). Power density of PyPa-SO₃H/SANF for*

various concentration gradients (i). Reproduced with permission from [163]. Copyright 2021, American Chemical Society. Schematic of the assembly of MoS_2/CNF composite membrane (j). TEM and elemental mapping of MoS_2 nanosheets (scale bars are all 1 μm) (k). TEM of CNF (scale bar, 500 nm) (l). Osmotic energy conversion of S-MoS_2 and M-MoS_2 (m). The comparison of zeta potential and water contact angle measurements, where M-MoS_2 shows a higher surface charge and hydrophilicity compared with S-MoS_2 (n). The adsorption of hydrated cation on the surface of metallic-1T (o) and semiconducting-2H phase (p). For the coexistence of the two phases of MoS_2, the mobile cations tend to adsorb on the surface of 1T phase (q). Reproduced with permission from [164]. Copyright 2021, American Chemical Society.

2.2.7. 2D/2D lamellar membranes

The 2D/2D heterointerfaces have several outstanding physical, chemical, and ion transportation characteristics. The 2D/2D membranes have been previously investigated for water purification applications [58, 88, 176]. These membranes have also been applied for osmotic power generation [177, 178]. In one paper by Yang et al., a 2D/2D composite lamellar membrane was formed via mixing MXene and boron nitride (BN) nanosheets (Figure 2.2.7 a) [177]. The BN was chosen as a nano-spacer due to its high surface charge density of -0.84 mC/m^2 and its high ionic conductivities [179, 180]. Due to the superhydrophilic nature of BN, the water contact angle of the composite membrane was reduced as compared with pristine MXene. As the content of BN was increased, the size of the 2D nanochannels expanded from 1.19 to 1.55 nm. A schematic diagram of the composite membrane with different internal structures is shown in Figure 2.2.7 b. For the membrane with low contents of BN, the channels are mainly constructed by the MXene-Mxene nanochannels. As BN content increases, the interlayer spacing is also enlarged due to the formation of BN-BN nanochannels. The enlarged interlayer spacings increased the diffusion current, but this came at the expense of reduced selectivity (Figure 2.2.7 c). The output power density of the MXene/BN composite membrane with 44 wt % of BN reached 2.3 W m^2 for 0.5 M / 0.01 M NaCl, which was twice compared with pristine MXene membrane (Figure 2.2.7 d) [177].

In another research by Zhang et al., the multilayer membrane was prepared via sequential filtration of graphene oxide (GO) and black phosphorous (BP) (Figure 2.2.7 e-f) [178]. As the number of GO layers is increased, the ion selectivity is also enhanced, but the osmotic current is diminished. The maximum power

density of 3.4 W m^2 (0.5 M / 0.01 M NaCl) was obtained for two layers of GO confined between the BP nanosheets (Figure 2.2.7 g-i) [178]. This research demonstrated that the sequential filtration of GO on top of BP had a higher power density compared with one-step filtration (simple mixing) of BP@GO mixture (Figure 2.2.7 j). This was ascribed to the different channel sizes of BP and GO, which develops a heterogeneous multilevel structure with asymmetric channel size [181]. The 2D/2D lamellar membranes are still in their infancy, and there is plenty of room for investigating several types of these membranes for osmotic power generation application.

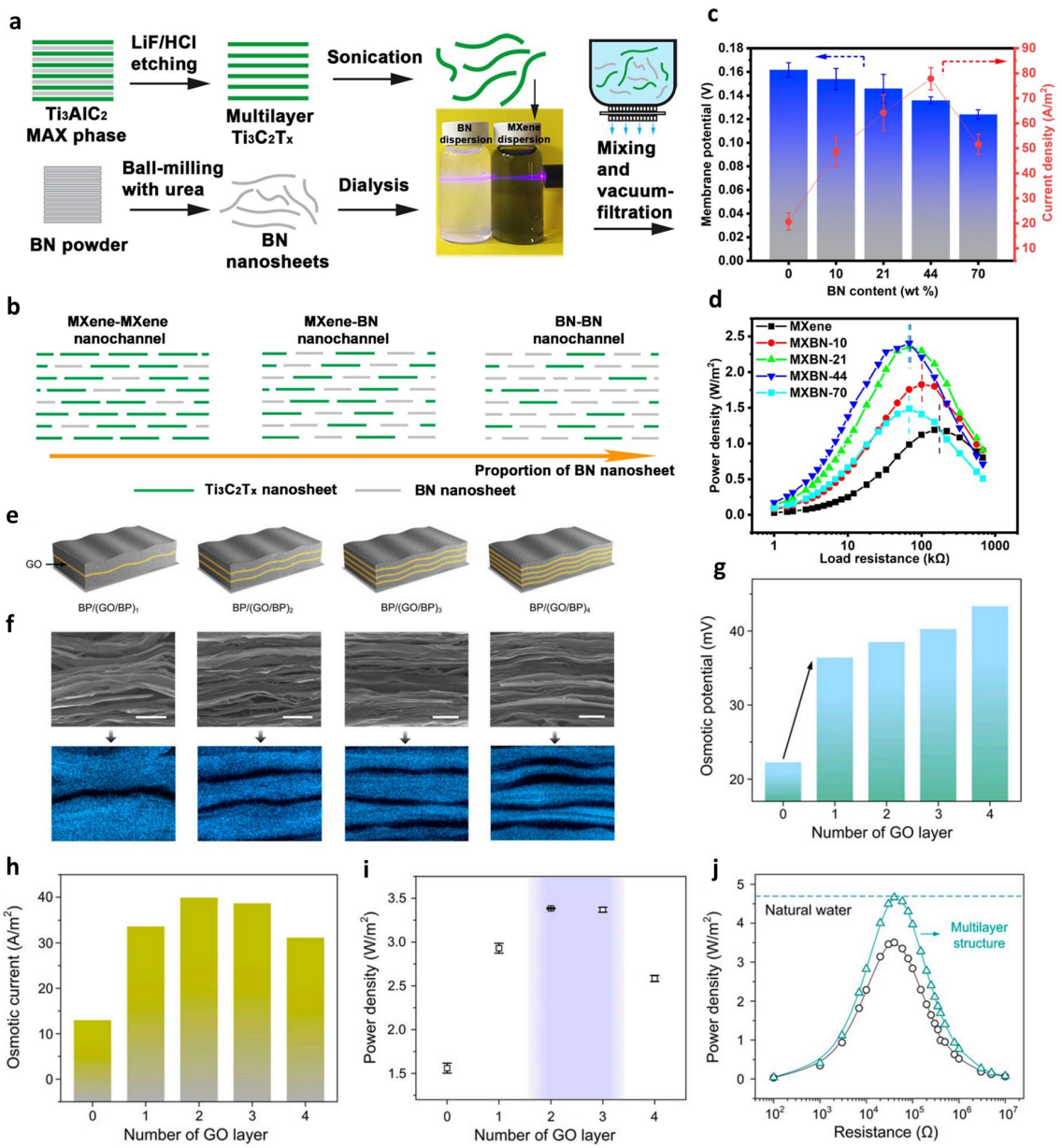

Figure 2.2.7. 2D/2D lamellar membranes. *The schematic diagram for the fabrication process of 2D/2D MXene/BN composite membrane (a). Schematic diagram of the three possible configurations of the nanochannels (b). Membrane potential and current density (c), and output power density as a function of BN contents (d). Reproduced with permission from [177]. Copyright 2021, American Chemical Society. Schematic illustration of multilayer composite membranes of GO and BP (e). Cross-section SEM and EDX mapping of multilayer membranes with increasing numbers of GO. The blue stripes represent the BP, and the black stripes represent the GO (f). Influence of the number of GO layers on the osmotic potential (g), osmotic current (h), and the overall power density (i). Comparison of the power density of multilayer membrane prepared by sequential filtration (triangle) with the composite membrane prepared via simple mixing of GO and BP (circle) (j). Reproduced with permission from [178]. Copyright 2020, National Academy of Sciences.*

Table 2.2.1. Performance comparison of 2D membranes for osmotic power generation.

Membrane Classification	Membrane Type	Thickness	Power density (W m^{-2})	Test conditions	Ref.
Atom-thick 2D nanopore	Nanoporous MoS_2 (pore size = 10 nm)	0.65 nm	10^6	KCl	[136]
	Nanoporous Carbon (pore size = 3.6 nm)	2.0 nm	67	0.5 M/ 0.01 M NaCl	[140]
	Covalent organic framework (pore size = 2.4 nm)	1.1 nm	203.8	Sea water/ river water	[141]
2D lamellar	Kaolinite nanoclays	25 μm	0.18	100-fold KCl	[143]
	Montmorillonite nanoclays	11.2 μm	0.18	1000-fold KCl	[144]
	Carbon nitride	250 nm	0.21	0.1mM/ 0.1M KCl	[145]
	Graphene oxide membrane-pairs	10 μm	0.77	0.5 M/ 0.01 M NaCl	[147]
	MXene membrane-pairs	~	4.6	0.5 M/ 0.01 M NaCl	[148]
2D lamellar with nanopores	Graphene (pore size = 5 nm)	~	1.15	1 M/ 10^{-6} M NaCl	[156]
	Vermiculite (pore size = 20 nm)	2.1 μm	4.1	0.5 M/ 0.01 M NaCl	[157]
	MXene (pore size = 5-15 nm)	0.6 μm	17.5	100-fold KCl	[154]
2D/1D membranes	Covalent organic framework/Kevlar nanofibers	7.2 μm	8.7	0.5 M/ 0.01 M NaCl	[163]
	MoS_2 (metallic) /cellulose nanofiber	4.0 μm	5.2	0.5 M/ 0.01 M NaCl	[164]
	MXene/Kevlar nanofibers	2.0 μm	3.92	0.5 M/ 0.01 M NaCl	[165]
	Graphene oxide/Cellulose nanofiber	9.0 μm	4.19	0.5 M/ 0.01 M NaCl	[166]
	Graphene oxide/Silk nanofiber	5.0 μm	5.07	0.5 M/ 0.01 M NaCl	[167]
	Boron nitride/ Kevlar nanofiber	1.0 μm	0.6	0.5 M/ 0.01 M NaCl	[168]
2D/2D membranes	MXene/boron nitride	10.0 μm	2.3	0.5 M/ 0.01 M NaCl	[177]
	Black phosphorus /Graphne oxide	8.0 μm	3.4	0.5 M/ 0.01 M NaCl	[178]

2.2.8. Conclusion and Perspective

In this review article, we surveyed several classes of two-dimensional membranes for salinity gradient power generation application. The membranes in this paper were classified based on their nano-structural and nano-engineering features. These include atom-thick membranes with nanopores, 2D lamellar membranes, 2D lamellar membranes with nanopores, nanocomposite of 2D materials and 1D nanofibers (2D/1D membranes), and the hybrid of two types of 2D materials (2D/2D membranes). Atom-thick membranes with nanopores transport ions through the nano-sized pores, and they benefit from a high osmotic conductance due to their ultrathin thickness. However, due to their atomic thickness, they tend to possess poor mechanical properties for practical applications. 2D lamellar membranes transport ions via interlayer channels and the slits between two neighboring nanosheets. Ease of fabrication and their adequate stability render these membranes more promising for practical applications. The ionic transport through 2D lamellar membranes can be improved via the formation of in-plane pores on the surface of nanosheets. In this regard, the ionic diffusion can be enhanced in the vertical direction, which can drastically increase the power density. In addition, the intertwining of 2D nanosheets with 1D nanofibers can further introduce additional space charge effects that can enhance the permselectivity and the ion transportation of these membranes. The 2D materials can also be applied as hybrid composites with other 2D materials, forming 2D/2D interfaces. This technique tunes the interlayer spacings and the physical properties of the membranes, which consequently affect the ion transportation properties.

Although satisfactory progress has been made in applying 2D materials for osmotic power generation, there is still plenty of room for further research and exploration in this field. 1) Regarding atom-thick membranes with nanopores, the selectivity of the membrane is directly pertinent to the pore sizes and the pore chemistry. In this regard, there is a demand for fundamental research, both experimental and theoretical studies, on several atom-thick 2D materials with various pore chemistries. Additionally, the recent research on the bottom-up fabrication of atom-thick membranes needs further attention as it can solve the hurdles in developing large-sized atom-thick membranes with nanopores [140,

141]. 2) Regarding 2D lamellar membranes with nanopores, there is plenty of room to develop techniques to form nano-sized pores of different sizes on several types of 2D nanosheets. The previous research in this area demands further consideration [154, 156, 157]. 3) Moreover, the research on 2D/2D membranes is in its infancy, and several types of 2D/2D heterointerfaces can be applied in this field. The recent study on tuning interlayer spacings via 2D/2D coupling is of utmost importance [177]. More importantly, the effect of 2D/2D heterointerface on the ionic transportation properties demands further focus. It is anticipated that the research on 2D materials-based membranes could make salinity gradient power generation one step closer to practical development. 4) The issues regarding the decrease of power density with an increase in the testing area demand immediate attention for these membranes' scale-up for practical application. The recent research regarding this issue is of utmost importance [141, 142].

2.3. Progress and prospects of 2D materials for capacitive desalination

Ion adsorption has been the principle mechanism in supercapacitors and ion storage and capture from seawater. Moreover, the electrochemical water desalination functions based on a similar principle where ions are electro-adsorbed on the surface of capacitive materials based on electrical double layer properties. The discovery of 2D materials have revolutionized the ion adsorption industries for several interesting applications. Good electronic conductivity, abundant functional groups, large surface area, and well-oriented nanochannels in 2D materials, in their pristine and re-stacked forms, can render possible these materials for ion adsorption applications. In this section, the properties of several 2D materials for ion adsorption with a particular focus on capacitive water desalination is reviewed.

2.3.1. Introduction

Capacitive deionization (CDI) is a modern technique to purify water, having several advantages compared with the traditional membrane-based reverse osmosis technique. Specifically, at low concentrated solutions, CDI can show tremendous efficiency. CDI works based on the mechanism of electrical double layer (EDL). In this case, the external voltage is first applied on electronically-conductive porous materials and this causes electro-adsorption of counter-ions towards the surface of electrode. As long as the external voltage is applied, the ions remain adsorbed on the surface of porous electrode. In this case, ions are removed from the brackish water and they are adsorbed on the surface of electrode, thereby, reducing the salt concentration in the water. After the electro-adsorption process is completed, another water stream is injected and external voltage is reversed where the ions are released back into the waste-stream, and electrodes will be ready for the next water desalination cycle.

In order to have this reversible ion adsorption/desorption cycles, electrochemical materials with exquisitely-tailored channels are demanded. Moreover, it is

desired that the channels should be well-arranged so that during large cycling the materials can still perform without the loss of performance. Moreover, the electrode materials are required to possess good electronic conductivity, so sufficient applied voltage can produce adequate electrical fields for initiating the adsorption/desorption process without loss of efficiency.

In this regard, 2D materials stand out as the most promising choice for capacitive ion adsorption since they have excellent electronic conductivity properties. Moreover, abundant nano-galleries, formed via re-stakced 2D nanosheets, can form ion transportations pathways that could ease the ion adsorption. 2D materials have been previously applied for capacitive desalination, including graphitic carbon nitrides, transition metal carbides (MXene) and MoS_2. In this chapter, a brief introduction will be outlined followed by advances on each of these 2D materials for capacitive desalination, including material characterisation, application merits, and desalination performance.

2.3.2. Graphitic carbon nitride

Graphene and graphene oxide have been tried for CDI previously. However, the lack of functional groups on graphene and low conductivity of graphene oxide shifted the focus to another alternatives. Graphitic carbon nitride is a structural analogue to graphene that is composed of carbon and nitrogen. These materials are made of nanosheets that are constructed triazine units, formed by the pyrolysis of nitrogen-containing precursors such as urea or melamine.

In one research by Wang et al., boron carbon nitride nanosheets where prepared by mixing the urea-pyrolized graphitic carobn nitride with boric acid under heating [182]. Boron-doped carbon nitride (BCN) has the merits of both boron nitride and graphene, where several bonds such as C-C, B-N, B-C, and C-N exists [183]. These bonds can tailor the electronic as well as functionalities of these materials. The composite materials not only showed high surface area of 330 $m^2\ g^{-1}$, but also favoured from the synergistic effect of B and N atoms, that resulted in fast ion diffusion and good charge transfer capability with the salt adsorption capacity (SAC) of 13.6 mg g^{-1} [182]. In another research by Yu et al. protonated carbon

nitride was mixed by graphene oxide to develop a nanocomposite electrode (Figure 2.3.1 a) [184]. The asymmetric device composed of the composite electrode as the negative electrode, and the active carbon as the positive electrode showed electrosorption capacity of 8.36 mg g^{-1} under 50 mg L^{-1}. Figure 2.3.1 b shows that as the external applied voltage is increased, the Salt electrosoption rate (SER) increased, manifested by the increased electrical double layer properties at the electrodes, thereby enhancing the electrosorption capacity. The Ragone plot shows that the plots are moving towards upper right, under higher voltage and adsorption time, indicating a higher salt electrosorption capacity (SEC) and SER at higher voltages (Figure 2.3.1. c).

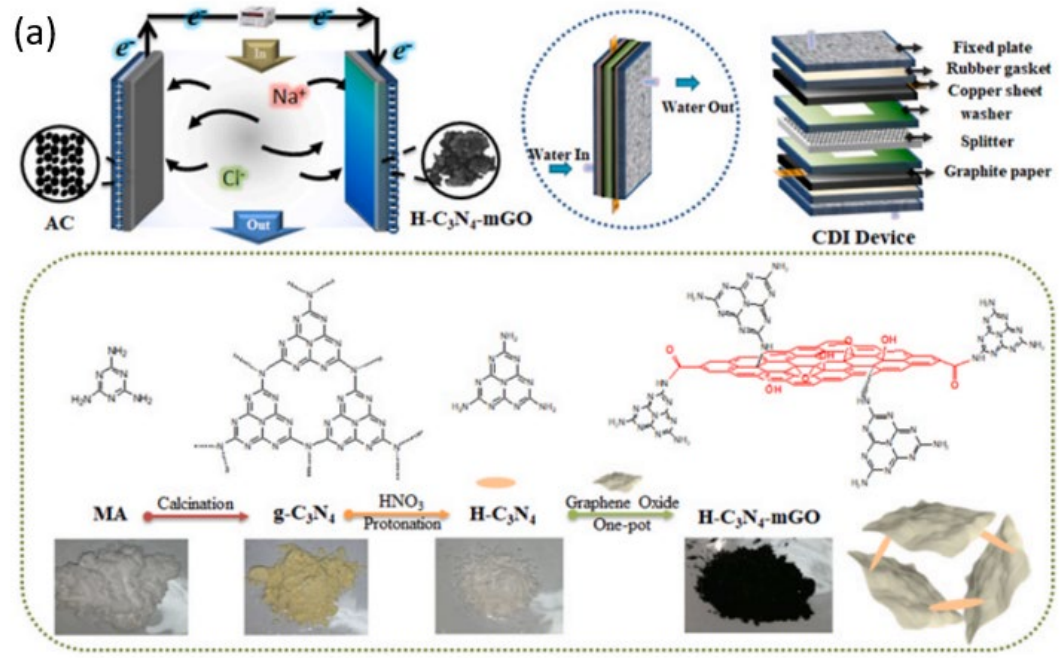

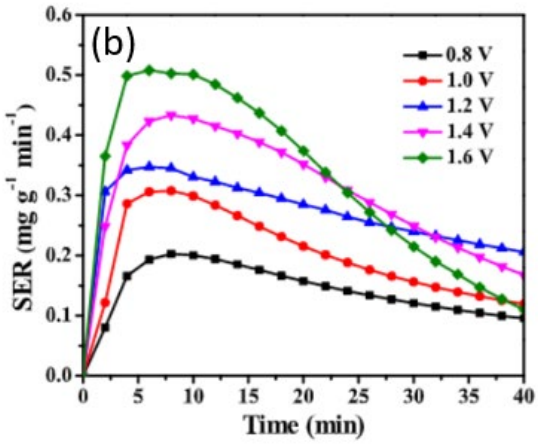

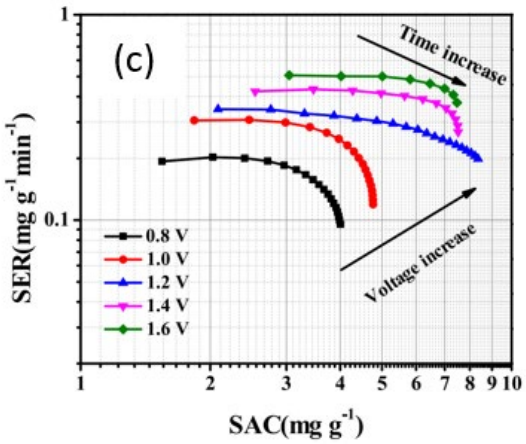

Figure 2.3.1. graphitic carbon nitride for CDI. Schematic diagram of the synthesis procedure for the development of protonated graphitic carbon nitride and graphene oxide (a). SER (b) and Ragone plot of the electrode (c). Reproduced with permission from [184]. Copyright 2022, Elsevier.

2.3.3. MXene

MXene is a type of transition metal carbide/nitride which is prepared from the exfoliation of the bulk MAX phase, where M is the transition metal, A is the element from the group 13 or 14, and X is carbon or nitrogen. After the A layer is etched away from the bulk phase, MX layers bond with surface termination groups of -O, -F, or -OH are obtained [185]. The first report of MXene for CDI is by Srimuk et al. with the desalination capacity of ~13 mg g^{-1} [186]. This value is improved in the past few years of research via several nano structural and chemical tunings.

In the past years, several attempts were made by researchers to increase the capacity of MXene for capacitive desalination [187-189]. In one paper by Ma et al., the free-standing MXene electrode was prepared with the merits of high surface area and excellent ion adsorption [187]. The MXene prepared by mixed etching with LiF/LiCl is beneficial for reducing the content of -F and decreasing the interlayer distances. The preparation of this free-standing structure is shown in (Figure 2.3.2. a-f). Under charge, the cell voltage increases and NaCl conductivity decreases. Under discharge, the cell voltage decreases accompanied by a raise in NaCl concentration to the initial value (Figure 2.3.2. g). As the current density is increased, more ions are attracted towards electrode surface and hence, the desalination capacity is increased. The free-standing electrode show stable performance with the high ion storage capacity up to 68 mg g^{-1} (Figure 2.3.2. h). In another research by Amiri et al., the nitrogen was doped into porous MXene and this resulted in the enhanced electronic conductivity of the nanosheets [188]. Moreover, the pore engineering strategy further increased the surface area. Overall, the outstanding performance of 117 mg g^{-1} was achieved for a salt concentration 5,000 mg L^{-1}. These studies show that the electronic and ion adsorption properties of MXene can be successfully tailored for CDI application.

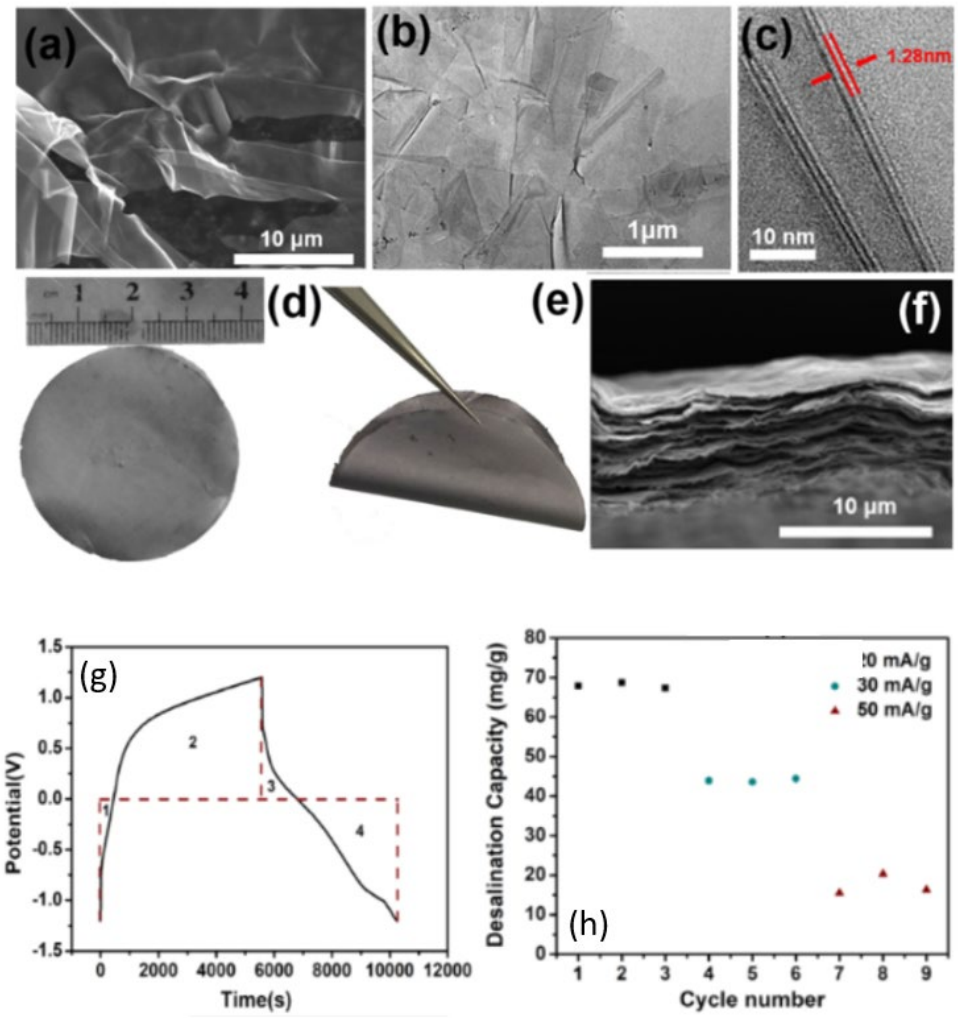

Figure 2.3.2 MXene for CDI. SEM (a), TEM (b-c) of MXene after delamination procedure. Free-standing MXene film (d-e). Cross-section SEM image the MXene film (f). Cell potential during a cycle of desalination/salination (g). Desalination capacity and different current densities (h). Reproduced with permission from [187]. Copyright 2020, Elsevier.

2.3.4. MoS_2

In the family of transition metal dichalcogenides, Molybdenum disulfide (MoS_2) has been applied for CDI applications [190-192]. MoS_2 is composed of weakly coupled layer, where one layer of Mo atoms is sandwiched by two layers of S atoms [193]. MoS_2 exists in two common phases that are trigonal prismatic or octahedral coordination of Mo atoms, developing the semiconducting 2H phase or metallic 1T phase, respectively [194].

Of these two phases, the metallic phase promotes the electrochemical intercalation of ions with a high efficiency [190]. In one study by Xin et al., the chemically-exfoliated MoS_2 generate the SAC of 8.81 mg $g^{-1.}$ This moderate performance was attributed to the unique 2D channels and good electronic conductivity of the 1T phase. The preparation of MoS_2 nanoflakes is shown in Figure 2.3.3 a-f. Interestingly, compared with the bulk phase, the desalination capacity of chemically exfoliated MoS_2 is much higher than its bulk counterpart due to its larger surface area and abundance of functional groups on the nanosheets' surfaces (Figure 2.3.3. g). In addition, the mass and specific volume increases for increased salt concentrations, reaching a maximum value of 16.5 mg g^{-1} for 400 mM NaCl (Figure 2.3.3. h) [190].

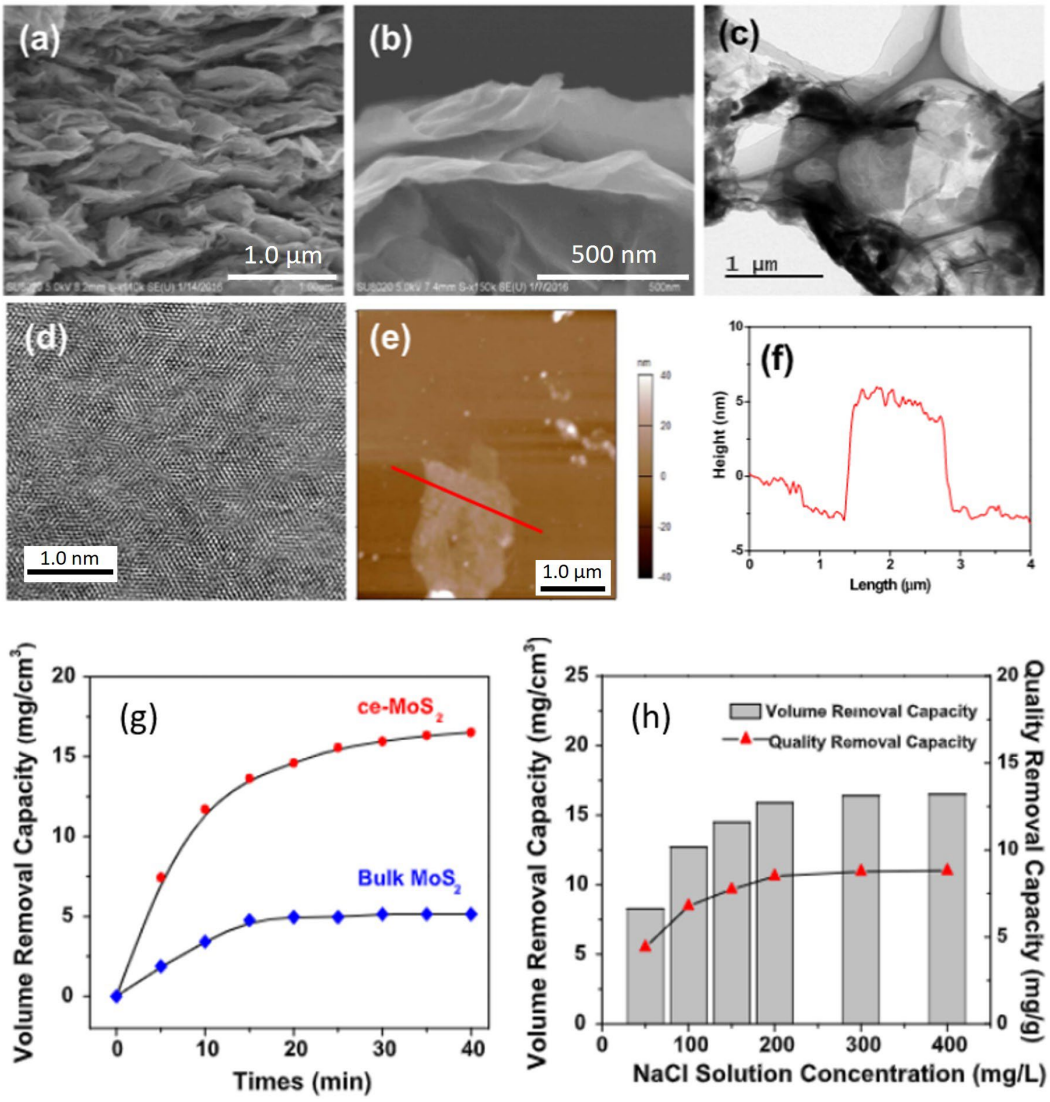

Figure 2.3.3. MoS_2 for CDI. Cross-section SEM of multilayer MoS_2 (a), SEM image (b), TEM (c), HRTEM (d), AFM (e), and height profile of the of the bilayer MoS_2 (h). Desalination capacity vs.

time for the bulk and chemically exfoliated MoS_2 (g). Ion adsorption capacity based on volume and mass vs. different NaCl concentrations (h). Reproduced with permission from [190]. Copyright 2017, Elsevier.

2.3.5. Conclusion and perspective

Two dimensional materials based on graphitic carbon nitride, MXene and MoS_2 were briefly outline in this section. The ordered nanochannels together with rich surface functionalities render these materials good candidates for CDI. The salt adsorption coefficient of these materials can be further improved. One issue that decrease the desalination performance in 2D materials is the lack of charge storage properties, originating mainly from the lack of nanochannels order and low charge transfer, that hinder the effective ion adsorption in these materials. Development of self-assembled heterostructure where the ions can move through well-oriented galleries for effective transportation and adsorption is one direction to achieve good ion storage capacitive. In addition, tailoring the interface properties of these 2D materials, together with functional groups modification, render possible the efficient adsorption.

Chapter 3: Serosa-Mimetic Nanoarchitecture Membranes for Highly Efficient Osmotic Energy Generation

3.1. Abstract

Osmotic energy stored between seawater and freshwater is a clean and renewable energy source. However, developing high-efficiency and durable permselective membranes for harvesting osmotic energy remains a long-standing bottleneck. Herein, we report that a nanocomposite membrane with mimetic biological serosa structure can achieve high-performance osmotic energy generation through the coupling of two-dimensional (2D) sulfonated-covalent organic framework (COF) nanosheets and anion-grafted aramid nanofibers (ANFs). As verified by theoretical calculations and experimental investigations, the 2D COF nanosheets not only provide abundant one-dimensional (1D)/2D nanofluidic channels to synergistically benefit an ultra-fast ion migration, but also enable high cation permselectivity via the covalently tethered anions. The grafted ANFs increase the mechanical strength of membrane and further improve the ion diffusion/rectification. When applied in an osmotic power generator, the biomimetic membrane delivered a power density of 9.6 W m^{-2}, far surpassing the commercial benchmark of 5.0 W m^{-2}. This work could boost the viability of osmotic energy conversion toward a sustainable future.

3.2. Introduction

Large amount of osmotic energy can be harvested from the salinity difference between sea water and fresh water [93]. The release of Gibbs free energy from mixing sea water and fresh water is estimated up to 0.8 kilowatts per cubic meter. The theoretical total amount of energy available from harnessing salinity gradients is in the range of 1.4-2.6 TW based on the global discharges of rivers

into oceans, equal to 9-17 % of today's global electricity use [195]. This abundant source of "blue energy" is a reliable and sustainable source of power generation with minimal daily variation (compared with the unpredictability of solar and wind powers) and negligible environmental impact (*e. g.* no pollution or carbon dioxide emissions) [104]. Reverse electrodialysis (RED) is the main technology for harvesting such osmotic energy [196]. Utilizing RED, electricity can be generated for domestic and industrial power supply, which could significantly reduce our dependence on non-renewable fossil fuels [197].

Permselective membranes are the core component of the RED technology. An ideal permselective membrane should simultaneously possess high permselectivity (to avoid Gibbs free energy loss caused by direct mixing), high ionic conductivity (to ensure fast ion transport and high power output), and sufficient mechanical strength (to avoid membrane rupture due to pressure imbalance) [198]. Currently, two-dimensional (2D) materials, such as graphene oxide [199], MoS_2 [136], boron nitride [200], and Mxenes [201], have been applied to develop permselective membranes for RED. The stacks of 2D nanosheets with interlayer spaces between them act as nanofluidic channels, reducing the transport resistance and enabling the ion flux [202]. However, the real-world applications of these 2D material based-membranes have been still impeded by several intrinsic drawbacks. These include: (1) The low nanochannel density and the relative long ion diffusion distances, leading to limited ion transport dynamics; (2) The insufficient ion-selective property, which reduces the efficiency; (3) The poor mechanical strength with low durability in water, which exists in most of these membranes [168]. Therefore, developing high-performance permselective membranes based on molecular design for efficiently harvesting osmotic energy is highly desired but still remains a challenge.

Nature has developed numerous perfect systems over billion years of evolution. Learning from nature is an eternal theme in human survival and sustainable development. Serosa structures are widely found in living organisms, either terrestrials, aquatic or marine. Such membranes surrounds many specific body organs (*e. g.* hearts, kidneys, brains, eyeballs, *etc.*) and protect them against mechanical stresses, penetration by parasitic species and unwanted diffusion in or out by chemical substances [203]. In these serosas, many ion channels and

ion pumps are embedded, providing massive pathways for selective ion diffusion [204]. Meanwhile, collagen fibers are also tightly wrapped around the cells, enhancing the membrane strength and maintaining the structural integrity of cells [205]. Inspired by this unique biological nanoarchitecture, herein for the first time, we report a biomimetic membrane composed of sulfonated 2D covalent organic framework (COF, denoted as PyPa-SO_3H) nanosheets and styrene sulfonic sodium (SSNa)-grafted aramid nanofibers (ANFs) for osmotic energy generation. On the one hand, imitating the structure of living cell membranes, the porous PyPa-SO_3H nanosheets simultaneously possess abundant one-dimensional (1D) nanofluidic nanochannels vertically along the lamination direction and 2D nanochannels parallel to the lamination direction, synergistically endowing ultrafast ion migration dynamics. Moreover, such COF nanosheets enable high cation permselectivity via the covalently tethered anion groups. On the other hand, the SSNa-grafted ANFs (SANFs) not only function like collagen fibers to dramatically increase the membrane strength and enhance the membrane stability in water, but also increase the interlayer spacing of adjacent nanosheets to boost ion diffusion and further improve the ion selectivity. When applied for harvesting osmotic energy from the mixing of natural sea and river water, the serosa-inspired PyPa-SO_3H/SANF membrane delivered a high output power density of 9.6 W m^{-2} with a low intermediate resistance, far outperforming commonly used ion-exchange membranes (<2.2 W m^{-2}) and attaining almost twice the commercial benchmark (5 W m^{-2}) [206]. Density functional theory (DFT) calculations and molecular dynamics (MD) simulations reveal that such superior performance can be attributed to the synergistic effect of PyPa-SO_3H nanosheets and SANFs. This work elucidates the great promise of such “bionic” design for developing high-performance permselective membrane-based osmotic power generators.

3.3. Methods

3.3.1. Chemicals

TFPPY (97%), Pa-SO_3H (99%), 1, 4-diaminobenzene (98%), DMSO (99%), 1, 4-dioxane (99.5%), acetic acid (AcOH, 99.5%), potassium hydroxide (KOH, 95%), sodium chloride (NaCl, 99.5%), N, N-dimethylformamide (DMF, 99%), tetrahydrofuran (THF, 99.5%), methanol (99.5%), benzophenone (BP, 99%), acetone (99%), SSNa (99%) and bulk Kevlar were purchased from Aladdin Co., Ltd. All the chemicals were used as received without further treatment.

3.3.2. Material Synthesis

TFPPY (140 mg, 0.226 mmol) and Pa-SO_3H (85 mg, 0.452 mmol) were suspended in anhydrous 1, 4-dioxane (21.0 mL) in the presence of aqueous acetic acid (4.2 mL, 3.0 M) in a Pyrex tube. The mixture was then degassed by freeze pump-thaw technique three times under a liquid nitrogen bath and then sealed under vacuum. The tube was heated at 120 °C for 7 days. Upon cooling to room temperature, the precipitate was collected by filtration and washed by DMF, THF and methanol, dried under vacuum to obtain PyPa-SO_3H as yellow powders (133 mg, 78%). For comparison, PyPa was synthesized following a same procedure except for replacing the Pa-SO_3H by 1,4-diaminobenzene in the raw materials list.

To prepare PyPa-SO_3H ultrathin sheets, the as-synthesized PyPa-SO_3H were mixed with NaCl evenly and then ball-milled in a jar. The weight ratio of PyPa-SO_3H: NaCl was set as 1:3000. After that, the PyPa-SO_3H coated NaCl was filtered and washed with deionized water to remove the NaCl, and further freeze-dried to obtain exfoliated PyPa-SO_3H nanosheets. PyPa nanosheets were prepared following the same procedure.

Firstly, ANFs were prepared by adding 1 g bulk Kevlar and 1 g KOH into 100 mL DMSO. The mixture was magnetically stirred for 1 week at room temperature to obtain the ANFs. Subsequently, a two-step photo-grafting method was carried out to graft SSNa monomer onto the ANFs. First, 1 mL ANF suspension was cast on a clean glass substrate and dried in air. After that, 0.5 mL 10 wt% BP in acetone solution was added onto the ANF membrane. Then the as-treated ANF membrane was sandwiched between two pieces of transparent glass and exposed to UV-irradiation from a Hg UV lamp (with an irradiation peak intensity

of 5 W m^{-2}) for 5 min at room temperature. The BP-treated membrane was washed with acetone and dried at room temperature to remove the residual BP, and then re-sandwiched between two pieces of glass in the presence of 0.5 mL 0.1 M SSNa in deionized water. The ANF membrane was subjected to a UV re-irradiation for 20 mins at room temperature. Finally, the as-grafted membrane was repeatedly extracted with deionized water to remove the residual monomer and oligomer, and then dried at 60 °C under vacuum to a constant weight. The grafting degree on the ANFs can be calculated as $(W_g–W_b)/W_o \times 100$ %, where W_b and W_g are the weights of the blank ANFs and SANFs, respectively.

The PyPa-SO_3H nanosheets were dispersed in DMSO, and further mixed with SANFs with a weight ratio of 9:1. The mixture was sonicated for 30 min and stirred for 2 h to form a uniform suspension. The PyPa-SO_3H/SANF mixture was vacuum filtered on a nylon membrane filter (pore size of 0.22 μm, Whatman) and washed with deionized water 3 times. After drying in vacuum at 60 °C for 24 h, the PyPa-SO_3H/SANF membrane was easily peeled off the substrate.

3.3.3. Material Characterizations

The morphology of the synthesized products was analyzed by SEM (S-4800), AFM (FM-Nanoview 6800AFM), transmission electron microscopy (TEM, Hitachi H-7500) and HR-TEM (FEI F20) with attached X-ray energy dispersive spectrometry (EDS). The structure and chemical components of the products were characterized by XRD (D8 Advance diffractometer with Cu Kα radiation (λ = 1.5406 Å)), FT-IR (Bruker VERTEX 70), XPS (ESCALAB 250 with 150 W Al K*α* probe beam), N_2 adsorption /desorption at 77 K (Tristar II 3020 instrument). The thermal stability of the composite membranes was quantified by thermogravimetric analysis (TGA, Pyris 1 TGA) from 25 °C to 800 °C with a heating rate of 5 °C min^{-1} in nitrogen atmosphere. The mechanical characterization of the composite membranes was conducted on a tensile-compressive tester (M5-2) with a loading rate of 1 mm min^{-1}. The Zeta potentials of PyPa-SO_3H powders and SNAFs were performed in solution system using a Zetasizer (Nano ZSP, Malvern Instruments Ltd., Malvern, UK). The water contact

angles were measured on a goniometer (Data Physics OCA 35) by using water droplets of 4 μL.

3.3.4. Electrical measurements

The transmembrane ionic transport and subsequent osmotic energy conversion tests were performed with an electrochemical workstation (Chenhua, CHI 660E). The osmotic energy conversion was investigated by measuring the I-V curves in presence of a transmembrane concentration gradient. The sweeping voltage was from -0.4 V to 0.4 V with a step of 0.04 V. The voltage is swept from positive to the negative to study the iodic-like behaviours and the symmetrical structure of the membrane. The experimental setup can be represented in terms of an equivalent circuit as shown in Figure S1.27. The composite membrane was mounted between a two-compartment electrochemical cell. The testing membrane area was about 3×10^4 μm^2. Lab-made Ag/AgCl electrodes were used to apply a transmembrane electrical potential and held stable during the testing process (Supplementary Note S1.1 and S1.2). The cation transference number was calculated based on an equation shown in Supplementary Note S1.3. All testing data was recorded after the current reached a steady state. The testing NaCl solutions were all prepared using ultrapure water (18.2 MΩ cm), meanwhile the natural sea water was collected from Manly Beach in Australia.

3.3.5. Computations

All DFT calculations were performed using $DMol^3$ program[207]. The generalized gradient approximation with Perdew-Burke-Ernzerhof functional (GGA-PBE) was used for the exchange-correlation energy [208]. Spin-polarized calculations were employed with the double numerical polarization basis set. To accommodate the van der Waals interactions, the semi-empirical Tkatchenko-Scheffler (TS) scheme was included for dispersion correction [209]. DFT semi-core pseudopotentials were applied for the core-electron treatment. The Brillouin zone was sampled by a Monkhorst-Pack grid as *Γ*-point for all systems [210]. The SCF convergence for each electronic energy was set as 1.0×10^{-6} Ha, and the geometry optimization convergence criteria were set up as follows: 1.0×10^{-5} Ha

for energy, 0.002 Ha $Å^{-1}$ for force, and 0.005 Å for displacement, respectively. Na ion migration pathways were examined by linear and quadratic synchronous transit (LST/QST) methods in combination with the conjugated gradient (CG) refinement [211].

For the MD simulation, the models of PyPa and PyPa-SO_3H were built using Materials Studio. The Lennard-Jones non-bonded parameters were selected based on Rappe *et al* [212]. Based on Rappe *et al*, The non-bonded distance parameters (unit in Å) was obtained to be 2.886, 3.851, 3.66, 3.5, 2.983, 3.947, and non-bonded energy parameters (unit in kcal/mol) was obtained to be 0.044, 0.105, 0.069, 0.060, 0.030, 0.227, for the elements of Hydrogen, Carbon, Nitrogen, Oxygen, Sodium, Chloride, respectively [212].The simulation was conducted using 0.5 M NaCl solution. Information on the size of NaCl solution diffusion box is given in Supplementary Note 4. The electric field was set to be 225 Kcal mol^{-1} A^{-1} e^{-1}. The packing of water molecules and ions were performed using Packmol software [213]. The electric field was applied in -Z direction and +Y direction for in-plane and interlayer Na^+ ion transport, respectively. The directions of the electric fields were reversed for Cl^- ion diffusion. The MD simulation was performed via Nanoscale Molecular Dynamics (NAMD). The system was initially minimized using isothermal-isobaric (NPT) ensemble for 2 ps. The production run was performed for 30 ps in periodic boundary conditions via the canonical (NVT) ensemble, and the simulation was visualized using visual molecular dynamics (VMD) software.

3.4. Results and discussion

3.4.1. Material Characterization

PyPa-SO_3H was rationally designed for constructing an anionic framework with well-defined and directional ion channels. The rod-like PyPa-SO_3H COF powders can be facilely synthesized from tetrakis (p-formylphenyl) pyrene (TFPPY) and 2, 5-diaminebenzene sulfonic acid (Pa-SO_3H) (inset of Figure 3.1 a and Figure S1.1-1.2). The X-ray diffraction (XRD) pattern reveals a staggered A-B stacking conformation of PyPa-SO_3H (Figure 3.1 a) with high crystallinity, which is different

from the A-A packing eclipsed arrangement of PyPa without the sulfonic acid group (Figure S1.3). The pore size of a single-layer PyPa-SO_3H COF unit is 23 Å based on the simulated conformation, which is consistent with previous reports [214]. Under the A-B stacking mode, the pore size reduces to 11.5 Å due to the mismatching of pristine pores (Figure S1.4). The PyPa-SO_3H was characterized by Fourier transform infrared spectroscopy (FT-IR), which showed C=N stretching at 1662 cm^{-1} and -O=S=O stretching at 1168 cm^{-1} (Figure S1.5) [215]. This COF shows high thermal stability up to ≈500 ^oC (Figure S1.6). After exfoliated into nanosheets (details are shown in Experimental section), the PyPa-SO_3H sample delivers a large Brunauer-Emmett-Teller (BET) surface area of ≈1110 m^2 g^{-1} (Figure S1.7). Such abundant mesopores distributed across the PyPa-SO_3H nanosheets are expected to benefit rapid ion diffusion. Moreover, the channel radius of these pores is close to the Debye length of the electric double layer, leading to a surface charge-governed ionic transport with high ion selectivity [107, 216]. The PyPa-SO_3H nanosheets possess a lateral width of ≈300 nm and a thickness of ≈4.8 nm according to the high-resolution transmission electron microscopy (HR-TEM) and atomic force microscopy (AFM, Figure S1.8) characterizations, respectively. Furthermore, the PyPa-SO_3H nanosheets exhibit an enhanced cation permeability (Figure S1.9) in the pH range of 4-9, and can form stable dispersions in common organic solvents (*e. g.* dimethyl sulfoxide (DMSO), Figure S1.10). These facilitate the assembly of free-standing PyPa-SO_3H-based membranes.

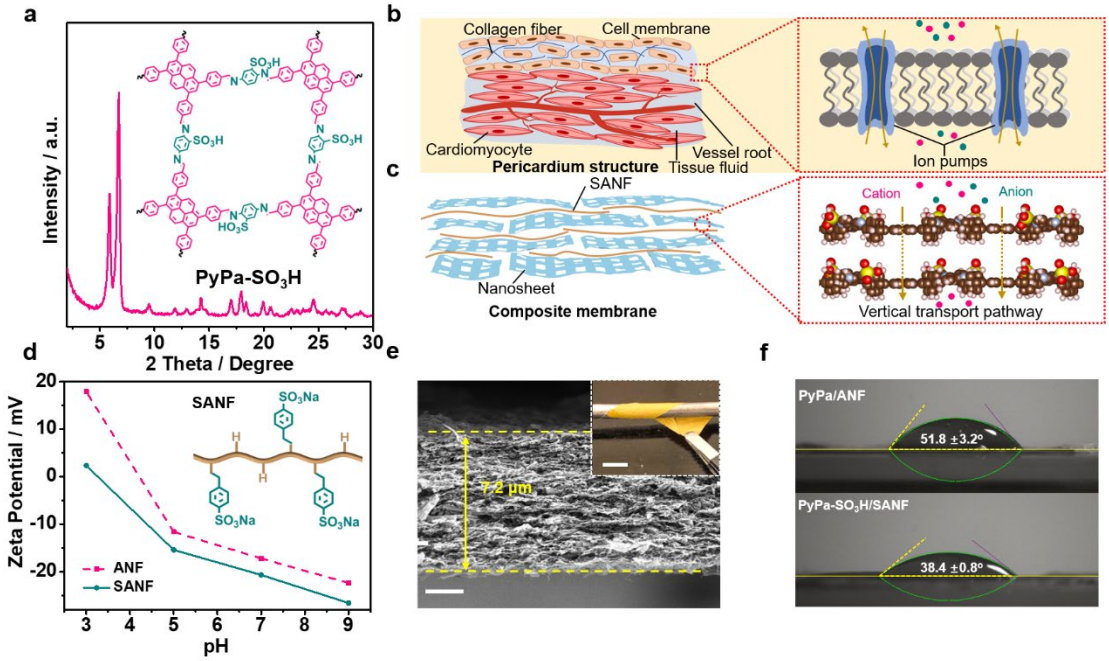

Figure 3.1. Characterization of PyPa-SO₃H/SANF membrane. *(a) XRD patterns of PyPa-SO₃H powder. The chemical structure of PyPa-SO₃H is shown in inset. Schematic illustrations of (b) pericardium structure (left) and the ion pumps on the cell membrane (right); and (c) PyPa-SO₃H/SANF composite membrane. (d) Zeta potential of ANF and SANF. The structure of SANF is shown in inset. (e) Optical (inset) and cross-sectional SEM images of PyPa-SO₃H/SANF membrane. Scale bars: 200 nm in Figure 2c and 1 cm in its inset. (f) Contact angles of water on PyPa/ANF and PyPa-SO₃H/SANF membranes.*

Figure S1.11 illustrates the fabrication procedure for SANF, which was grafted by a two-step ultraviolet (UV)-introduced photografting polymerization strategy based on our previous work [217]. The SANFs possess unique merits compared with other 1 D nanospacers (*e. g.* carbon nanotubes (CNTs) [218, 219] and single walled carbon nanotubes (SWNTs) [220]) in the preparation of composite membrane. First, SANFs exhibit ultrahigh aspect ratio, strength and modulus, which provide the composite membrane with high flexibility and robustness. Secondly, the negatively charged surface of SANFs significantly improves the ion selectivity of the composite membrane. Additionally, the low cost and simple grafting method of SANFs facilitates their practical application. The FT-IR (Figure S1.12) and X-ray photoelectron spectrum (XPS, Figure S1.13) results demonstrate a successful surface graft polymerization of SSNa onto the ANF. The degree of grafting of the ANF was controlled to be 5.1 %. Subsequently, the PyPa-SO₃H/SANF membranes were prepared by directly filtering the DMSO dispersion of PyPa-SO₃H nanosheets and SANFs (Figure S1.14). The PyPa-

SO_3H/SANF membrane exhibit a hierarchical pore structure, which possesses 11.5 Å micropores across the A-B stacking PyPa-SO_3H COF (Figure S1,4) and 2-25 nm mesopores stacked between the nanosheets (Figure S1.15). As shown in Figure 3.1 b and c, the structure of the as-developed PyPa-SO_3H/SANF membrane resembles that of pericardium as a representative serosa. The pericardium structure is comprised of large number of pericardium cells distributing in the presence of tissue fluid and abundant collagen fibers. The collagen fibers are tightly wrapped around the pericardium cells, providing high strength and protecting the stability inside the heart (Figure 3.1 b, left panel). Meanwhile, the massive ion pumps in the cell membrane efficiently maintain the ionic imbalance between the inside and outside of pericardium cells by selectively transporting ions (Figure 3.1 b, right panel). Thus, the pericardium structure enables high ion permselectivity and fast ion migration as well as high mechanical strength [94]. Imitating the structure of the cell membrane in pericardium, the PyPa-SO_3H nanosheets possess large number of ordered vertical channels and covalently tethered anion groups, thus permitting fast ion transportation and high cation permselectivity, respectively (Figure 3.1 c, right panel). Moreover, the SANFs act as collagen fibers to significantly enhance the membrane strength and well-maintain the membrane stability in water (Figure 3.1 c, left panel). The negative zeta potential values of ANF fibers obviously increased after SSNa grafting in the pH range of 4-9 (Figure 3.1 d), which further promotes the permselectivity. Therefore, this biomimetic PyPa-SO_3H/SANF hybrid membrane is expected to meet the requirements of high-efficiency osmotic energy generation.

As shown in the scanning electron microscope (SEM) images in Figure S1.16 and Figure 3.1 e, the PyPa-SO_3H/SANF membrane exhibits a surface morphology consisting of stacked PyPa-SO_3H nanosheets and plenty of holes, and the thickness is around 7.2 μm. The membrane shows a lamellar structure, with SANF acting as cross-linker between the nanosheets. The PyPa-SO_3H/SANF membrane displays high flexibility (Figure 3.1 e, inset) with an ultimate mechanical strength as high as 48.2 MPa (Figure S1.17). For comparation, the strength of stacked PyPa-SO_3H membrane is only 5.8 MPa. The high mechanical strength of the hybrid membrane is crucial for the real-world

application in osmotic power generators. The water wettability of such a hybrid membrane is shown in Figure 3.1 f. The static contact angle of water on pristine PyPa/ANF membrane was measured to be 51.8 ± 3.2° (Figure 3.1 e, upper panel), which was reduced to 45.9 ± 1.4° after the SSNa grafting on ANFs (PyPa-SO_3H/ANF, Figure S1.18) and 38.4 ± 0.8° after the sulfonation of PyPa nanosheets (PyPa-SO_3H/SANF, lower panel of Figure 3.1 f), respectively. Such an enhanced hydrophilicity would increase the interface contact with water and hence accelerate the ion migration through the membrane.

3.4.2. Transmembrane Ionic Transport Properties

To characterize the transmembrane ionic transport properties, the PyPa-SO_3H/SANF membranes were squeezed between symmetric H-type electrochemical cells containing NaCl solution of various concentrations (Figure S1.19). Figure 3.2 a shows a series of ionic current-voltage (I-V) response curves recorded in NaCl electrolyte with concentrations ranging from 10^{-6} M to 0.5 M. All the curves present a linear ohmic behavior, ascribed to the symmetric structure of the electrochemical testing system. Therefore, the electric conductance (G), which can be calculated as $G=I/\Delta V$, reveals the charge-governed ionic transport through the PyPa-SO_3H/SANF membrane [221]. Figure 3.2 b shows the electric conductance as a function of salt concentration. The values of the effective conductance exhibit a linear relationship with the salt concentration in the high concentration region (>1 mM), which is related to a bulk diffusion behavior. In contrast, the conductances become almost a constant in the low salt region (<1 mM), demonstrating a surface-charge-governed ion transport behavior [222]. The conductance values of the PyPa-SO_3H/SANF membrane varies from 10^{-6}-10^{-3} S m^{-1} with the salinity gradient. This value is obviously higher than the previous reports of other membrane materials [223, 224], indicating an ultrafast ion migration through the hybrid membrane.

Applying chemical potential gradients could provide further insight into the ion transport process. By collecting I-V curves in the presence of a transmembrane concentration gradient, the values of diffusion potential (V_{diff}) and diffusion current (I_{diff}) can be directly derived from the measured open-circuit voltage and short-

circuit current, respectively (Table S1.1) [225]. Figure 3.2 c shows the representative I-V curves of the PyPa-SO_3H/SANF membrane recorded under 0.5 M/0.1 mM NaCl concentration gradient. Under a reverse concentration gradient, the I_{diff} and V_{diff} show similar absolute values to those under forward concentration gradient, but are of the different polarities due to the opposite ion diffusion direction. This indicates the symmetry of the PyPa-SO_3H/SANF membrane with no preferential direction for ion diffusion. Furthermore, the I_{diff} and V_{diff} values both increase with increased concentration gradient (Figure 3.2 d). The corresponding transference number of Na^+ (t_+) was calculated to be 0.82 (Figure 3.2 e) in a 500-fold concentration gradient, which is dramatically higher than those of PyPa-SO_3H/ANF (0.75), PyPa/ANF (0.73), PyPa (0.68) membranes and the previously reported values[10, 22]. Such a high transference number is mainly due to the sulfonation of PyPa nanosheets and the SSNa grafting on ANFs, clearly validating a high ion permselectivity which is crucial for the electrical energy creation from salinity gradients. Furthermore, neglecting any effects related to the pores and differences in ion activities, the osmotic electrostatic potential difference between the two sides of the membranes (E_{osm}) can be calculated as [226, 227]:

$$E_{osm} = S \times \beta \quad (1)$$

Where S is the ion selectivity coefficient of the nanofluidic channel, which can be defined as: $S = \sqrt{2\phi}$. Here, ϕ is energy conversion efficiency, calculated by $\phi = \frac{1}{2}(2t_+ - 1)^2$. Meanwhile, β is a simplified concentration difference coefficient expressed as:

$$\beta = \frac{RT}{zF} \ln \frac{c_H}{c_L} \quad (2)$$

where R, T, z, F, c_H, c_L are ideal gas constant, temperature, charge number, Faraday constant, the concentrations of concentrated solution and the dilute solution, respectively. As shown in Figure 3.2 f, the osmotic potential of the PyPa-SO_3H/SANF membrane was 93.2 mV in a 500-fold concentration gradient, which is obviously higher than other membrane samples, suggesting a high driving force for osmotic power and a reduced Gibbs free energy loss that dissipates as Joule heating.

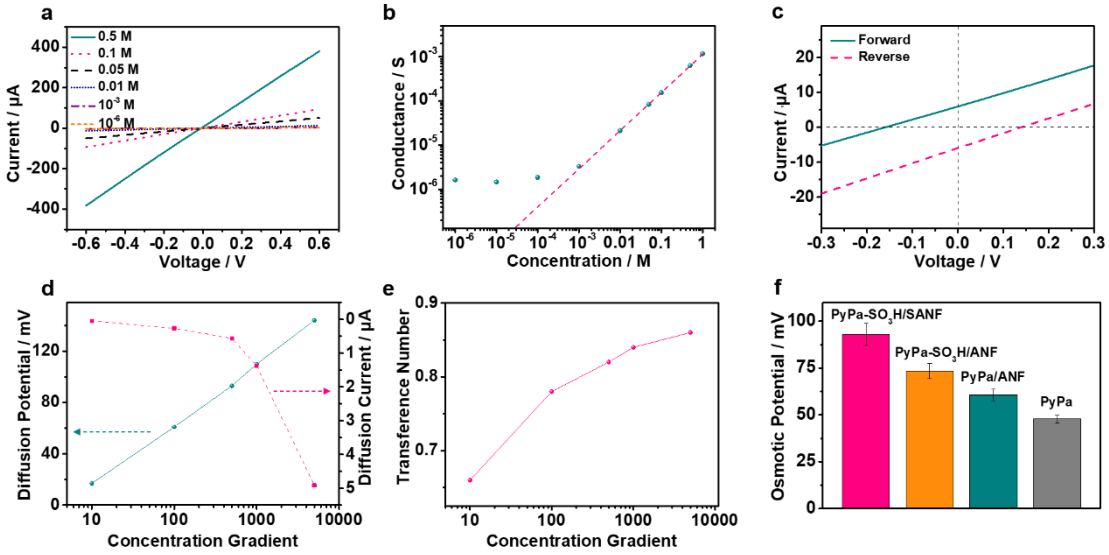

Figure 3.2. Transmembrane ionic transport properties of PyPa-SO₃H/SANF. *(a) I-V curves and (b) conductance of PyPa-SO₃H/SANF membranes sandwiched between symmetric H-type cells containing NaCl solution of various concentrations. The dots represent experimental data, while dashed line represents fitting result. (c) I-V curves of PyPa-SO₃H/SANF membrane with 5000-fold NaCl concentration gradient under forward and reverse diffusion directions. (d) Recorded I_{diff} and V_{diff} and (e) Transferences number of PyPa-SO₃H/SANF membranes with different concentration gradients. (f) Osmotic potential values of different membranes in the presence of 500-fold NaCl concentration gradient. The low concentration side is set as 0.1 mM NaCl.*

3.4.3. Osmotic Energy Conversion

The harvested electric power from the PyPa-SO₃H/SANF membrane is determined by transferring the power to an external circuit with an electrical load resistor (Figure 3.3 a). Standard artificial sea water (0.5 M NaCl) and river water (0.01 M NaCl) were filled into the two sides of H-type cells, respectively, and the current densities ($I_{osmosis}$) were recorded by changing an external resistance load (R_L). The output power density of the resistor (P_L) is accordingly calculated using the equation: $P_L = I_{osmosis}^2 R_L$ [228]. It is seen that, with increasing R_L, the current density continuously decreased (Figure 3.3 b), and the output power reached a maximum value at an intermediate resistance of ≈5 kΩ (Figure 3.3 c). Furthermore, the composition of permselective membranes showed a significant influence on the output power density. The PyPa-SO₃H: SANF ratio was optimized as 9: 1 in the preparation of PyPa-SO₃H/SANF membrane (Figure S1.20) meanwhile the membrane thickness was optimized as 7.2 μm (Figure S1.21). As shown in Figure 3.3 c and Figure S1.22, the maximum power density

of PyPa-SO_3H/SANF membrane reached 8.7 W m^{-2}, which is significantly higher than that of the PyPa-SO_3H/ANF (7.4 W m^{-2}), PyPa/SANF (6.8 W m^{-2}), PyPa/ANF (6.4 W m^{-2}), and PyPa (2.5 W m^{-2}) membranes. To simulate a practical application, a PyPa-SO_3H/SANF membrane was applied to harvest energy from the salinity difference between the natural sea water and river water. As shown in Figure 3.3 d, the maximum power density delivered a value of 9.6 W m^{-2}, far exceeding the value of commercial benchmark (5 W m^{-2}). The osmotic energy conversion performance did not significantly change even when the test area of PyPa-SO_3H/SANF membrane was enlarged to 20.74 mm^2 (Figure S1.23). Moreover, the output energy density increased with the raise of the concentration gradient. Utilizing the PyPa-SO_3H/SANF membrane, the output energy density researched 10.5 W m^{-2}, 62.9 W m^{-2} and 73.5 W m^{-2} in the cases of 61.4-fold (artificial *Mediterranean Sea* water|river water), 500-fold (artificial *Salt-Dome* solution) and 614-fold (artificial *Death Sea* water|river water) concentration gradients, respectively (Figure 3.3 e), demonstrating the special application merits in estuaries with large concentration difference.

Such superior performance of the PyPa-SO_3H/SANF membrane can be explained as follows. Firstly, a large number of orderly arranged pores are vertically distributed on the PyPa-SO_3H nanosheets, providing enhanced cross-membrane flux. Secondly, the intercalation by SANF nanofibers sufficiently enlarges the interlayer spaces of the hybrid membrane, which accelerates the ion diffusion [229]. Moreover, the elaborate sulfonation of PyPa nanosheets and SSNa grafting on ANFs synergistically contribute to superior water wettability and high cation permselectivity, thus resulting in high-efficiency osmotic energy production. To the best of our knowledge, the power density obtained in this work is higher than most of the previously reported macroscopic-scale nanofluidic membrane-based RED (Figure 3.3 f and Table S1.2)[201, 215, 224, 228, 230-234]. More importantly, without continuous electrolyte replenishing, the current density on the external circuit exhibited negligible attenuation for 72 hours (Figure 3.3 g), demonstrating the durability of the PyPa-SO_3H/SANF membrane in osmotic energy generation. The PyPa-SO_3H/SANF membrane also shows excellent working stability. Compared with the PyPa membrane that crumbled after soaking in water for only one day (Figure S1.24), the PyPa-SO_3H/SANF

composite membrane well-maintained its integrity even after immersing in water for one month (Figure 3.3 h), and the power output did not present obvious attenuation. This validates the great application viability of such a biomimetic membrane in practical osmotic energy harvesting.

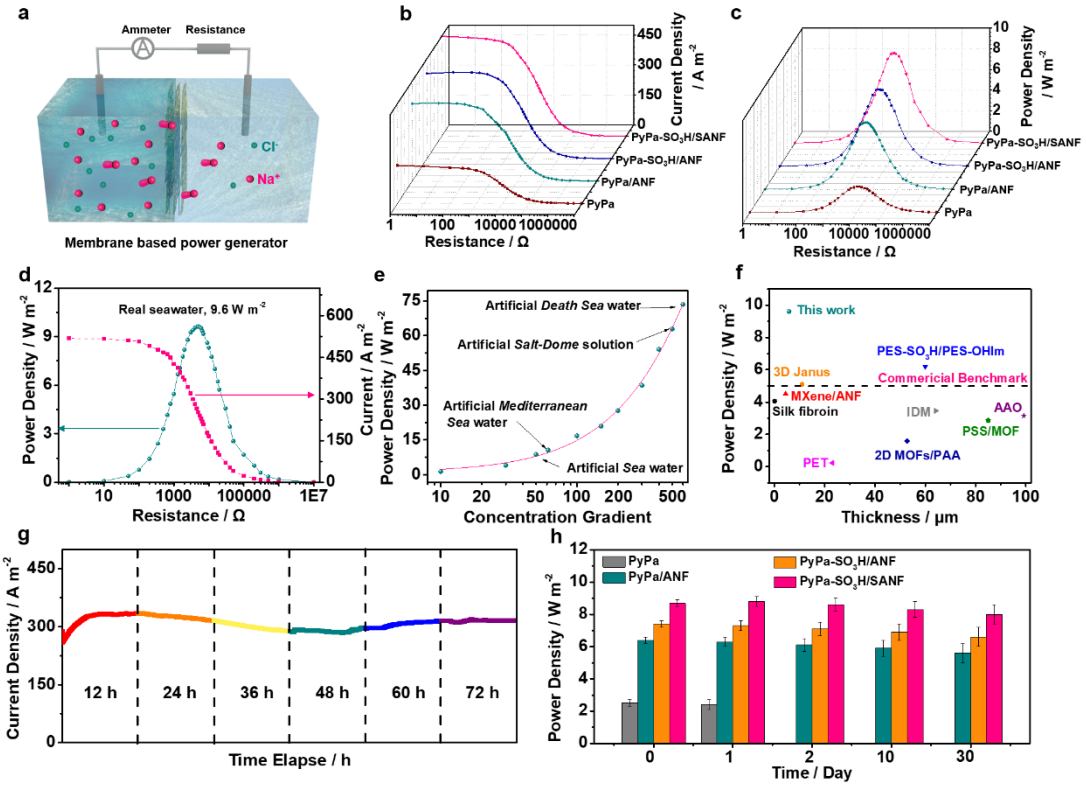

Figure 3.3. Osmotic energy conversion behaviour of PyPa-SO₃H/SANF. *(a) Schematic of the osmotic energy conversion process. (b) Current density and (c) power output of different membranes as functions of load resistance in the presence of artificial sea water|river water. (d) Power output of a PyPa-SO₃H/SANF membrane between natural sea water|river water with a resistance load of 5 KΩ. (e) Power density of a PyPa-SO₃H/SANF membranes with different concentration gradients. (f) Comparison of osmotic energy conversion performance with reported macroscopic-scale nanofluidic membranes under the same testing conditions. (g) Current-time curve of a PyPa-SO₃H/SANF membrane in artificial sea water|river water without electrolyte replenishing with a resistance load of 5 KΩ. (h) The power densities of different membranes after immersing in water for several days.*

3.4.4. Theoretical Computations

The unique Na ion transference phenomena of PyPa-SO₃H nanosheets were theoretically calculated by density functional theory (DFT). The Na ion migration inside the stacked PyPa-SO₃H nanosheets was investigated by comparing energy barriers in two types of anisotropic pathways (the inset in Figure 3.4 a-b).

It is seen that two peaks appear in the energy curve of the horizontal Na ion transport pathway (Figure 3.4 a), mainly due to the fact that Na ions need additional energy to escape from the electrostatic attraction when passing through the two SO_3H-tethered regions (the inset in Figure 3.4 a). Meanwhile, in the vertical Na ion transport pathway, the diffusion of Na ions deviates from the vertical direction due to electrostatic attraction (the inset in Figure 3.4 b). Noticeably, the Na ion migration in the vertical pathway along the lamination direction possesses a low energy barrier (0.78 eV, Figure 3.4 b) comparable to that in the horizontal pathway (0.80 eV, Figure 3.4 a), indicating an excellent mobility of the Na atom through the intraformational nanochannels of PyPa-SO_3H nanosheets in the vertical direction. It is well-known that the ion cannot pass through a conventional 2D nanosheet (*e. g.* graphene, boron nitride and molybdenum disulfide) along the vertical direction (*i. e.* energy barrier equals ∞). As a result, a membrane based on these conventional 2D nanosheets, the ion transport is mainly limited in the interlayer spaces between 2D nanosheets acting as 2D lamellar nanochannels [235]. Therefore, the ion transport across such membranes in the vertical direction is usually low due to the intricate transport path with long diffusion distance (Figure 3.4 d) [236]. In contrast, PyPa-SO_3H is a novel crystalline porous material with abundant permselective nanopores along the stacking direction. These high density 1D nanochannels with short vertical diffusion distance significantly increase the cross-membrane ion flux (Figure 3.4 e). Considering the synergetic effect of both vertical 1D diffusion channels and horizontal 2D diffusion channels (Figure 3.4 f), the energy barrier of Na ion migration through stacked PyPa-SO_3H nanosheets further reduces to 0.69 eV (Figure 3.4 c), thus giving rise to the ultra-high ion transport dynamics. Taking into account the larger interlayer spacing brought by the SANF nanospacers, the energy barrier through the horizontal pathway will undoubtedly be lower to further promote the Na ion transport.

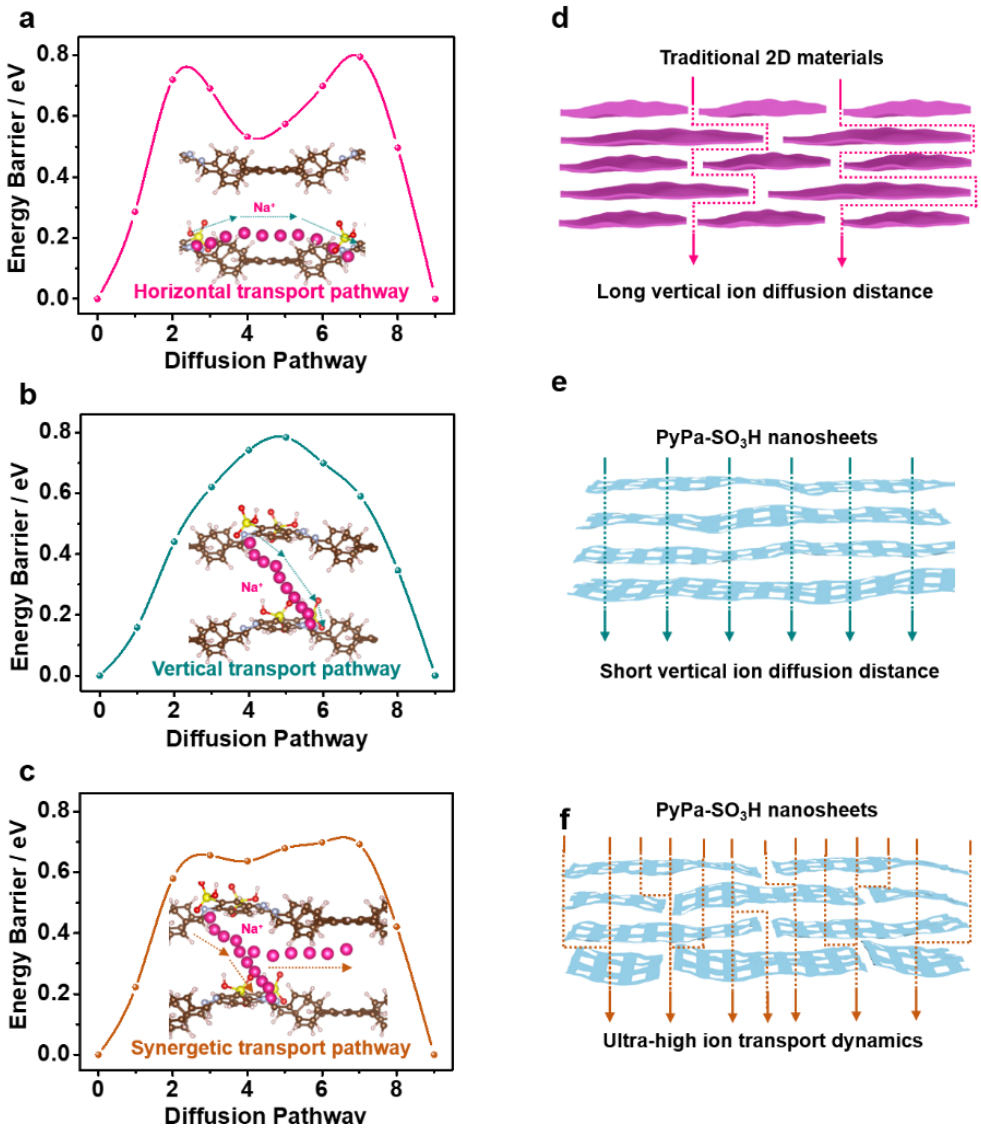

Figure 3.4. DFT calculations of PyPa-SO₃H/SANF. *(a-c) The Na ion migration energy barriers through stacked PyPa-SO₃H nanosheets in (a) horizontal, (b) vertical directions, and (c) both horizontal and vertical directions. (d) Schematic illustration of the ion migration pathway through stacked conventional 2D nanosheets, and (e-f) the ion migration pathway through stacked PyPa-SO₃H nanosheets in (e) vertical and (f) both horizontal and vertical directions. Atom colors: purple (sodium), brown (carbon), pink (hydrogen), grey (nitrogen), red (oxygen), yellow (sulfur).*

Molecular dynamics (MD) simulations were performed to further elucidate the cation transfer mechanism in the PyPa-SO₃H/SANF membrane. Figure 3.5 a-b show the simulation model comprised of stacked layers of COF, water, and salt ions. Both PyPa and PyPa-SO₃H/SANF membrane were solvated by water molecules in the vertical direction, and sodium and chloride ions reservoirs were positioned at the top of the model. Figure 3.5 a displays eight monolayers of PyPa stacked with the interlayer spacings of 0.65 nm (*i. e.* the theoretical value of the stacked PyPa nanosheets). Additionally, Figure 3.5 b displays eight monolayers

of PyPa-SO_3H/SANF with the interlayer spacings of 25 nm. The interlayer spacing for the PyPa-SO_3H/SANF model was assumed to be similar to SANF's diameter (Figure S1.25). The PyPa and PyPa-SO_3H/SANF were also solvated in the horizontal direction and ionized with sodium and chloride ions (Figure S1.26). Figure 3.5 c-d show the transfer quantity of a selected ion (*i. e.* the number of Na^+ or Cl^- ions transferring across the membrane during the simulation time) obtained from the MD simulations. Meanwhile, the corresponding ionic currents (I_{Na^+} and I_{Cl^-}) can be calculated as the product of the slope values for the linear regions of charge transfer-time curves and the elementary charge (*i. e.* 1.6×10^{-19} C). The Na ion transference number, t_+, can be is calculated as:

$$t_+ = \frac{I_{Na^+}}{I_{Na^+} + I_{Cl^-}} \quad (3)$$

It is seen that the I_{Na^+} of PyPa-SO_3H/SANF membranes in the vertical direction (0.0106 μA, Figure 3.5 d) is much higher than that of the PyPa membrane (0.0048 μA, Figure 3.5 c). This mainly originates from the fact that the electrostatic attraction between negatively charged PyPa-SO_3H and Na^+ promotes Na^+ transfer. Meanwhile, the I_{Na^+} of PyPa-SO_3H/SANF membrane in the horizontal direction (0.0038 μA, the inset in Figure 3.5 d) is higher than that of the PyPa membrane (0.0031 μA, the inset in Figure 3.5 c) due to larger interlayer spacing enabled by the introduction of SANF nanofibers. Furthermore, the t_+ values of the PyPa-SO_3H/SANF membrane are much larger than those of the PyPa membrane in both diffusion directions (*i. e.* 0.702 *vs.* 0.580 in the vertical direction; 0.624 *vs.* 0.558 in the horizontal direction). This indicates a strong cation permselectivity of the PyPa-SO_3H/SANF membrane. The increased I_{Na^+} and t_+ in the PyPa-SO_3H/SANF hybrid membrane synergistically improve the osmotic energy conversion performance.

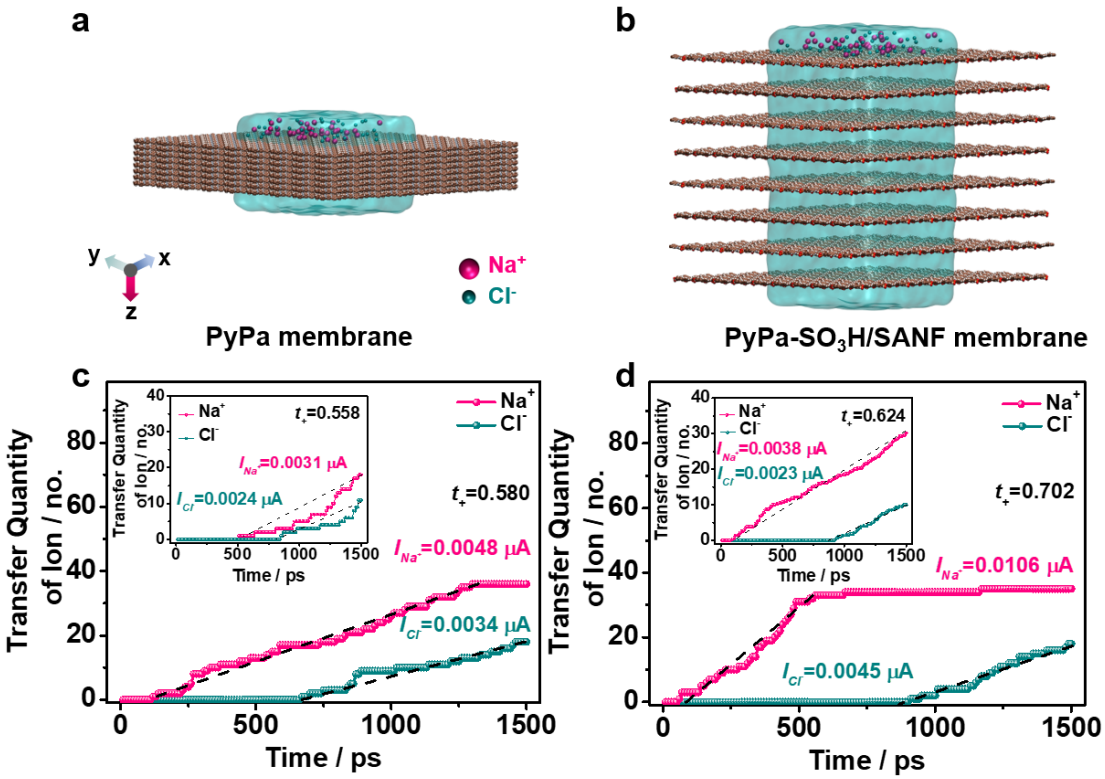

Figure 3.5. MD simulations of PyPa-SO₃H/SANF. *(a, b) 3D view of ion diffusion across (a) PyPa and (b) PyPa-SO₃H/SANF membranes in vertical pathway in NaCl solution. (c, d) Transfer quantity of Na^+ or Cl^- across (c) PyPa and (d) PyPa-SO₃H/SANF membranes in the vertical direction as a function of simulation time. The charge transfers in the horizontal direction are shown in the insets.*

3.5. Conclusion

‘

In summary, by replicating the architecture of the serosa, we have developed a PyPa-SO₃H/SANF composite membrane for highly efficient osmotic energy generation. The porous PyPa-SO₃H nanosheets with abundant 1D/2D nanochannels not only synergistically realize ultrafast ion transport, but also enable high cation permselectivity due to the covalently tethered anion groups. The mechanically strong SANFs significantly improve the membrane strength and its durability in water. Moreover, they further enhance the ion selectivity and enlarge the cross-membrane flux by increasing the interlayer spacing between PyPa-SO₃H nanosheets. The synergistic effects of the functional PyPa-SO₃H nanosheets and SANFs endow longevity and high-power generation in osmotic energy generators. The PyPa-SO₃H/SANF membranes achieved a maximum power density of 9.6 W m^{-2} for the natural sea/river water system, demonstrating

great promise for real-world applications. Meanwhile, we have revealed and highlighted the nanoscale correlation between ion permselectivity/ion transport kinetics and the energy-conversion performance through both theoretical and experimental investigations. Our key findings pave a new avenue in the exploration of renewable “blue energy”. Furthermore, the bio-inspired design strategy and controllable synthesis of permselective membranes in this work could be extended to a wide range of ion transport applications including water purification, desalination, and batteries, and thus boosting a sustainable future.

Chapter 4: Vacancy Engineering for High-Efficiency Nanofluidic Osmotic Energy Generation

4.1. Abstract

Two-dimensional (2D) nanofluidic membranes have shown great promise in harvesting osmotic energy from the salinity difference between seawater and fresh water. However, the output power densities are strongly hampered by insufficient membrane permselectivity. Herein, we demonstrate that vacancy engineering is an effective strategy to enhance the permselectivity of 2D nanofluidic membranes to achieve high-efficiency osmotic energy generation. Phosphorus vacancies were facilely created on $NbOPO_4$ (NbP) nanosheets, which remarkably enlarged their negative surface charge. As verified by both experimental and theoretical investigations, the vacancy-introduced NbP (V-NbP) exhibited fast transmembrane ion migration and high ionic selectivity originating from the improved electrostatic affinity of cations. When applied in a natural river water | seawater osmotic power generator, the macroscopic-scale V-NbP membrane delivered a record-high power density of 10.7 W m^{-2}, far exceeding the commercial benchmark of 5.0 W m^{-2}. This work endows the remarkable potential of vacancy engineering for 2D materials in nanofluidic energy devices.

4.2. Introduction

The osmotic energy between river water and seawater has been recognized as a clean and renewable “blue energy” source. Utilization of this osmotic energy could generate enormous power of ~1 TW [94], which is significantly higher than the global wind and solar power generation (~730 and 710 GW, respectively, the data of 2020) [95]. Besides, compared with the unpredictable wind and solar energy, this unintermittent blue energy with minimal daily variation is more

reliable for domestic and industrial power supplies [130]. By virtue of reverse electrodialysis (RED) technique, electricity can be generated from the osmotic energy, remarkably reducing excessive dependence on nonrenewable fossil fuels [112].

The core component of RED is permselective membranes [110]. Currently, two-dimensional (2D) materials, including graphene oxide [167], boron nitride [179], black phosphorous [178], transition metal oxides/dichalcogenides [164], MXene [165], and covalent organic frameworks [163], have been utilized to develop permselective membranes for RED. The abundant nanofluidic channels between the interlayer spacing of stacked 2D nanosheets significantly reduce the ion transport resistance and facilitate high ionic flux [113]. However, the output power densities of these existing 2D nanofluidic membranes are generally lower than 7 W m^{-2} [237], mainly due to the insufficient permselectivity that increases the Gibbs free energy loss. Several works have been reported on improving the ion-selectivity of 2D nanofluidic membranes via tuning the surface charge of nanosheets, including surface coating using permselective polymers [148, 238], introducing surficial functional groups [239, 240], and modifying the phase structure of 2D materials [164]. However, the polymer coating inevitably sacrifices the ion transport dynamics. The complexity in the treatment processes of the surficial functionalization and phase modification of 2D materials profoundly restrict their application; meanwhile, the durability of the membranes based on as-treated nanosheets in water is questionable [109]. To date, there has still been a lack of efficient strategies in tailoring the surface charge of 2D materials to realize high-performance osmotic power generation membranes.

Vacancy engineering has been proven to be an effective method to manipulate the electronic structure and modify the surface charge of 2D materials without deteriorating the chemical stability [45, 241]. However, to the best of our knowledge, vacancy-derived charge enlargement of nanosheets has never been applied to develop permselective membranes for osmotic energy harvesting. Herein, for the first time, we demonstrate that creating atomic vacancies on 2D materials can efficiently enhance the permselectivity of nanofluidic membranes as high-efficiency osmotic power generators. Niobium phosphate ($NbOPO_4$, denoted as NbP) nanosheets were chosen as a demonstration model,

considering their low energy barrier for ion diffusion that is expected to boost osmotic energy conversion [242]. Phosphorus (P) vacancies were created in NbPs through a facile acid etching process, which can dramatically improve the membrane hydrophilicity. Density functional theory (DFT) calculations, molecular dynamics (MD) simulations together with experimental investigations reveal that the P vacancies significantly enhance the negative surface charge of NbP nanosheets, enlarging the affinity to the transporting cations in the electrolyte. This renders the stacked membrane with excellent cation selectivity and high ionic flux to boost the power generation; as a result, the maximum output power density of the vacancy-introduced NbP (denoted as V-NbP) membrane under a 50-fold NaCl gradient was ~300 % higher than that of the pristine NbP membrane. When natural river water and seawater were mixed, the V-NbP membrane achieved a considerable output power density of 10.7 W m^{-2}, far outperforming the state-of-the-art macroscopic-scale 2D nanofluidic membranes (<7 W m^{-2}), and more than double the commercial benchmark (5 W m^{-2}). This work highlights the crucial roles of atomic vacancy engineering for 2D materials in modulating ion diffusion as well as osmotic energy conversion.

4.3. Methods

4.3.1. Chemicals

Niobium oxalate hexahydrate ($C_{10}H_5NbO_{20}\cdot 6H_2O$, 98 %) was purchased from Santa Cruz Biotechnology. Phosphoric acid (H_3PO_4, 85 %), dimethyl sulfoxide (DMSO, 99 %), potassium hydroxide (KOH, 95 %), 2-isopropanol (IPA, 99 %), sodium chloride (NaCl, 99 %) were purchased from Sigma-Aldrich. Kevlar yarns were purchased from Aladdin Co., Ltd.

4.3.2. Material Synthesis

Bulk NbP was first synthesized according to a previously reported method [243]. Briefly, 3.32 g of niobium oxalate was dissolved in 110 mL deionized water,

followed by adding 5 ml phosphoric acid and refluxing at 110 °C for 16 h. The obtained white precipitate was collected by centrifugation and then repeatedly washed with water and acetone. After that, the bulk NbP was dried in vacuum at 60 °C. NbP powder was first ultrasonicated in water with a concentration of 2 mg mL^{-1} for 20 min to get exfoliated NbP nanosheets. Subsequently, phosphoric acid was dropwise added to the NbP nanosheet suspension until reaching a final concentration of 0.5 M, and then stirred at room temperature for 1 day to complete the chemical etching process. Afterward, the powders were washed and dried in vacuum to obtain V-NbP. To fabricate membranes with identical thickness of ~7 μm, 10 mg of the as-synthesized NbP or V-NbP was first re-dispersed in 20 mL DMSO to get a uniform suspension of nanosheets, and then mixed with a 0.1 mg mL^{-1} ANF suspension in DMSO obtained by chemical etching of Kevlar yarns [163], with a NbP/V-NbP: ANF weight ratio of 100: 11.5. The mixture was subsequently filtered on a nylon substrate (pore size of 0.22 μm, Whatman) and washed with distilled water. After drying under vacuum at 60 °C for 24 h, the NbP and V-NbP membranes could be easily peeled-off from the nylon substrate.

4.3.3. Material Characterizations

The morphology of the samples was captured by field-emission SEM (Zeiss Supra 55VP), transmission electron microscopy (TEM, JEM 2100F), and HAADF-STEM (FEI F20) with attached X-ray energy dispersive spectrometry (EDS). XPS was conducted on an ESCALAB250Xi (Thermo Scientific, U.K.) equipped with monochromatic Al K alpha (energy 1486.68 eV). The ICP-MS was evaluated on Nexion5000, PerkinElmer USA, and the powder samples were dissolved in aqua regia solution prior to the analysis. The concentration of Sodium and chloride ions were analyzed using a multi-parameter analyzer (DZS-706, INESA Scientific Instruments Co., Ltd, Shanghai, China), where Na^+ ions were analyzed using Ion Selective Electrodes (ISE, 972207) and Cl^- ions using ISE, 972102. The mechanical strength of membranes was assessed by a tensile-compressive tester (M5-2) at a loading rate of 1 mm min^{-1}. The zeta potentials were measured using Zetasizer Nano (ZS90, Malvern Instruments Ltd., Malvern, England). XRD patterns were collected on a Bruker D8 Focus diffractometer using an incident

wavelength of 0.154 nm (Cu Kα radiation). The N_2 adsorption/desorption isotherms were collected using a Micromeritics automatic physisorption analyzer. The static water contact angles were measured at room temperature using an OCA25 contact angle measuring instrument (Dataphysics OCA 35, Germany) using 4 μL droplets. H-type glass cells were used to investigate the diffusion of anionic dyes (i.e., methyl orange) through different membranes. Half of the cell was filled with 40 mg L^{-1} aqueous solution of methyl orange, while the other half of the cell was filled with deionized water. These two parts of the H-type cell were connected via different membranes, and then the color change over time was recorded by a digital camera while the anion concentration was detected via UV-Vis (Agilent Cary 60, USA).

4.3.4. Electrical Measurements

The osmotic energy conversion tests were evaluated with an electrochemical workstation (VMP3 Potentiostat Biologic) and the current densities were recorded after reaching a steady state value. A permselective membrane was pressed between the two parts of H-type cell, whose testing area was 3×10^4 μm^2. The NaCl testing solutions were prepared by mixing deionized water and a certain amount of NaCl salt, and the natural seawater was collected from Manly beach in Australia. Laboratory-made Ag/AgCl electrodes were deployed to measure the osmotic potential and current. The transmembrane ionic transport was examined with *I-V* curves in the presence of a transmembrane concentration gradient at a sweeping voltage of −0.4 to +0.4 V with a step of 0.04 V. A two-compartment H-type cell was used to test the *I-t* curves to evaluate the osmotic energy performance, whose configuration was provided in Figure S1.9b. The *I-t* curves were used to evaluate the osmotic energy performance, and the current densities were recorded after reaching a steady state value. The NaCl testing solutions were prepared using ultrapure water (18.2 MΩ cm), and the natural seawater was collected from Manly beach in Australia. The membranes' area exposed to electrolyte was about 3×10^4 μm^2. Laboratory-made Ag/AgCl electrodes were deployed to apply electrical potential (See Supplementary Note S1 and Note S2

for electrode preparation and calibration). The cation transference number was calculated based on the equation shown in Supplementary Note S4.

4.3.5. Computations

DFT calculations were performed using the Vienna Ab initio Simulation Package (VASP) with projector-augmented wave (PAW) potentials [244, 245]. The exchange-correlation interactions of the electrons were described by Perdew-Burke-Ernzerholf (PBE) functional within generalized gradient approximation (GGA) [246, 247]. The cut-off value for plane-wave basis set was set to 400 eV. To eliminate the physical interactions caused by periodic boundary conditions, the vacuum spaces were set at about 20 Å. The convergence criteria for energy and the ionic force were set to 10^{-4} eV and 0.01 eV $Å^{-1}$, respectively. Γ-centered k mesh of 7×7×1 was used for geometry optimization with 2×2×1 supercell. The diffusion of Na^+ was explored by the climbing nudged elastic band (cNEB) method [248]. The MESP maps were computed via the GFN2-xTB Hamiltonian method and analyzed by Multiwfn [249-252].

MD simulations were carried out by Nanoscale Molecular Dynamics (NAMD) with Lennard-Jones nonbonded parameters taken from Rappe et al. [253, 254]. The crystal structure of NbP was obtained from the previous literature [243]. The packing of waters and ions was done by PACKMOL [255]. For water adsorption experiment, a single NbP or V-NbP nanosheet was solvated with water molecules. After energy minimization, the system was started with 1 ns of canonical (NVT) ensemble, followed by 1 ns of isothermal-isobaric (NPT) ensemble. A temperature of 300 K and a pressure of 1 bar was applied during the simulations. The RDF was calculated for both NbP and V-NbP models by calculating the distances between the hydrogen atoms of water molecules and the oxygen atoms of NbP or V-NbP. For ion diffusion experiment, 8 layers of NbP or V-NbP models were used. The interlayer spacings between the nanosheets were selected to be 8 Å, 12 Å, 16 Å and 20 Å. The multilayer structures were hydrated with water molecules. Subsequently, the water molecules were positioned at the two sides of the hydrated multilayer structure, and one side was solvated with 0.5 M Na^+ and Cl^- ions until equilibrium. Electric field was applied in

the X direction to stimulate ion diffusion. After energy minimization, the system was initially started using 2 ps of NPT, and the production run was conducted using 150 ps NVT. During the MD simulations, the slabs of nanosheets were static while the water molecules and ions were dynamic. The information on the size of MD simulation systems is provided in Supplementary Note S5. All visualizations were done by Visual Molecular Dynamics (VMD) and VESTA [256, 257].

4.4. Results and discussion

4.4.1. Material Characterizations

NbP nanosheets with or without P vacancies were fabricated to demonstrate the effect of atomic vacancy on permselectivity. The bulk NbP was synthesized in the presence of a mild oxalic acid system [243], and then NbP nanosheets were obtained by exfoliating the bulk counterpart in water (Figure 4.1 a, left and middle panels). The as-obtained NbP sheets exhibited a 2D morphology as thin flakes (see the scanning electron microscopy (SEM) images in Figure S2.1a-b) with a thickness of ~5 nm, corresponding to 8 layers of 2D crystal structure (see the atomic force microscopy (AFM) images Figure S2.1c). X-ray diffraction (XRD, Figure S2.1d) patterns and the in-plane diffraction rings of selected area electron diffraction (SAED, Figure S2.1e) affirmed NbP's crystallinity assigned to a triclinic structure in the P1 space group [258]. Furthermore, P vacancies were facilely created on the NbP nanosheets using a room-temperature acid etching method (the right panel of Figure 4.1 a). It is noted that the etching procedure did not obviously alter the crystallinity, elemental distribution, and the thickness of the NbP nanosheets (Figure S2.2). Abundant P vacancies unambiguously appeared in the atomic-resolution high angle annular dark field (HAADF)-scanning transmission electron microscopy (STEM) image of (Figure 4.1 b and Figure S2.3) of the V-NbP nanosheets based on the well-matched atomic structure model, while the niobium (Nb) and oxygen (O) atoms are preserved. The P content in the aqua regia solution of V-NbP (16.9 g L^{-1}) was much lower than that of NbP (19.4 g L^{-1}) based on the inductively coupled plasma mass spectrometry

(ICP-MS, the inset of Figure 4.1 c) result, consistent with the X-ray photoelectron spectroscopy (XPS, Figure S2.4) analysis and further verifying the formation of P vacancies during the selective etching procedure. Moreover, the zeta potential of V-NbP (-37.2 mV) was dramatically larger than that of NbP (-28.6 mV, the inset of Figure 4.1 c), validating an enhanced electrostatic effect originating from the vacancy introduction. MD simulations were performed to further elucidate the bond distances between the hydrogen atoms of water molecules and the oxygen atoms of NbP and V-NbP sheets (Figure S2.5). Both NbP and V-NbP delivered radial distribution function (g(r)) values higher than 1.0 due to their hydrophilic nature [259]. In addition, V-NbP showed a higher g(r) of 3.2 than that of the NbP (i. e. 2.3); meanwhile, the first water adsorption peak blue shifted from 1.71 Å to 1.67 Å (Figure 4.1 c). Such enlarged water molecule quantity near the surface of V-NbP demonstrates an enhanced hydrophilicity [260], which is mainly due to the reinforced electrostatic attraction with water molecules caused by the augmented negative surface charge of V-NbP nanosheets. The enhanced hydrophilicity of V-NbP would boost the interface contact with water and thereby facilitate transmembrane ion transport.

The NbP and V-NbP membranes were prepared by directly filtering their DMSO dispersions for osmotic energy generation applications. Around 11.5 % aramid nanofiber (ANF) was added to enhance the strength of the membranes (Figure S2.6). The as-fabricated V-NbP membrane displayed high flexibility (Figure 4.1 d, inset) with a cross-sectional morphology consisting of stacked nanosheets, and the thickness was around 7.4 μm (Figure 4.1 d) with an interlayer spacing of ~8 Å (Figure S2.7). The V-NbP membrane exhibited an improved Brunauer-Emmett-Teller (BET) surface area (31.72 m^2 g^{-1}) compared with the NbP membrane (25.3 m^2 g^{-1}, Figure S2.8a), mainly due to the lateral size shrinkage of NbP nanosheets (from around 500 nm to 300 nm, Figure S2.1c and Figure S2.2c) after the etching procedure. This increased porosity of V-NbP membrane is expected to accelerate ion migration dynamics (Figure S2.8b). The static contact angle of water on the NbP membrane was measured to be 62.70° (Figure 4.1 e, upper panel), which was reduced to 43.57° after the vacancy engineering (V-NbP membrane, the lower panel of Figure 4.1 e). Such improved hydrophilicity is well-consistent with the above MD simulation results.

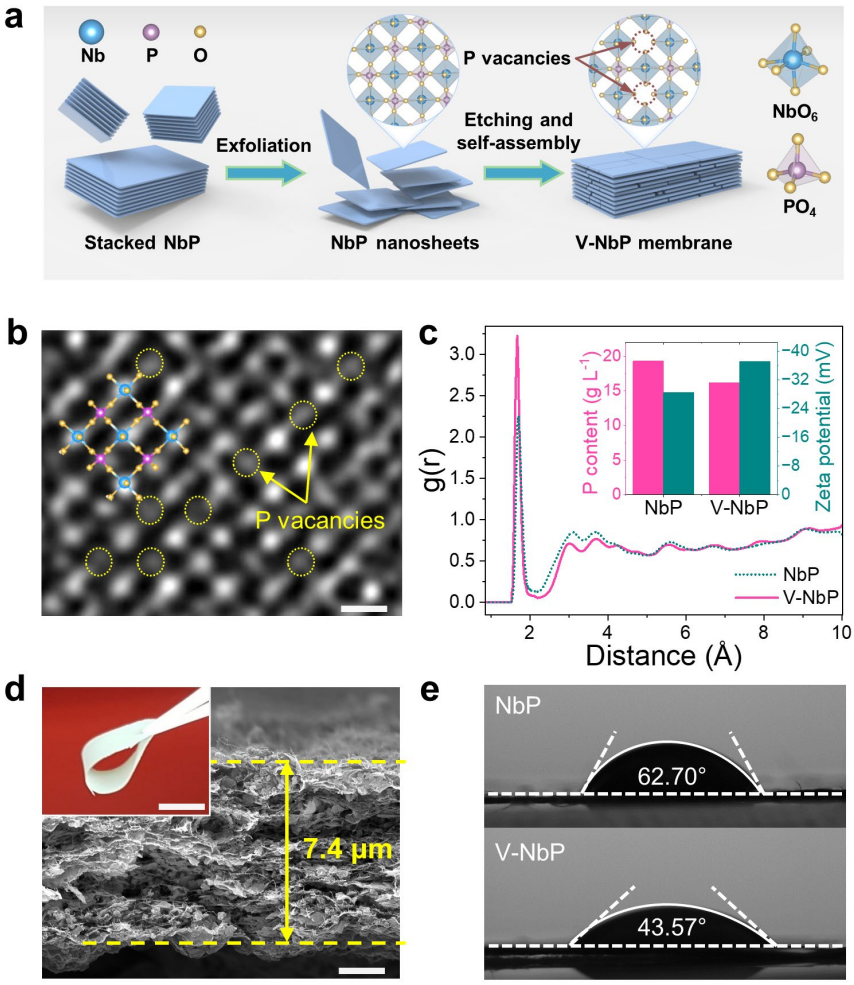

Figure 4.1. Characterizations of a V-NbP membrane. *(a) Schematic of the synthesis and chemical etching procedures of NbP nanosheets, resulting in the creation of P vacancies to form V-NbP nanosheets. (b) HAADF- STEM image of V-NbP nanosheets (scale bar: 0.5 nm). P: purple atoms, Nb: blue atoms, O: yellow atoms, P vacancy: circles. (c) Radial distribution functions for the distance between water molecules and the surface of NbP and V-Nb nanosheets. The P content and zeta potential values of NbP and V-NbP nanosheets were shown in inset. (d) Optical image (inset, scale bar: 1.5 cm) and cross-section SEM image (scale bar: 2 μm) of NbP membrane. (e) Static water contact angle analysis for NbP and V-NbP membranes.*

4.4.2. Transmembrane Ionic Transport Properties

The transmembrane ionic transport properties were examined via a symmetric H-type electrochemical cell containing NaCl solutions with various concentrations (Figure S2.9). Figure 4.2 a shows the *I-V* curves under a concentration difference of 1.0 M | 0.01 M NaCl. Osmotic potential (V_{osm}) and osmotic current (I_{osm}) were corrected by subtracting the contribution of redox potentials on the electrodes

(Figure S2.10). Both the V-NbP and NbP membranes exhibited a negative value of V_{osm} and a positive value of I_{osm}, representing their cation permselectivity. The V-NbP membrane delivered higher V_{osm} (64 mV) and I_{osm} (33 μA) values than those of the NbP membrane (45 mV and 7.5 μA, respectively), which can be attributed to the improved cation transportation of V-NbP membrane induced by its enhanced substantial surface charge and porosity. A series of *I-V* curves recorded in NaCl electrolyte with concentrations ranging from 10^{-6} to 1 M are shown in Figure S2.11. All the curves behaved as linear ohmic behavior ascribed to the symmetrical structure of membranes. The transmembrane ionic conductance as a function of salt concentrations were plotted in Figure 4.2 b. It is seen that the conductance illustrated a linear relationship at higher concentration gradients (>1 mM), demonstrating a bulk behavior. Meanwhile, the conductance maintained almost constant at lower concentration gradients (<1 mM), representing a surface charge-governed ionic transport phenomenon [167, 178, 179]. The V-NbP membrane depicted high conductance values varying from ~0.4 μS to ~0.5 mS with the salinity gradients, remarkably higher than those of the NbP membrane and most previously reported macroscopic-scale 2D nanofluidic membranes [165, 177, 178], indicating an ultrafast ion migration through the membrane. For NaCl aqueous solution, the transmembrane ionic conductance could be expressed as [261]:

$$G = G_{bulk} + G_{surface} = \frac{eN_A c(\mu_+ + \mu_-)WH}{L} + \frac{2\mu_+ \sigma W}{L} \quad (1)$$

where G_{bulk} depicts the bulk ionic conductance and dominates the slash region in Figure 4.2 b, which is correlated with the width (W), height (H) and length (L) of the nanochannels, the bulk salt concentration (c) and mobilities of cations (μ_+) and anions (μ_-). e and N_A are elementary charge and Avogadro's constant, respectively. The second term, $G_{surface}$, displays the ionic conductance governed by surface charge, which is the main contributor to the plateau region in Figure 4.2 b. It depends on the surface charge density (σ), μ_+, W and L. At a certain point where $G = 2G_{bulk}$, one can directly derive σ by

$$\sigma = \frac{eN_A c(\mu_+ + \mu_-)H}{2\mu_+} = \frac{eN_A CH}{2t_+} \quad (2)$$

where $t_+ = \frac{\mu_+}{\mu_+ + \mu_-}$. For NaCl solutions, the typical concentrations (where $G = 2G_{bulk}$) are ~1 mM for V-NbP and ~0.1 mM for NbP, respectively. Considering H corresponds the the channel height derived from XRD data, the estimate surface charge density of V-NbP is ~0.057 C m^{-2}, significantly larger than that of the NbP (only ~0.006 C m^{-2}). Such results demonstrate V-NbP is more negatively charged, well-consistent with zeta potential profiles.

Moreover, under a reverse concentration gradient, I_{osm} and V_{osm} of the V-NbP membrane showed similar absolute values to those under a forward concentration gradient; however, the polarities were different owing to the opposite ionic diffusion directions (Figure S2.12). This confirms the symmetry of the V-NbP membrane without preferential direction for ion diffusion. The correlations between I_{osm} and V_{osm} are exhibited in Figure 4.2 c. The I_{osm} and V_{osm} values of V-NbP membrane both increased with the increased concentration gradient, and higher than those of the NbP membrane due to the enhanced ion diffusion flux and cation permselectivity. The cation transference number (t_+) of V-NbP membrane was calculated to be 0.70 at a concentration difference of 1000-fold, and V-NbP showed a higher t_+ than NbP at a range of salinity gradients, much higher than that of the NbP membrane (i. e., 0.64; Figure 4.2 d). Such a high t_+ value is crucial for the generation of electrical energy from salinity gradients. Based on the calculated t_+, the energy conversion efficiency was found to be 8.2 % under 1000-fold concentration difference.

The cation permeability of the V-NbP membrane was visually measured using H-shaped cells filled with blank distilled water in the right chamber (RC), and anionic dye (i. e. methyl orange) aqueous solution in the left chamber (LC) (Figure 4.2 e). In the H-cell separated by a commercial Celgard 3501 membrane, the dye anions continuously diffused through the Celgard membrane and reached the opposite side of the cell. The anion concertation in the RC gradually increased from 0 to 4.2 mg L^{-1} during the 48 h aging based on the ultraviolet-visible (UV-Vis) absorption spectra characterization (Figure 4.2 f, upper panels), reflected by a rapid color change of blank water from transparent to orange color (Figure 4.2 e, upper panels). In shape contrast, in the cell connected by the V-NbP membrane, the water in the RC remained clear after 48 h (Figure 4.2 e, lower panels), meanwhile the anion concertation maintained constant as the initial

values in both the LC (40 mg L^{-1}) and RC (0 mg L^{-1}) (Figure 4.2 f, lower panels). This indicates a significant suppression of anion transport by the V-NbP membrane via repulsive electrostatic interactions (i. e. Donnan exclusion)., verifying the superior cation permselectivity of V-NbP membrane. An identical phenomenon was observed for NbP membrane where anionic dye could be fully blocked during 48 h of test (Figure S2.13). This indicates both NbP and V-NbP membranes have negative surface charges that block the permeation of anionic dyes. We have investigated the cation (Na^+) transporting behavior of V-NbP membrane in the methyl orange permeation test. The Na^+ concentrations were tested using a multi-parameter analyzer (DZS-706, INESA Scientific Instruments Co., Ltd, Shanghai, China) with a ISE, 972207 ion selective electrode. As seen from the upper panel of Figure S2.14, for the Celgard membrane, the Na^+ concentration continuously reduced from 2.90 to 1.04 mg L^{-1} in the left chamber (LC), meanwhile kept increasing from 0 to 0.77 mg L^{-1} in the right chamber (RC) after 48 h test. This trend is consistent with the concentration change of anionic dye in the upper panel of Figure 4.2 f. For comparation, the V-NbP membrane maintained constant anion concertation due to a block of anion penetrating (the lower panel of Figure 4.2 f). However, the Na^+ ion freely passed through the V-NbP membrane, giving rise to a decrease in LC and an increase in RC for Na^+ concentrations (the lower panel of Figure S2.14). This phenomenon can be attributed to the Gibbs-Donnan effect: the counter-ions of permselective membranes preferred to transport to the side with lower concentration, resulting in a charge imbalance to suppress continuous permeation [94]. Diffusion of Na^+ and Cl^- ions through the V-NbP membrane was investigated using an H cell filled with 0.5 M NaCl on one side and deionized water on the other side. For the V-NbP membrane, the concentration change of Na^+ was significantly greater than the Cl^- during the 48 h test due to the Gibbs−Donnan effect of the permselective membrane (Figure S2.15 a), and the calculated Na^+ transference number (t+, ~0.7 in Figure S2.15 b) matched well with the value derived from the I−V curve. On the contrary, the concentration changes of Na^+ and Cl^- were quite consistent for the Celgard membrane during the 48 h test (Figure S2.15 c), indicating an insufficient permselectivity reflected by a t+ value of ~0.5 (Figure S2.15 d). The above results verify the superior cation permselectivity of the V-NbP membrane.

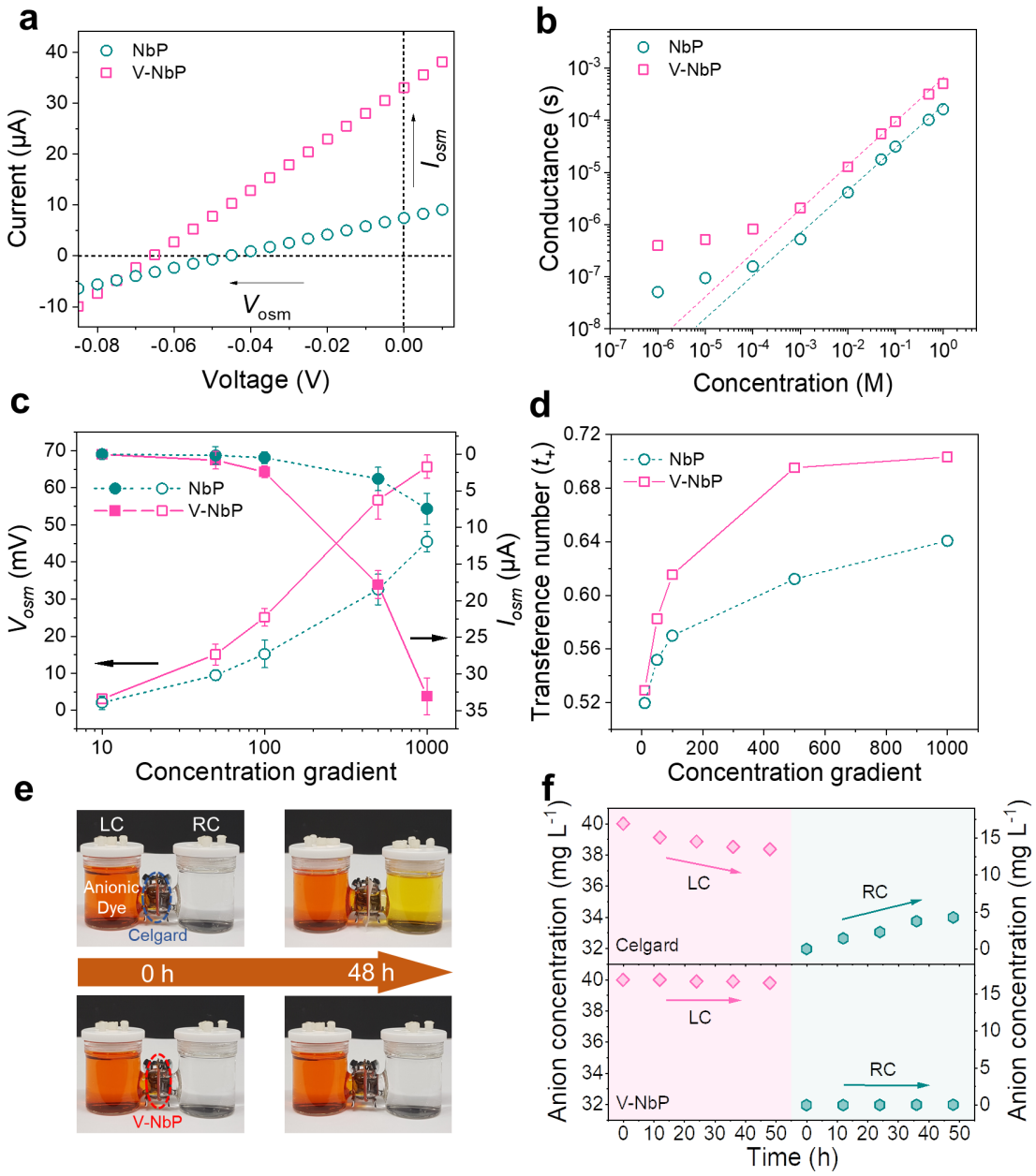

Figure 4.2. Transmembrane ionic transport properties of V-NbP. *(a) I-V curves under a concentration gradient of 1 M | 0.01 M NaCl and (b) conductance at various concentration gradients of NbP and V-NbP membranes. The dots represent experimental data while dashed lines represent fitting results of bulk phase. (c) Recorded I_{osm} and V_{osm} values and (d) transference numbers of NbP and V-NbP membranes under different concentration gradients. (e) Visual demonstration of anionic dye diffusion through commercial Celgard membrane and V-NbP membrane after 48 h at room temperature, and (f) the corresponding concentration changes of anionic dye in each chamber of the H-shaped cell along with aging time.*

4.4.3. Osmotic Energy Conversion

The harvested osmotic energy from the NbP membrane was quantified by transferring the power to an external circuit with a load resistance (R_L). The output

power density (P) can be calculated via $P = I^2 \times R_L$ by recording the generated current (I). As shown in Figure 4.3 a, the measured current densities decreased with increasing the load resistance, while the output power reached the maximum value at an intermediate resistance of 3 KΩ. Applying 50-fold NaCl concentration gradients, the V-NbP membrane delivered an output power density of 9.7 Wm^{-2}, which was ~300 % higher than that of the NbP membrane. The effect of acid etching concentration on the nanofluidic performance was further examined. As the etching concentration increased, the content of phosphorous atoms decreased while the surface charge became more negative. This demonstrates that the content of P atoms and the surface charge can be successfully tuned by changing the concentration of acid etchant. The optimum power density was achieved for an etching concentration of 0.5M. Further increasing the etching degree reduced the cation permselectivity, which is directly attributed to the reduced concentration gradient at highly charged surfaces (See Figure S2.16 for a detailed analysis of the influence of acid etching concentration on the performance). The effect of electrolyte pH on the surface charge and cation transportation dynamics of V-NbP membrane was further investigated. When the electrolyte pH rose from 3 to 11, the conductance and zeta potentials of the V-NbP membrane increased from ~190 μS to 880 μS and -19 mV to -50 mV, respectively (Figure 4.3 b). Consequently, the power density of the V-NbP membrane remarkably augmented from 4.2 W m^{-2} to 15.8 W m^{-2} (Figure S2.17), demonstrating a performance improvement in alkaline solutions. Furthermore, cations with smaller hydration layer sizes (Li^+: 3.8 Å, Na^+: 3.6 Å, K^+: 3.3 Å) [262], and larger diffusion coefficients (Li^+: 1.03 × 10^{-9} m^2 s^{-1}, Na^+: 1.33 × 10^{-9} m^2 s^{-1}, K^+: 1.96 × 10^{-9} m^2 s^{-1}) [157] are more favorable to transport through the nanochannels in the permselective membrane and boost the osmotic energy conversion. As shown in Figure 4.3 c, the maximum power density using V-NbP membrane reached up to 5.3, 9.7, and 21.5 W m^{-2} using LiCl, NaCl, and KCl electrolytes, respectively, which can be evidenced by the conductances enlarged in the order of $Li^+ < Na^+ < K^+$ (Figure S2.18). This validates the application potential of V-NbP membrane in real-world multiple ion environments.

To examine the practical application of the V-NbP membrane, the power generation was evaluated based on the salinity differences between natural

Australian seawater and river water. The maximum power density reached a record-high value of 10.7 W m^{-2} (Figure 4.3 d), far surpassing the commercialization benchmark of 5.0 W m^{-2} and exceeding the reported macroscopic-scale 2D nanofluidic membranes (Figure 4.3 e and Table S2.1). Furthermore, the power density of V-NbP membrane increased with a rise in the concentration gradient. The osmotic power generation could reach up to 14.8 W m^{-2}, 96.2 W m^{-2}, and 115.4 W m^{-2} for the cases of 70-fold (artificial Persian-Gulf water | river water), 500-fold (artificial Salt-Dome solution | river water), and 614-fold (artificial Dead-Sea water | river water) concentration gradients, respectively (Figure 4.3 f). This illustrates the special application merits of V-NbP membrane in estuaries with high concentration differences. It is seen that the output current density of V-NbP membrane continuously decreased with the increase of testing area (Figure S2.19a), meanwhile the maximum power density reached 9.7, 5.91 and 3.84 W m^{-2} under a testing area of 0.03, 1 and 5 mm^2, respectively (Figure S2.19b). Such a size-effect on the power density widely exists in previous reports [94, 95], which could be attributed to the stronger ion concentration polarization caused by pore-pore interactions under large membrane size [130].

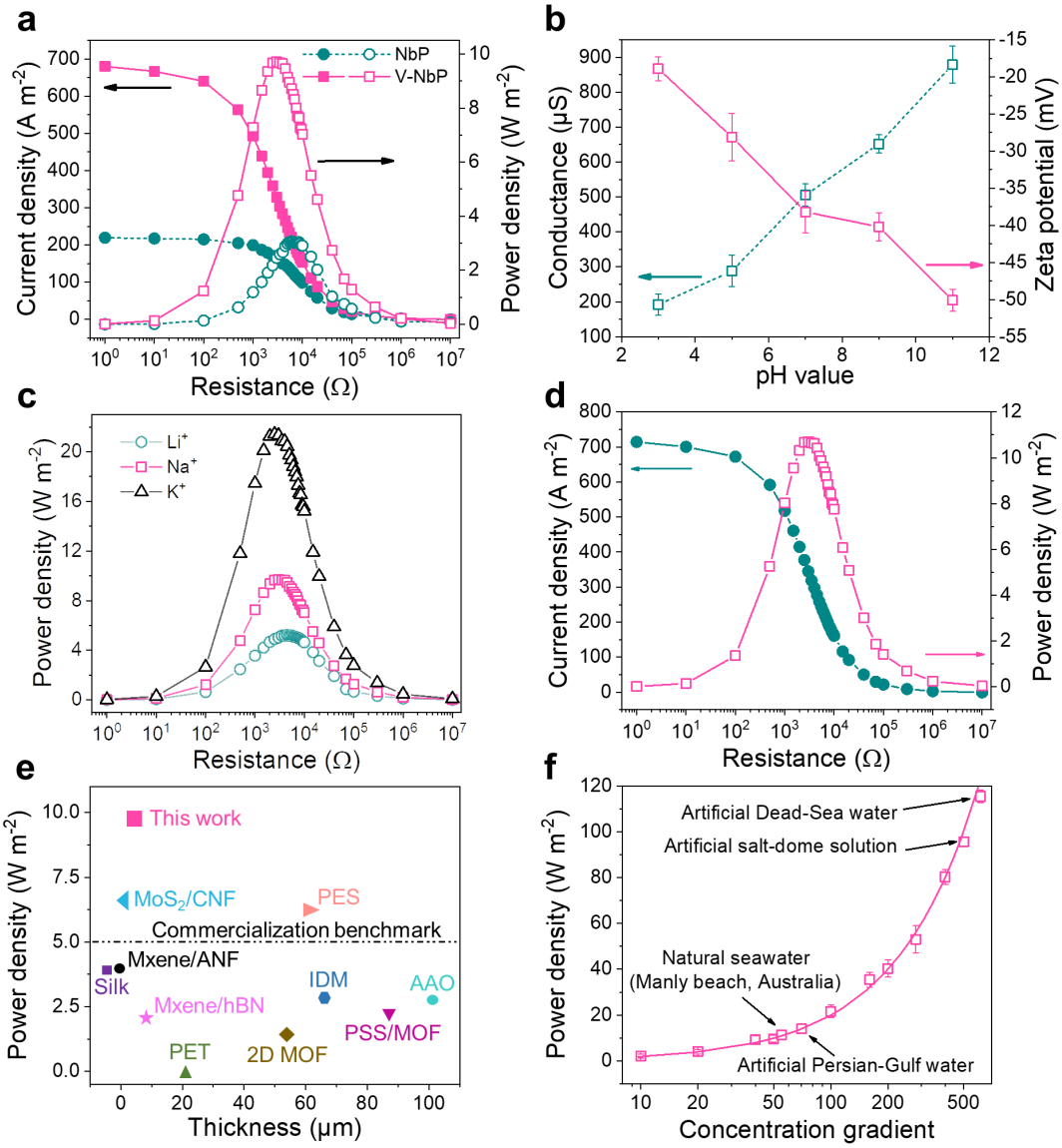

Figure 4.3. Osmotic energy conversion performance of V-NbP. *(a) Osmotic energy conversion of NbP and V-NbP membranes under a concentration gradient of 0.5 M | 0.01 M NaCl. (b) The influence of pH on the ionic conductance and surface charge of V-NbP membrane. (c) Power densities of V-NbP membrane using electrolyte with different cations at a concentration gradient of 0.5 M | 0.01 M. (d) Current density and power density profile of V-NbP membrane from natural Australian seawater | river water. (e) Performance comparison of V-NbP membrane in this work with reported macroscopic-scale 2D nanofluidic membranes. (f) Maximum power density of V-NbP membrane at different concentration gradients, simulating various estuaries on the planet.*

We have studied the stability of V-NbP membrane in an H-cell as described in Figure S2.9. Noticeably, the current density of the V-NbP membrane on the external circuit showed negligible attenuation for 60 h with an electrolyte renewal every 6 h to maintain the concentration gradient (Figure 4.4 a), indicating the durability of the V-NbP membrane in osmotic energy harvesting. Furthermore, the V-NbP membrane well-maintained its integrity after soaking in water for 90

days without pulverization or visible dimensional change (Figure S2.20); meanwhile, the output power density did not exhibit obvious attenuation (Figure 4.4 b). This demonstrates the excellent working stability of the V-NbP membrane in practical osmotic energy generation. A tandem device composed of wire-linked units was developed to examine the applicability of permselective membrane. Each unit was a couple of tanks connected with V-NbP membrane at a 50-fold NaCl concentration gradient (Figure 4.4 c). As shown in Figure 4.4 d, each unit generated an average voltage value of ~115 mV, and the overall output voltage of the device could be linearly enlarged by increasing the number of units. The output voltage reached up to 2.3 V when 20 units were linked together, which could power a red light emitting diode (LED) (Figure 4.4 e). The power density profiles of the tandem device show the maximum value of 176.7 W m^{-2} (Figure S2.21), that is approximately ~20 times than the individual compartments (9.7 W m^{-2}). This elucidates the viability of osmotic energy as a renewable and sustainable energy source. In addition, the commercial celgard membrane used in batteries was tested for osmotic power generation and the power density can reach up to nearly 0.8 W m^{-2} which is significantly less than the V-NbP membrane (Figure S2.22).

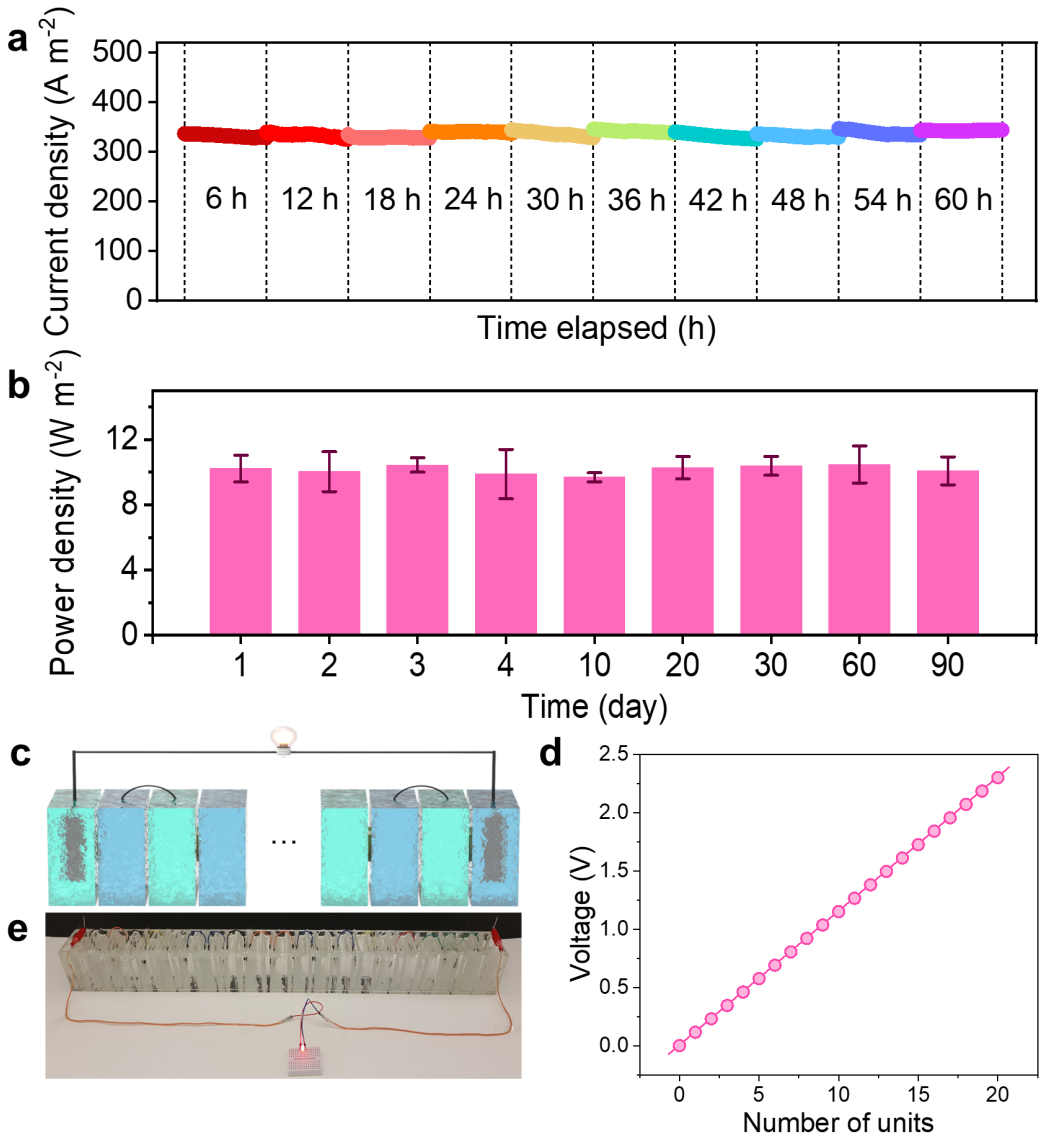

Figure 4.4. Operational stability and practical application of V-NbP. *(a) Current-time curve of V-NbP membrane under 0.5 M | 0.01 M NaCl at a load resistance of 3 KΩ. (b) Working stability of V-NbP membrane after soaking in water for several days. (c) Schematic illustration of the tandem device consisting of membrane units. (d) Correlation between the overall output voltage and the number of membrane units. (e) An energy harvesting device comprising 20 units of V-NbP membranes connected in series.*

4.4.4. Theoretical Computations

The molecular electrostatic potential (MESP) maps obtained by DFT method were shown in Figure 4.5 a-b to identify the role of P vacancies on the surface charge of NbP nanosheet. Red and blue colors denoted the regions with positive and negative charges, respectively. It is seen that the NbP nanosheet delivered an unevenly distributed negative surface charge where the electrons were

localized around the oxygen atoms (Figure 4.5 a). Interestingly, after the removal of P atoms, the electrostatic charge distribution became more uniform and negative on the V-NbP nanosheet (Figure 4.5 b). These results are well-consistent with the experimental zeta potential analysis (Figure 4.1 c, inset), and the dramatically stronger adsorption energy of Na^+ on the V-NbP surface (-6.313 eV) than on the pristine NbP surface (-5.104 eV, Figure S2.23). Furthermore, the horizontal diffusion energy barriers of Na ion transfer along the stacking direction were computed by DFT simulations. The energy barrier of Na^+ migration was 0.186 eV for the V-NbP nanosheets (Figure 4.5 d), much lower than that for the pristine NbP nanosheets (0.263 eV, Figure 4.5 c), indicating that the P vacancies significantly diminished the transport resistance and facilitated the dynamics of Na ions, thus greatly promoting the osmotic energy generation efficiency.

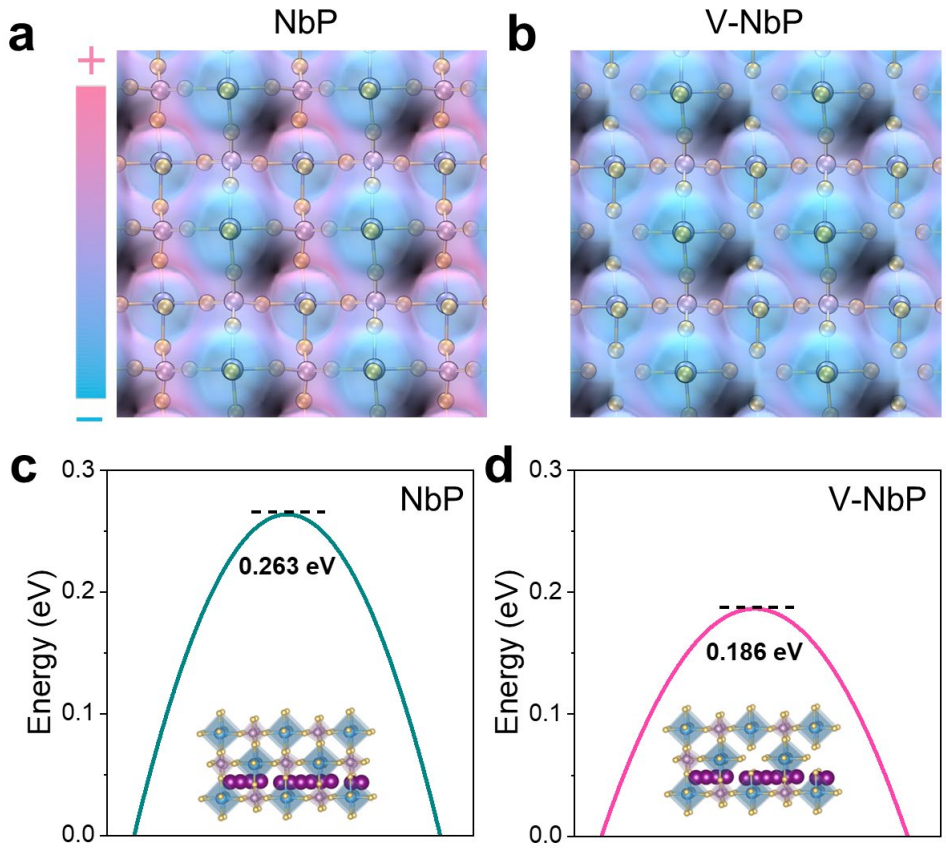

Figure 4.5. DFT calculations of V-NbP. *MESP maps of (a) NbP and (b) V-NbP nanosheets. Energy barriers of Na^+ diffusion in the horizontal diffusion pathways for (c) NbP and (d) V-NbP nanosheets.*

MD simulations were conducted to investigate the ionic transport properties through NbP and V-NbP nanosheets in the presence of water, Cl^- and Na^+ ions. As shown in the left panels of Figure 4.6 a, the V-NbP model was constructed by periodically removing the P atoms from the NbP model. 8 layers of NbP or V-NbP nanosheets were stacked with the experimental interlayer spacing value of 8 Å, and then two water boxes were positioned on each side of the stacked nanosheets. The left water box containing Na^+ and Cl^- ions was related to the high salinity region, while the right water box containing water molecules only represented the low salinity region (Figure 4.6 a, right panel). Mild electric fields were applied in the horizontal direction to simulate the ionic diffusion across the nanosheets' lamination direction. The quantities of Na^+ and Cl^- ions transporting through the membranes were plotted in Figure 4.6 b. The linear slope of the transfer quantity vs. time represented the ionic currents. It is seen that the Na^+ current value of V-NbP nanosheets (0.46 μA) was much higher than that of NbP nanosheets (0.36 μA), whereas the Cl^- current value of V-NbP nanosheets (0.15 μA) was much lower than that of the NbP nanosheets (0.23 μA). Accordingly, the simulated cation transference number (t_+) of V-NbP nanosheets was 0.74, obviously higher than that of NbP nanosheets (0.60) and very close to the experimentally calculated value (0.70). This improved Na^+ current value and cation transference number values of the V-NbP membrane synergistically enhance the osmotic energy conversion performance. Furthermore, the cation transference number of V-NbP nanosheets decreased with the enlarged interlayer spacing values (Figure 4.6 c), although the ionic currents increased (Figure S2.24). This demonstrates a trade-off between selectivity and permeability, highlighting the dominant role of surface charge engineering for 2D nanofluidic membranes on ionic transport in the narrow interlayer spacing conditions.

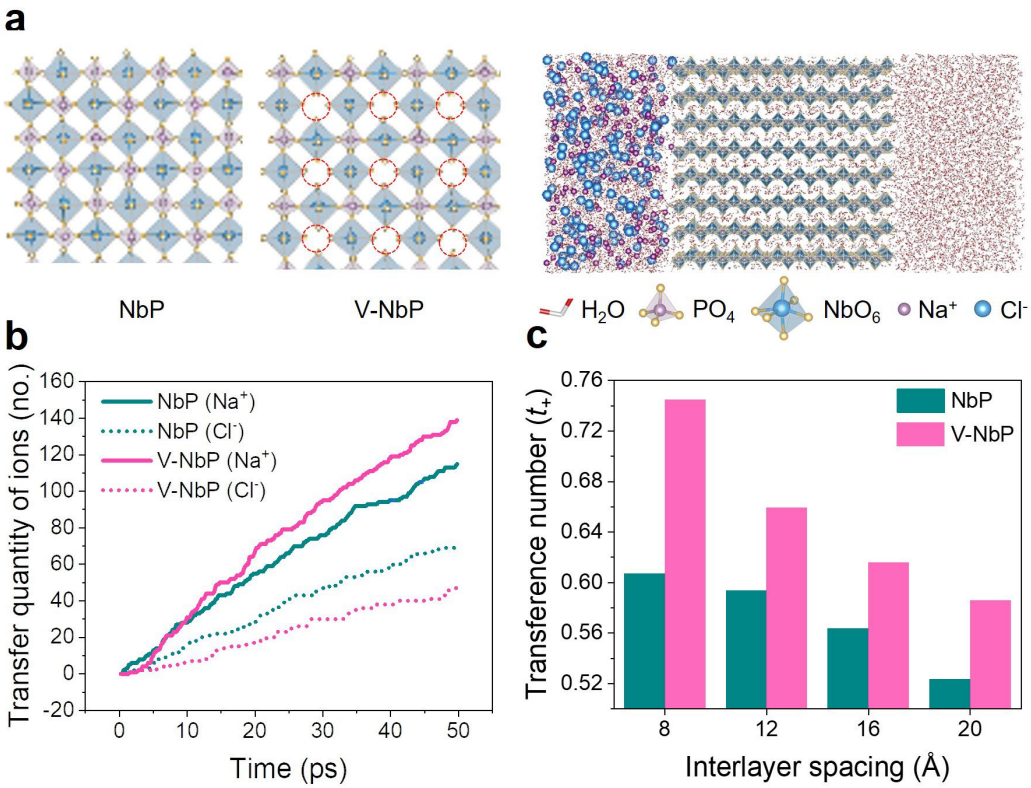

Figure 4.6. MD simulations of V-NbP. *(a) Models of NbP, V-NbP, and the solvated system containing water molecules, Na^+ and Cl^- ions. The dashed red circles denote the P-vacancy sites in the V-NbP model. (b) Transfer quantities of ions plotted vs. time for NbP and V-NbP nanosheets with a fixed interlayer spacing of 8 Å. (c) Cation transference numbers for NbP and V-NbP nanosheets as a function of interlayer spacings.*

4.5. Conclusions

In summary, we showcased that high-efficiency osmotic power generators can be developed via creating atomic vacancies on 2D nanofluidic membranes. By virtue of this strategy, we developed a stacked membrane based on vacancy-introduced NbP nanosheets for osmotic energy harvesting. Combining experimental analysis and theoretical calculations, the presence of vacancies can remarkably enhance the negative surface charge on NbP nanosheets, thus simultaneously improving the membrane hydrophilicity, cation selectivity and ionic flux. The as-developed vacancy-introduced NbP membrane delivered a maximum output power density ~300 % higher than the pristine NbP membrane under a 50-fold NaCl gradient. For the natural seawater | river water system, a record-high power density of 10.7 W m^{-2} was achieved using such vacancy-introduced membrane, demonstrating great promise for real-world osmotic power

generator applications. This work highlights the nanoscale correlation between atomic vacancy engineering for 2D materials and ion permselectivity/ion transport dynamics, providing a new venue to boost the osmotic energy conversion efficiency and holding a great promise for further advances in water science, 2D materials science, electrochemistry, and sustainable energy.

Chapter 5: Self-Assembled NbOPO4 Nanosheet/Reduced Graphene Oxide Heterostructure for Capacitive Desalination

5.1. Abstract

Capacitive deionization (CDI) is a promising and energy-efficient technology for desalination. The development of high-performance capacitive electrodes is essential for enhancing the CDI properties for practical applications. Here, a 2D heterostructure was rationally designed and synthesized by face-to-face restacking of $NbOPO_4$ nanosheets and reduced graphene oxide (rGO) via an electrostatic self-assembly process. The as-prepared 2D $NbOPO_4$/rGO heterostructure achieved an excellent ion storage capacity, electronic conductivity, and unimpeded ion kinetics. When applied as electrodes for CDI, the 2D $NbOPO_4$/rGO heterostructure delivered a high specific capacitance of 258.3 F g^{-1} and an electrosorption capacity of 73 mg g^{-1} for NaCl solution of 10,000 mg L^{-1} at an applied voltage of 1.2 V, which is more than five times larger than that of activated carbon. The heterostructure electrode also showed high desalination stability for up to 50 adsorption/desorption cycles. The high CDI performance is attributed to the strong 2D/2D coupling between $NbOPO_4$ nanosheets and rGO, which enhances the charge transportation across the heterointerface. The strong 2D/2D coupling was affirmed via the uniform and identical Raman shifts at various random regions, and larger XPS binding energy shifts for the self-assembled $NbOPO_4$/rGO heterostructure. This work demonstrated the potential of self-assembled nano-heterostructures for water desalination via capacitive deionization.

5.2. Introduction

Clean water demand has become a severe challenge to modern society due to population growth and industrial development. On account of the tremendous quantity of seawater and brine reservoirs on the planet, desalination has emerged as a promising strategy in addressing the freshwater shortage [105, 263, 264]. The most popular desalination techniques, such as reverse osmosis and thermal distillation, are suitable for processing highly concentrated saltwater. Still, they are costly and time-consuming for processing saltwater with low concentration [265-267].

Capacitive Deionization (CDI) is a relatively new water desalination technique that is highly suitable for removing ionic species from brackish water and low salt concentration solutions [268-270]. The CDI functions based on the electric double layer (EDL), which is the storage of ions on the surface of porous electrodes [271, 272]. In this way, an external voltage is applied, and anions and cations are electro-adsorbed on positive and negative electrodes, respectively. Thus, a reduced salt concentration is obtained in the water stream. After electrode saturation, the electro-adsorbed ions can be released from the electrodes via short-circuiting or reversing the applied voltage, yielding a water stream concentrated with salt ions [273, 274].

Carbon materials have been widely used for CDI, including activated carbon [275, 276], graphene [277, 278], carbon aerogels [279, 280], mesoporous carbon [281, 282], and carbon nanotubes [283, 284]. Despite having a high surface area and electronic conductivity, the salt adsorption capacity of these carbon materials are limited to 15-20 mg g^{-1}. This is due to the lack of faradaic charge storage properties, sluggish ion transport, and insufficient ion-accessible surfaces of conventional carbon materials [285-287]. Hence, the design of electrode materials with high electronic/ion transport properties, ion accessible surface areas, and pseudocapacitive capacitance should be the primary objective in achieving high-performance CDI [288-291].

Two-dimensional (2D) materials that are exfoliated from their layered precursors have the merit of high surface area, good electronic conductivity, and faradaic charge storage capabilities, rendering them highly promising for ion adsorption applications [182, 187-190, 192, 292]. Several 2D materials such as transition metal carbides (MXene) [187-189], transition metal dichalcogenides [190, 192,

292], and graphitic carbon nitrides have been tested for capacitive deionization [182]. However, the study is continuously ongoing to further improve the physical and electronic properties of 2D materials via numerous strategies such as doping, oxygen vacancy, and interface modulation [293, 294]. Among these techniques, interface modulation can increase the electronic conductivity and the surface area [295-297]. Interface modulation via the electrostatic self-assembly of oppositely charged nanosheets has received particular interest in recent years due to the excellent coupling at the heterointerface, giving rise to outstanding electrochemical properties [298-301]. A range of self-assembled two-dimensional materials such as MnO_2/graphene [298], $Ti_{0.87}O_2$/N-doped graphene [299], MoS_2/graphene [300], and Ni-Co-Al LDH/MXene have displayed tremendous potential for energy storage and conversion applications [301]. The ordered channels and interlayer galleries of 2D heterostructures could facilitate ion transport, increase ion accessible sites, and reduce the charge transfer resistance across the heterointerface [296]. These promising features of the self-assembled heterostructures could offer an efficient pathway to overcoming the limitations of the current CDI materials.

Transition metal phosphates (TMPs), $MO(PO_4)_x$, have significant potentials for electrochemical applications owing to their high electronic conductivity. This arises from the inductive effect of polyanionic $(PO_4)^{3-}$ groups that enhance the ionicity of metal-oxygen (M-O) bonds and hence, increase the bulk electronic conductivity [302-305]. To date, various TMPs have demonstrated high electronic conductivities and also have been exfoliated into ultrathin 2D nanosheets [243, 306, 307]. Among these TMPs, $NbOPO_4$ has demonstrated high aqueous stability and electronic conductivity, rendering it promising for supercapacitor applications [243]. Additionally, the excellent pseudocapacitive property of niobium-based compounds, originating from rich oxidation states of niobium makes this material a potential candidate for CDI-based water desalination [308-310].

In this research, we employed $NbOPO_4$ nanosheets and modified its interface via rGO using an electrostatic self-assembly process. Our multilayered $NbOPO_4$/rGO heterostructure showed a salt adsorption capacity of 73 mg g^{-1} for NaCl solution of 10,000 mg L^{-1} at an applied voltage of 1.2 V, which is one of the highest

reported performances in this field to date. The principal mechanisms for the high CDI performance are attributed to the efficient coupling at the heterointerface, leading to high ion storage capacity, ion kinetics, and charge transportation.

5.3. Methods

5.3.1. Chemicals

Niobium (V) oxalate hexahydrate ($C_{10}H_5NbO_{20}.6H_2O$) was purchased from Santa Cruz Biotechnology. Phosphoric acid (H_3PO_4 85 %), sulfuric acid (H_2SO_4 98 %), 2-Isopropanol (IPA), graphite flakes, hydrogen peroxide (H_2O_2, 30 %), potassium permanganate ($KMnO_4$), poly diallyl dimethylammonium chloride (PDDA 20 wt %), hydrazine hydrate (60 wt %), acetylene black, polyvinylidene difluoride (PVDF), N-methyl-2-pyrrolidone (NMP) were purchased from Sigma Aldrich. Activated carbon (XFP06, specific surface area=1500-1700 $m^2\ g^{-1}$) was purchased from Jiangsu XFNANO Materials Tech Co., Ltd. All the chemicals were used as received without further treatment.

5.3.2. Materials Synthesis

At first, the bulk $2NbOPO_4{\cdot}H_3PO_4{\cdot}H_2O$ was synthesized according to a previously reported method [243]. Briefly, niobium oxalate was mixed with H_3PO_4 and refluxed at 90 °C for 16 h. The resulting white precipitate was collected by centrifugation, washed with water and acetone several times, and then dried in a vacuum oven at 60 °C. Bulk $NbOPO_4.2H_2O$ was dispersed in isopropanol with a concentration of 0.6 mg L^{-1} and then ultrasonicated for 20 minutes to obtain $NbOPO_4$ nanosheets. The suspension was separated and collected for use. The GO was first developed using the improved Hummers' method [311]. Briefly, graphite flakes were refluxed with $KMnO_4$, H_3PO_4 (10 %) and H_2SO_4 (80 %). The resulting suspension was poured into an ice bath containing 1 % H_2O_2. The GO suspension was washed several times with DI water until neutral pH was achieved.

To make PDDA-rGO, 200 mL of a GO suspension (0.2 mg ml^{-1}) was mixed with 1.5 mL of a PDDA solution (20 wt %). Subsequently, 30 µL of hydrazine (60 wt %) was added, and the suspension was refluxed at 90 °C for 3 h. The resulting slurry was subjected to high-speed centrifugation at 12,000 rpm, and the recovered sediment was re-dispersed in water. Stable suspension of rGO was obtained by collecting the supernatant after centrifugation at 6,000 rpm.

The $NbOPO_4$/rGO heterostructure was prepared by a solution-phase self-assembly process. Specifically, suspensions of $NbOPO_4$ nanosheets and PDDA-rGO were mixed dropwise under continuous stirring at a determined mass ratio based on a hypothetical area matching model (Figure S3.5 and Note S3.1). The flocculate was recovered, washed by centrifugation, and then freeze-dried.The $NbOPO_4$-rGO was synthesized via mixing the suspensions of $NbOPO_4$ nanosheets and rGO, followed by freeze-drying. The ratio of rGO to $NbOPO_4$ was identical to that of $NbOPO_4$/rGO heterostructure.

5.3.3. Electrochemical Measurement

The $NbOPO_4$, $NbOPO_4$-rGO, $NbOPO_4$/rGO heterostructure, and activated carbon were prepared by mixing the active material, acetylene black, and PVDF at a ratio of (8:1:1) using NMP as the solvent. The slurry was coated on titanium mesh, followed by drying in a vacuum oven at 80 °C for 12 h. The mass loading was determined to be ~1 mg cm^{-2}. The measurements were performed using three-electrode configurations with Pt wire, Ag/AgCl and NaCl (1 mol L^{-1}) as the counter electrode, reference electrode, and electrolyte, respectively. The scan rates of CV measurements were chosen from 200 mV s^{-1} to 10 mV s^{-1}. The specific capacitance was calculated according to Note S3.2. For EIS measurement, a frequency range of 0.01 Hz to 200 kHz at an AC amplitude of 5 mV was applied. All the electrochemical tests were carried out with electrochemical workstation VMP3 Potentiostat Biologic.

5.3.4. Capacitive Deionization setup

The $NbOPO_4$, $NbOPO_4$-rGO, $NbOPO_4$/rGO heterostructure, and activated carbon electrodes were coated on a 3.7 cm × 3.7 cm titanium mesh using a similar procedure as making electrodes. To ensure the reproducibility of data, three electrodes were prepared form each material and the average value was taken as the final value for the capacitive deionization performance. A copper tape was attached to the electrodes, and copper wires were soldered to the copper tape. Nail polish was applied to the copper tape to prevent its corrosion during CDI test. Next, the electrodes were assembled into a CDI cell, and the two electrodes were separated by microfiber paper. Before CDI, the two electrodes were supplied with a salt solution without an external bias to stabilize the solution conductivity and minimize the initial physisorption. The CDI experiment was carried out in a batch mode using 50 mL of NaCl solutions of various concentrations. During the CDI process, the as-prepared NaCl solution was continuously fed into the CDI cell from a peristaltic pump, and the effluent was returned back to the tank. The flow rate was set constant to 7 mL min^{-1}. The asymmetric CDI unit was utilized, where $NbOPO_4$, $NbOPO_4$-rGO, $NbOPO_4$/rGO heterostructure served as the negative electrode, and activated carbon served as the positive electrode. The CDI test was conducted using constant voltage mode. During electrosorption, a constant charging voltage of 1.2 V was applied to the electrodes, and during the desorption, the discharging short-circuit voltage of 0 V was applied. Electrical conductivity was measured using HQ14d Portable Meter. The salt adsorption capacity (mg g^{-1}) was calculated according to Note S3.2.

5.3.5. Material Characterization

X-ray diffraction (XRD) patterns of the as-synthesized materials were measured using a Bruker D8 Discovery X-ray diffractometer. Field emission scanning electron microscope (FESEM) images were captured by a Zeiss Supra 55VP FESEM instrument with the sample loaded on a carbon tape. The morphology and structure of the hybrid materials were further analyzed by high-resolution transmission electron microscopy (HRTEM: Tecnai-G2 F30 STwin). The N_2 adsorption-desorption isotherms of the samples were collected using a Micromeritics automatic physisorption analyzer. The Zeta-potential values of

samples were tested by Malvern Zetasizer Nano-ZS90 particle analyzer. X-ray photoelectron spectroscopy (XPS) measurement was conducted on an ESCALAB250Xi (Thermo Scientific, UK) equipped with monochromatic Al K alpha (energy 1486.68 eV). Thermogravimetric analysis (TGA) was carried out by TG-DTA (SDT 2960) with a heating rate of 5 °C min-1 from room temperature to 800 °C in N_2 atmosphere. FTIR spectra were recorded on a NEXUS 670FTIR spectrometer. The thickness of NbOPO4 nanosheets was measured by AFM using a Bruker Dimension 3100 instrument with a MicroMasch NSC16 tip of 40 Nm−1 spring constant. The nanosheets were deposited on a mica plate for AFM measurement. Raman spectra were measured by a Renishaw in-Via Raman spectrometer system (Gloucestershire, UK) equipped with a Leica DMLB microscope (Wetzlar, Germany) and a 17 mW 633 nm Renishaw helium-neon laser operated at 100 % maximum power.

5.3.6. Theoretical Calculation

All calculations were carried out using DFT with the Perdew–Burke–Ernzerhof (PBE) form of the generalized gradient approximation (GGA) functional [246]. The Vienna *ab initio* simulation package (VASP) was employed [244, 312]. The energy cutoff for plane wave expansions was set to 400 eV, and the energy (converged to $1e^{-5}$ eV $atom^{-1}$) and force (converged to 0.01 eV $Å^{-1}$) were set as the convergence criteria for geometry optimization. A 2×2 periodic slab model was constructed to simulate the monolayer $NbOPO_4$ and $NbOPO_4$-$NbOPO_4$ bilayers, and a 2×2 periodic $NbOPO_4$ slab model and a 3×5 periodic rectangle graphene slab model was constructed to simulate the $NbOPO_4$-graphene bilayers (Figure S3.5). The Brillouin zones were sampled with the gamma-centered Monkhorst-Pack (5×5×1) k-points meshes for the models above [313]. As for the slab models, a vacuum space of 25 Å was added to the nonperiodic direction (*c* direction) to avoid interaction between periodic images. In addition, the DFT-D3 method was included to improve the description of the long-range weak van der Waals (vdW) interaction for all DFT calculations [247]. To assess the charge redistribution mechanism in $NbOPO_4$-rGO interface in the heterostructures, the $NbOPO_4$-graphene bilayers model was built, the lattice parameters along two

periodic directions were set as a = 12.33 Å, b = 12.77 Å. Charge redistribution was defined as $\Delta\rho = \rho_{NbOPO4+graphene} - \rho_{NbOPO4} - \rho_{graphene}$, where $\rho_{NbOPO4+graphene}$, ρ_{NbOPO4} and $\rho_{graphene}$ denote the charge distribution of the whole $NbOPO_4$-graphene bilayer system, $NbOPO_4$ monolayer and graphene monolayer.

5.4. Results and discussion

5.4.1. Material Characterization

The $NbOPO_4$ nanosheets were produced from the exfoliation of the layered bulk precursor $2NbOPO_4{\cdot}H_3PO_4{\cdot}H_2O$ (Figure 5.1 a-b). The exfoliated $NbOPO_4$ nanosheets displayed an average thickness of 4-6 nm, corresponding to 5-7 sub-layer structure, as observed via atomic force microscope (AFM) analysis (Figure S3.1). The flaky structure of the $NbOPO_4$ nanosheets is demonstrated in Figure 5.2 a. Transmission electron microscopy (TEM) image demonstrated semitransparent sheet-like morphology with a lateral size of ~250 nm (Figure 5.2 b). The $NbOPO_4$ nanosheet showed lattice fringes of 0.320 nm and 0.322 nm, which are pertinent to the (020) and (200) lattice planes, respectively (Figure 5.2 c). Additionally, the selected area diffraction (SAED) pattern demonstrated in-plane diffraction rings of $NbOPO_4$ (Figure 5.2 d). The exfoliated $NbOPO_4$ nanosheets in the suspension form were coupled with rGO using the electrostatic self-assembly process. The rGO was initially modified with a cationic polymer, poly (diallyl dimethylammonium chloride) (PDDA), yielding a positive surface charge. The SEM and TEM images show that the PDDA-rGO comprises thin atomic layers with a wrinkled sheet-like morphology (Figure S3.2). Additionally, the AFM images demonstrate that rGO nanosheets have a thickness of 0.8 nm that is increased to 1.5 nm upon the modification with PDDA (Figure S3.3). The zeta potential of $NbOPO_4$ and PDDA-rGO displays the negative and positive nature of the nanosheets at all pH ranges, respectively (Figure S3.4).

Due to the electrostatic attraction between positively charged rGO and negatively charged $NbOPO_4$, the $NbOPO_4$/rGO heterostructure can be self-assembled (Figure 5.1 c). The mass ratio between $NbOPO_4$ nanosheets and rGO is

theoretically estimated to be ~15 based on a hypothesized area-matching model (Figure S3.5 and Note S3.1). This value closely matches the actual mass content of rGO in our heterostructure, which was determined to be 6.7 wt % via TGA analysis (Figure S3.6). The $NbOPO_4$/rGO heterostructure displayed a 3D flaky and porous structure (Figure 5.2 e). This figure shows that the $NbOPO_4$/rGO heterostructure is composed of the wrinkled rGO that is incorporated into the $NbOPO_4$ nanosheets. The multilayered heterostructure of $NbOPO_4$/rGO can also be observed via a side-view scanning electron microscope (SEM) image in Figure S3.7. The TEM results indicate the restacking of $NbOPO_4$ with rGO, in which plate-like $NbOPO_4$ nanosheets are embedded in the large and wrinkled rGO nanosheets (Figure 5.2 f). The EDS mapping of $NbOPO_4$/rGO heterostructure shows a uniform elemental distribution, affirming the successful synthesis of $NbOPO_4$ nanosheets and the incorporation with rGO (Figure 5.2 j-n).

To study the effect of electrostatic coupling, we prepared randomly restacked nanosheets utilizing $NbOPO_4$ and unmodified rGO, denoted as $NbOPO_4$-rGO (Figure 5.1 d). This material demonstrated a morphology similar to the $NbOPO_4$/rGO heterostructure, in which the $NbOPO_4$ nanosheets with smaller sizes are embedded into the large-sized and wrinkled rGO nanosheets (Figure 5.2 g-h). Although $NbOPO_4$-rGO is identical to $NbOPO_4$/rGO heterostructure in terms of the morphology, the electrochemical performance is largely different due to the effect of heterointerface coupling that will be elucidated in the subsequent sections.

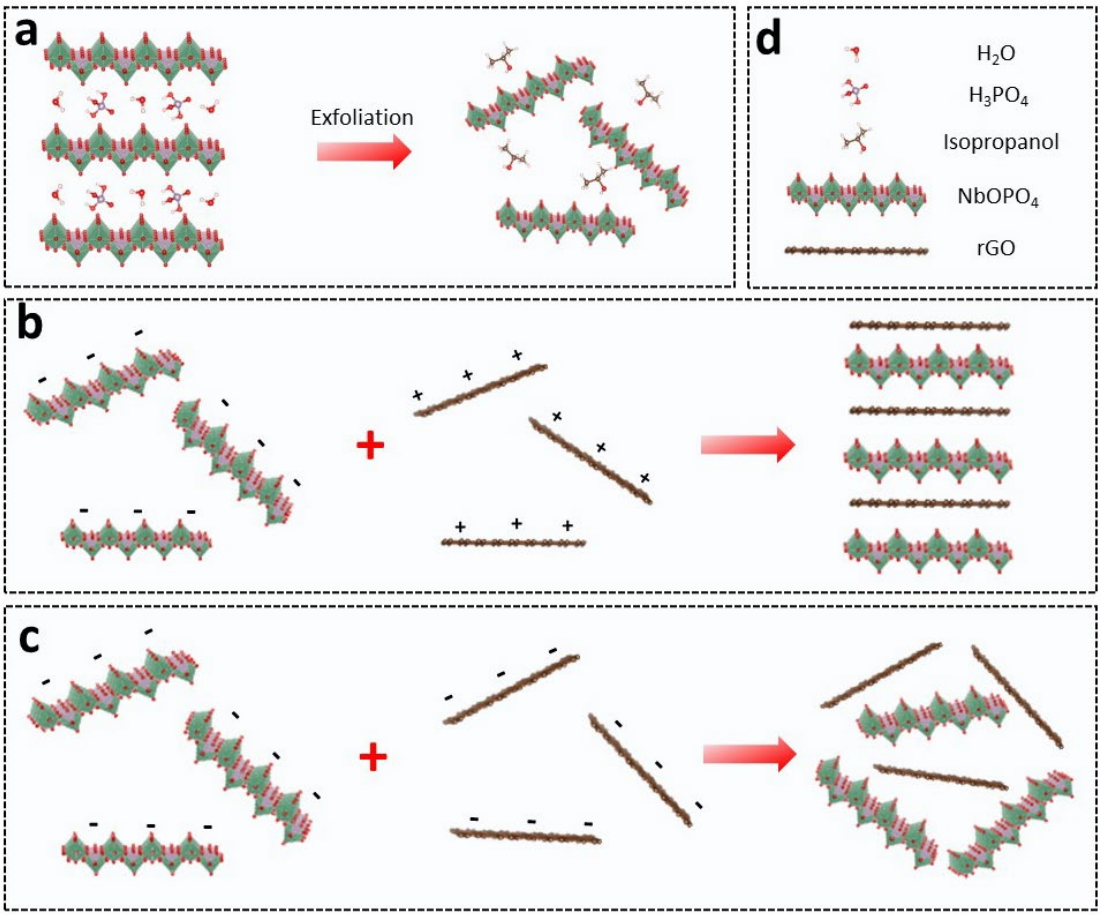

Figure 5.1. The schematic for the synthesis of $NbOPO_4$/rGO heterostructure. *(a) $NbOPO_4$ nanosheets, (b) $NbOPO_4$/rGO heterostructure, and (c) $NbOPO_4$-rGO. (d) The names of molecules and structures used in this schematic.*

The Raman analysis of $NbOPO_4$ nanosheets demonstrated the symmetric O-P-O modes at 927 cm^{-1} and Nb-O modes at 984 cm^{-1}, which is consistent with previous studies (Figure S3.8) [243]. The $NbOPO_4$/rGO heterostructure showed the additional D-band and G-band of graphene. The lattice mismatch between $NbOPO_4$ and rGO generates an interface-induced strain, which manifests itself in the stretching of Nb-O and O-P-O bonds in the in-plane direction. The interface-induced strain in $NbOPO_4$/rGO heterostructure resulted in the redshift of Raman bands to 815 cm^{-1} and 971 cm^{-1} for O-P-O and Nb-O modes, respectively. The XRD patterns of $NbOPO_4$, $NbOPO_4$-rGO, and $NbOPO_4$/rGO heterostructure are displayed in Figure 5.2 i. Based on the XRD analysis, all of the diffraction patterns of $NbOPO_4$ nanosheets could be indexed as a triclinic structure in the P1 space group [243]. Both $NbOPO_4$ nanosheets and $NbOPO_4$/rGO heterostructure displayed layered structures with a dominant (002) peak, corresponding to the

interlayer spacing of ~0.8 nm. The lower intensity of (002) peaks in $NbOPO_4$-rGO and $NbOPO_4$/rGO heterostructure represent a rather limited number of restacked $NbOPO_4$ nanosheets in the heterostructure compared with the pristine $NbOPO_4$ nanosheets. Based on the Scherrer formula, a thickness along the restacking direction of 16.4 nm, 10.54 nm, and 7.16 nm was estimated for $NbOPO_4$, NbOPO4-rGO, and $NbOPO_4$/rGO heterostructure, respectively.

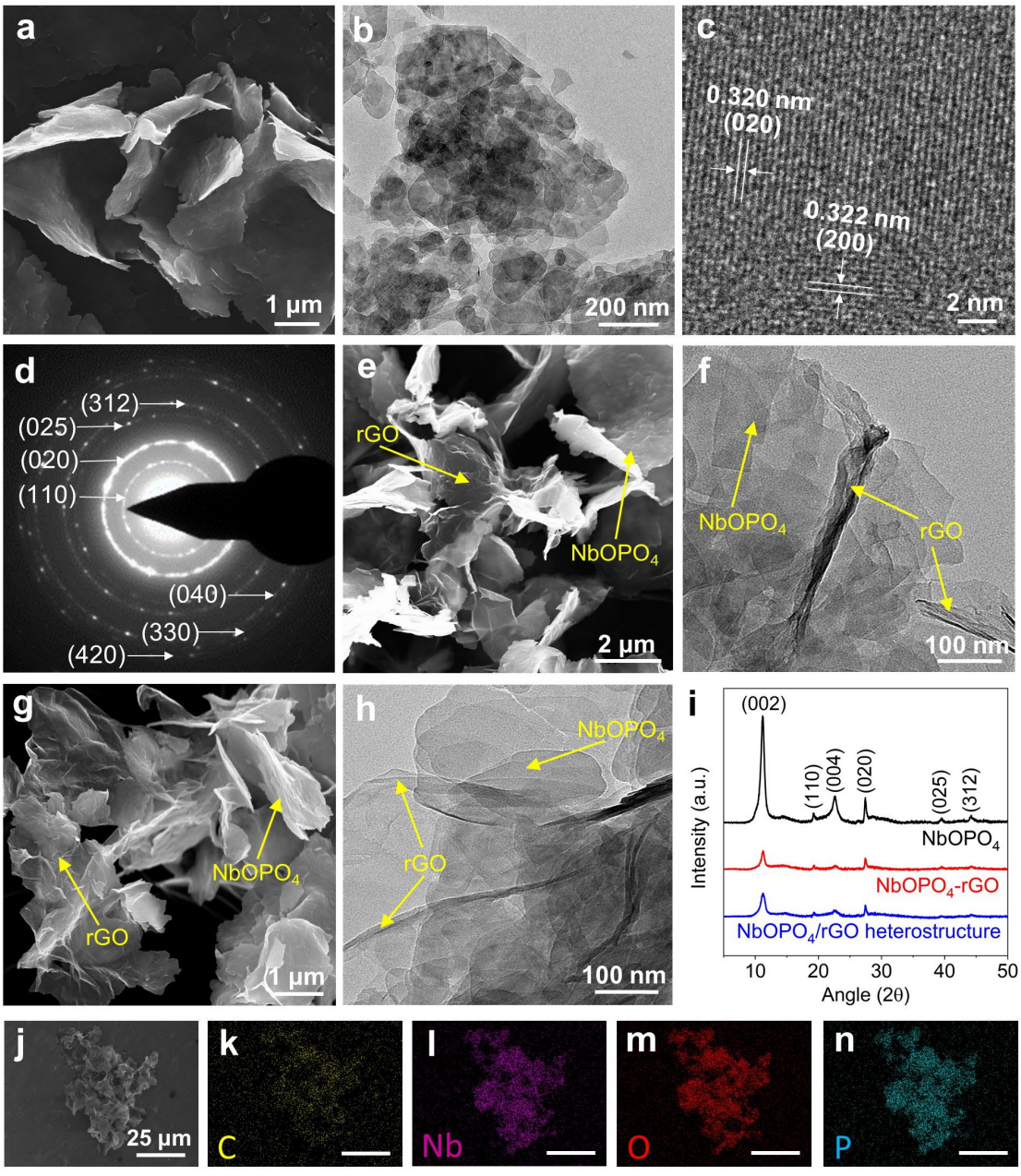

Figure 5.2. Characterizations of $NbOPO_4$/rGO heterostructure. *(a) SEM, (b) TEM, (c) HRTEM, and (d) SAED image of $NbOPO_4$ nanosheets. (e) SEM, and (f) TEM image of $NbOPO_4$/rGO heterostructure. (g) SEM, and (h) TEM image of $NbOPO_4$-rGO. (i) XRD pattern of $NbOPO_4$ nanosheets, $NbOPO_4$-rGO, and $NbOPO_4$/rGO heterostructure. (j) SEM image of $NbOPO_4$/rGO heterostructure, and the corresponding EDS mapping of (k) C, (l) Nb, (m) O, and (n) P element distribution.*

5.4.2. Electrochemical performance

The electrochemical performance of $NbOPO_4$/rGO heterostructure was initially evaluated via cyclic voltammetry (CV) analysis in a three-electrode system using pt, Ag/AgCl, and 1M NaCl as the counter electrode, reference electrode, and electrolyte, respectively. The CV curve of $NbOPO_4$/rGO heterostructure maintained its rectangular shape at a range of scan rates from 10 mV s^{-1} to 200 mV s^{-1}, which indicates its excellent capacity and rate capability (Figure S3.9). Figure 5.3 a displays the CV curves at a scan rate of 100 mV s^{-1}. Noticeably, $NbOPO_4$/rGO heterostructure showed a remarkably higher current density compared with $NbOPO_4$. The $NbOPO_4$-rGO depicted a significantly less current density than $NbOPO_4$/rGO heterostructure. To further elucidate the electrochemical performances of these three electrodes, the specific capacitance was measured at various scan rates from 10 to 200 mV s^{-1}. Based on Figure 5.3 b, the $NbOPO_4$/rGO heterostructure exhibited a higher capacitance of 258.3 F g^{-1}, more than three times and two times than $NbOPO_4$ nanosheets and $NbOPO_4$-rGO, respectively.

The BET surface area of bare $NbOPO_4$ was determined to be 27.63 m^2 g^{-1}, and this value increases to 49.71 m^2 g^{-1} for $NbOPO_4$/rGO heterostructure (Please see Figure S3.10, Table S3.1, and Note S3 for further details on N_2 adsorption-desorption isotherms and pore size distributions). This is due to the fact that rGO can prevent the restacking of $NbOPO_4$, therefore increasing its surface area [295, 296]. The BET surface area of the $NbOPO_4$/rGO heterostructure is higher than several pseudocapacitive materials such as MoS_2 and MXene for high-performance CDI [186, 187, 190]. However, the obtained surface area for $NbOPO_4$/rGO heterostructure is relatively lower than other EDL-based carbon materials [314]. Given the high specific capacitance of our $NbOPO_4$/rGO heterostructure, the ion storage mechanism cannot only rely on the EDL (like in activated carbon) but instead be ascribed to pseudocapacitance where ions are intercalated between $NbOPO_4$ and rGO nanosheets. This phenomenon is fully elucidated in previous reports [186, 187].

The electrical conductivity and ion diffusion of the electrodes are the key factors in the CDI process that could be analyzed using the EIS technique [315]. The Nyquist plots of $NbOPO_4$, $NbOPO_4$-rGO, and $NbOPO_4$/rGO heterostructure are presented in Figure 5.3 c. The $NbOPO_4$/rGO heterostructure shows the smallest semicircle at the high-frequency region compared with the other two materials. This is representative of the small charge transfer resistance and the good electrical conductivity of the $NbOPO_4$/rGO heterostructure. Based on the EIS fitting, NbOPO4/rGO heterostructure showed the smallest charge transfer resistance, with the value of 0.698 Ω (Please see Figure S3.11 and Table S3.2). Additionally, the line gradient at the low-frequency region corresponds to the ion diffusion process [316]. This line corresponds to the Warburg impedance, and a steeper line gradient corresponds to a faster ion diffusion, therefore being more representative of an ideal capacitor [182]. Both $NbOPO_4$-rGO and $NbOPO_4$/rGO heterostructure showed more vertical lines than the pristine $NbOPO_4$, representing their enhanced ion diffusion process. The R_s value or the equivalent series resistance (ESR) mostly depends on testing conditions, and the R_s values could be altered by various parameters such as electrolytes, electrode clamps, etc. In fact, for the analysis of electrode materials, the R_{ct} value may suffice, which gives the value of charge transfer resistance. Significant differences in the ESR values have also been reported in previous research [316]. Still, no explanation was provided since the R_s value is not directly related to electrode materials, and it is most pertinent to the testing conditions.

The cycle life is a crucial criterion for assessing electrodes for practical applications. Cycling stability was evaluated for the $NbOPO_4$/rGO heterostructure electrode via CV at the scan rate of 100 mV s^{-1}, and 95.7 % of the initial capacitance was retained after 5,000 cycles (Figure 5.3 d). These results strongly attest that our heterostructure has not only superior electrochemical performance but is also highly stable for practical application. Moreover, EIS data did not show noticeable differences in the first, 200th, and 600th CV cycles, thereby, no physical or chemical change occurs, and surface area or electronic properties of the $NbOPO_4$/rGO heterostructure remains intact upon cycling (Figure S3.12).

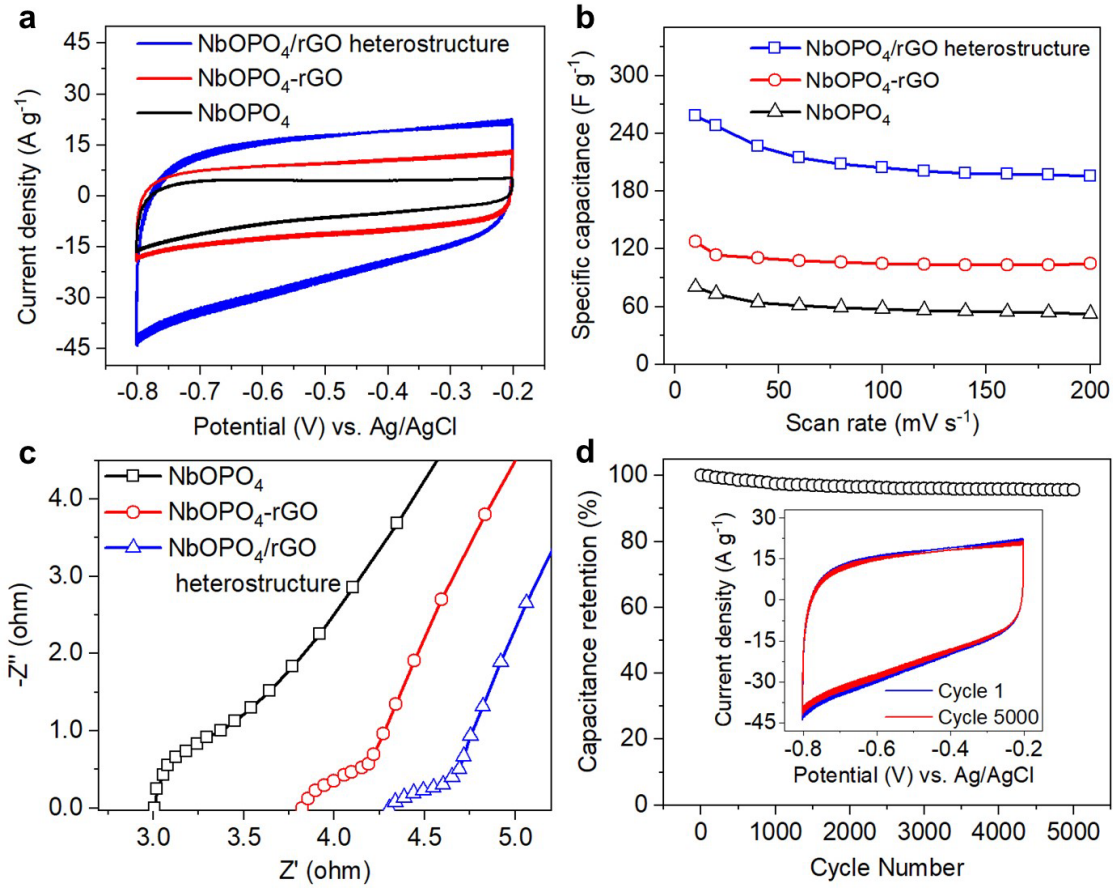

Figure 5.3. The electrochemical performance of the electrode materials. *(a) CV curves at 100 mV s^{-1}, (b) specific capacitance at various scan rates, and (c) the EIS spectra for $NbOPO_4$, $NbOPO_4$-rGO, and $NbOPO_4$/rGO heterostructure. (d) The cycling stability of $NbOPO_4$/rGO heterostructure was collected for 5,000 cycles (inset depicts the CV curves at first and the last cycle).*

5.4.3. The importance of heterointerface coupling

The superior electrochemical performance is directly pertinent to the role of the synthesis method on the coupling of $NbOPO_4$ and rGO. For the $NbOPO_4$/rGO heterostructure, the electrostatic attraction between positively-charged rGO and negatively-charged $NbOPO_4$ results in the self-assembled heterostructure, which is immediately flocculated upon mixing (Figure 5.4 a). In contrast, unmodified rGO with the negative surface charge does not produce a flocculated product owing to the lack of interaction between the two negatively charged nanosheets (Figure 5.4 b). This obviously affirms that electrostatic attraction is the primary factor in forming a uniform and ordered heterostructure.

To systematically elucidate the role of synthesis method on the interface coupling, Raman analysis was performed on ten random regions for $NbOPO_4$/rGO heterostructure and $NbOPO_4$-rGO. The optical images of these ten regions that are used for Raman analysis are demonstrated in Figure S3.13. Both samples demonstrated Raman red-shifts, which indicates the successful coupling between $NbOPO_4$ and rGO. Self-assembled $NbOPO_4$/rGO heterostructure displayed uniform Raman peaks with identical redshifts for Nb-O and O-P-O modes (Figure 5.4 c). In contrast, randomly restacked $NbOPO_4$-rGO showed partial and non-consistent redshifts with low intensities for Nb-O and O-P-O modes. Some of the regions (regions 1, 7, and 10) even showed no redshifts, corresponding to the pristine $NbOPO_4$, which is indicative of the lack of coupling between $NbOPO_4$ and rGO (Figure 5.4 d). The consistent Raman redshifts mean that self-assembled heterostructure is composed of uniform face-to-face placement of $NbOPO_4$ and rGO on one another. In comparison, non-consistent Raman redshifts are illustrative of the weak coupling between $NbOPO_4$ and rGO, where the nanosheets are randomly stacked in a disordered fashion.

To further affirm the role of heterointerface coupling on the elements' electronic states, we have analyzed the materials using the XPS technique. Figure 5.4 e-g depict the high-resolution Nb3d, P2p, and O1s XPS spectra of $NbOPO_4$, $NbOPO_4$-rGO, and $NbOPO_4$/rGO heterostructure. The Nb3d spectrum is composed of Nb-$3d_{5/2}$ and Nb-$3d_{3/2}$ that are located approximately at ~207 eV and 210 eV, respectively (Figure 5.4 e). This affirms that the chemical state of niobium is only Nb^{5+} and that no other chemical states could be found [243]. Additionally, the P2p spectrum is comprised of P-$2p_{3/2}$ and P-$2p_{1/2}$ that are located at 133 eV and 134 eV, respectively, being typical of the phosphate group (Figure 5.4 f). The O1s spectrum is composed of peaks at around 531 eV and 533 eV that are typical of the oxygen atoms in [NbO_6] and [PO_4], respectively (Figure 5.4 g) [243]. Figure 5.4 e-g demonstrates that the Nb3d, P2p, and O1s peaks of both $NbOPO_4$-rGO and $NbOPO_4$/rGO heterostructure are shifted to lower binding energies compared with the pristine $NbOPO_4$ nanosheets. It has been reported in previous works that the XPS shifts correspond to the orbital distortion of the elements in the presence of heterostructure coupling [317]. As the heterointerface coupling gets more robust, the distortion of the electronic

structure of the elements gets stronger as well, manifesting itself in a more significant XPS peak shift. The $NbOPO_4$/rGO heterostructure demonstrated larger binding energy shifts for the entire electronic states of Nb, P, and O, compared with the $NbOPO_4$-rGO (Figure 5.4 h). These results affirmed a stronger heterointerface coupling between $NbOPO_4$ and rGO in $NbOPO_4$/rGO heterostructure compared with $NbOPO_4$-rGO.

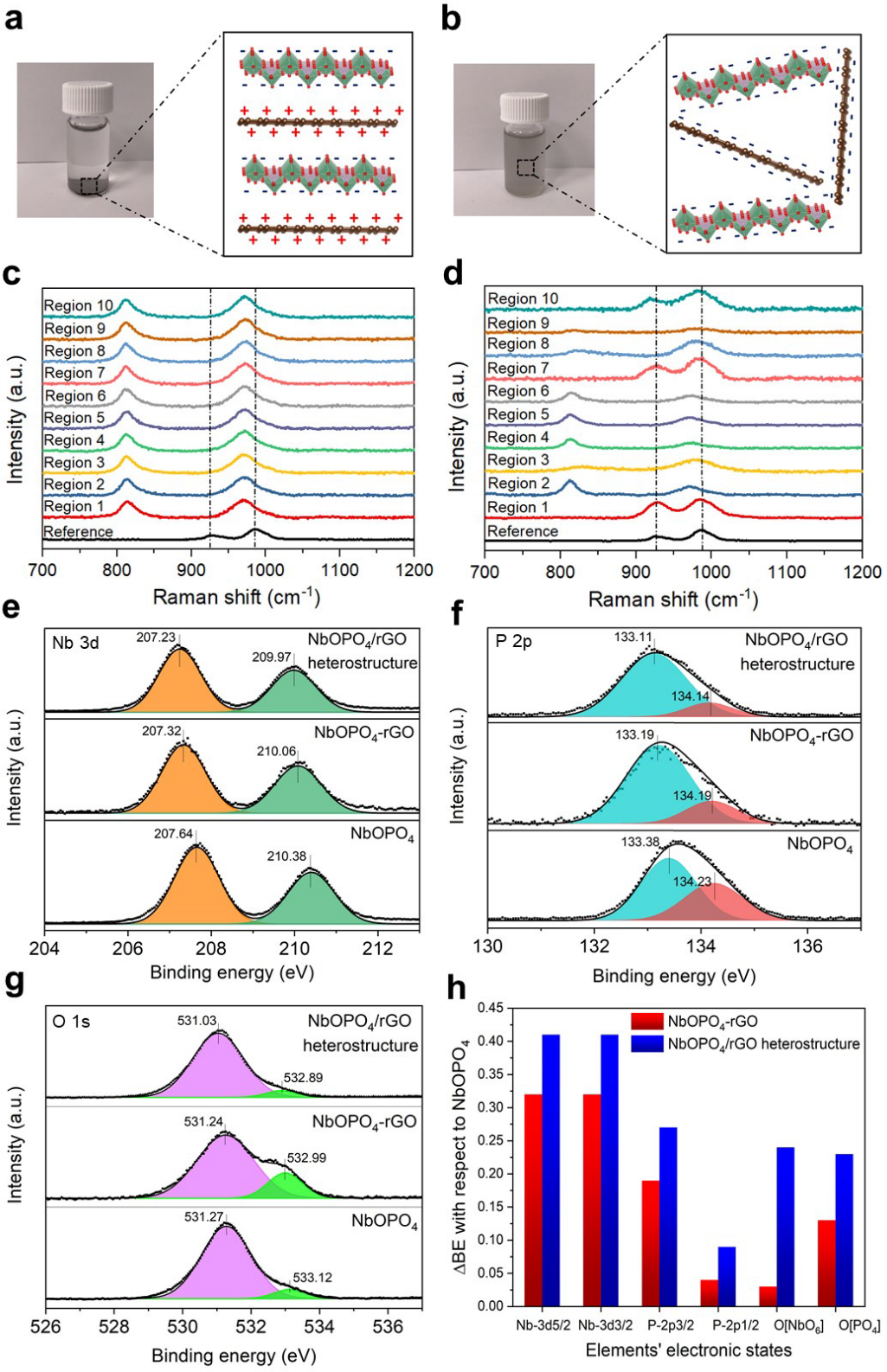

Figure 5.4. Characterizations of heterointerface coupling in $NbOPO_4$/rGO heterostructure. *(a) The visual representation of the stacking configuration of $NbOPO_4$ and rGO for self-assembled $NbOPO_4$/rGO heterostructure, and (b) randomly-restacked $NbOPO_4$-rGO nanosheets. (c) Raman spectra were collected at ten random regions for self-assembled $NbOPO_4$/rGO heterostructure, and (d) randomly-restacked $NbOPO_4$-rGO nanosheets (The black curve represent the pristine $NbOPO_4$ which is denoted as the Reference). High-resolution XPS spectra of (e) Nb3d, (f) P2p,*

and (g) O1s for $NbOPO_4$, $NbOPO_4$-GO, and $NbOPO_4$/rGO heterostructure. (h) The binding energy shifts (ΔBE) between $NbOPO_4$/rGO heterostructure and $NbOPO_4$-rGO with respect to the pristine $NbOPO_4$, for the electronic states of Nb, P, and O.

DFT calculations were performed to further clarify the role of interface coupling on the heterointerface charge transfer. The density of states (DOS) calculations proved the formation of new DOS near the Fermi level of $NbOPO_4$ that clarifies its improved electronic conductivity. Furthermore, bandgap reduction was observed at the heterostructure, together with a change from semiconducting to metallic. This is clearly attributed to the overlap of conduction and valence bands at the Fermi level (Figure 5.5 a). This result evidently demonstrates that the electronic structure of $NbOPO_4$ has been modified via interface coupling with graphene. In addition, charge density difference (CDD) contour plots depicted a robust electronic coupling at the heterointerface, with yellow and blue regions representing areas where electrons are gained and lost, respectively (Figure 5.5 b). The localized electron charges at the heterointerface affirm the excellent charge transfer from $NbOPO_4$ towards graphene. The DFT results attest that the interface plays a crucial role in the electronic conductivity and the charge transportation properties of the heterostructure. In fact, strong coupling of $NbOPO_4$ and rGO will result in a more efficient charge redistribution at the heterointerface. While, the weak coupling will leave some areas of the $NbOPO_4$-rGO uncoupled, which subsequently degrades the electronic conductivity and charge transportation. Hence, the self-assembled $NbOPO_4$/rGO heterostructure could achieve higher electrochemical performance compared with the randomly-restacked $NbOPO_4$-rGO nanosheets due to the more robust and intact interface coupling.

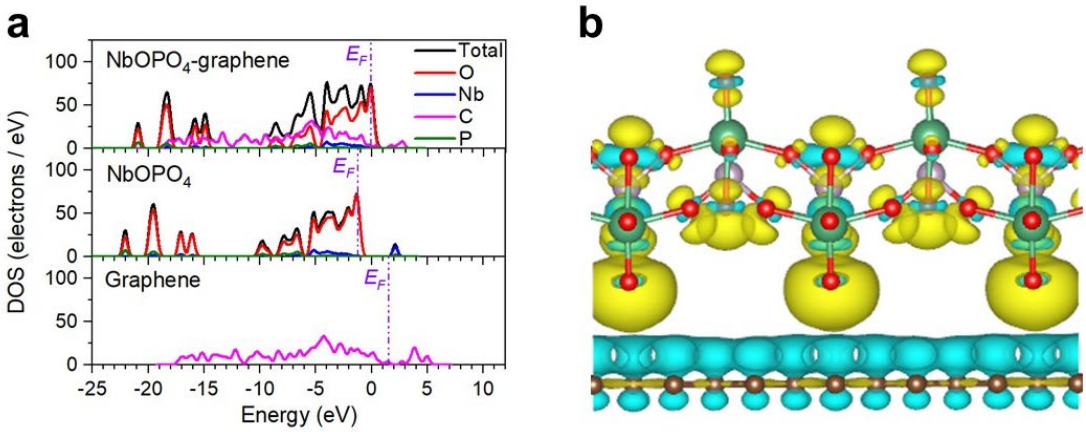

Figure 5.5. DFT calculations of NbOPO₄/rGO heterostructure. *(a) DOS calculation for graphene, NbOPO₄, and NbOPO₄-graphene heterostructure. (b) Charge redistribution at the interface of NbOPO₄-graphene heterostructure (yellow: gaining electrons, blue: losing electrons).*

5.4.4. CDI performance

The CDI performance of $NbOPO_4$/rGO heterostructure was further evaluated at the operating voltage of 1.2 V. The $NbOPO_4$ nanosheets and $NbOPO_4$-rGO were also tested for comparison. The salt adsorption capacity (SAC) of the three electrodes as a function of NaCl concentration from 100 mg L^{-1} to 10,000 mg L^{-1} is demonstrated in Figure 5.6 a. Our self-assembled heterostructure delivered a high SAC of 73 mg g^{-1} at NaCl concentration of 10,000 mg L^{-1} that is ~2.1 times and ~1.4 times higher than the pristine $NbOPO_4$ and $NbOPO_4$-rGO, respectively. This performance is more than five times and three times higher than that of control activated carbon and rGO electrodes with a SAC of 14.7 mg g^{-1} and 22.6 mg g^{-1}, respectively (Figure S3.14). Besides, this performance is higher than that of several recently reported materials, including porous carbon nanofibers [268, 286], graphene hollow shells [269], iron-nitrogen doped carbon tubes [271], porous MXene and nitrogen-doped MXene [188, 189], MoS_2 and MoS_2@nitrogen-doped carbon [190, 192], and MOF and MOF@COF (Figure 5.6 b and Table S3.3) [318-320].

Electrosorption rate is an essential parameter for practical CDI devices. The $NbOPO_4$/rGO heterostructure can deionize water to its maximum capacity within 8 minutes. Compared with pristine $NbOPO_4$ and $NbOPO_4$-rGO, the $NbOPO_4$/rGO heterostructure demonstrates a slightly faster electrosorption rate due to its superior specific capacitance and lower charge transfer resistance, which

accelerates the ion kinetics (Figure 5.6 c). In addition, the CDI Ragone plot of $NbOPO_4$/rGO heterostructure shifts towards the upper and more right region compared to $NbOPO_4$-rGO and $NbOPO_4$, suggesting a higher mean desalination rate (MDR) and SAC of the $NbOPO_4$/rGO heterostructure (Figure S3.15). The $NbOPO_4$/rGO heterostructure can deionize water at various voltages of 0.8 V, 1.0 V, and 1.2 V. The electrosorption capacity increases from 16 mg g^{-1} to 35 mg g^{-1} upon elevating the applied voltage (Figure S3.16). The $NbOPO_4$/rGO heterostructure can also achieve NaCl desorption within 8 minutes upon the application of 0 V (Figure S3.17). Furthermore, the $NbOPO_4$/rGO heterostructure showed excellent cycling stability up to 50 adsorption/desorption cycles with repeated CDI operation. In fact, an average desalination capacity of 35 mg g^{-1} was retained, implicating no sign of performance degradation or electrode fouling (Figure 5.6 d).

To summarize, the self-assembly procedure results in excellent heterointerface coupling of $NbOPO_4$ and rGO with an ordered face-to-face arrangement. Furthermore, the unique architecture yields outstanding electrochemical and CDI performance. This is ascribed to the strong heterointerface coupling between $NbOPO_4$ and rGO, decreasing the charge transfer resistance and accelerating the ion diffusion through the $NbOPO_4$/rGO heterostructure. Improved electronic and physical coupling, together with the small charge transfer resistance, increase the specific capacitance and the salt adsorption capacity.

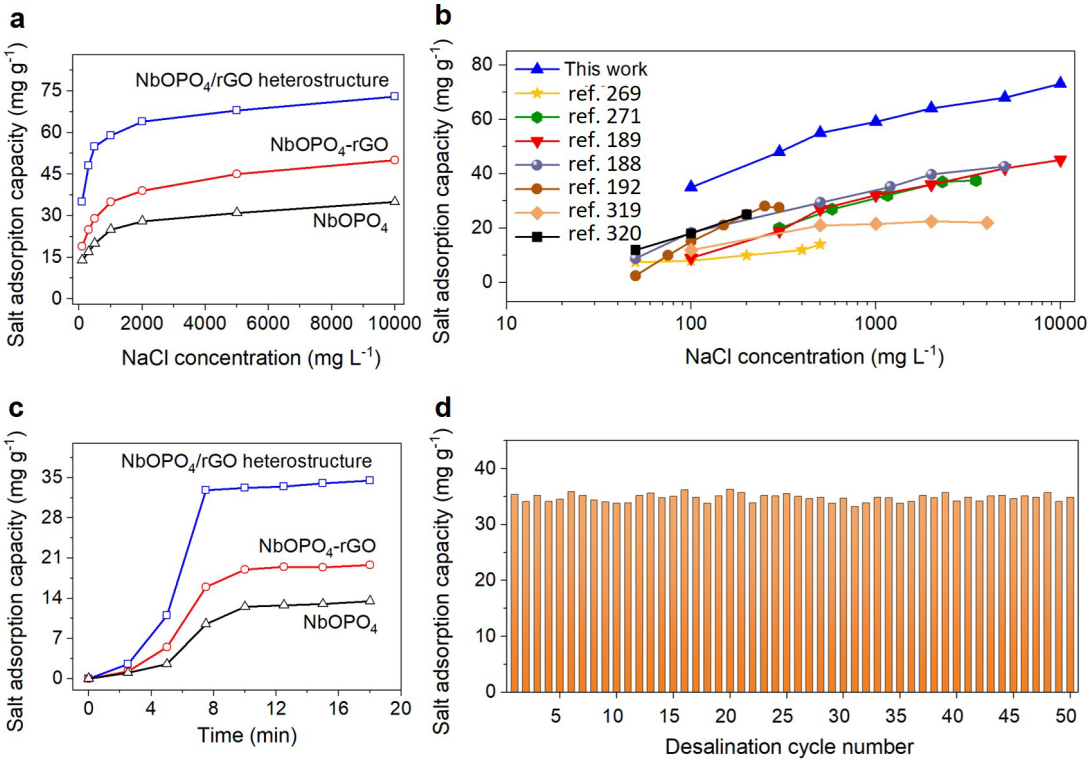

Figure 5.6. The CDI performance of the electrode materials. *(a) Electrosorption performance as a function of NaCl concentration ranging from 100 mg L^{-1} to 10,000 mg L^{-1} at the operating voltage of 1.2 V, for $NbOPO_4$, $NbOPO_4$-rGO, and $NbOPO_4$/rGO heterostructure. (b) The electrosorption performance comparison of the current work compared with several recently reported materials. The reference numbers correspond to these materials: graphene hollow shells [269], iron-nitrogen doped carbon tubes [271], porous MXene [189], porous nitrogen-doped MXene [188], MoS_2@nitrogen-doped carbon [192], MOF [319], and MOF@COF [320]. (c) Electrosorption rate at NaCl concentration of 100 mg L^{-1} at the operating voltage of 1.2 V, for $NbOPO_4$, $NbOPO_4$-rGO, and $NbOPO_4$/rGO heterostructure. (d) The cycling stability of $NbOPO_4$/rGO heterostructure, measured at NaCl concentration of 100 mg L^{-1}.*

5.5. Conclusions

In this study, we successfully synthesized a 2D heterostructure based on face-to-face restacking of $NbOPO_4$ and rGO via the electrostatic self-assembly technique. The as-prepared $NbOPO_4$/rGO heterostructure demonstrated high ion storage capacity, which can be attributed to the strong heterointerface coupling between $NbOPO_4$ and rGO. DFT calculations depicted that coupling of $NbOPO_4$ and graphene increases the bulk electronic conductivity and charge redistribution across the heterointerface. The self-assembly procedure generated a strong physical 2D-2D coupling that was manifested by the uniform and identical Raman shifts at various random regions in our heterostructure. Additionally, XPS results

demonstrated a large peak shift for the self-assembled $NbOPO_4$/rGO heterostructure, indicating strong electronic coupling. Consequently, the strong physical and electronic heterointerface coupling further reduced the charge transfer resistance and increased its specific capacitance. The high ion storage capacity and the high electronic conductivity of the $NbOPO_4$/rGO heterostructure yielded a specific capacitance of 258.3 Fg^{-1} and a salt electrosorption capacity of 73 mg g^{-1} for NaCl concentration of 10,000 mg L^{-1}. This work sheds light on the importance of heterointerface coupling between 2D materials as a design strategy for the fabrication of highly-efficient devices for various functional applications.

Chapter 6: Conclusion and Outlook

Ionic devices from electrochemical devices to nanofluidic devices function based on the mechanism of ionic transport and adsorption. These devices range from the existing technologies such as batteries, fuel cells, supercapacitors to undeveloped future technologies such as capacitive desalination, osmotic power generation, and ionic transistors. Hence, it is crucial to understand the mechanism and study the applications of these devices to improve the current technologies and also shape the future technologies.

From the materials perspective, the most promising type of materials that can be applied for this application are two-dimensional materials. 2D materials are highly promising in this field due to their ultra thin thickness, abundant functional groups, ease of fabrication into thin films, and ability to tailor nano-pores for ionic transport and adsorption applications. Moreover, the interlayer galleries in re-stacked 2D materials can act as ion transport channels that can facilitate the dynamics and diffusions of ions. In this thesis, we have investigated the science and applications of ionic transportation and adsorption through two-dimensional materials.

In Chapter 2, we provide a literature review. In order to engineer the ion transport in 2D materials, it is crucial to understand the mechanism of ionic sieving. Hence, we provide a literature review on the ionic sieving mechanism through 2D materials. The size exclusion and electrostatic repulsion phenomenon's are fully discussed first. Several types of 2D materials together with their physical and chemical modifications are discussed. Next, we provide several structures of 2D membranes that are specifically tailored to transport ions and counter-ions. The ionic selectivity, ionic transport, and membrane architecture are fully elaborated with applications targeting nanofluidic osmotic energy generation. Lastly, we end this chapter by providing a brief literature review on the ion adsorption in 2D materials with applications targeting capacitive water desalination.

In Chapter 3, we present a work on serosa-mimetic nanoarchitecture membrane for osmotic power generation. In this chapter, a bio-mimetic structure is developed that is inspired by the architecture of serosa. The membrane is made

by covalent organic frameworks that have vertical ion diffusion pathways. Moreover, the structure is further intertwined by 1D nanofibers to enhance its horizontal cation permselectivity, cation dynamics, and also mechanical strength. In addition, we incorporate sulfonate functional groups to enhance its ionic performance. This chapter is supported by several experimental and computational (DFT+MD) simulations, further affirming the enhancement of ionic diffusion and ionic selectivity via incorporating the sulfonate functional groups. The highest power achieved is 9.6 W m^{-2} using natural seawater/river water.

In Chapter 4, we present a work on engineering phosphorous vacancies on the surface of niobium oxyphosphate (NbP) nanosheets. We have utilized a facile acid etching strategy to selectively etch away the phosphorous atoms from the metal oxide structure. Several characterizations such as HAADF, ICP-MS and XPS, further affirm the success of the selective phosphorous etching form the structure. The removal of phosphorus atoms modifies the surface charge of the NbP structure that is supported by DFT and Zeta potential analysis. Increased surface charge further enhance the cation dynamics and selectivity that is affirmed by several ionic transport measurements and DFT+MD simulations. The highest power density achieved is 10.7 W m^{-2} using Australian seawater, that is much higher than the commercialization benchmark of 5 W m^{-2}. Moreover, a tandem of several membrane pairs can generate a sufficient voltage of up to more than 2V, which can power a red LED.

In Chapter 5, we have developed a self-assembled heterostructure by the electrostatic coupling between two types of nanosheets. Two cases are considered which are strong coupling (electrostatic attraction between nanosheets) and weak coupling (random architecture). Moreover, we have proved with Raman analysis that the interaction at the 2D/2D interface is stronger for the electrostatically re-stacked heterostructure as it shows uniform Nb-O and P-O shifts. Moreover, XPS analysis shows a higher binding energy shift. DFT calculations demonstrate the importance of coupling on the Fermi level of this structure, further affirming the crucial role of coupling on the electronic conductivity of the material. The strongly-coupled heterostructure shows a better electrochemical performance than the weakly-coupled structure, and the highest capacitive water desalination performance of 73 mg g^{-1} is achieved.

In terms of ion transportation, the future research direction can focus on the 2D/2D coupling and its effect on ion transportation. Moreover, the fabrication of atomically-thin materials can solve the issue of permeability vs. selectivity trade-off as ions can be readily transported and diffused at high rates. In this case, the nature of pore chemistries and their influence on ionic selectivity is a crucial issue to consider. In terms of ion adsorption, other types of 2D materials with different functional groups can be investigated. In this regard, the electrostatic interactions and hence the strength of 2D/2D coupling can be tailored, which can lead to the development of several functional devices. In summary, it is envisioned that further research into the science and application of 2D materials and their nanofluidic membranes for ionic transport and adsorption can lead to the development of modern technologies with high impacts on human life.

Appendices

Appendix 1- Supporting Information for Serosa-Mimetic Nanoarchitecture Membranes for Highly Efficient Osmotic Energy Generation

Note S1.1: Preparation of the lab-made Ag/AgCl electrodes

To prepare the Ag/AgCl electrode, silver wire was polished using sandpaper. Then, a layer of AgCl was deposited on the silver wire by electroplating in a CHI 660E electrochemical workstation. In this electroplating procedure, the silver wire was used as the anode and a Pt electrode was used as the cathode, meanwhile 0.5 M NaCl solution was applied as the electrolyte. A current of 1 mA was subjected to the terminals for 30 mins with a voltage range of -1 to -2 V. The electroplated wires were then rinsed with deionized water and dried in the oven.

Note S1.2: Electrode calibration

During the I-V testing, V_{mea}, V_{redox}, V_{diff}, and R_o represent the measured potential, the redox potential generated by the unequal potential drop at the electrode-solution interface, the diffusion potential contributed by the ion selective membrane and the inner resistance of the membrane, respectively. The measured V_{mea} consists of two parts (*i.e.* V_{redox} and V_{diff}). Due to asymmetrical structure of the silver-silver chloride electrodes and non-uniformity in the thickness of AgCl, there is an unequal potential across the two electrodes which should be subtracted from the osmotic potential. In this work, the value of V_{redox} was measured using an experimental method [136]. The membrane was replaced by a nonselective polyethylene terephthalate (PET) membrane containing a single micro-window. In this case, the measured potential was contributed solely by V_{redox}. Conductance was calculated by I_{diff}/V_{diff} measured in different concentration gradient. During the calibration process, the electrode potential remained stable as the diffusion of ions did not affect the bulk concentration obviously. Such an experimental method can largely preclude the influence brought by many unexpected factors such as the contamination and electrode imperfection.

Note S1.3: Cation transference number

For a given concentration gradient, the cation transference number, t_+, can be calculated as:

$$t_+ = \frac{1}{2}\left(\frac{E_{diff}}{\frac{RT}{zF} ln\left(\frac{r_{c_H} C_H}{r_{c_L} C_L}\right)} + 1\right) \quad \text{(S1)}$$

where E_{diff}, R, T, F, z, *r*, and *c* refer to the diffusion potential, universal gas constant, absolute temperature, Faraday constant, charge number, activity coefficient of ions and ion concentration, respectively [117].

Note S1.4: The size of NaCl solution diffusion box in MD simulations

For MD simulation model of vertical ion diffusion in PyPa and PyPa-SO_3H/SANF, the box size was set to be 136 $Å_x$ × 136 $Å_y$ × 20 $Å_z$. For horizontal ion diffusion model of PyPa, the box size was set to be 280 $Å_x$ × 78 $Å_y$ × 20 $Å_z$. In the case of horizontal ion diffusion model of PyPa-SO_3H/SANF, the box length along Z axis increased proportionally with the enlarged interlayer spacing, giving a total box size to be 280 $Å_x$ × 78 $Å_y$ × 100 $Å_z$. Furthermore, in the inset of Figure 3.6 d, the transfer quantity of ion in the PyPa-SO_3H/SANF was corrected (*i. e.* the transfer quantity of $ion_{corrected}$= transfer quantity of ion × 20 $Å_z$/100 $Å_z$) to eliminate the influence of different area on the ionic currents in the horizontal direction.

Note S1.5: FTIR sepctra

The characteristic absorption peaks located at 1641 (υ C=O), 1548 cm^{-1} (υ C-N linked to aromatic ring) and 1513 cm^{-1} (υ C=C on the aromatic ring) appear in the spectrum of pristine ANF fibers [321]. As for the spectrum of SSNa monomer, the peaks at 1189, 1137 and 1051 cm^{-1} are assigned to the stretch vibrations of SO_3^- group and the peak at 907 cm^{-1} is related to the C=C bending vibration[322]. After surface grafting, the absorption peaks of the SO_3^- enlarge, meanwhile the C=C bending vibration peak almost disappears in the spectrum of SANF, indicating a successful conversion of SSNa monomer on the ANF surface.

Supporting Figures and Tables

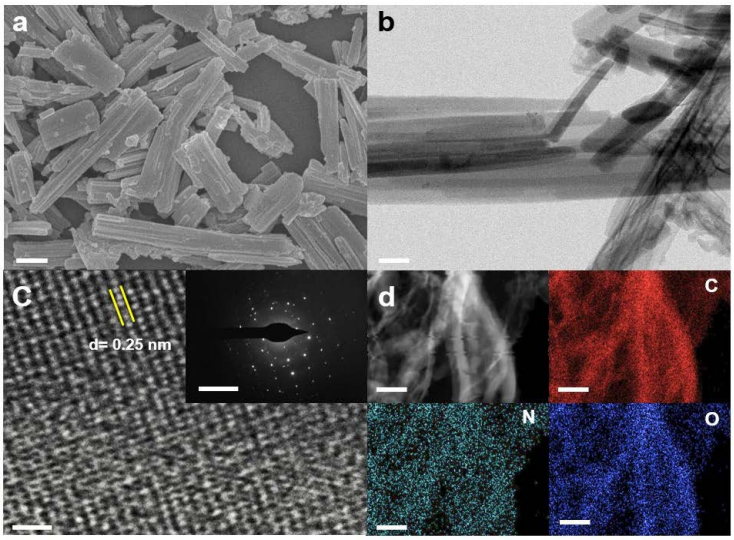

Figure S1.1. *(a) SEM image (scale bar: 500 nm). (b) TEM image (scale bar: 200 nm). (c) HR-TEM image (scale bar: 1 nm; inset: selected area electron diffraction (SAED) image with a scale bar of 20 nm^{-1}) and (d) EDS mapping (scale bar: 200 nm) of PyPa powders.*

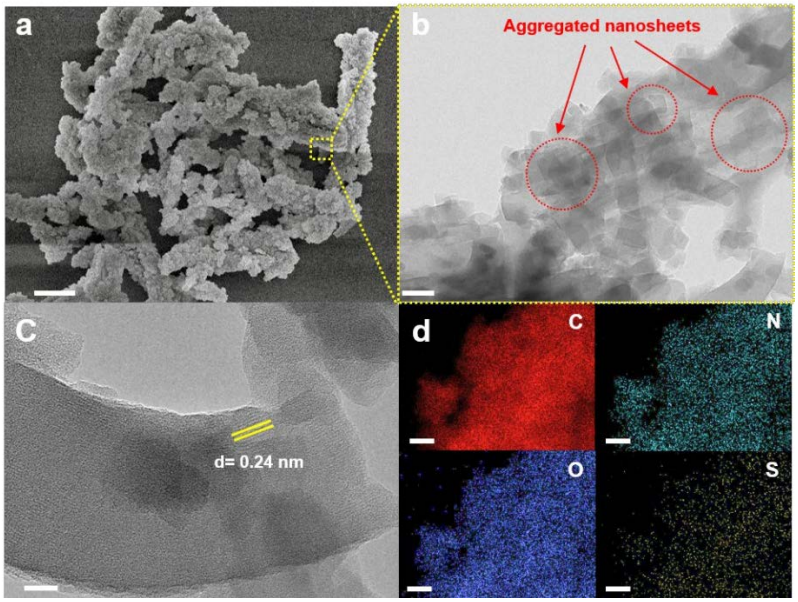

Figure S1.2. *(a) SEM image (scale bar: 2 µm). (b) TEM image (scale bar: 100 nm) of PyPa-SO_3H COF powders synthesized by "one-pot" method. (c) HR-TEM image (scale bar: 20 nm) and (d) EDS mapping (scale bar: 200 nm) of PyPa-SO_3H powders.*

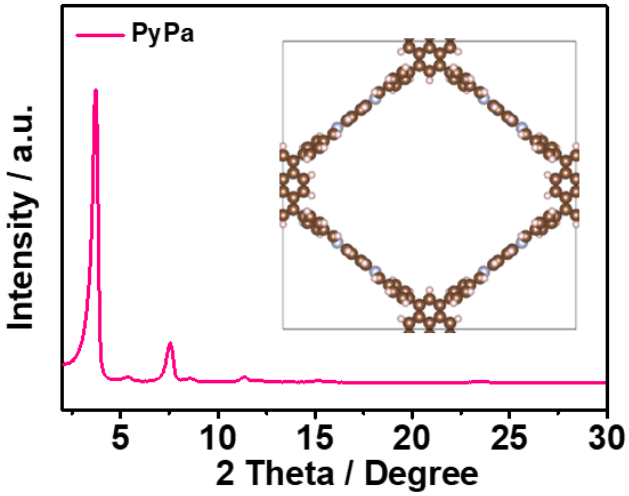

Figure S1.3. *XRD pattern of PyPa powder.*

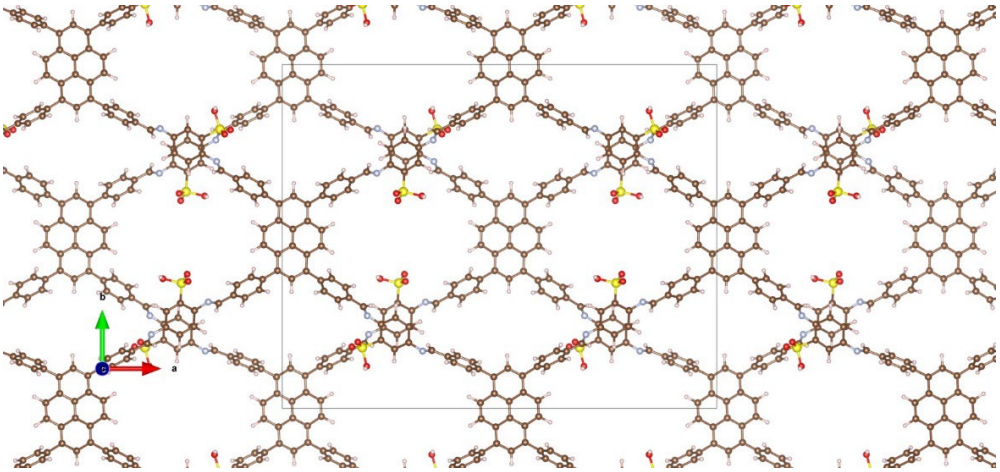

Figure S1.4. *The simulated conformation of PyPa-SO₃H COF in A-B stacking mode.*

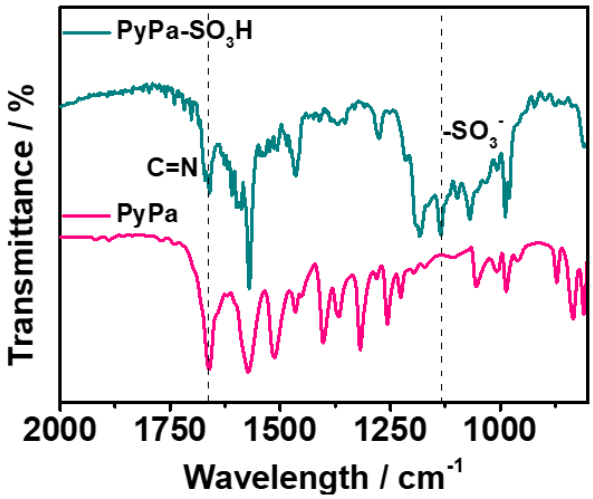

Figure S1.5. *FT-IR spectra of PyPa and PyPa-SO₃H.*

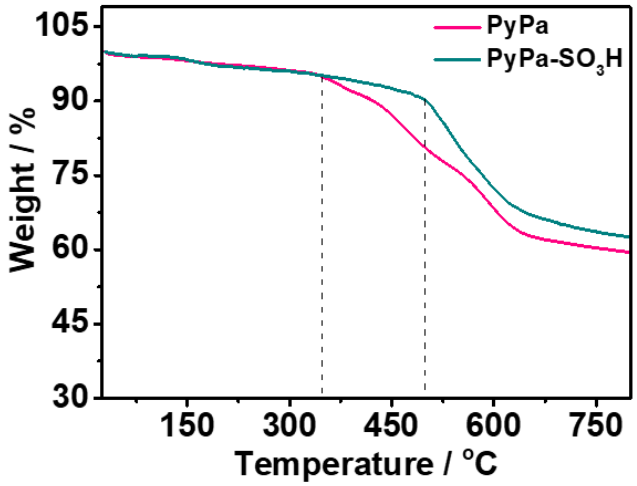

Figure S1.6. *TGA curves of PyPa and PyPa-SO₃H.*

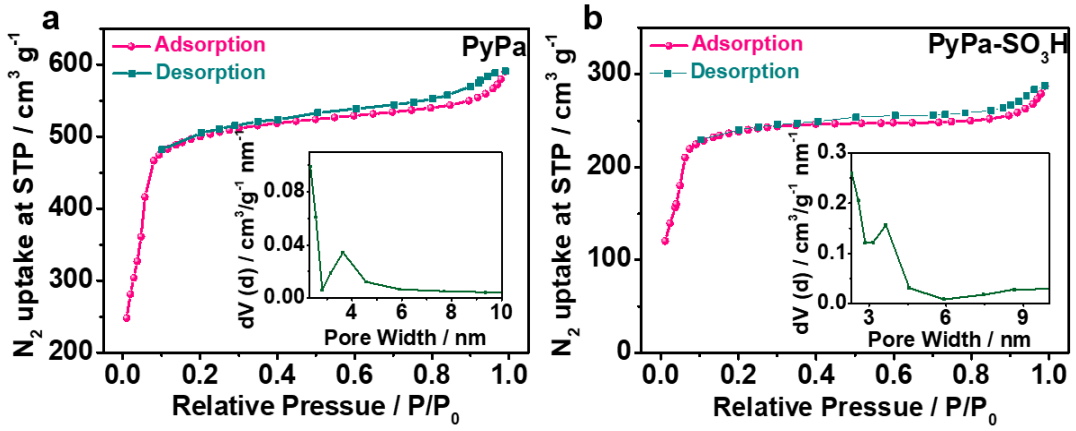

Figure S1.7. *Nitrogen sorption isotherm of (a) PyPa (with a BET surface area of 2697 $m^2 g^{-1}$) and (b) PyPa-So₃H nanosheets recorded at 77 K. The pore size distributions are shown in inset.*

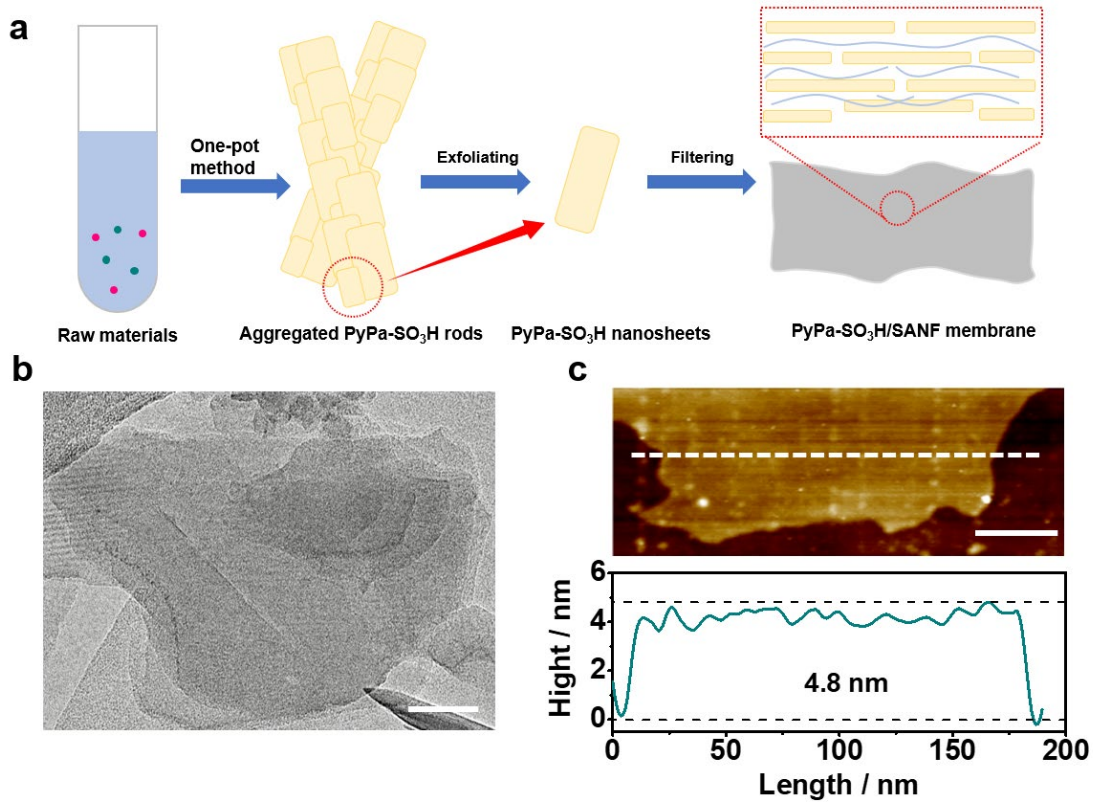

Figure S1.8. *(a) Schematic illustration of the synthesis route of PyPa-SO₃H nanosheets and PyPa-SO₃H/SANF membrane. (b) HR-TEM image of PyPa-SO₃H nanosheets. Scale bar: 50 nm. (c) AFM image of PyPa-SO₃H nanosheets on mica. The bottom panel shows the corresponding height profile. Scale bar: 50 nm.*

The PyPa-SO₃H molecule is a 2 D COF. However, the PyPa-SO₃H powders synthesized by “one-pot” method exhibited a rod-shaped morphology (Figure S1.2 a) consisting of stacked nanosheets (Figure S1.2 b). These PyPa-SO₃H rods were further exfoliated into PyPa-SO₃H nanosheets, and subsequently assembled into free-standing permselective membranes (Figure S1.8 a).

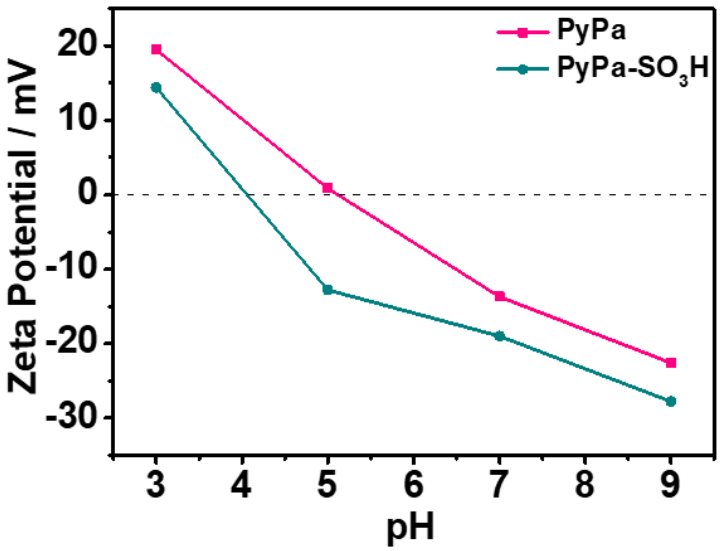

Figure S1.9. *Zeta potential of PyPa and PyPa-SO_3H nanosheets.*

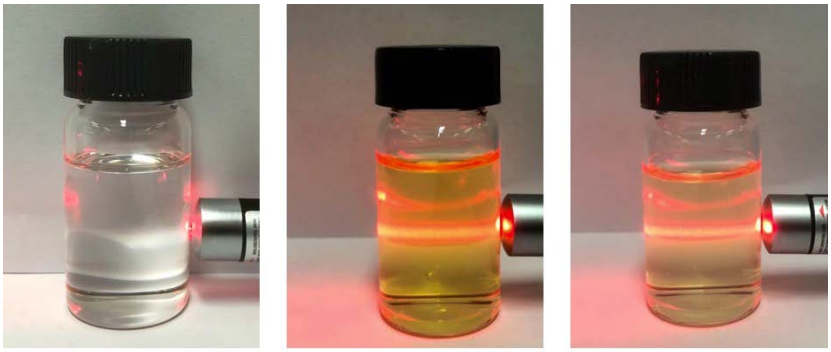

Figure S1.10. *Photograph of PyPa and PyPa-SO_3H nanosheets dispersed in DMSO.*

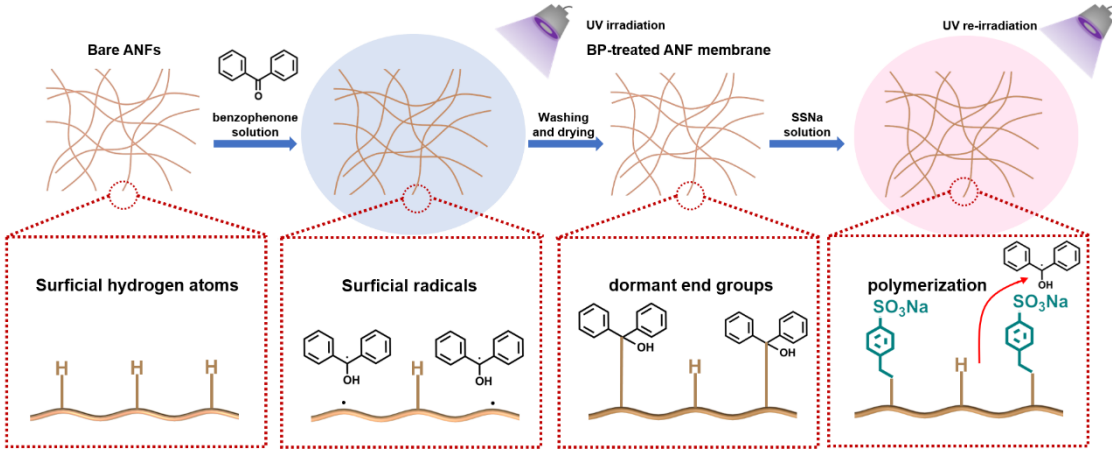

Figure S1.11. *Illustration of the preparation of SANFs.*

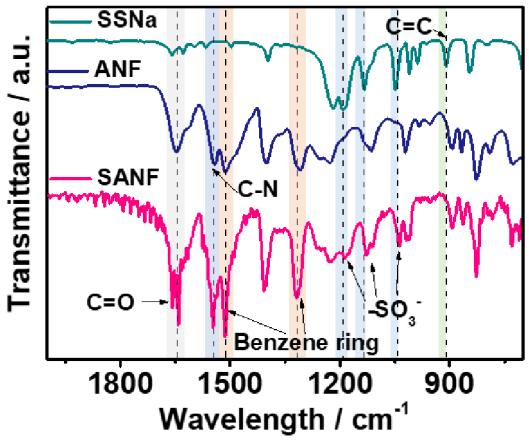

Figure S1.12. *FT-IR of ANF, SSNa monomer and SANF (Supplementary Note 5).*

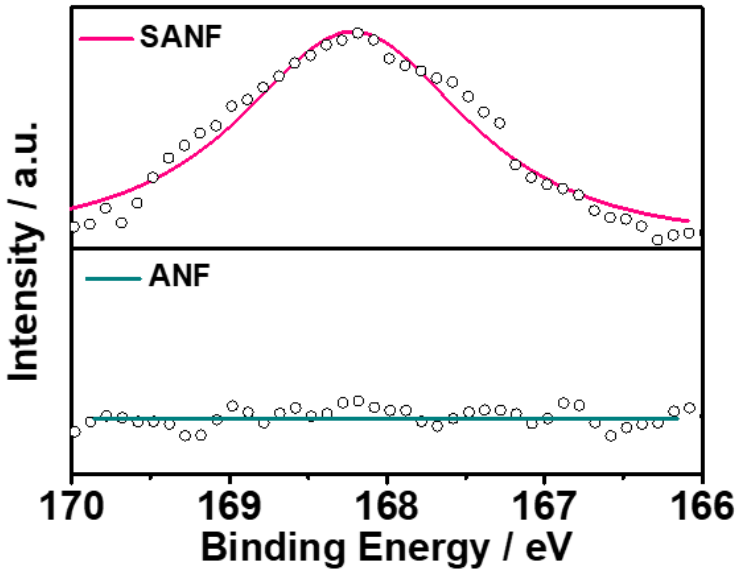

Figure S1.13. *S 2p XPS spectrum of ANF and SANF. The hollow dots represent experimental data while the solid line represent fitting result. The S 2p XPS of SANFs presents a new peak at about 168.2 eV, which is assigned to the presence of strong electron withdrawing group of -SO_3^- in SANF [323]. This further demonstrates a successful surface graft polymerization of SSNa onto the ANF.*

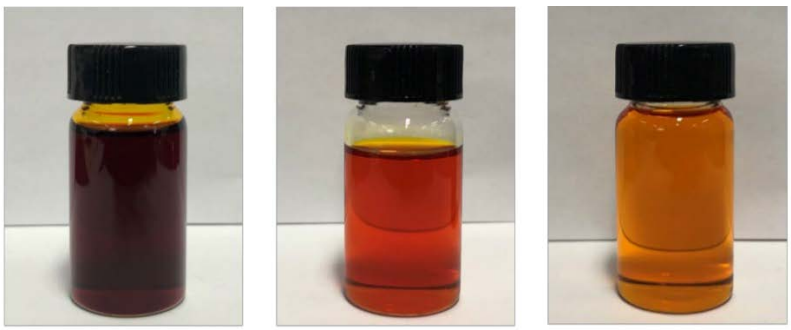

Figure S1.14. *Photograph of ANF (10 mg mL^{-1}), ANF (1 mg mL^{-1}) and SANF (1 mg mL^{-1}) in DMSO.*

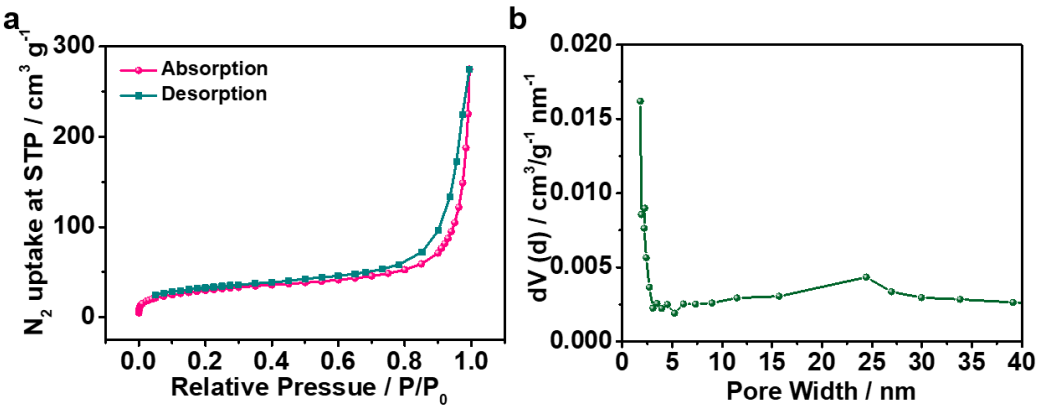

Figure S1.15. *(a) Nitrogen sorption isotherm of PyPa-SO₃H/SANF composite membrane recorded at 77 K. The BET surface area is 120 m^2 g^{-1}. (b) Pore size distribution of the PyPa-SO₃H/SANF composite membrane based on N_2 adsorption/desorption measurement.*

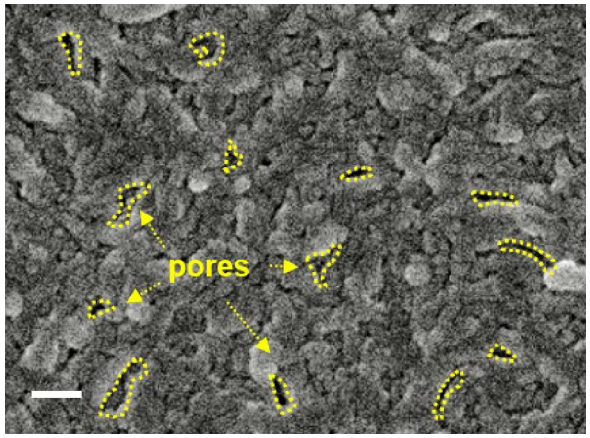

Figure S1.16. *Top-view SEM images of PyPa-SO₃H/SANF membrane. Scale bar: 200 nm.*

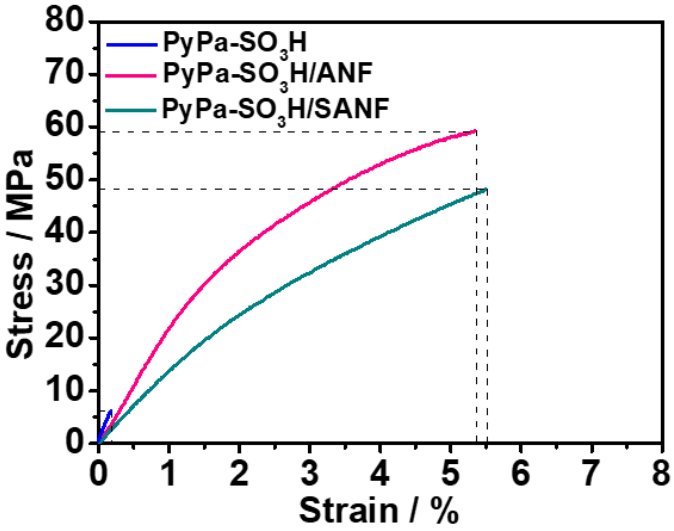

Figure S1.17. *Tensile stress-strain curves of different membranes. The ultimate strength of PyPa-SO₃H/SANF is slightly lower than that of PyPa-SO₃H/ANF, maybe due to the surface degradation of fibers during the UV irradiation in the grafting process.*

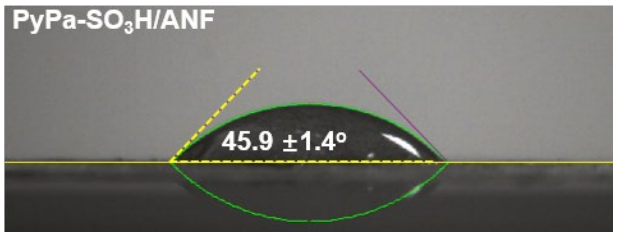

Figure S1.18. *Contact angle of water on PyPa-SO_3H/ANF composite membrane.*

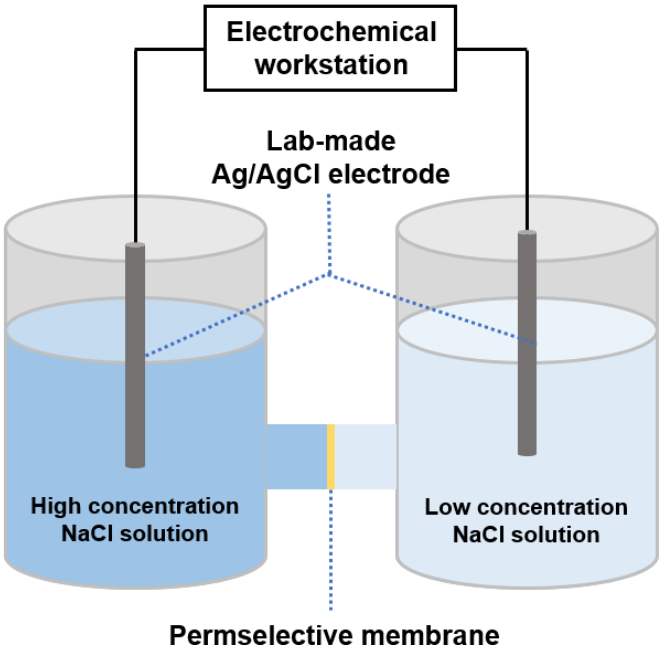

Figure S1.19. *Schematic illustration of the experimental setup to measure the transmembrane ionic transport.*

Table S1.1. *List of V_{mea}, V_{redox}, and V_{diff} and corresponding cation transference number, t_+, of a PyPa-SO_3H/SANF membrane (the low concentration side is set to be 0.1 mM NaCl).*

	10-fold	100-fold	500-fold	1000-fold	5000-fold
V_{mea} (mV)	23	95	149	176	239
V_{redox} (mV)	6	34	56	62	88
V_{diff} (mV)	17	61	93	110	144
I_{mea} (μA)	58	442	1532	2392	6042
I_{redox} (μA)	23	177	969	1016	1131
I_{diff} (μA)	45	265	563	1376	4911
t_+	0.66	0.78	0.82	0.84	0.86

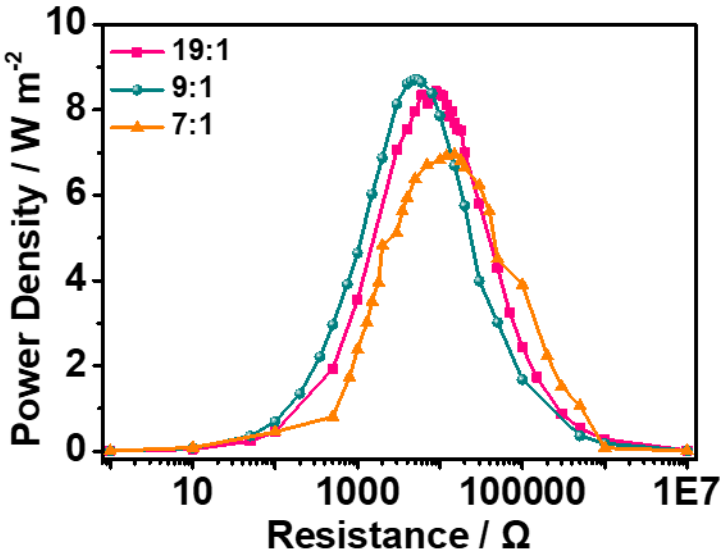

Figure S1.20. *Power outputs of PyPa-SO_3H/SANF composite membranes with different PyPa-SO_3H: SANF ratios as functions of load resistance in the presence of artificial sea water|river water.*

We have tested the power output performance of PyPa-SO_3H/SANF composite membranes with different PyPa-SO_3H: SANF ratios. As shown in Figure S1.20, the output power density dramatically increased from 6.9 W m^{-2} to 8.7 W m^{-2} when the PyPa-SO_3H: SANF ratio increased from 7: 1 to 9: 1 due to the increased amount of nanofluidic nanochannels. Furthermore, the output power density almost kept constant when the ratio was over 9: 1 (*e. g.* 8.4 W m^{-2} when the PyPa-SO_3H: SANF reached 19: 1). Considering that the excessive PyPa-SO_3H content will reduce the mechanical strength of the membrane, the ratio of 9: 1 was chosen as the optimized PyPa-SO_3H: SANF in the membrane preparation.

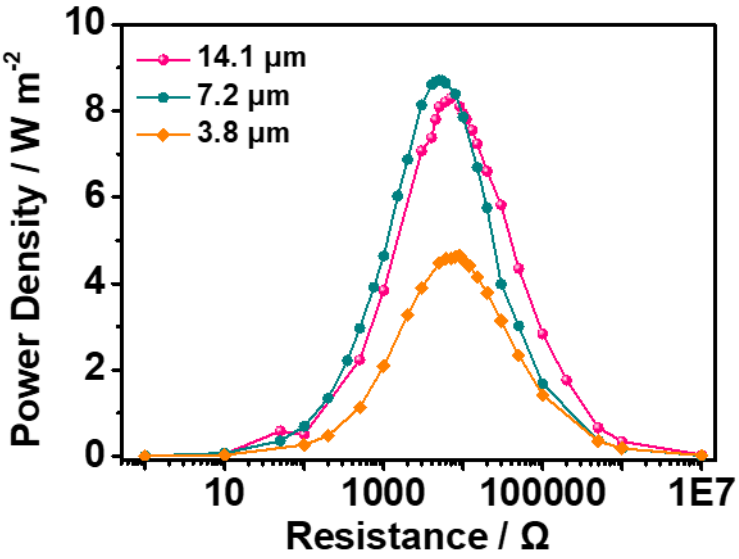

Figure S1.21. *Power outputs of PyPa-SO_3H/SANF membranes with different thicknesses as functions of load resistance in the presence of artificial sea water|river water.*

We have tested the power output performance of PyPa-SO_3H/SANF composite membranes with different thicknesses. The output power was improved from 8.3 to 8.7 W m^{-2} when the membrane thickness was reduced from 14.1 to 7.2 μm. This demonstrates that within a certain range, reducing the membrane thickness can improve the power density due to the decreased internal resistance and the shorten ion diffusion path of the composite membrane. However, when the membrane thickness was further reduced to 3.8 μm, the membrane became fragile and less dense, results in a power density as low as 4.6 W m^{-2} owing to the lower ion permeability. Therefore, 7.2 μm was chosen as the optimized membrane thickness in this research.

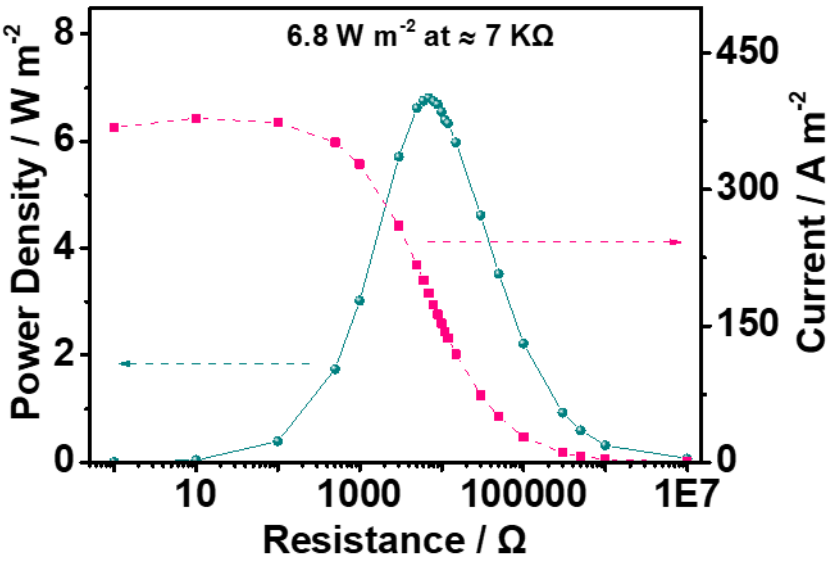

Figure S1.22. *Power output of PyPa/SANF membrane as functions of load resistance in the presence of artificial sea water|river water.*

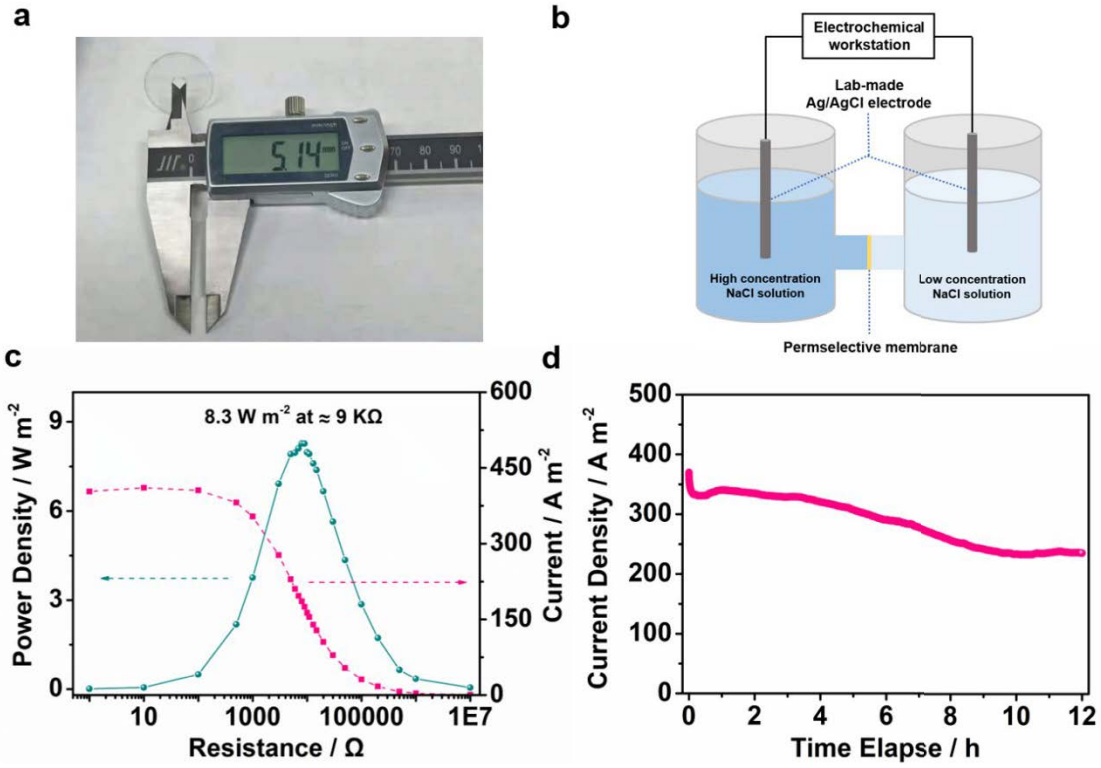

Figure S1.23. *(a) Photograph of the test fixture to fix the permselective membrane for osmotic energy conversion. (b) Schematic illustration of the experimental setup to measure the transmembrane ionic transport. (c) Power output of a PyPa-SO_3H/SANF membrane between natural sea water|river water with a membrane area of 20.74 mm^2. (d) Current-time curve of a PyPa-SO_3H/SANF membrane in artificial sea water|river water without electrolyte replenishing with a membrane area of 20.74 mm^2.*

It is known that within the range of practical operation, a smaller test area of the permselective membrane would lead to an osmotic energy conversion

performance closer to the theoretical value of membrane material. To verify the accuracy of our tested osmotic energy conversion performance, we enlarged the test area of PyPa-SO_3H/SANF membrane to 20.74 mm^2 (*i. e.* a pore diameter of 5.14 mm on the fixture, Figure S1.23 a-b). The output power (8.3 W m^{-2}, Figure S1.23 c) was close to that obtained from a 3 × 10^4 um^2 membrane area (*i. e.* 8.7 W m^{-2}), demonstrating that our test result is highly reliable. Furthermore, to verify the ability of PyPa-SO_3H/SANF membrane to withstand the osmotic pressure and water pressure at larger scale (*i. e.* an test area of 20.74 mm^2, Figure S1.23 a), we have tested the durability of PyPa-SO_3H/SANF membrane in artificial sea water|river water without electrolyte replenishing (Figure S1.23 b). The current density on the external circuit maintained 65.6 % of its starting value after 12 hours (Figure S1.23 d), confirming the structural robustness of the PyPa-SO_3H/SANF membrane in osmotic energy generation.

Table S1.2. *Comparison of different types of composite membranes.*

Solution (M)	Membrane	Thickness (μm)	Resistance (KΩ)	Power Density (W m^{-2})	Ref
NaCl (0.5/0.01)	Silk-based hybrid membranes	65	23	2.8	[324]
NaCl (0.5/0.01)	Silk fibroin membrane	0.1	7	4.0	[230]
NaCl (0.5/0.01)	MXene/ANF composite membrane	4.5	27	4.5	[201]
NaCl (0.5/0.01)	Polyelectrolyte hydrogel	210	23	5.0	[196]
NaCl (0.5/0.01)	$Ti_3C_2T_x$ MXene membranes		5	4.6	[325]
NaCl (0.5/0.01)	GOM	10	10	0.7	[223]
NaCl (0.5/0.01)	PES-SO_3H/PES-OHIm	60		6.2	[215]
NaCl (0.5/0.01)	PET	23	100	0.2	[231]
NaCl (0.5/0.01)	ionic diode membrane (IDM)	64.2	10	3.4	[232]
NaCl(0.5/0.001)	Janus membrane	0.5	N/A	3.8	[326]

NaCl (0.5/0.001)	Janus 3D porous membrane	11	N/A	5.1	[228]
KCl (0.5/0.01)	AAO Membrane	99.2	20	3.1	[234]
KCl (0.5/0.01)	PSS/MOF	85	N/A	2.8	[224]
KCl (1/0.001)	2D MOFs/PAA	52.8	N/A	1.6	[233]
NaCl (0.5/0.01)	This work	7.2	5	9.6	

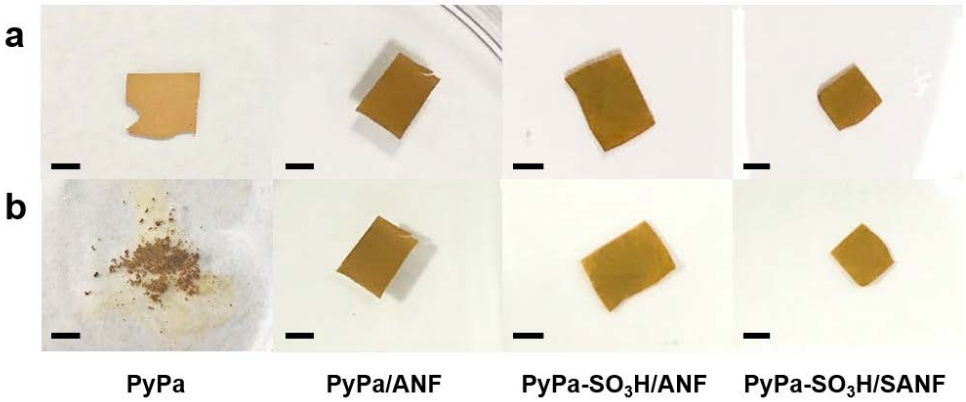

Figure S1.24. *Pictures of (a) pristine membranes and (b) membranes after immersing in water for 1 month (scale bar: 0.3 mm).*

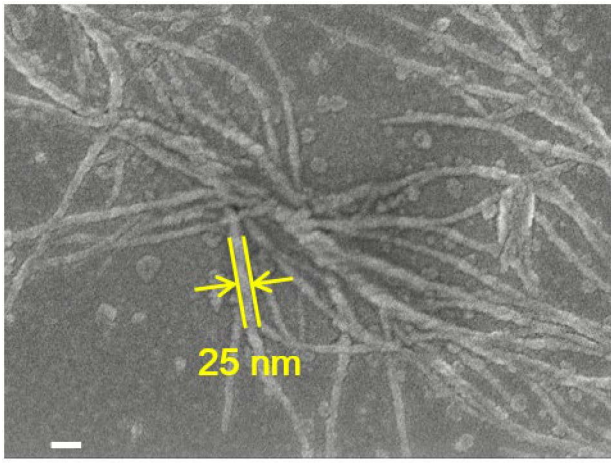

Figure S1.25. *SEM image of SANFs. Scale bar: 50 nm.*

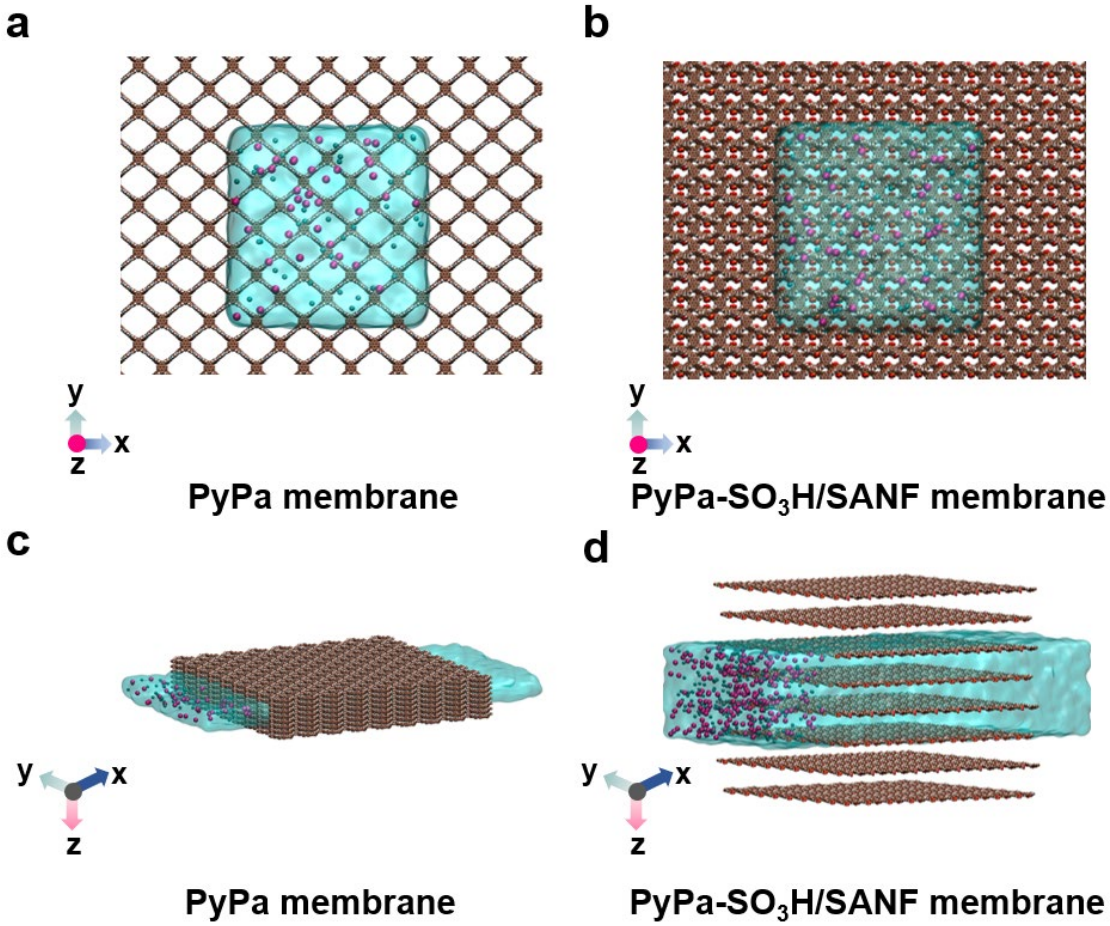

Figure S1.26. *(a, b) Top view of ion diffusion across (a) PyPa, (b) PyPa-SO_3H/SANF membranes in vertical pathway in NaCl solution. (c, d) 3D view of ion diffusion across (c) PyPa and (d) PyPa-SO_3H/SANF membranes in horizontal pathway.*

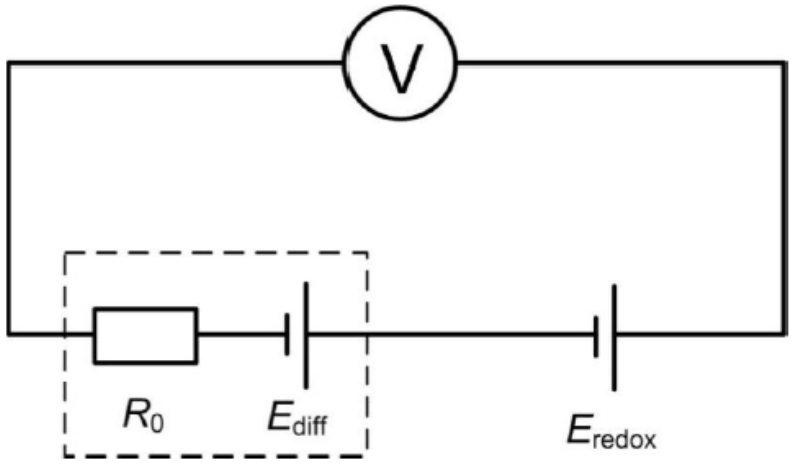

Figure S1.27. *The equivalent circuit of the membrane-based power source.*

Appendix 2- Supporting Information for Vacancy Engineering for High-Efficiency Nanofluidic Osmotic Energy Generation

Note S2.1: Preparation of the lab-made Ag/AgCl electrodes

To develop homemade Ag/AgCl electrodes, a silver wire was polished, then a layer of AgCl was electrodeposited using an electrochemical workstation. In the electrodeposition process, the silver wire and platinum electrode were utilized as working and reference electrodes, respectively. The electrolyte was 0.5 M NaCl solution. A current of 1mA was applied for 30 min and the voltage fluctuated in a range of -1 to -2 V. Finally, the as-prepared Ag/AgCl electrodes were rinsed with deionized water and dried in the oven.

Note S2.2: Electrode calibration

When performing the *I-V* measurements, V_{oc}, V_{redox}, V_{osm}, and R_o represent the measured open-circuit potential, the redox potential generated by the inequivalent potential drop at the electrode-solution interface, the osmotic potential contributed by the ion-selective membrane, and the membrane's inner resistance, respectively. The V_{oc} comprises two parts (i.e. V_{redox} and V_{osm}). The value of V_{redox} can be obtained based on the previous report [163]. The membrane was replaced with a nonselective polyethylene terephthalate (PET) membrane with a single micro-window. In this regard, the measured potential was contributed by V_{redox} only. Conductance was calculated by I_{osm}/V_{osm} and measured in different concentration gradients. During the calibration process, the electrode potential was maintained stable as ion diffusion did not alter the bulk concentration.

Note S2.3: Tandem device details

Boron-silicate water containers were glued together to form tandem device. The containers were alternately filled with fresh water (0.01 M) or salt water (0.5 M), and separated by V-NbP membranes with testing area of 3×10^4 μm^2. Copper wires were placed to tandem-connect the fresh water | salt water container couples together, and Ag/AgCl electrodes were applied to test the performance of osmotic energy generation.

Note S2.4: Cation transference number and energy conversion efficiency

For membranes with a negative surface charge, the cations flow from the high concentration region to the low concentration region in the presence of a chemical potential gradient. In this case, the cation transference number (t_+) can be calculated as follows:

$$t_+ = \frac{1}{2}\left(\frac{V_{osm}}{\frac{RT}{zF}\ln\left(\frac{r_{C_H}C_H}{r_{C_L}C_L}\right)} + 1\right) \quad \text{(S1)}$$

where V_{osm}, R, T, F, z, r, and c corresponds to the osmotic potential, universal gas constant, absolute temperature, Faraday constant, charge number, activity coefficient of ions and ion concentration, respectively. The short circuit current (I_{sc}) and open circuit voltage (V_{oc}) are acquired by the *I*-*V* curve. The values of osmotic current (I_{osm}) and osmotic voltage (V_{osm}) can be further obtained via electrode calibration as described in Note S2.

The energy conversion efficiency (φ) was determined by:

$$\varphi = \frac{1}{2}(2t_+ - 1)^2 \quad \text{(S2)}$$

where t_+ is the cation transference number of the permselective membrane.

Note S2.5: MD simulations

For water adsorption computation, a single NbP or V-NbP nanosheets (65 Å by 65 Å by 6 Å) was hydrated with water molecules. The overall size of the simulation box after water hydration was 105 Å by 105 Å by 46 Å. For ion diffusion computation, the size of the multilayer system was 65 Å in the x direction and 65 Å in the y direction. The size in the z direction was 62 Å, 90 Å, 118 Å, 147 Å for interlayer spacings of 8 Å, 12 Å, 16 Å and 20 Å, respectively. The overall size of the multilayer system after solvating with water molecules was 140 Å in the x direction and 65 Å in the y direction. The size in the z direction was 65 Å, 95 Å, 128 Å 160 Å for interlayer spacings of 8 Å, 12 Å, 16 Å and 20 Å, respectively.

The ionic currents can be calculated by the slope of Transfer quantity of ions vs. Time plot. Assuming ions carry a charge of 1.6×10^{-19} C, the ionic currents (μA) can be found using the following equation:

$$Ionic\ currents\ (\mu A) = \frac{Transfer\ quantity\ of\ ions\ (no.)}{Time\ (ps)} \times \frac{1.6\times10^{-19}\ C}{10^{-12}\ s} \times 10^6 \quad \text{(S3)}$$

After obtaining the ionic currents, the simulated t_+ is correspondingly calculated via the following equation:

$$t_+ = \frac{I_{Na^+}}{I_{Na^+} + I_{Cl^-}} \quad \text{(S4)}$$

where, I_{Na^+} and I_{Cl^-} are the simulated Na and Cl ion current, respectively.

Supplementary Figures and Tables:

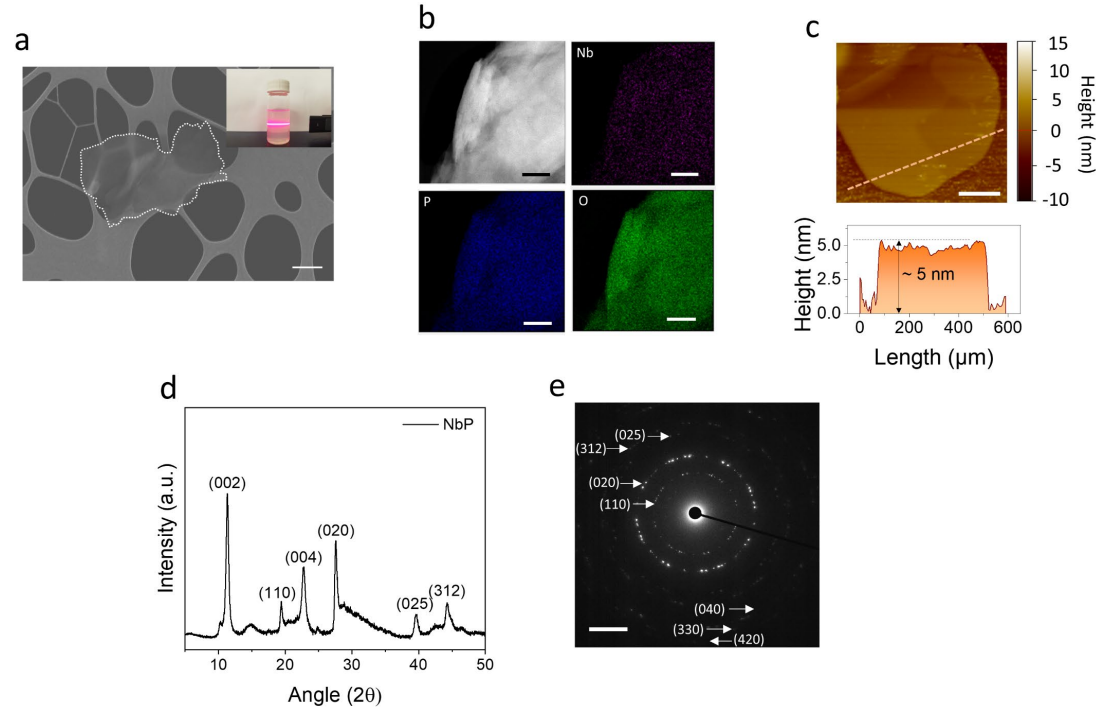

Figure S2.1. *Characterization of NbP nanosheets. (a) SEM image (scale bar: 400 nm) of the NbP nanosheets and Tyndal effect of NbP dispersions in water (inset); (b) Energy dispersive X-ray spectroscopy (EDX) spectra (scale bar: 100 nm), (c) AFM image and corresponding height profile (scale bar: 150 nm), (d) XRD spectra, and (e) SAED pattern (scale bar: 2 1/nm) of NbP nanosheets.*

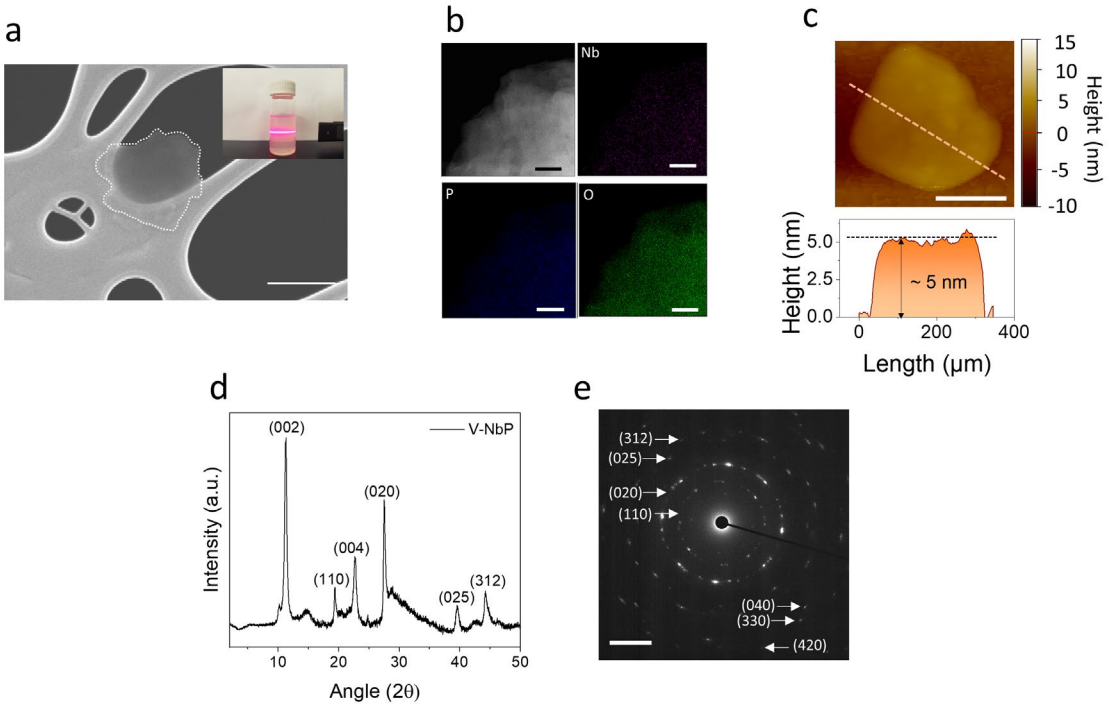

Figure S2.2. *Characterization of V-NbP nanosheets. (a) SEM image (scale bar: 200 nm) of V-NbP nanosheets and Tyndal effect of V-NbP dispersions in water (inset); (b) EDX spectra (scale bar: 50 nm), (c) AFM image and corresponding height profile (scale bar: 150 nm), (d) XRD spectra, and (e) SAED pattern (scale bar: 2 1/nm) of V-NbP nanosheets.*

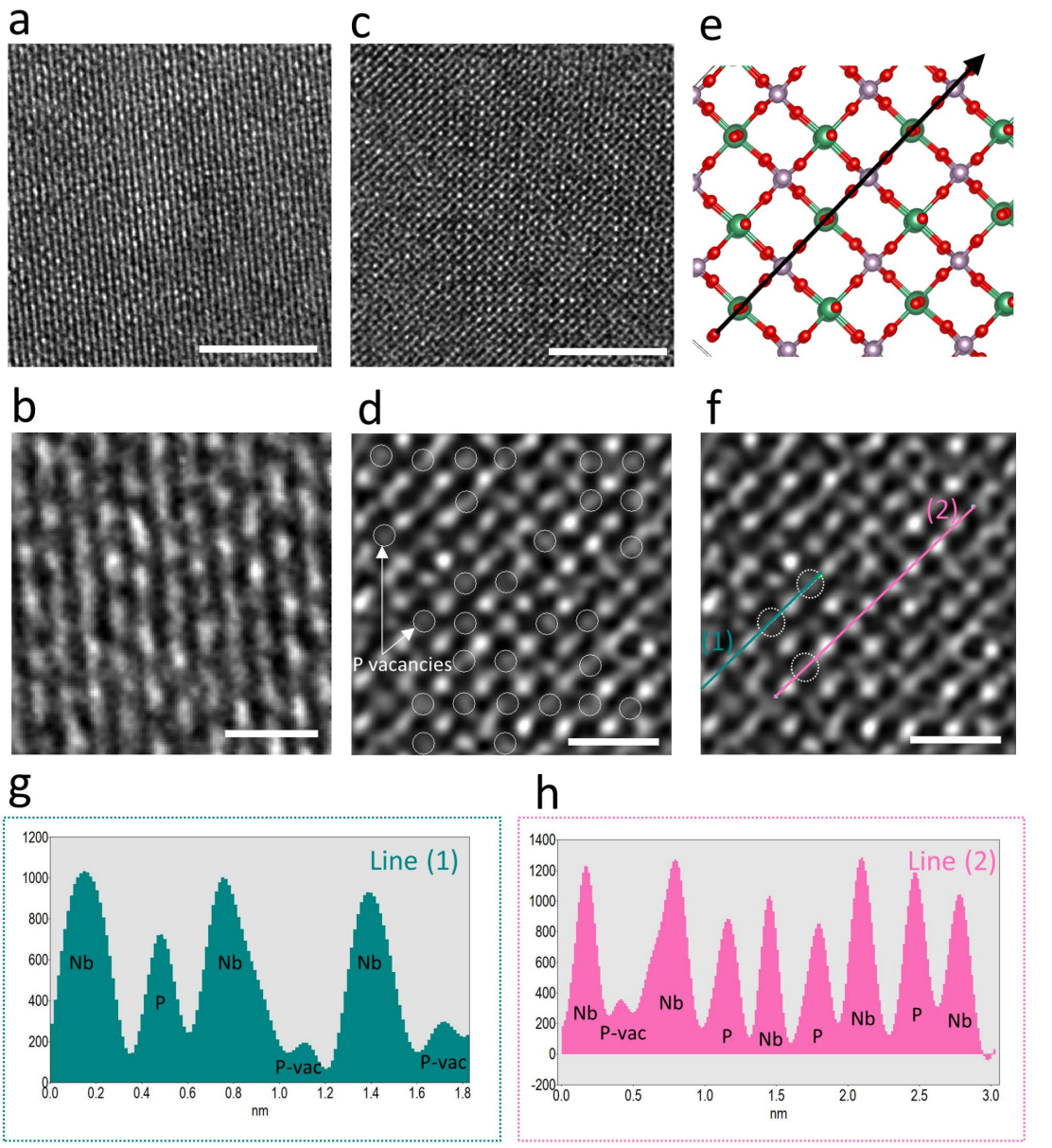

Figure S2.3. *Characterizations of P vacancy sites using HAADF-STEM. HAADF-STEM images of (a, b) NbP and (c, d) V-NbP nanosheets. (e) Crystal structure of NbP with the direction of the line scan used to analyze the image. (f) HAADF-STEM image of V-NbP showing the line scan. (g) The line scan (1) and (h) line scan (2). The P-vacancy sites can be seen at the sites where the intensity is low. Scale bars for (a) and (c): 5 nm, and for (b), (d) and (f): 1 nm.*

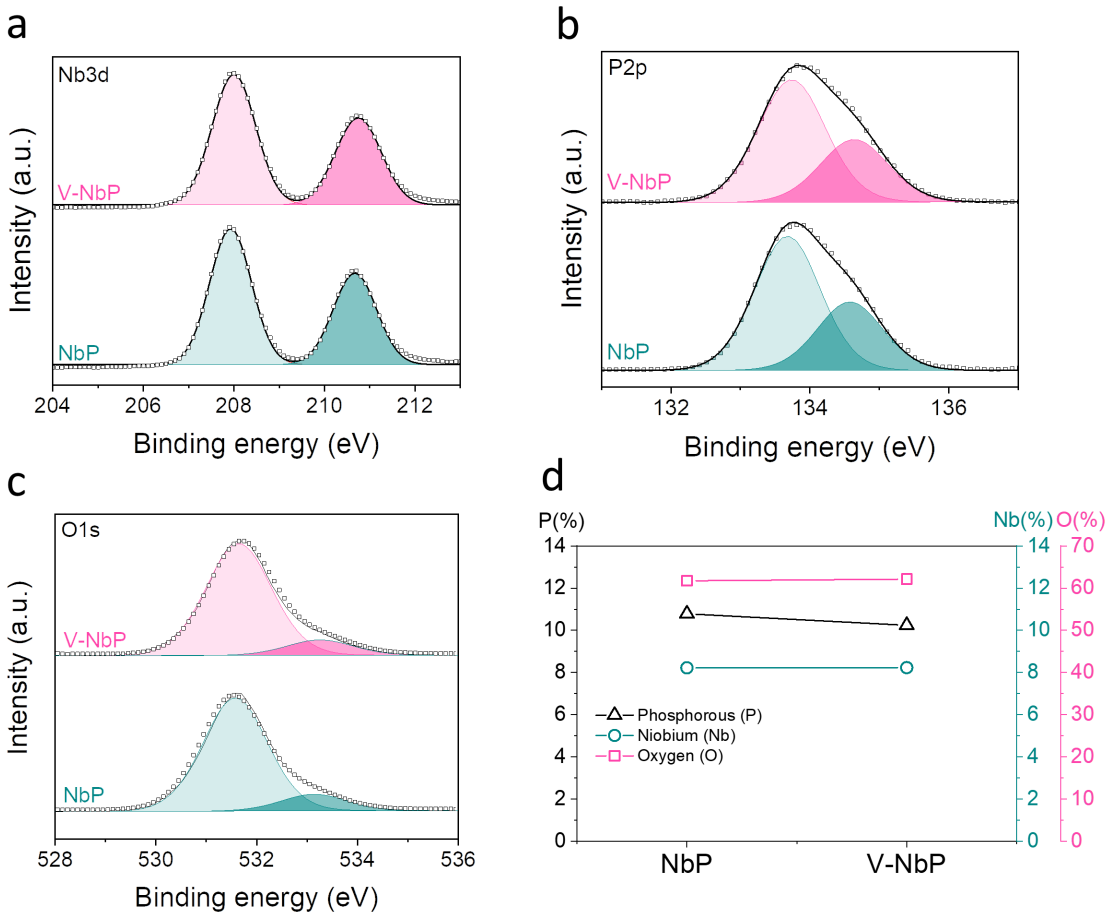

Figure S2.4. *XPS analysis of NbP and V-NbP. (a) The Nb 3d spectra, (b) P 2p spectra, (c) O 1s spectra, and (d) the atomic contents of Nb, P and O for NbP and V-NbP. Nb^{5+}: Nb $3d_{5/2}$: 207 eV; Nb $3d_{3/2}$: 210 eV [327]. Phosphate: P $2p_{3/2}$: 133 eV; P $2p_{1/2}$: 134 eV; O1s: 533 eV [243]. The NbO_6: O1s: 531 eV [243]. It is seen that the P atomic percentage remarkably decreased after acid etching while the Nb atomic percentage remained constant, mainly due to the weaker strength of the P-O bond compared with the Nb-O bond.*

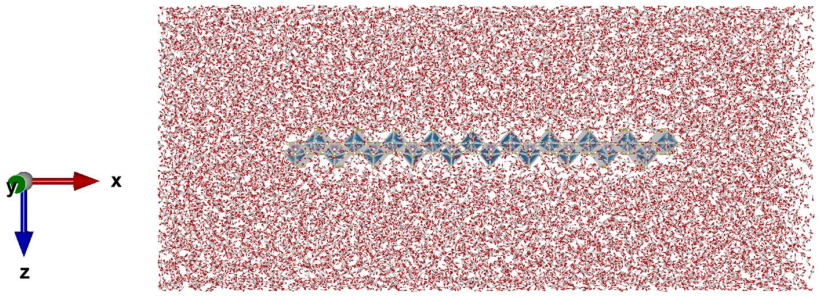

Figure S2.5. *MD simulation model for water adsorption analysis where a single NbP or V-NbP nanosheet was surrounded by water molecules.*

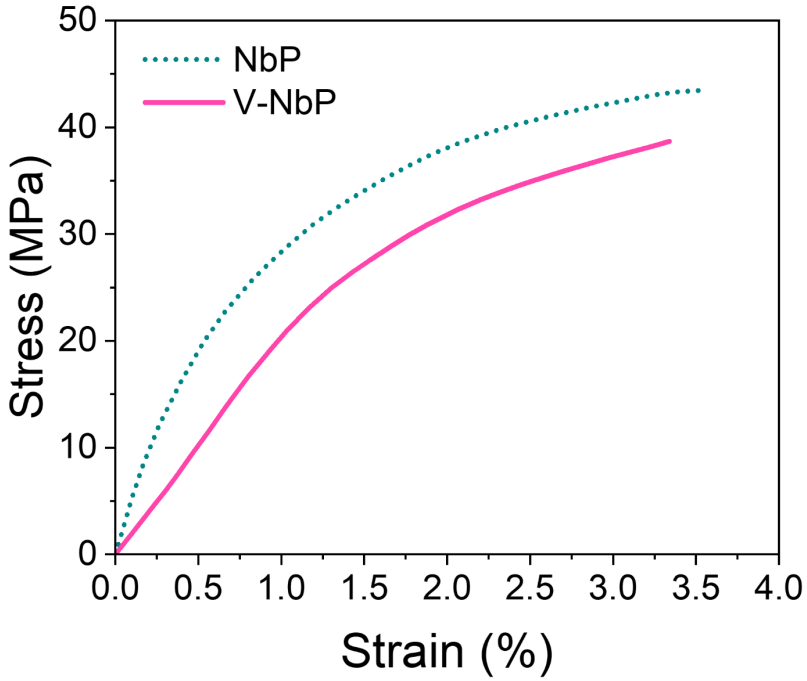

Figure S2.6. *Mechanical strength of NbP and V-NbP membranes. Both NbP and V-NbP showed high mechanical strength of ~43 MPa and ~39 MPa, respectively.*

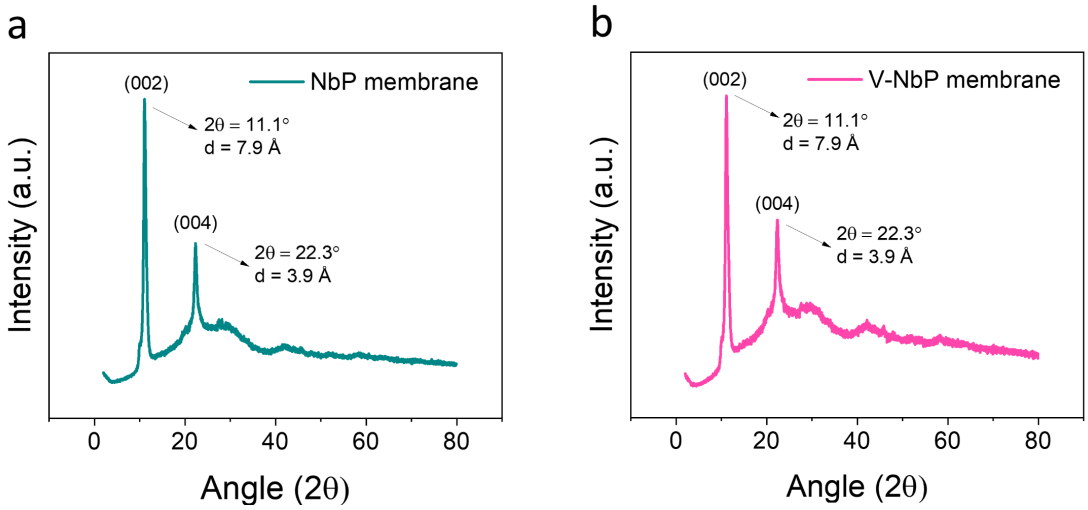

Figure S2.7. *XRD of (a) NbP and (b) V-NbP membranes showing their interlayer spacings. Both NbP and V-NbP membranes exhibited analogous interlayer spacings of ~8 Å.*

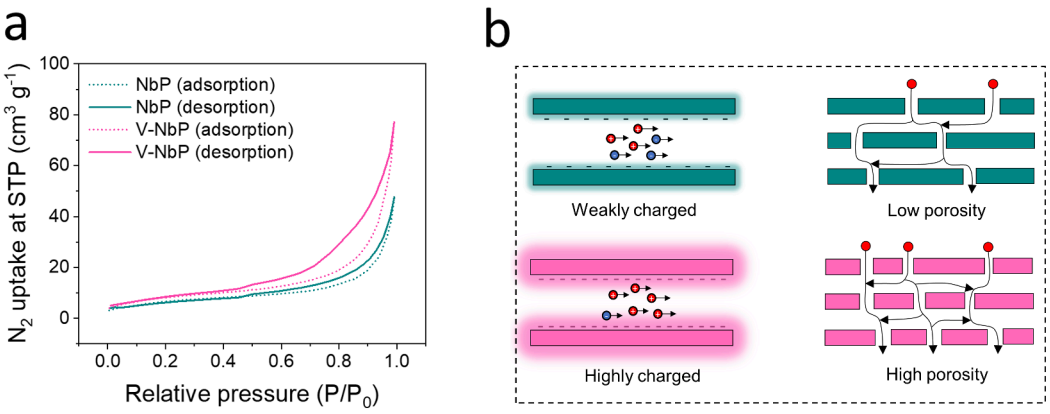

Figure S2.8. *(a) N_2 adsorption/desorption of NbP and V-NbP membrane. (b) Schematic illustrations of the ion transport through the NbP (upper panels) and V-NbP (lower panels) membranes.*

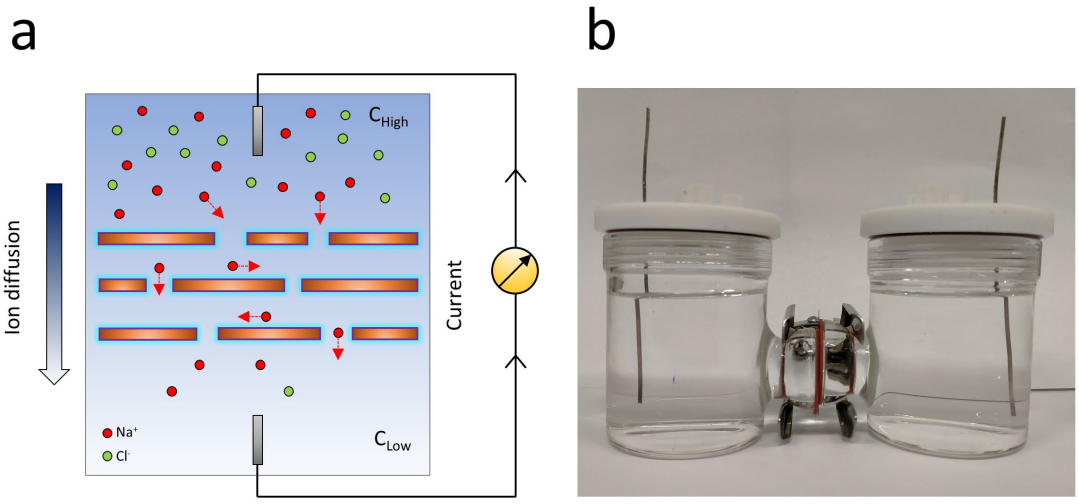

Figure S2.9. *(a) Schematic of the electrochemical setup used to measure ion transport. (b) Configuration of the H-type cell used to the measure the ionic transport.*

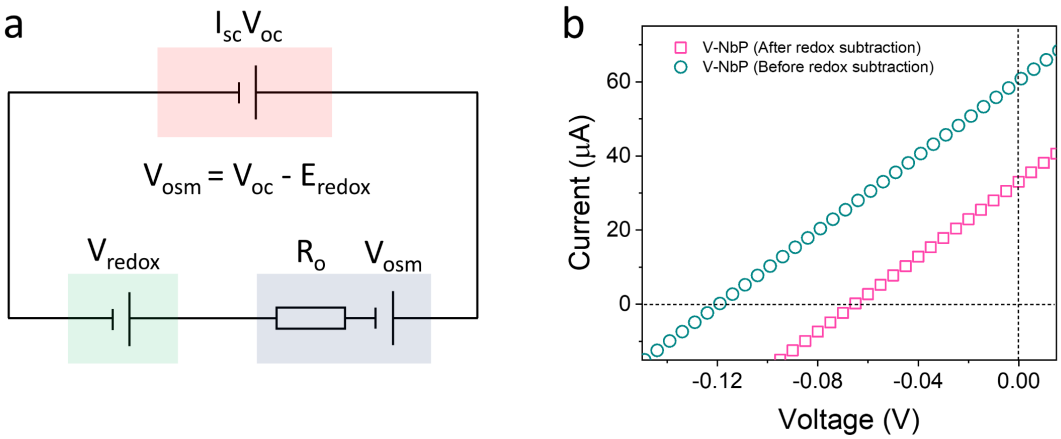

Figure S2.10. *(a) Equivalent circuit diagram of the power source. (b) I-V curves of the V-NbP membrane under a concentration gradient of 1.0 M | 0.01 M NaCl, before and after subtracting the contribution of redox potential.*

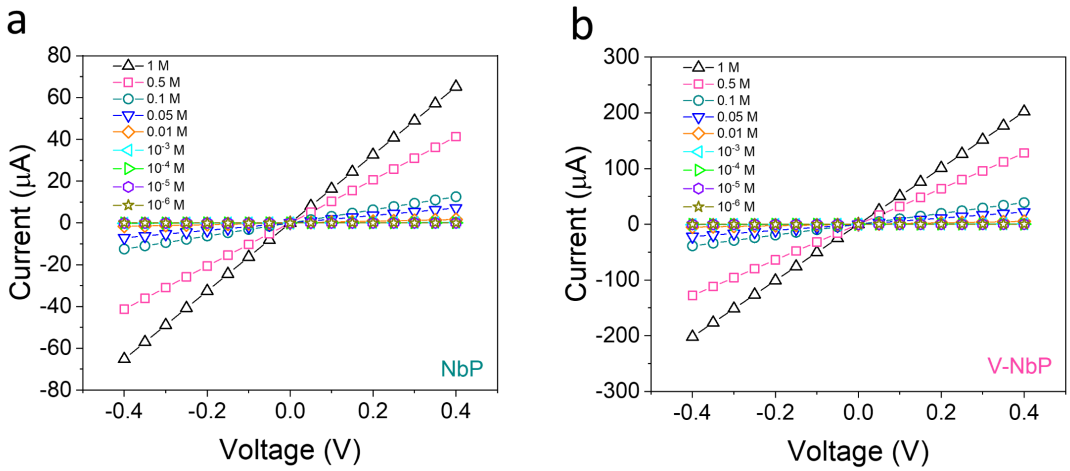

Figure S2.11. *I-V curves of (a) NbP and (b) V-NbP membranes recorded under a range of NaCl concentrations. The concentration on the high side was varied from 1 M to 10^{-6} M. The concentration at the low side was set to be deionized water.*

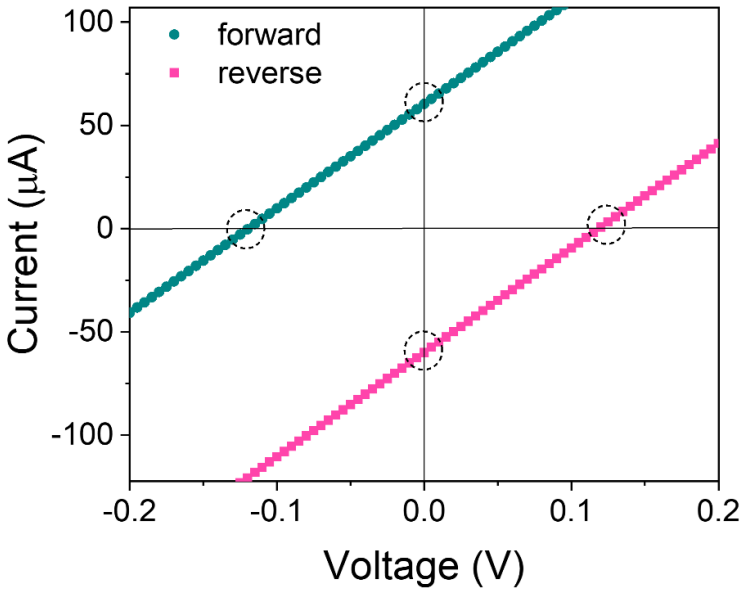

Figure S2.12. *I-V curves of V-NbP recorded at a concentration gradient of 1.0 M | 0.01 M NaCl, under forward and reverse diffusion directions.*

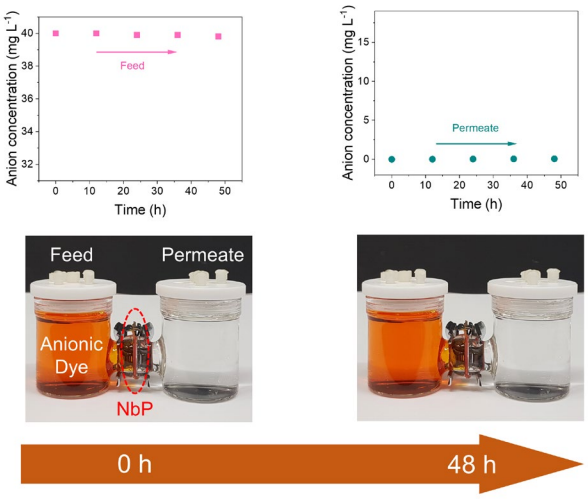

Figure S2.13. *Visual demonstration of anionic dye diffusion through NbP membrane after 48 h at room temperature, and the corresponding concentration changes of anionic dye in each chamber of the H-shaped cell along with aging time.*

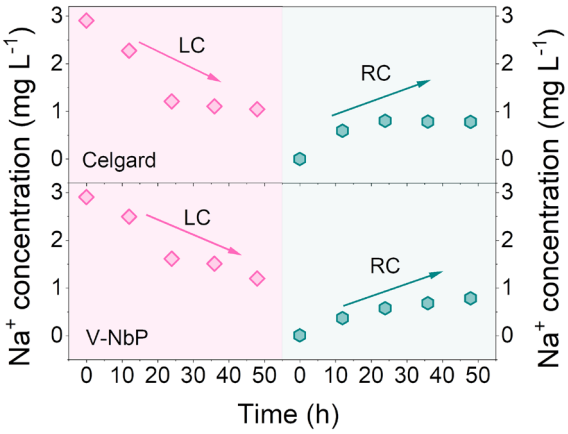

Figure S2.14. *Concentration changes of a Na^+ in each chamber of the H-shaped cell filled with methyl orange (40 mg L^{-1}) in the LC and deionized water in the RC along with aging time.*

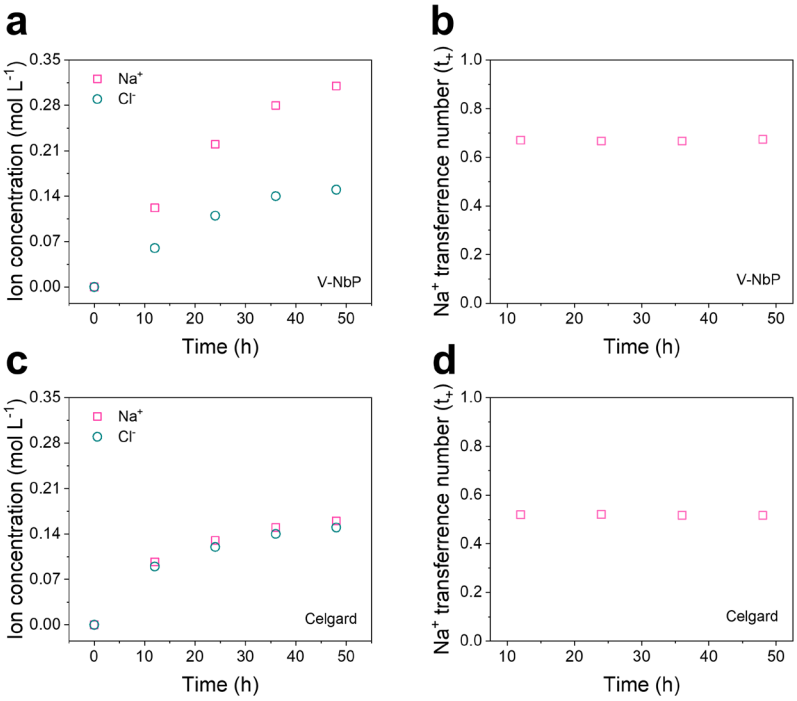

Figure S2.15. *NaCl permeation test in an 0.5 M NaCl | distilled water H-cell configuration. (a) The Na^+ concentration in the right chamber (RC, distilled water side) of H-shaped cell with V-NbP membrane and (b) the corresponding Na^+ transference number; (c) The Na^+ concentration in RC of H-shaped cell with Celgard membrane and (d) the corresponding Na^+ transference number.*

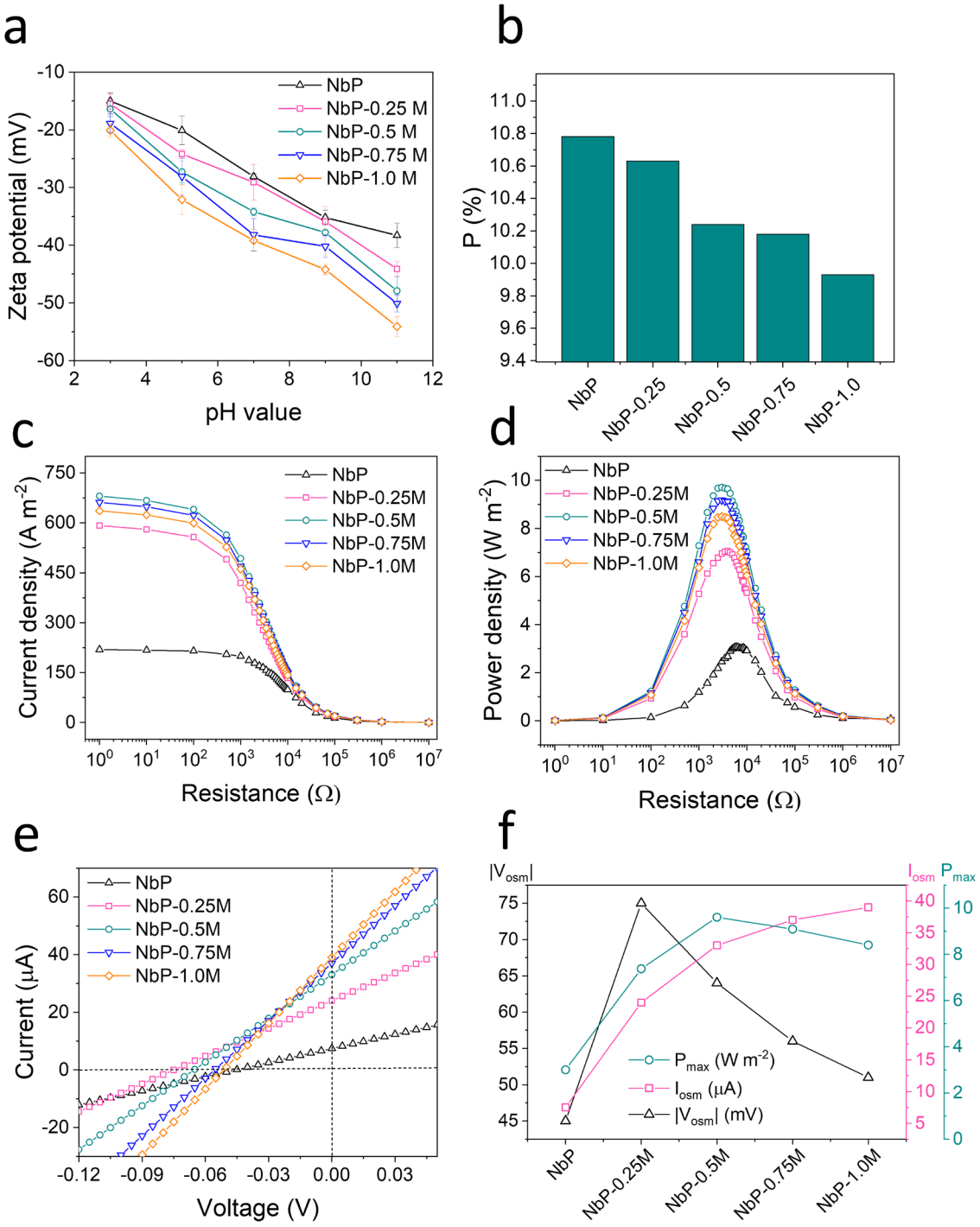

Figure S2.16. *Influence of acid etching concentrations on the performance. (a) Zeta potential at different pH values, (b) XPS of P atoms, (c) current density, (d) power density, (e) I-V curves, and (f) comparison of $|V_{osm}|$, I_{osm} and P_{max}. The current density and I-V curves were measured at concentration gradients of 0.5 M | 0.01 M NaCl and 1.0 M | 0.01 M NaCl, respectively.*

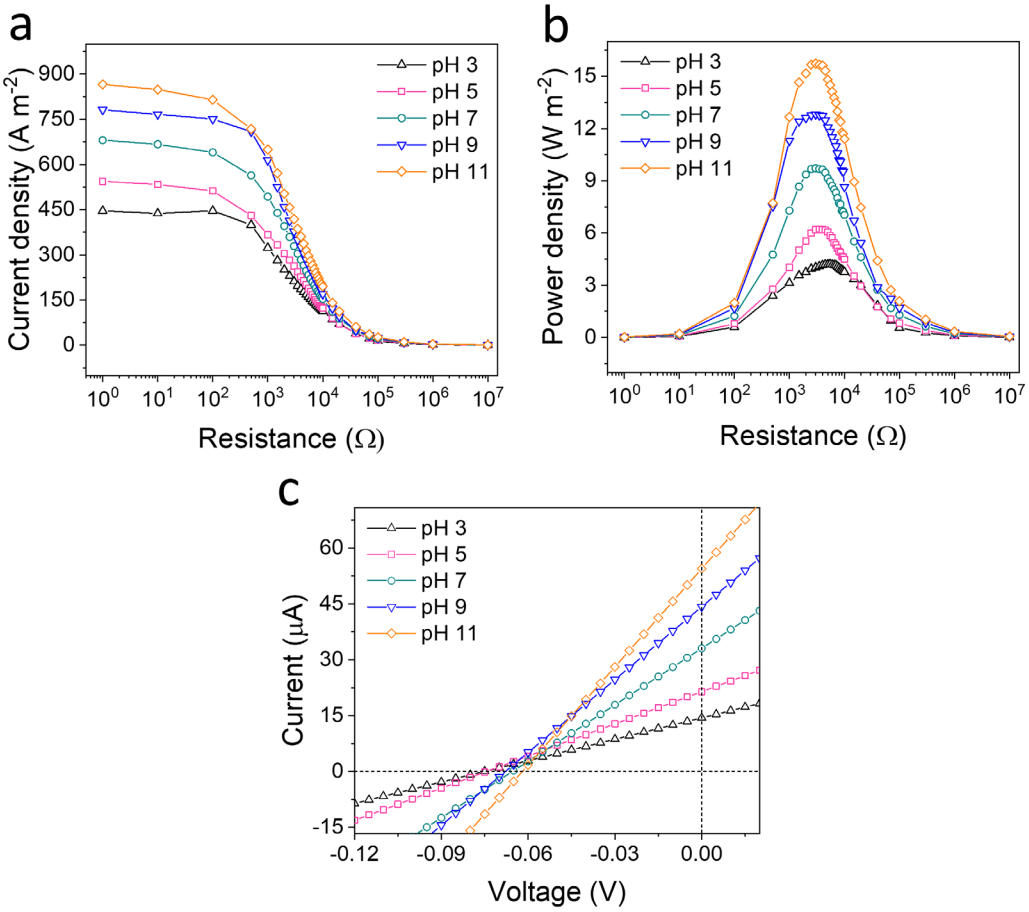

Figure S2.17. *(a) Current density, (b) power density, and (c) I-V curves of V-NbP membrane in aqueous solutions with different pH values. The current density and I-V curves were measured at concentration gradients of 0.5 M | 0.01 M NaCl and 1.0 M | 0.01 M NaCl, respectively.*

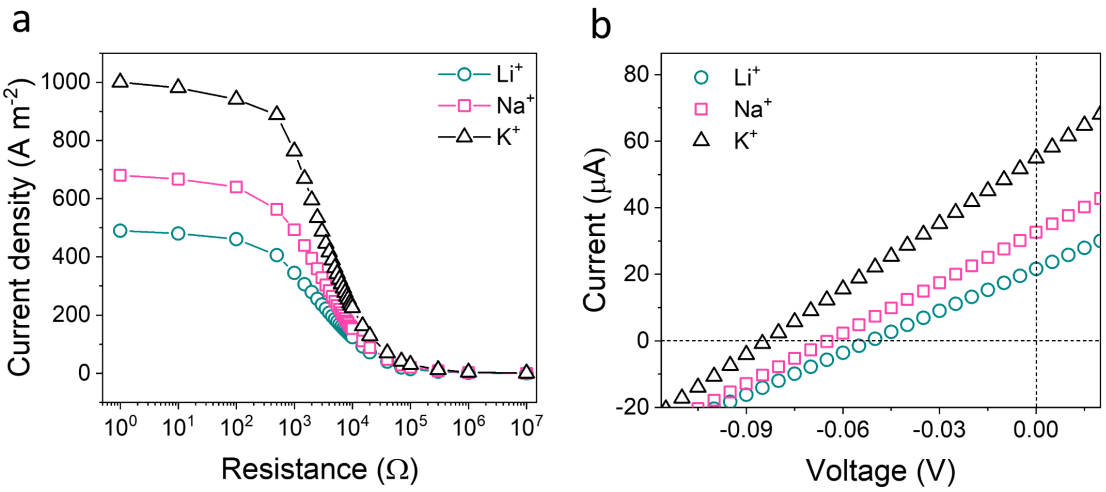

Figure S2.18. *(a) Power density profiles and (b) I-V curves of V-NbP membrane for electrolytes with different cations. The current density and I-V curves were measured at concentration gradients of 0.5 M | 0.01 M NaCl and 1.0 M | 0.01 M NaCl, respectively.*

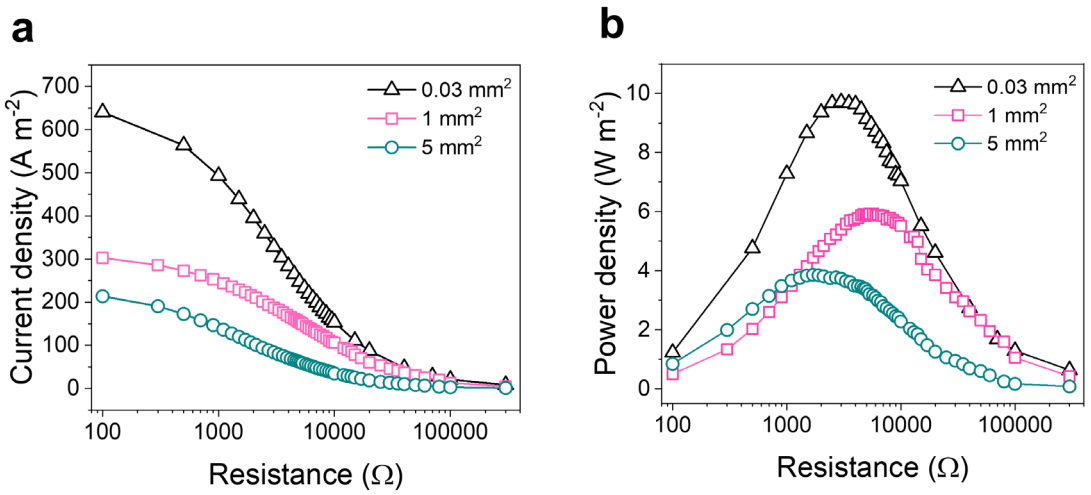

Figure S2.19. *The (a) current density and (b) power density profiles of V-NbP membrane under different membrane testing areas.*

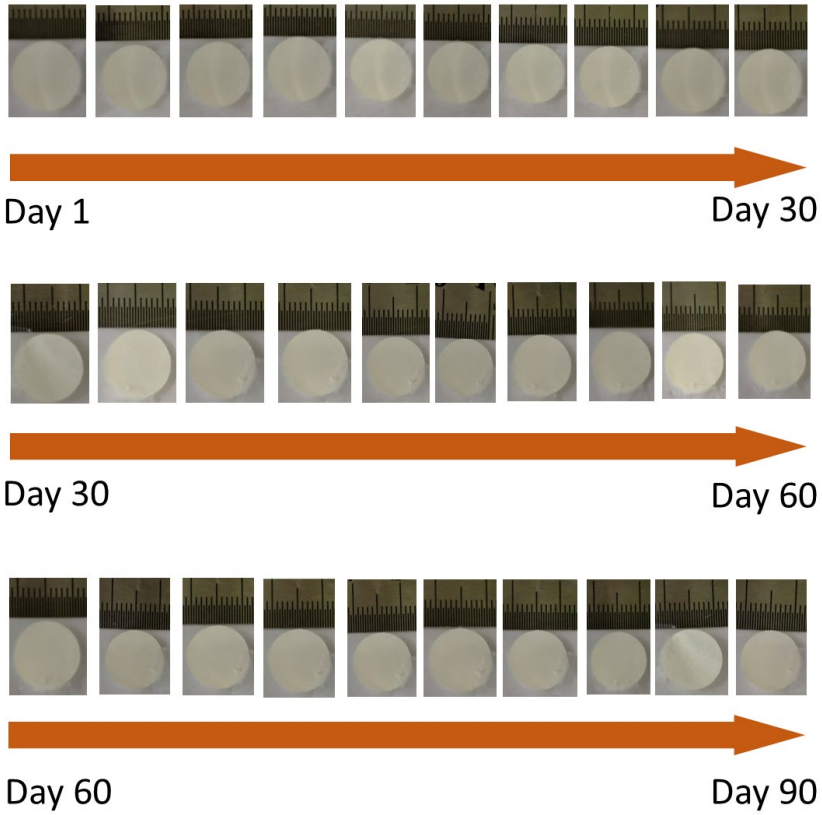

Figure S2.20. *Stability of V-NbP membrane in water. The images were taken every 3 days.*

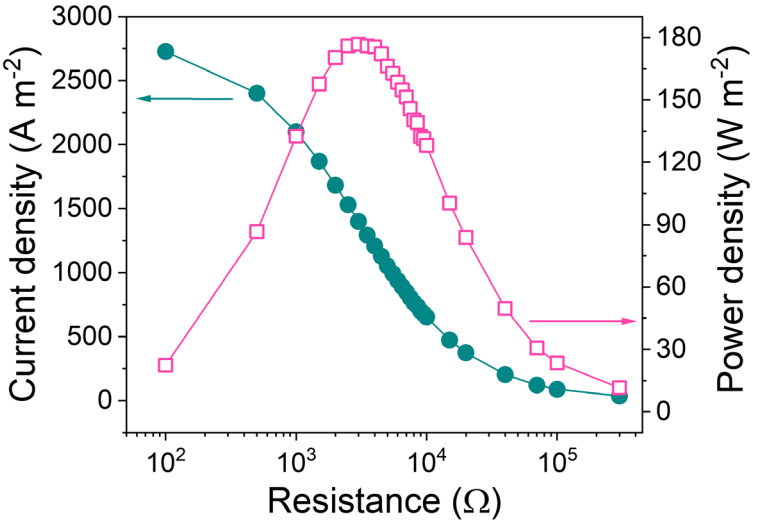

Figure S2.21. *The current density and power density profiles of the tandem device, consisting of 20 units of V-NbP membranes.*

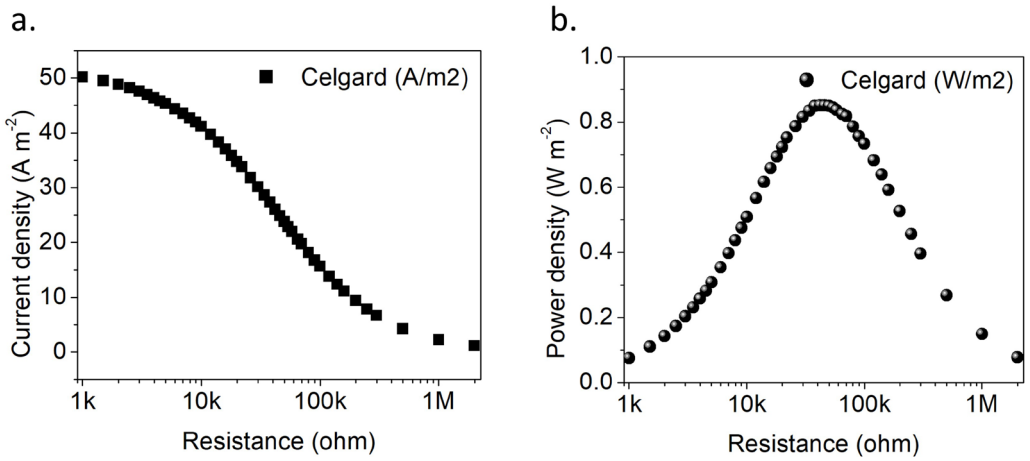

Figure S2.22. *The current density (a) and power density (b) profiles of the celgard membrane under 0.5M / 0.01 M NaCl solution.*

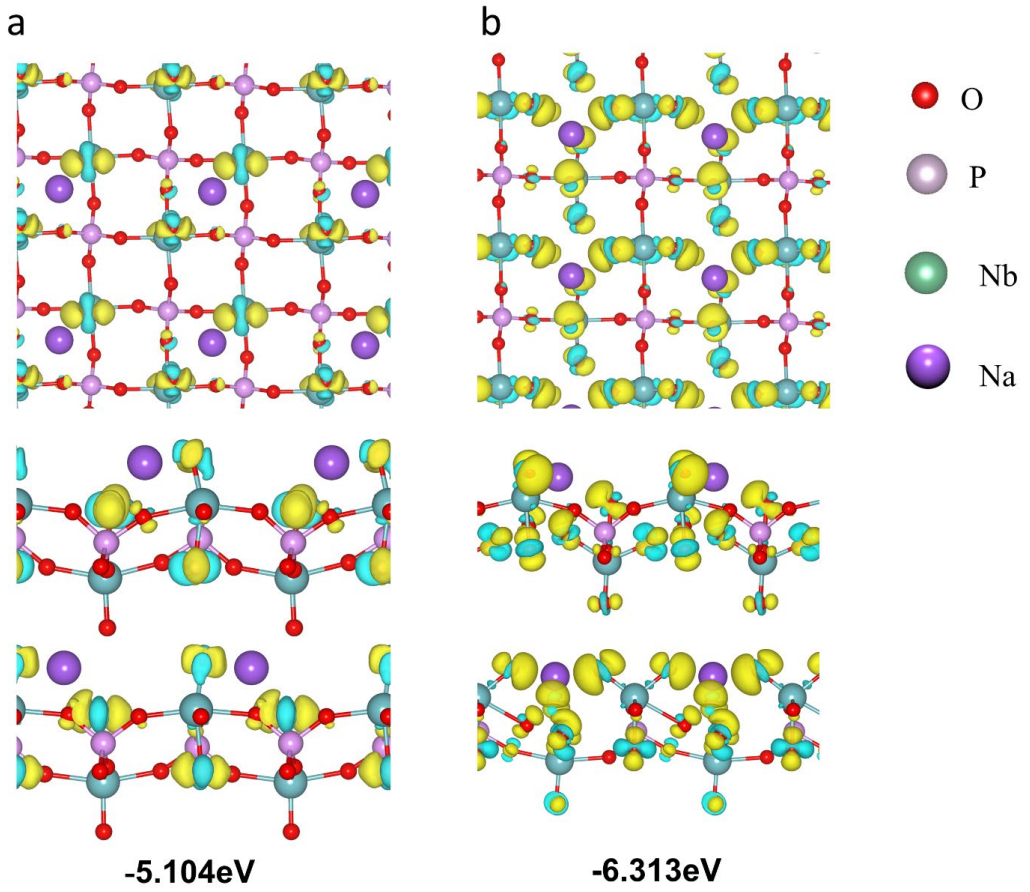

Figure S2.23. *DFT calculations to simulate the adsorption of Na^+ ions on the surface of (a) NbP and (b) V-NbP nanosheets. Atom colors: Purple (sodium), green (niobium), pink (phosphorus), red (oxygen). The binding energy of sodium ion on the surface of NbP and V-NbP nanosheets are presented in unit eV.*

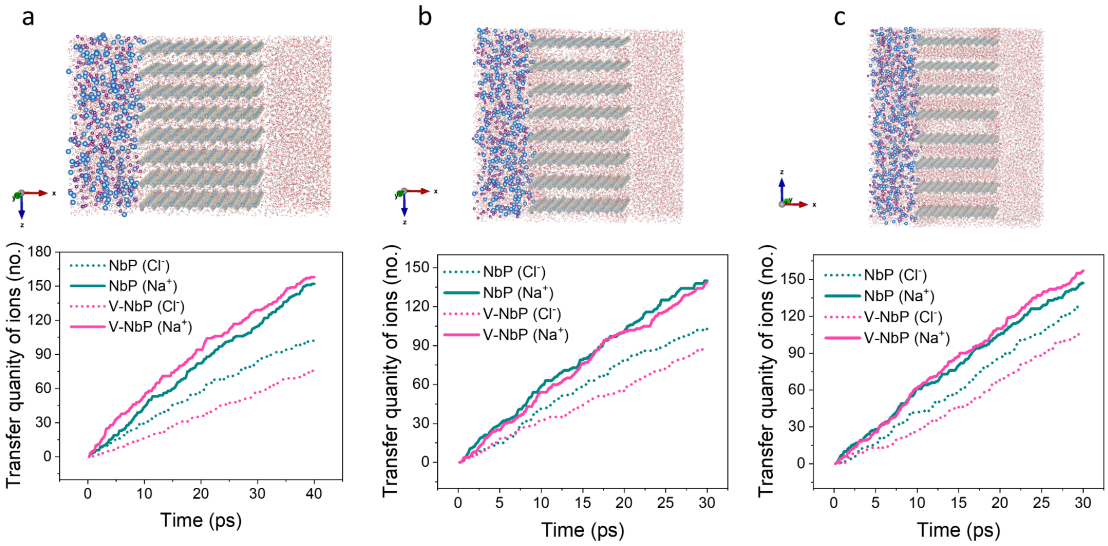

Figure S2.24. *MD simulation models and the corresponding transfer quantities of ions plotted vs. time for NbP and V-NbP nanosheets with interlayer spacing values of (a) 12 Å, (b) 16 Å, and (c) 20 Å.*

Table S2.1. *Performance comparison of the V-NbP membrane in this work with reported macroscopic-scale 2D nanofluidic membranes.*

Membrane	Thickness	Power density (W m^{-2})	Test conditions	Ref.
Kaolinite nanoclays	25 μm	0.18	100-fold KCl	[143]
Montmorillonite nanoclays	11.2 μm	0.18	1000-fold KCl	[144]
Carbon nitride	250 nm	0.21	0.1mM | 0.1M KCl	[145]
Graphene oxide membrane-pairs	10 μm	0.77	0.5 M | 0.01 M NaCl	[147]
MXene membrane-pairs	~	4.6	0.5 M | 0.01 M NaCl	[148]
Graphene (pore size = 5 nm)	~	1.15	1 M | 10^{-6} M NaCl	[156]
Vermiculite (pore size = 20 nm)	2.1 μm	4.1	0.5 M | 0.01 M NaCl	[157]
MXene (pore size = 5-15 nm)	0.6 μm	17.5	100-fold KCl	[154]
Covalent organic framework/Kevlar nanofibers	7.2 μm	8.7	0.5 M | 0.01 M NaCl	[163]
MoS_2 (metallic) /cellulose nanofiber	4.0 μm	5.2	0.5 M | 0.01 M NaCl	[164]
MXene/Kevlar nanofibers	2.0 μm	3.92	0.5 M | 0.01 M NaCl	[165]
Graphene oxide/Cellulose nanofiber	9.0 μm	4.19	0.5 M | 0.01 M NaCl	[166]
Graphene oxide/Silk nanofiber	5.0 μm	5.07	0.5 M | 0.01 M NaCl	[167]
Boron nitride/ Kevlar nanofiber	1.0 μm	0.6	0.5 M | 0.01 M NaCl	[168]
MXene/boron nitride	10.0 μm	2.3	0.5 M | 0.01 M NaCl	[177]
Black phosphorus /Graphene oxide	8.0 μm	3.4	0.5 M | 0.01 M NaCl	[178]
V-NbP	**7.4 μm**	**10.7**	**Natural seawater | river water**	**This work**
V-NbP	**7.4 μm**	**21.5**	**0.5 M | 0.01 M KCl**	**This work**

Appendix 3- Supporting Information for Self-Assembled NbOPO4 Nanosheet/Reduced Graphene Oxide Heterostructure for Capacitive Desalination

Note S3.1. Hypothetical Area matching model

The $NbOPO_4$ and rGO were restacked face-to-face to develop $NbOPO_4$/rGO heterostructure. The mass ratio of rGO and $NbOPO_4$ could be calculated based on a hypothetical area-matching model. The in-plane structure of $NbOPO_4$ with a rectangular unit cell a_{NbOPO4} = 0.6485 nm and b_{NbOPO4} = 0.6415 nm is shown in Figure S3.5 a. The model of rGO was assumed to be similar to the graphene, and the in-plane structure of graphene with a rectangular unit cell a_{rGO}= 0.4287 nm and b_{rGO}= 0.2463 nm is shown in Figure S3.5 b. The 2D weight density of rGO was found according to Equation (1), and the 2D weight density of $NbOPO_4$ monolayer was found according to Equation (2) [298, 307].

$$W(rGO) = \frac{4M(rGO)}{(a_{rGO} \times b_{rGO} \times N_A)} \quad (1)$$

$$W(NbOPO_4) = \frac{2M(NbOPO_4)}{(a_{NbOPO_4} \times b_{NbOPO_4} \times N_A)} \quad (2)$$

where N_A is the Avogadro's number and $M(rGO)$ = 12.0 g mol^{-1} and $M(NbOPO_4)$ = 203.875 g mol^{-1}, are the formula weights of rGO and $NbOPO_4$, respectively. The mass ratio of $NbOPO_4$ monolayer to rGO under the area balance 1:1 is found to be 2.15, as shown:

$$\frac{m(NbOPO_4)}{m(rGO)} = \frac{W(NbOPO_4)}{W(rGO)} = \frac{2M(NbOPO_4) \times (a_{rGO} \times b_{rGO} \times N_A)}{4M(rGO) \times (a_{NbOPO_4} \times b_{NbOPO_4} \times N_A)} = 2.15$$

The exfoliated $NbOPO_4$ nanosheets had a thickness of ~6.0 nm (Figure S3.1), corresponding to seven $NbOPO_4$ monolayers. Accordingly, the mass ratio between $NbOPO_4$ nanosheets and rGO could be estimated to be 7 * 2.15 = 15.05. The mass ratio of rGO to $NbOPO_4$ is found to be $\frac{1}{15.05} \times 100 = 6.6 \ wt\%$. This value closely matches the calculated mass percentage of rGO using TGA results (6.7 wt%), as observed in Figure S3.6.

Note S3.2. Specific capacitance and Desalination Capacity calculations

The specific capacitance was calculated according to Equation (3):

$$C = \frac{\int IdV}{2v\Delta Vm} \quad (3)$$

where C (F g^{-1}) is the specific capacitance, I (A) is the current, ΔV (V) is the potential window, v (V s^{-1}) is the scan rate, and m (g) is total mass loading of the active materials.

The salt adsorption capacity (SAC, mg g^{-1}) and mean desalination rate (MDR, mg g^{-1} min^{-1}) was calculated based on Equation (4) and Equation (5), respectively:

$$SAC = \frac{(C_i - C_f) \times V}{m} \quad (4)$$

$$MDR = \frac{SAC}{t} \quad (5)$$

where C_i and C_f (mg L^{-1}) are the initial and equilibrium concentration of NaCl solution, respectively. V (L) is the volume of the NaCl solution in the CDI cell, m (g) is the mass loading of the active material, and t is the desalination time (min).

Note S3.3. Surface area and pore distribution analysis

The microstructure and specific surface area were further investigated by N_2 adsorption/desorption measurements. As shown in Figure S3.10 a-c, standard type-IV behavior was observed for $NbOPO_4$, $NbOPO_4$-rGO, and $NbOPO_4$/rGO heterostructure. Based on the BET method, the pristine $NbOPO_4$ had a surface area of 27.63 m^2 g^{-1} and a pore volume of 0.08 cm^3 g^{-1}. $NbOPO_4$/rGO heterostructure had a surface area of 49.71 m^2 g^{-1} and a pore volume of 0.209 cm^3 g^{-1}. The $NbOPO_4$-rGO demonstrated a BET surface area of 45.28 m^2 g^{-1} and a pore volume of 0.182 cm^3 g^{-1} that is lower than the $NbOPO_4$/rGO heterostructure. The increase of surface area and pore volume for $NbOPO_4$/rGO heterostructure is because rGO can prevent the restacking of $NbOPO_4$, allowing for more surface area in the heterostructure. This phenomenon is elucidated in previous publications [295, 296].

The pore size distribution for $NbOPO_4$ and $NbOPO_4$/rGO heterostructure was calculated according to the BJH method and plotted in Figure S3.10 d-f. The $NbOPO_4$ showed pore sizes of 3.81 nm. This is ascribed to the spaces/channels formed between the nanosheets when they are restacked on each other. The pore size distribution for $NbOPO_4$/rGO heterostructure shows reduced pore sizes of 2.55 nm. This could be due to the rGO wrapping around $NbOPO_4$, which covers the pristine ~3.81 nm pores and develops smaller pores. Additionally, $NbOPO_4$-rGO shows a pore size of 2.76 nm, which is larger compared with $NbOPO_4$/rGO heterostructure. This is due to the inefficient coupling of rGO and $NbOPO_4$ in $NbOPO_4$-rGO, which results in the pore size of $NbOPO_4$-rGO being smaller than pristine $NbOPO_4$ but larger than $NbOPO_4$/rGO heterostructure.

Note S3.4. CDI Ragone plot

The CDI Ragone plot shifts to the upper and more right region that suggest a higher desalination capacity and mean desalination rate (MDR) with the increasing order for $NbOPO_4$ < $NbOPO_4$-rGO < $NbOPO_4$/rGO heterostructure (Figure S3.14 a). Figure S3.14 b shows that the MDR keeps increasing linearly up to 7.5 minutes, reaching its maximum value for all electrode materials. For the three electrodes, the maximum MDR occurs at 7.5 minutes with the value of 4.37 mg g^{-1} min^{-1}, 2.13 mg g^{-1} $min^{-1,}$ and 1.26 mg g^{-1} min^{-1} for $NbOPO_4$/rGO heterostructure, $NbOPO_4$-rGO, and $NbOPO_4$, respectively. The linear increase of MDR could be related to the gradual increase of Na^+ diffusion throughout the desalination process, which gradually increases the MDR. This phenomenon has also been observed in previous papers [287].

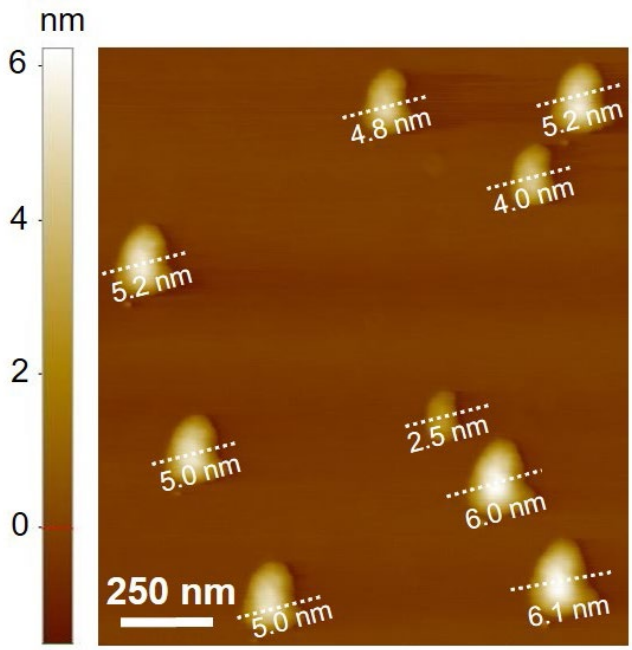

Figure S3.1. *The AFM of $NbOPO_4$ nanosheets. The height of the $NbOPO_4$ nanosheets is marked in this figure.*

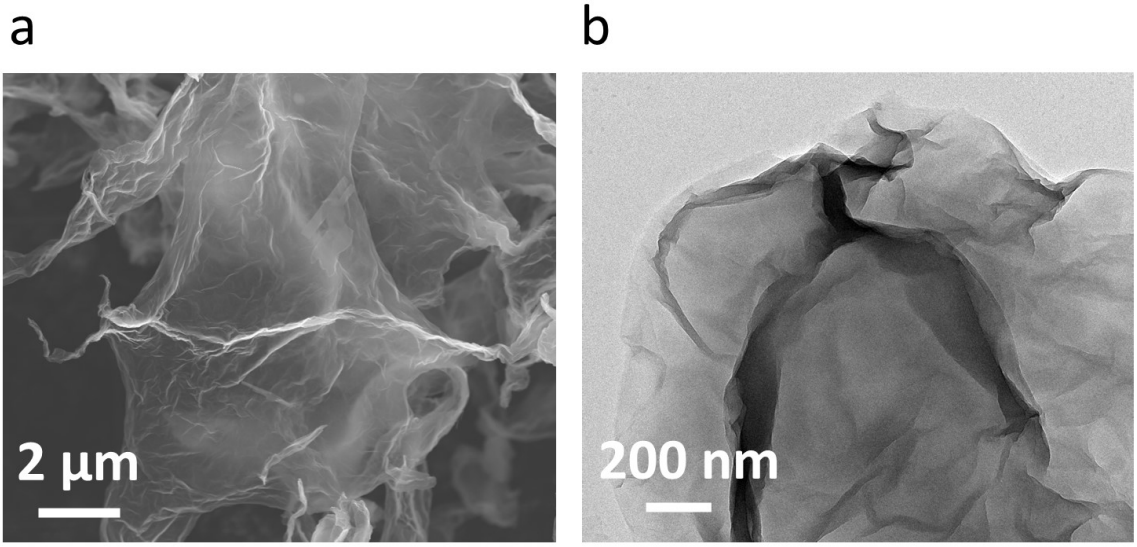

Figure S3.2. *(a) The SEM and (b) TEM of PDDA-rGO nanosheets.*

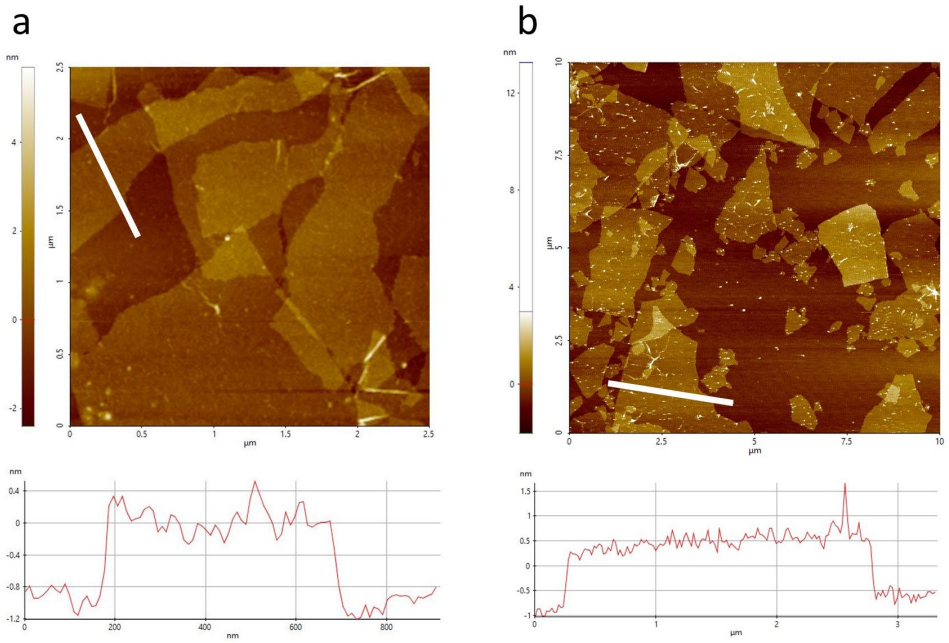

Figure S3.3. *The AFM of (a) rGO and (b) PDDA-rGO nanosheets. The rGO shows a thickness of 0.8 nm, and the PDDA-rGO shows an increased thickness of 1.5 nm.*

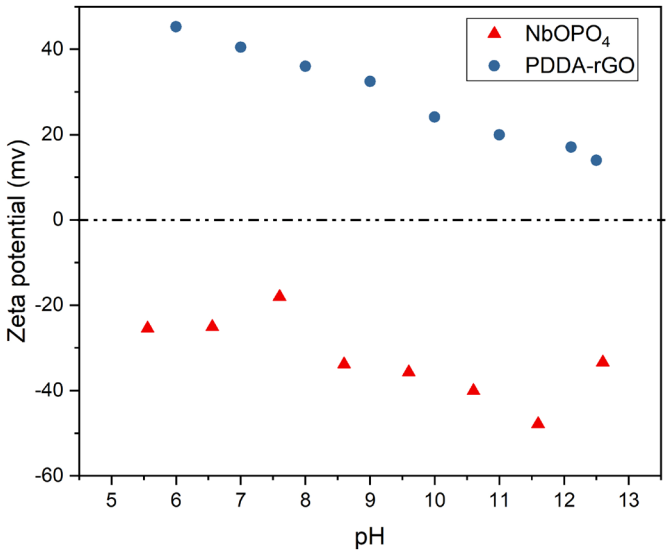

Figure S3.4. *The measurement of Zeta potential at different pH ranges for $NbOPO_4$ and PDDA-rGO.*

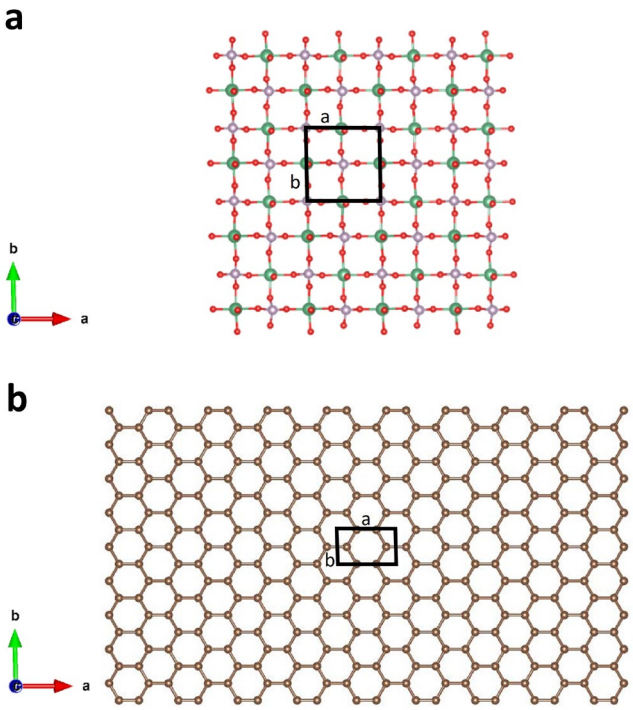

Figure S3.5. *(a) The model of $NbOPO_4$, and (b) graphene that is used for the calculation of $NbOPO_4$/rGO heterostructure mass ratio via hypothetical area matching model. The calculation details are shown in Note S1.*

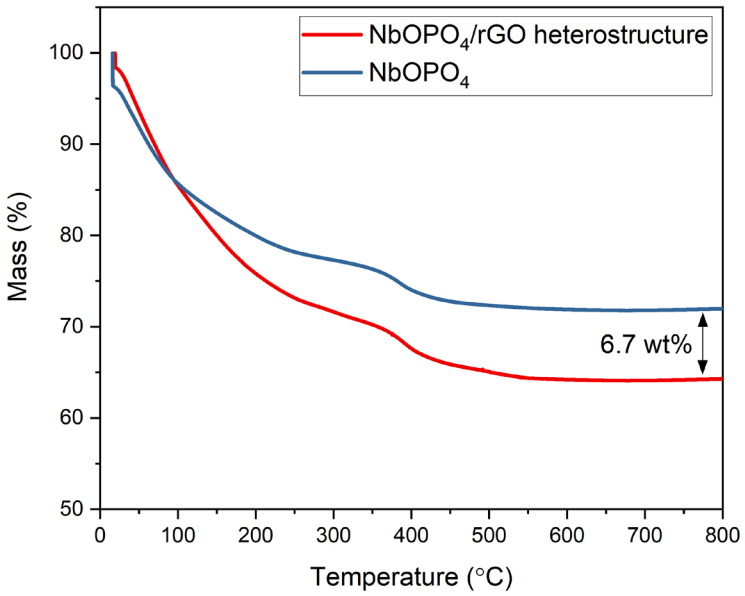

Figure S3.6. *The TGA analysis of $NbOPO_4$/rGO heterostructure and the restacked $NbOPO_4$ nanosheets. The weight loss of the pristine $NbOPO_4$ nanosheets is 71.4%, attributed to the removal of isopropanol molecules trapped between the $NbOPO_4$ nanosheets. The weight loss of $NbOPO_4$/rGO heterostructure is 64.7%, corresponding to the removal of isopropanol molecules and the combustion of PDDA-rGO. Hence, the content of PDDA-rGO is determined to be 6.7 wt%.*

(a)

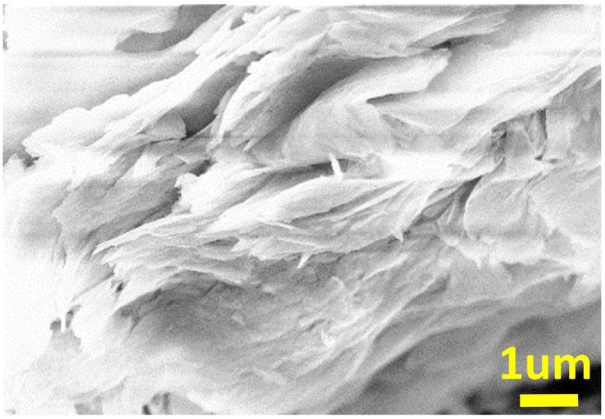

(b)

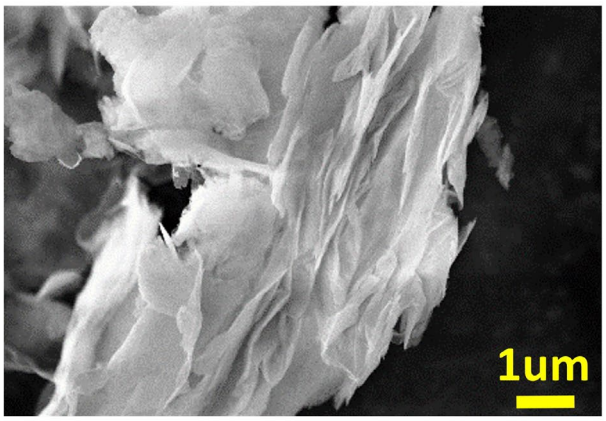

Figure S3.7. *Cross-section SEM images of $NbOPO_4$/rGO heterostructure at different angles.*

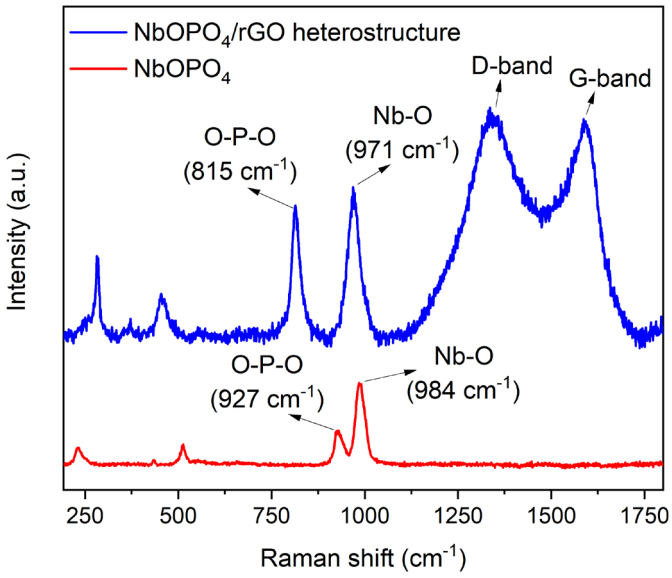

Figure S3.8. *Raman spectra of $NbOPO_4$ nanosheets and $NbOPO_4$/rGO heterostructure.*

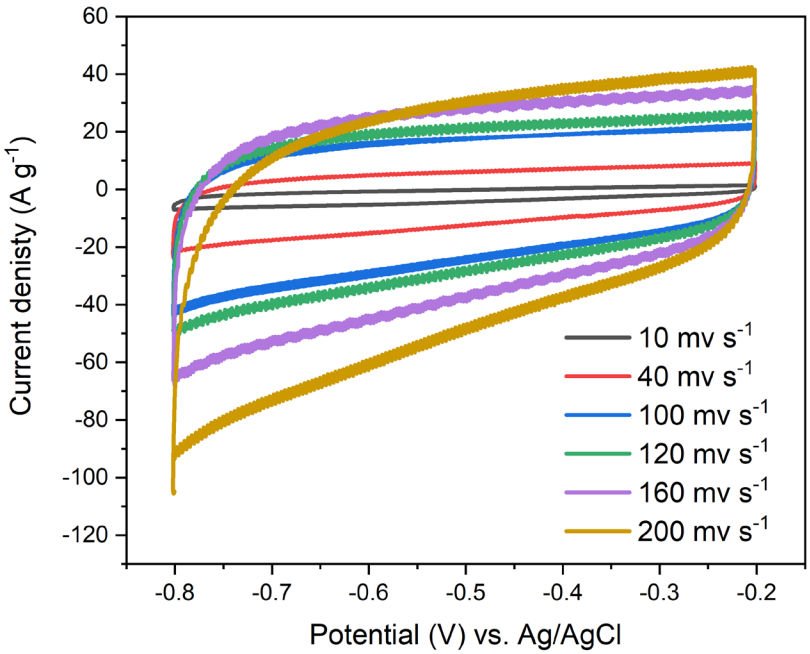

Figure S3.9. *CV curves of $NbOPO_4$/rGO heterostructure performed from 10 mV s^{-1} to 200 mV s^{-1}.* The experiment was conducted using Pt wire, Ag/AgCl and 1M NaCl as counter electrode, reference electrode and electrolyte, respectively.

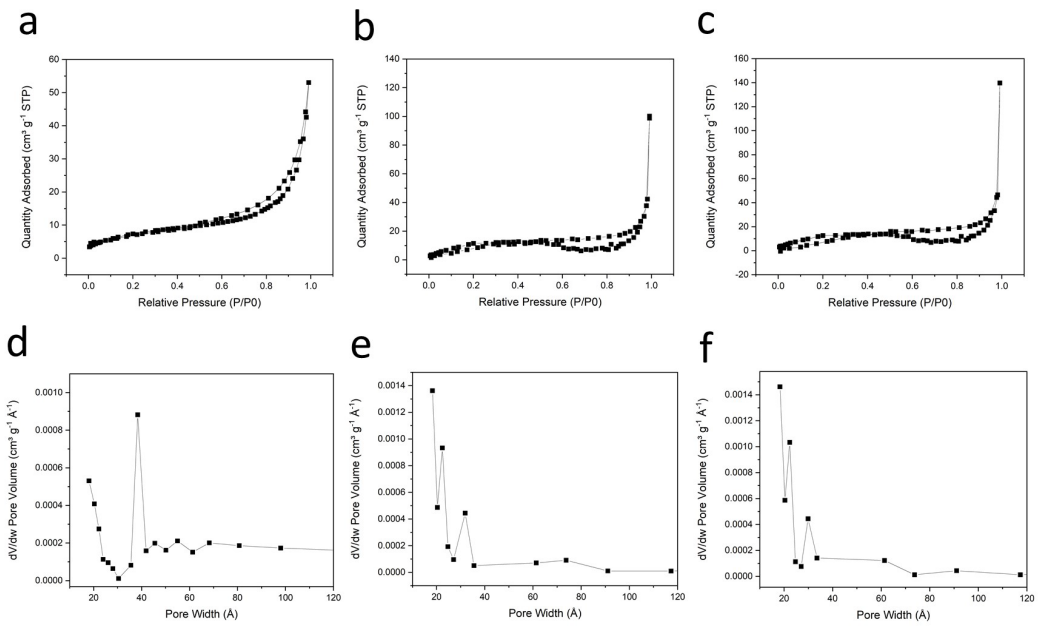

Figure S3.10. *The N_2 adsorption-desorption isotherms and pore size distribution of (a,d) $NbOPO_4$, (b,e) $NbOPO_4$-rGO and (c,f) $NbOPO_4$/rGO heterostructure.*

Table S3.1. *Surface area and porosity parameters*

	BET surface area ($m^2\ g^{-1}$)	Pore volume ($cm^3\ g^{-1}$)	Average pore diameter (nm)
$NbOPO_4$	27.63	0.08	3.81
$NbOPO_4$-rGO	45.28	0.182	2.76
$NbOPO_4$/rGO heterostructure	49.71	0.209	2.55

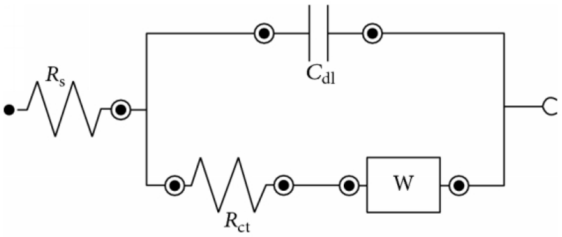

Figure S3.11. *Equivalent circuit diagram for the modelling of EIS plot.*

Table S3.2. *The EIS parameters for $NbOPO_4$, $NbOPO_4$-rGO, and $NbOPO_4$/rGO heterostructure.*

	R_s (Ω)	**R_{ct} (Ω)**	**C_{dl} (μF)**
$NbOPO_4$	3.023	2.983	31.29
$NbOPO_4$-rGO	3.87	1.118	143.5
$NbOPO_4$/rGO heterostructure	4.32	0.698	174.2

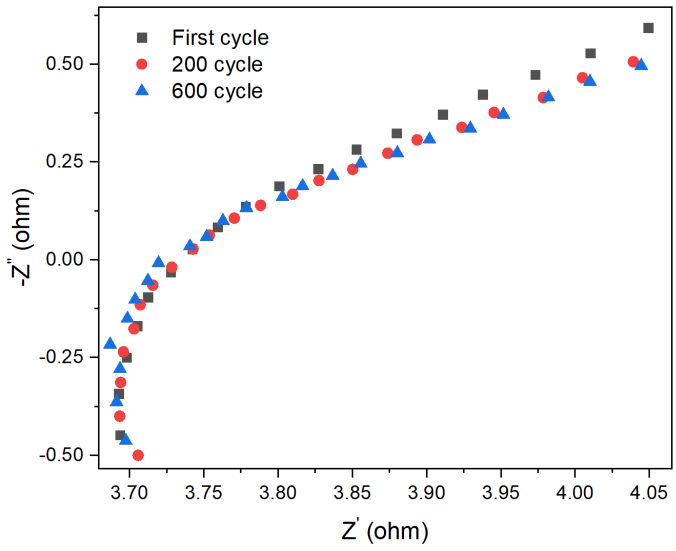

Figure S3.12. The EIS plot at the initial CV cycles, followed by 200th and 600th cycles for $NbOPO_4$/rGO heterostructure.

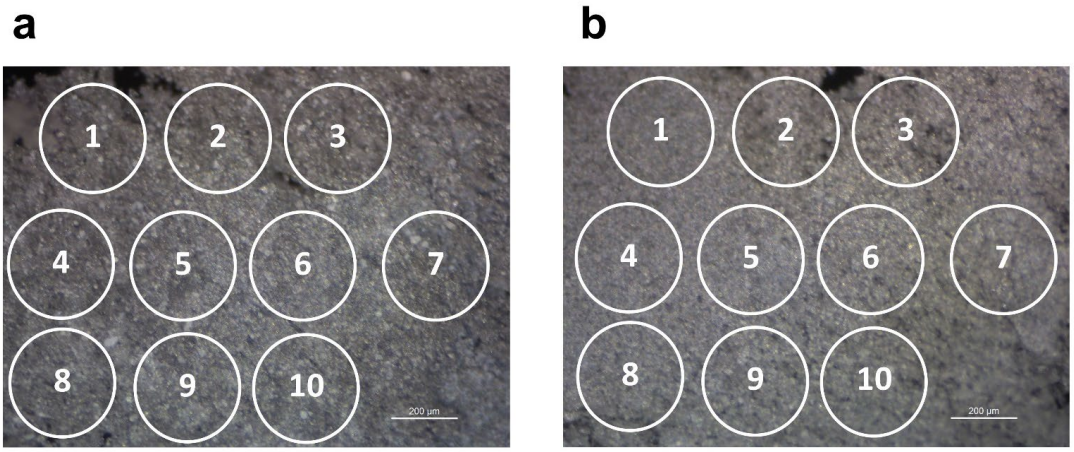

Figure S3.13. *The optical microscope image of the Raman instrument depicting: (a) $NbOPO_4$/rGO heterostructure, and (b) $NbOPO_4$-rGO. The Raman analysis was performed on ten different regions for both samples, denoted as region 1 until region 10.*

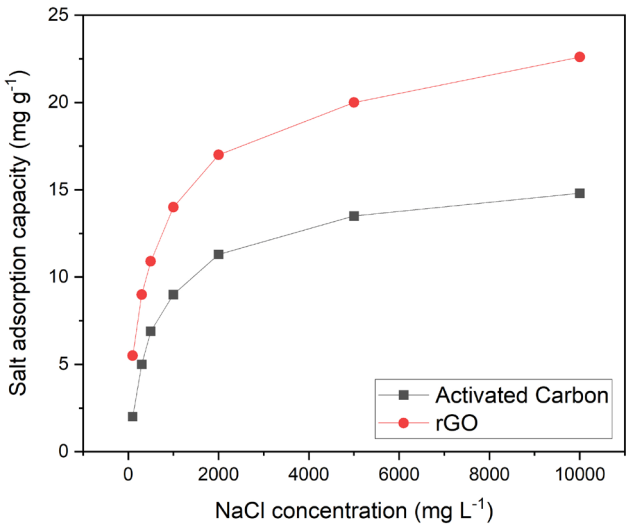

Figure S3.14. *The salt adsorption capacity of activated carbon and rGO electrodes at a range of NaCl concentrations from 100 mg L^{-1} to 10,000 mg L^{-1} at the operating voltage of 1.2 V.*

Table S3.3. *CDI Performance comparison of the current work compared with the previously reported materials.*

	Voltage (V)	NaCl concentration (mg L^{-1})	SAC (mg g^{-1})	MDR (mg g^{-1} min^{-1})	Ref.
Postively/negatively charged Carbon nanofiber	1.2	500	30.4	1.0	[287]
MOF	1.2	500	20.3	14.4	[319]
Iron-nitrogen doped carbon tubes	1.2	500	27.3	6.1	[271]
Graphene hollow shells	1.2	500	27.4	0.6	[269]

MOF/nitrogen doped carbon tubes	1.2	500	35.7	9.3	[273]
Carbon derived from Zeolitic imidazolate framework	1.2	250	14.19	4.2	[272]
Porous carbon	1.2	250	10.3	1.7	[266]
Porous carbon fibers	1.0	500	30.0	38.0	[286]
Crbon nanotube/Na doped MnO2	1.4	500	32.7	5.7	[328]
$NbOPO_4$	**1.2**	**500**	**19.7**	**1.26**	**(This work)**
$NbOPO_4$-rGO	**1.2**	**500**	**29.1**	**2.13**	**(This work)**
$NbOPO_4$/rGO heterostructure	**1.2**	**500**	**54.8**	**4.37**	**(This work)**

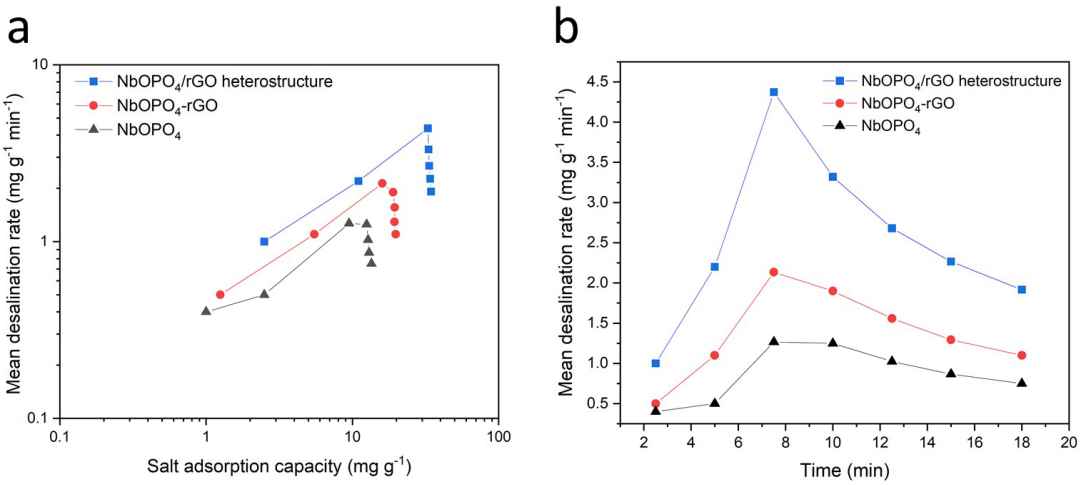

Figure S3.15. *(a) CDI Ragone plot and (b) mean desalination rate vs. time for $NbOPO_4$, $NbOPO_4$-rGO, and $NbOPO_4$/rGO heterostructure for NaCl concentration of 100 mg L^{-1} at the operating voltage of 1.2 V.*

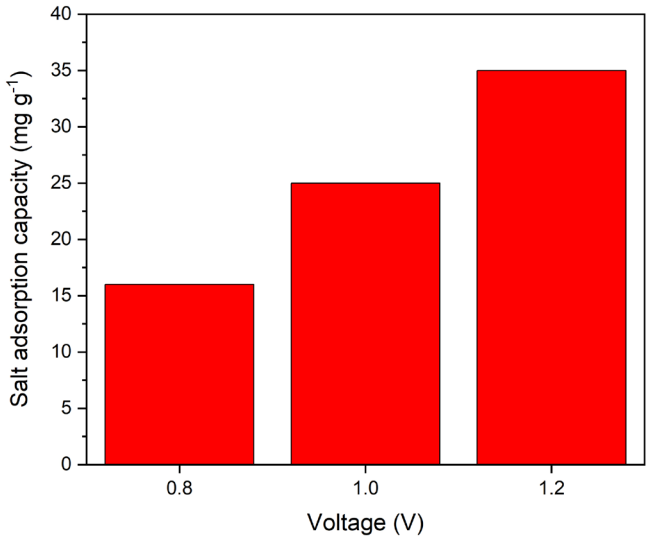

Figure S3.16. *The salt adsorption capacity of $NbOPO_4$/rGO heterostructure vs. applied voltage at NaCl concentration of 100 mg L^{-1}.*

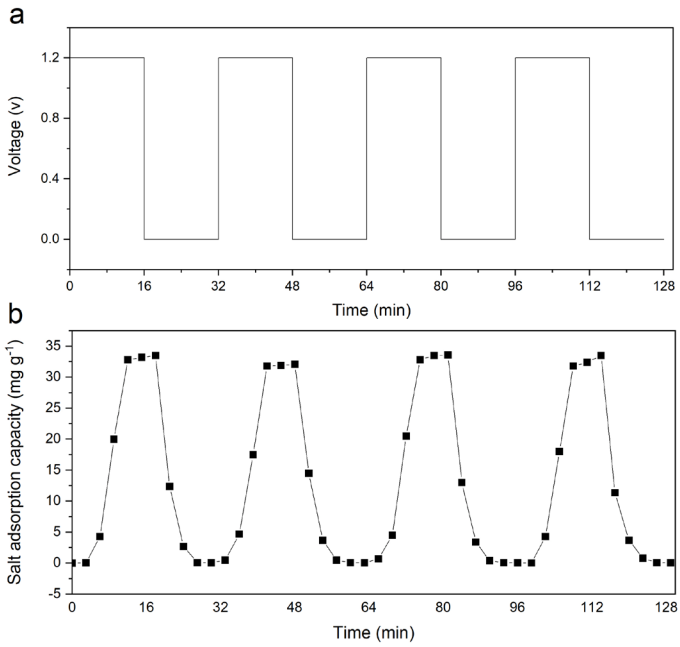

Figure S3.17. *(a) The externally applied voltage and (b) the corresponding salt adsorption/desorption cycles for $NbOPO_4$/rGO heterostructure at NaCl concentration of 100 mg L^{-1}. The application of the external voltage of 1.2 V corresponds to the desalination (salt adsorption), and 0 V corresponds to salination (salt desorption).*

Bibliography

[1] A. Lee, J.W. Elam, S.B. Darling, Membrane materials for water purification: design, development, and application, Environ. Sci.: Water Res. Technol., **2016**, 2, 17-42.
[2] T. Oki, S. Kanae, Global hydrological cycles and world water resources, Science, **2006**, 313, 1068-1072.
[3] J.R. Werber, C.O. Osuji, M. Elimelech, Materials for next-generation desalination and water purification membranes, Nat. Rev. Mater., **2016**, 1, 1-15.
[4] J.F. Anthoni, The chemical composition of seawater, Magnesium, **2006**, 2701, 96-062.
[5] B. Tansel, Significance of thermodynamic and physical characteristics on permeation of ions during membrane separation: Hydrated radius, hydration free energy and viscous effects, Sep. Purif. Technol., **2012**, 86, 119-126.
[6] W.J. Koros, C. Zhang, Materials for next-generation molecularly selective synthetic membranes, Nat. Mater., **2017**, 16, 289-297.
[7] J.R. Werber, A. Deshmukh, M. Elimelech, The critical need for increased selectivity, not increased water permeability, for desalination membranes, Environ. Sci. Technol. Lett., **2016**, 3, 112-120.
[8] P. Marchetti, M.F. Jimenez Solomon, G. Szekely, A.G. Livingston, Molecular separation with organic solvent nanofiltration: a critical review, Chem. Rev. (Washington, DC, U. S.), **2014**, 114, 10735-10806.
[9] Y. Han, Z. Xu, C. Gao, Ultrathin graphene nanofiltration membrane for water purification, Adv. Funct. Mater., **2013**, 23, 3693-3700.
[10] L. Huang, M. Zhang, C. Li, G. Shi, Graphene-based membranes for molecular separation, J. Phys. Chem. Lett., **2015**, 6, 2806-2815.
[11] D.H. Seo, S. Pineda, Y.C. Woo, M. Xie, A.T. Murdock, E.Y. Ang, Y. Jiao, M.J. Park, S.I. Lim, M. Lawn, Anti-fouling graphene-based membranes for effective water desalination, Nat. Commun., **2018**, 9, 1-12.
[12] K.M. Gupta, K. Zhang, J. Jiang, Water desalination through zeolitic imidazolate framework membranes: Significant role of functional groups, Langmuir, **2015**, 31, 13230-13237.
[13] Z. Hu, Y. Chen, J. Jiang, Zeolitic imidazolate framework-8 as a reverse osmosis membrane for water desalination: Insight from molecular simulation, J. Chem. Phys., **2011**, 134, 134705.
[14] B. Corry, Designing carbon nanotube membranes for efficient water desalination, J. Phys. Chem. B, **2008**, 112, 1427-1434.
[15] Z. Zheng, R. Grünker, X. Feng, Synthetic two-dimensional materials: a new paradigm of membranes for ultimate separation, Adv. Mater. (Weinheim, Ger.), **2016**, 28, 6529-6545.
[16] B. Mi, Graphene oxide membranes for ionic and molecular sieving, Science, **2014**, 343, 740-742.
[17] Y. You, V. Sahajwalla, M. Yoshimura, R.K. Joshi, Graphene and graphene oxide for desalination, Nanoscale, **2016**, 8, 117-119.
[18] R. Nair, H. Wu, P. Jayaram, I. Grigorieva, A. Geim, Unimpeded permeation of water through helium-leak–tight graphene-based membranes, Science, **2012**, 335, 442-444.

[19] R. Joshi, P. Carbone, F.C. Wang, V.G. Kravets, Y. Su, I.V. Grigorieva, H. Wu, A.K. Geim, R.R. Nair, Precise and ultrafast molecular sieving through graphene oxide membranes, Science, **2014**, 343, 752-754.
[20] S. Dervin, D.D. Dionysiou, S.C. Pillai, 2D nanostructures for water purification: graphene and beyond, Nanoscale, **2016**, 8, 15115-15131.
[21] G. Liu, W. Jin, N. Xu, Two-dimensional-material membranes: a new family of high-performance separation membranes, Angew. Chem., Int. Ed., **2016**, 55, 13384-13397.
[22] G. Liu, W. Jin, N. Xu, Graphene-based membranes, Chem. Soc. Rev., **2015**, 44, 5016-5030.
[23] P. Liu, J. Hou, Y. Zhang, L. Li, L. Xiaoquan, Z. Tang, Two-dimensional material membranes for critical separations, Inorganic Chemistry Frontiers, **2020**.
[24] S.P. Surwade, S.N. Smirnov, I.V. Vlassiouk, R.R. Unocic, G.M. Veith, S. Dai, S.M. Mahurin, Water desalination using nanoporous single-layer graphene, Nat. Nanotechnol., **2015**, 10, 459.
[25] W. Li, W. Wu, Z. Li, Controlling interlayer spacing of graphene oxide membranes by external pressure regulation, ACS Nano, **2018**, 12, 9309-9317.
[26] J. Abraham, K.S. Vasu, C.D. Williams, K. Gopinadhan, Y. Su, C.T. Cherian, J. Dix, E. Prestat, S.J. Haigh, I.V. Grigorieva, Tunable sieving of ions using graphene oxide membranes, Nat. Nanotechnol., **2017**, 12, 546.
[27] J.-h. Song, H.-W. Yu, M.-H. Ham, I.S. Kim, Tunable Ion Sieving of Graphene Membranes through the Control of Nitrogen-Bonding Configuration, Nano Lett., **2018**, 18, 5506-5513.
[28] Z. Lu, Y. Wei, J. Deng, L. Ding, Z.-K. Li, H. Wang, Self-Crosslinked MXene (Ti3C2T x) Membranes with Good Antiswelling Property for Monovalent Metal Ion Exclusion, ACS Nano, **2019**, 13, 10535-10544.
[29] M. Zhang, K. Guan, Y. Ji, G. Liu, W. Jin, N. Xu, Controllable ion transport by surface-charged graphene oxide membrane, Nat. Commun., **2019**, 10, 1253.
[30] G.-R. Xu, J.-M. Xu, H.-C. Su, X.-Y. Liu, H.-L. Zhao, H.-J. Feng, R. Das, Two-dimensional (2D) nanoporous membranes with sub-nanopores in reverse osmosis desalination: Latest developments and future directions, Desalination, **2019**, 451, 18-34.
[31] A. Boretti, S. Al-Zubaidy, M. Vaclavikova, M. Al-Abri, S. Castelletto, S. Mikhalovsky, Outlook for graphene-based desalination membranes, npj Clean Water, **2018**, 1, 1-11.
[32] T. Jain, B.C. Rasera, R.J.S. Guerrero, M.S. Boutilier, S.C. O'hern, J.-C. Idrobo, R. Karnik, Heterogeneous sub-continuum ionic transport in statistically isolated graphene nanopores, Nat. Nanotechnol., **2015**, 10, 1053.
[33] S.C. O'Hern, D. Jang, S. Bose, J.-C. Idrobo, Y. Song, T. Laoui, J. Kong, R. Karnik, Nanofiltration across defect-sealed nanoporous monolayer graphene, Nano Lett., **2015**, 15, 3254-3260.
[34] D. Cohen-Tanugi, J.C. Grossman, Water desalination across nanoporous graphene, Nano Lett., **2012**, 12, 3602-3608.
[35] M. Heiranian, A.B. Farimani, N.R. Aluru, Water desalination with a single-layer MoS 2 nanopore, Nat. Commun., **2015**, 6, 1-6.
[36] G.A. Ferrari, A.B. de Oliveira, I. Silvestre, M.J. Matos, R.J. Batista, T.F. Fernandes, L.M. Meireles, G.S. Eliel, H. Chacham, B.R. Neves, Apparent Softening of Wet Graphene Membranes on a Microfluidic Platform, ACS Nano, **2018**, 12, 4312-4320.
[37] Y. Yang, X. Yang, L. Liang, Y. Gao, H. Cheng, X. Li, M. Zou, R. Ma, Q. Yuan, X. Duan, Large-area graphene-nanomesh/carbon-nanotube hybrid membranes for ionic and molecular nanofiltration, Science, **2019**, 364, 1057-1062.

[38] M.S. Dresselhaus, A. Jorio, M. Hofmann, G. Dresselhaus, R. Saito, Perspectives on carbon nanotubes and graphene Raman spectroscopy, Nano Lett., **2010**, 10, 751-758.
[39] M.E. Suk, N.R. Aluru, Ion transport in sub-5-nm graphene nanopores, J. Chem. Phys., **2014**, 140, 084707.
[40] P. Masih Das, J.P. Thiruraman, Y.-C. Chou, G. Danda, M. Drndic, Centimeter-scale nanoporous 2D membranes and ion transport: porous MoS2 monolayers in a few-layer matrix, Nano Lett., **2018**, 19, 392-399.
[41] J. Feng, K. Liu, M. Graf, M. Lihter, R.D. Bulushev, D. Dumcenco, D.T. Alexander, D. Krasnozhon, T. Vuletic, A. Kis, Electrochemical reaction in single layer MoS2: nanopores opened atom by atom, Nano Lett., **2015**, 15, 3431-3438.
[42] Y. Yamada, K. Murota, R. Fujita, J. Kim, A. Watanabe, M. Nakamura, S. Sato, K. Hata, P. Ercius, J. Ciston, Subnanometer vacancy defects introduced on graphene by oxygen gas, J. Am. Chem. Soc., **2014**, 136, 2232-2235.
[43] Y. Li, W. Zhao, M. Weyland, S. Yuan, Y. Xia, H. Liu, M. Jian, J. Yang, C.D. Easton, C. Selomulya, Thermally reduced nanoporous graphene oxide membrane for desalination, Environ. Sci. Technol., **2019**, 53, 8314-8323.
[44] M.A. Shannon, P.W. Bohn, M. Elimelech, J.G. Georgiadis, B.J. Marinas, A.M. Mayes, Science and technology for water purification in the coming decades, World Scientific2010, pp. 337-346.
[45] J.P. Thiruraman, K. Fujisawa, G. Danda, P.M. Das, T. Zhang, A. Bolotsky, N. Perea-López, A. Nicolaï, P. Senet, M. Terrones, Angstrom-size defect creation and ionic transport through pores in single-layer MoS2, Nano Lett., **2018**, 18, 1651-1659.
[46] G.H. Ryu, A. France-Lanord, Y. Wen, S. Zhou, J.C. Grossman, J.H. Warner, Atomic Structure and Dynamics of Self-Limiting Sub-Nanometer Pores in Monolayer WS2, ACS Nano, **2018**, 12, 11638-11647.
[47] L.-C. Lin, J. Choi, J.C. Grossman, Two-dimensional covalent triazine framework as an ultrathin-film nanoporous membrane for desalination, Chem. Commun. (Cambridge, U. K.), **2015**, 51, 14921-14924.
[48] Y. Yang, W. Li, H. Zhou, X. Zhang, M. Zhao, Tunable C 2 N Membrane for High Efficient Water Desalination, Sci. Rep., **2016**, 6, 29218.
[49] W. Zhou, M. Wei, X. Zhang, F. Xu, Y. Wang, Fast Desalination by Multilayered Covalent Organic Framework (COF) Nanosheets, ACS Appl. Mater. Interfaces, **2019**, 11, 16847-16854.
[50] Z. Cao, V. Liu, A. Barati Farimani, Water Desalination with Two-Dimensional Metal–Organic Framework Membranes, Nano Lett., **2019**, 19, 8638-8643.
[51] Y. Li, L. Xu, H. Liu, Y. Li, Graphdiyne and graphyne: from theoretical predictions to practical construction, Chem. Soc. Rev., **2014**, 43, 2572-2586.
[52] S. Lin, M.J. Buehler, Mechanics and molecular filtration performance of graphyne nanoweb membranes for selective water purification, Nanoscale, **2013**, 5, 11801-11807.
[53] J. Kou, X. Zhou, H. Lu, F. Wu, J. Fan, Graphyne as the membrane for water desalination, Nanoscale, **2014**, 6, 1865-1870.
[54] M. Xue, H. Qiu, W. Guo, Exceptionally fast water desalination at complete salt rejection by pristine graphyne monolayers, Nanotechnology, **2013**, 24, 505720.
[55] X. Liu, N.K. Demir, Z. Wu, K. Li, Highly water-stable zirconium metal–organic framework UiO-66 membranes supported on alumina hollow fibers for desalination, J. Am. Chem. Soc., **2015**, 137, 6999-7002.
[56] Z. Wang, X. Xu, J. Kim, V. Malgras, R. Mo, C. Li, Y. Lin, H. Tan, J. Tang, L. Pan, Nanoarchitectured metal–organic framework/polypyrrole hybrids for brackish water desalination using capacitive deionization, Mater. Horiz., **2019**, 6, 1433-1437.

[57] C.-N. Yeh, K. Raidongia, J. Shao, Q.-H. Yang, J. Huang, On the origin of the stability of graphene oxide membranes in water, Nat. Chem., **2015**, 7, 166.
[58] P. Sun, Q. Chen, X. Li, H. Liu, K. Wang, M. Zhong, J. Wei, D. Wu, R. Ma, T. Sasaki, Highly efficient quasi-static water desalination using monolayer graphene oxide/titania hybrid laminates, NPG Asia Mater., **2015**, 7, e162-e162.
[59] C.D. Williams, P. Carbone, F.R. Siperstein, In silico design and characterization of graphene oxide membranes with variable water content and flake oxygen content, ACS Nano, **2019**, 13, 2995-3004.
[60] G. Shi, Q. Meng, Z. Zhao, H.-C. Kuan, A. Michelmore, J. Ma, Facile fabrication of graphene membranes with readily tunable structures, ACS Appl. Mater. Interfaces, **2015**, 7, 13745-13757.
[61] H. Liu, H. Wang, X. Zhang, Facile fabrication of freestanding ultrathin reduced graphene oxide membranes for water purification, Adv. Mater. (Weinheim, Ger.), **2015**, 27, 249-254.
[62] A.V. Talyzin, V.L. Solozhenko, O.O. Kurakevych, T. Szabó, I. Dékány, A. Kurnosov, V. Dmitriev, Colossal Pressure-Induced Lattice Expansion of Graphite Oxide in the Presence of Water, Angew. Chem., Int. Ed., **2008**, 47, 8268-8271.
[63] P. Sun, R. Ma, H. Deng, Z. Song, Z. Zhen, K. Wang, T. Sasaki, Z. Xu, H. Zhu, Intrinsic high water/ion selectivity of graphene oxide lamellar membranes in concentration gradient-driven diffusion, Chem. Sci., **2016**, 7, 6988-6994.
[64] L. Huang, Y. Li, Q. Zhou, W. Yuan, G. Shi, Graphene oxide membranes with tunable semipermeability in organic solvents, Adv. Mater. (Weinheim, Ger.), **2015**, 27, 3797-3802.
[65] L. Chen, G. Shi, J. Shen, B. Peng, B. Zhang, Y. Wang, F. Bian, J. Wang, D. Li, Z. Qian, Ion sieving in graphene oxide membranes via cationic control of interlayer spacing, Nature, **2017**, 550, 380-383.
[66] A. Ghaffar, L. Zhang, X. Zhu, B. Chen, Scalable graphene oxide membranes with tunable water channels and stability for ion rejection, Environ. Sci.: Nano, **2019**, 6, 903-915.
[67] L. Ding, L. Li, Y. Liu, Y. Wu, Z. Lu, J. Deng, Y. Wei, J. Caro, H. Wang, Effective ion sieving with Ti 3 C 2 T x MXene membranes for production of drinking water from seawater, Nat. Sustainability, **2020**, 3, 296-302.
[68] Z. Jia, Y. Wang, Covalently crosslinked graphene oxide membranes by esterification reactions for ions separation, J. Mater. Chem. A, **2015**, 3, 4405-4412.
[69] W.-S. Hung, C.-H. Tsou, M. De Guzman, Q.-F. An, Y.-L. Liu, Y.-M. Zhang, C.-C. Hu, K.-R. Lee, J.-Y. Lai, Cross-linking with diamine monomers to prepare composite graphene oxide-framework membranes with varying d-spacing, Chem. Mater., **2014**, 26, 2983-2990.
[70] Y. Qian, X. Zhang, C. Liu, C. Zhou, A. Huang, Tuning interlayer spacing of graphene oxide membranes with enhanced desalination performance, Desalination, **2019**, 460, 56-63.
[71] N. Meng, W. Zhao, E. Shamsaei, G. Wang, X. Zeng, X. Lin, T. Xu, H. Wang, X. Zhang, A low-pressure GO nanofiltration membrane crosslinked via ethylenediamine, J. Membr. Sci., **2018**, 548, 363-371.
[72] W.-S. Hung, Y.-H. Chiao, A. Sengupta, Y.-W. Lin, S.R. Wickramasinghe, C.-C. Hu, H.-A. Tsai, K.-R. Lee, J.-Y. Lai, Tuning the interlayer spacing of forward osmosis membranes based on ultrathin graphene oxide to achieve desired performance, Carbon, **2019**, 142, 337-345.
[73] M. Zhang, Y. Mao, G. Liu, G. Liu, Y. Fan, W. Jin, Molecular bridges stabilize graphene oxide membranes in water, Angew. Chem., Int. Ed., **2019**, 59, 1689-1695.

[74] K. Nakagawa, H. Yamashita, D. Saeki, T. Yoshioka, T. Shintani, E. Kamio, H. Kreissl, S. Tsang, S. Sugiyama, H. Matsuyama, Niobate nanosheet membranes with enhanced stability for nanofiltration, Chem. Commun. (Cambridge, U. K.), **2017**, 53, 7929-7932.
[75] S. Kim, X. Lin, R. Ou, H. Liu, X. Zhang, G.P. Simon, C.D. Easton, H. Wang, Highly crosslinked, chlorine tolerant polymer network entwined graphene oxide membrane for water desalination, J. Mater. Chem. A, **2017**, 5, 1533-1540.
[76] S. Kim, R. Ou, Y. Hu, X. Li, H. Zhang, G.P. Simon, H. Wang, Non-swelling graphene oxide-polymer nanocomposite membrane for reverse osmosis desalination, J. Membr. Sci., **2018**, 562, 47-55.
[77] S. Park, K.-S. Lee, G. Bozoklu, W. Cai, S.T. Nguyen, R.S. Ruoff, Graphene oxide papers modified by divalent ions—enhancing mechanical properties via chemical cross-linking, ACS Nano, **2008**, 2, 572-578.
[78] A. Nicolaï, B.G. Sumpter, V. Meunier, Tunable water desalination across graphene oxide framework membranes, Phys. Chem. Chem. Phys., **2014**, 16, 8646-8654.
[79] X. Qian, N. Li, Q. Wang, S. Ji, Chitosan/graphene oxide mixed matrix membrane with enhanced water permeability for high-salinity water desalination by pervaporation, Desalination, **2018**, 438, 83-96.
[80] Y. Wang, R. Ou, H. Wang, T. Xu, Graphene oxide modified graphitic carbon nitride as a modifier for thin film composite forward osmosis membrane, J. Membr. Sci., **2015**, 475, 281-289.
[81] M. Safarpour, A. Khataee, V. Vatanpour, Thin film nanocomposite reverse osmosis membrane modified by reduced graphene oxide/TiO2 with improved desalination performance, J. Membr. Sci., **2015**, 489, 43-54.
[82] L. Jin, Z. Wang, S. Zheng, B. Mi, Polyamide-crosslinked graphene oxide membrane for forward osmosis, J. Membr. Sci., **2018**, 545, 11-18.
[83] R. Hu, Y. He, C. Zhang, R. Zhang, J. Li, H. Zhu, Graphene oxide-embedded polyamide nanofiltration membranes for selective ion separation, J. Mater. Chem. A, **2017**, 5, 25632-25640.
[84] W. Hirunpinyopas, E. Prestat, S.D. Worrall, S.J. Haigh, R.A. Dryfe, M.A. Bissett, Desalination and nanofiltration through functionalized laminar MoS2 membranes, ACS Nano, **2017**, 11, 11082-11090.
[85] H. Li, T.-J. Ko, M. Lee, H.-S. Chung, S.S. Han, K.H. Oh, A. Sadmani, H. Kang, Y. Jung, Experimental Realization of Few Layer Two-Dimensional MoS2 Membranes of Near Atomic Thickness for High Efficiency Water Desalination, Nano Lett., **2019**, 19, 5194-5204.
[86] M. Deng, K. Kwac, M. Li, Y. Jung, H.G. Park, Stability, molecular sieving, and ion diffusion selectivity of a lamellar membrane from two-dimensional molybdenum disulfide, Nano Lett., **2017**, 17, 2342-2348.
[87] L. Ries, E. Petit, T. Michel, C.C. Diogo, C. Gervais, C. Salameh, M. Bechelany, S. Balme, P. Miele, N. Onofrio, Enhanced sieving from exfoliated MoS 2 membranes via covalent functionalization, Nat. Mater., **2019**, 18, 1112-1117.
[88] X. Xie, C. Chen, N. Zhang, Z.-R. Tang, J. Jiang, Y.-J. Xu, Microstructure and surface control of MXene films for water purification, Nat. Sustain., **2019**, 2, 856-862.
[89] B. Feng, K. Xu, A. Huang, Covalent synthesis of three-dimensional graphene oxide framework (GOF) membrane for seawater desalination, Desalination, **2016**, 394, 123-130.
[90] M. Zhang, J. Sun, Y. Mao, G. Liu, W. Jin, Effect of substrate on formation and nanofiltration performance of graphene oxide membranes, J. Membr. Sci., **2019**, 574, 196-204.

[91] N.Y. Yip, D. Brogioli, H.V. Hamelers, K. Nijmeijer, Salinity gradients for sustainable energy: primer, progress, and prospects, Environ. Sci. Technol., **2016**, 50, 12072-12094.
[92] X. Wang, P.L. McCarty, J. Liu, N.-Q. Ren, D.-J. Lee, H.-Q. Yu, Y. Qian, J. Qu, Probabilistic evaluation of integrating resource recovery into wastewater treatment to improve environmental sustainability, Proc. Natl. Acad. Sci. U. S. A, **2015**, 112, 1630-1635.
[93] S. Chu, A. Majumdar, Opportunities and challenges for a sustainable energy future, Nature, **2012**, 488, 294-303.
[94] Y. Zhou, L. Jiang, Bioinspired nanoporous membrane for salinity gradient energy harvesting, Joule, **2020**, 4, 2244-2248.
[95] T. Ahmad, D. Zhang, A critical review of comparative global historical energy consumption and future demand: The story told so far, Energy Rep., **2020**, 6, 1973-1991.
[96] W.-G. Kim, D.-W. Kim, I.-W. Tcho, J.-K. Kim, M.-S. Kim, Y.-K. Choi, Triboelectric nanogenerator: Structure, mechanism, and applications, ACS Nano, **2021**, 15, 258-287.
[97] Y. Wang, T. Guo, Z. Tian, K. Bibi, Y.Z. Zhang, H.N. Alshareef, MXenes for Energy Harvesting, Adv. Mater., **2022**, 2108560.
[98] S. Chou, R. Wang, L. Shi, Q. She, C. Tang, A.G. Fane, Thin-film composite hollow fiber membranes for pressure retarded osmosis (PRO) process with high power density, J. Membr. Sci., **2012**, 389, 25-33.
[99] R.R. Gonzales, A. Abdel-Wahab, S. Adham, D.S. Han, S. Phuntsho, W. Suwaileh, N. Hilal, H.K. Shon, Salinity gradient energy generation by pressure retarded osmosis: A review, Desalination, **2021**, 500, 114841.
[100] M. Kurihara, M. Hanakawa, Mega-ton Water System: Japanese national research and development project on seawater desalination and wastewater reclamation, Desalination, **2013**, 308, 131-137.
[101] C. Klaysom, T.Y. Cath, T. Depuydt, I.F.J. Vankelecom, Forward and pressure retarded osmosis: potential solutions for global challenges in energy and water supply, Chem. Soc. Rev., **2013**, 42, 6959-6989.
[102] B. Kang, H.J. Kim, D.-K. Kim, Membrane electrode assembly for energy harvesting from salinity gradient by reverse electrodialysis, J. Membr. Sci., **2018**, 550, 286-295.
[103] G. Laucirica, M.E. Toimil-Molares, C. Trautmann, W. Marmisollé, O. Azzaroni, Nanofluidic osmotic power generators–advanced nanoporous membranes and nanochannels for blue energy harvesting, Chem. Sci., **2021**, 12, 12874-12910.
[104] K. Xiao, L. Jiang, M. Antonietti, Ion transport in nanofluidic devices for energy harvesting, Joule, **2019**, 3, 2364-2380.
[105] J. Safaei, P. Xiong, G. Wang, Progress and prospects of two-dimensional materials for membrane-based water desalination, Mater. Today Adv., **2020**, 8, 100108.
[106] M.B. Asif, S. Iftekhar, T. Maqbool, B.K. Paramanik, S. Tabraiz, M. Sillanpää, Z. Zhang, Two-dimensional nanoporous and lamellar membranes for water purification: Reality or a myth?, Chem. Eng. J., **2021**, 432, 134335.
[107] A.R. Koltonow, J. Huang, Two-dimensional nanofluidics, Science, **2016**, 351, 1395-1396.
[108] L. Wang, M.S. Boutilier, P.R. Kidambi, D. Jang, N.G. Hadjiconstantinou, R. Karnik, Fundamental transport mechanisms, fabrication and potential applications of nanoporous atomically thin membranes, Nat. Nanotechnol., **2017**, 12, 509-522.

[109] D. Pakulski, W. Czepa, S.D. Buffa, A. Ciesielski, P. Samorì, Atom-Thick Membranes for Water Purification and Blue Energy Harvesting, Adv. Funct. Mater., **2020**, 30, 1902394.
[110] J. Gao, Y. Feng, W. Guo, L. Jiang, Nanofluidics in two-dimensional layered materials: inspirations from nature, Chem. Soc. Rev., **2017**, 46, 5400-5424.
[111] X. Tong, S. Liu, J. Crittenden, Y. Chen, Nanofluidic membranes to address the challenges of salinity gradient power harvesting, ACS Nano, **2021**, 15, 5838-5860.
[112] Z. Zhang, L. Wen, L. Jiang, Nanofluidics for osmotic energy conversion, Nat. Rev. Mater., **2021**, 6, 622-639.
[113] W. Xin, L. Jiang, L. Wen, Two-dimensional nanofluidic membranes toward harvesting salinity gradient power, Acc. Chem. Res., **2021**, 54, 4154-4165.
[114] J.R. Werber, A. Deshmukh, M. Elimelech, The Critical Need for Increased Selectivity, Not Increased Water Permeability, for Desalination Membranes, Environ. Sci. Technol. Lett., **2016**, 3, 112-120.
[115] P. Xu, D. Zheng, H. Xu, The feasibility and mechanism of reverse electrodialysis enhanced photocatalytic fuel cell-Fenton system on advanced treatment of coal gasification wastewater, Sep. Purif. Technol., **2019**, 220, 183-188.
[116] Y. Lee, H.J. Kim, D.-K. Kim, Power generation from concentration gradient by reverse electrodialysis in anisotropic nanoporous anodic aluminum oxide membranes, Energies, **2020**, 13, 904.
[117] W. Ouyang, W. Wang, H. Zhang, W. Wu, Z. Li, Nanofluidic crystal: a facile, high-efficiency and high-power-density scaling up scheme for energy harvesting based on nanofluidic reverse electrodialysis, Nanotechnology, **2013**, 24, 345401.
[118] L. Cao, W. Guo, W. Ma, L. Wang, F. Xia, S. Wang, Y. Wang, L. Jiang, D. Zhu, Towards understanding the nanofluidic reverse electrodialysis system: well matched charge selectivity and ionic composition, Energy Environ. Sci., **2011**, 4, 2259-2266.
[119] I. Vlassiouk, S. Smirnov, Z. Siwy, Ionic selectivity of single nanochannels, Nano Lett., **2008**, 8, 1978-1985.
[120] I. Vlassiouk, S. Smirnov, Z. Siwy, Nanofluidic ionic diodes. Comparison of analytical and numerical solutions, ACS Nano, **2008**, 2, 1589-1602.
[121] M. Macha, S. Marion, V.V. Nandigana, A. Radenovic, 2D materials as an emerging platform for nanopore-based power generation, Nat. Rev. Mater., **2019**, 4, 588-605.
[122] R.A. Tufa, S. Pawlowski, J. Veerman, K. Bouzek, E. Fontananova, G. Di Profio, S. Velizarov, J.G. Crespo, K. Nijmeijer, E. Curcio, Progress and prospects in reverse electrodialysis for salinity gradient energy conversion and storage, Appl. Energy, **2018**, 225, 290-331.
[123] J. Veerman, D. Vermaas, Reverse electrodialysis: fundamentals, Sustainable energy from salinity gradients, **2016**, 77-133.
[124] J.-P. Hsu, S.-C. Lin, C.-Y. Lin, S. Tseng, Power generation by a pH-regulated conical nanopore through reverse electrodialysis, J. Power Sources, **2017**, 366, 169-177.
[125] H. Tian, Y. Wang, Y. Pei, J.C. Crittenden, Unique applications and improvements of reverse electrodialysis: A review and outlook, Appl. Energy, **2020**, 262, 114482.
[126] B. Derjaguin, S. Dukhin, M. Koptelova, Capillary osmosis through porous partitions and properties of boundary layers of solutions, J. Colloid Interface Sci., **1972**, 38, 584-595.
[127] A. Siria, P. Poncharal, A.-L. Biance, R. Fulcrand, X. Blase, S.T. Purcell, L. Bocquet, Giant osmotic energy conversion measured in a single transmembrane boron nitride nanotube, Nature, **2013**, 494, 455-458.

[128] R. Moritz, G. Zardalidis, H.-J.r. Butt, M. Wagner, K. Müllen, G. Floudas, Ion size approaching the Bjerrum length in solvents of low polarity by dendritic encapsulation, Macromolecules, **2014**, 47, 191-196.
[129] N.Y. Yip, D.A. Vermaas, K. Nijmeijer, M. Elimelech, Thermodynamic, energy efficiency, and power density analysis of reverse electrodialysis power generation with natural salinity gradients, Environ. Sci. Technol., **2014**, 48, 4925-4936.
[130] A. Siria, M.-L. Bocquet, L. Bocquet, New avenues for the large-scale harvesting of blue energy, Nat. Rev. Chem., **2017**, 1, 1-10.
[131] K. Sint, B. Wang, P. Král, Selective ion passage through functionalized graphene nanopores, J. Am. Chem. Soc., **2008**, 130, 16448-16449.
[132] K. Yazda, K. Bleau, Y. Zhang, X. Capaldi, T. St-Denis, P. Grutter, W.W. Reisner, High Osmotic Power Generation via Nanopore Arrays in Hybrid Hexagonal Boron Nitride/Silicon Nitride Membranes, Nano Lett., **2021**, 21, 4152-4159.
[133] H. Wang, L. Su, M. Yagmurcukardes, J. Chen, Y. Jiang, Z. Li, A. Quan, F.M. Peeters, C. Wang, A.K. Geim, Blue energy conversion from holey-graphene-like membranes with a high density of subnanometer pores, Nano Lett., **2020**, 20, 8634-8639.
[134] S.P. Surwade, S.N. Smirnov, I.V. Vlassiouk, R.R. Unocic, G.M. Veith, S. Dai, S.M. Mahurin, Water desalination using nanoporous single-layer graphene, Nat. Nanotechnol., **2015**, 10, 459-464.
[135] M. Heiranian, A.B. Farimani, N.R. Aluru, Water desalination with a single-layer MoS2 nanopore, Nat. Commun., **2015**, 6, 1-6.
[136] J. Feng, M. Graf, K. Liu, D. Ovchinnikov, D. Dumcenco, M. Heiranian, V. Nandigana, N.R. Aluru, A. Kis, A. Radenovic, Single-layer MoS2 nanopores as nanopower generators, Nature, **2016**, 536, 197-200.
[137] M. Hosseini, J. Azamat, H. Erfan-Niya, Improving the performance of water desalination through ultra-permeable functionalized nanoporous graphene oxide membrane, Appl. Surf. Sci., **2018**, 427, 1000-1008.
[138] M. Caglar, I. Silkina, B.T. Brown, A.L. Thorneywork, O.J. Burton, V. Babenko, S.M. Gilbert, A. Zettl, S. Hofmann, U.F. Keyser, Tunable anion-selective transport through monolayer graphene and hexagonal boron nitride, ACS Nano, **2019**, 14, 2729-2738.
[139] M.I. Walker, K. Ubych, V. Saraswat, E.A. Chalklen, P. Braeuninger-Weimer, S. Caneva, R.S. Weatherup, S. Hofmann, U.F. Keyser, Extrinsic cation selectivity of 2D membranes, ACS Nano, **2017**, 11, 1340-1346.
[140] X. Liu, M. He, D. Calvani, H. Qi, K.B. Gupta, H.J. de Groot, G. Sevink, F. Buda, U. Kaiser, G.F. Schneider, Power generation by reverse electrodialysis in a single-layer nanoporous membrane made from core–rim polycyclic aromatic hydrocarbons, Nat. Nanotechnol., **2020**, 15, 307-312.
[141] J. Yang, B. Tu, G. Zhang, P. Liu, K. Hu, J. Wang, Z. Yan, Z. Huang, M. Fang, J. Hou, Q. Fang, X. Qiu, L. Li, Z. Tang, Advancing osmotic power generation by covalent organic framework monolayer, Nat. Nanotechnol., **2022**, DOI: 10.1038/s41565-022-01110-7.
[142] G. Bian, N. Pan, Z. Luan, X. Sui, W. Fan, Y. Xia, K. Sui, L. Jiang, Anti-Swelling Gradient Polyelectrolyte Hydrogel Membranes as High-Performance Osmotic Energy Generators, Angew. Chem., **2021**, 133, 20456-20462.
[143] H. Cheng, Y. Zhou, Y. Feng, W. Geng, Q. Liu, W. Guo, L. Jiang, Electrokinetic Energy Conversion in Self-Assembled 2D Nanofluidic Channels with Janus Nanobuilding Blocks, Adv. Mater., **2017**, 29, 1700177.

[144] Y. Zhou, H. Ding, A.T. Smith, X. Jia, S. Chen, L. Liu, S.E. Chavez, Z. Hou, J. Liu, H. Cheng, Nanofluidic energy conversion and molecular separation through highly stable clay-based membranes, J. Mater. Chem. A, **2019**, 7, 14089-14096.
[145] K. Xiao, P. Giusto, L. Wen, L. Jiang, M. Antonietti, Nanofluidic Ion Transport and Energy Conversion through Ultrathin Free-Standing Polymeric Carbon Nitride Membranes, Angew. Chem. Int. Ed., **2018**, 57, 10123-10126.
[146] Z. Zhang, W. Shen, L. Lin, M. Wang, N. Li, Z. Zheng, F. Liu, L. Cao, Vertically Transported Graphene Oxide for High-Performance Osmotic Energy Conversion, Adv. Sci., **2020**, 7, 2000286.
[147] J. Ji, Q. Kang, Y. Zhou, Y. Feng, X. Chen, J. Yuan, W. Guo, Y. Wei, L. Jiang, Osmotic power generation with positively and negatively charged 2D nanofluidic membrane pairs, Adv. Funct. Mater., **2017**, 27, 1603623.
[148] L. Ding, D. Xiao, Z. Lu, J. Deng, Y. Wei, J. Caro, H. Wang, Oppositely charged Ti3C2Tx MXene membranes with 2D nanofluidic channels for osmotic energy harvesting, Angew. Chem. Int. Ed., **2020**, 59, 8720-8726.
[149] S. Hong, F. Ming, Y. Shi, R. Li, I.S. Kim, C.Y. Tang, H.N. Alshareef, P. Wang, Two-dimensional Ti3C2T x MXene membranes as nanofluidic osmotic power generators, ACS Nano, **2019**, 13, 8917-8925.
[150] P. Liu, Y. Sun, C. Zhu, B. Niu, X. Huang, X.-Y. Kong, L. Jiang, L. Wen, Neutralization reaction assisted chemical-potential-driven ion transport through layered titanium carbides membrane for energy harvesting, Nano Lett., **2020**, 20, 3593-3601.
[151] K. Cao, Z. Jiang, X. Zhang, Y. Zhang, J. Zhao, R. Xing, S. Yang, C. Gao, F. Pan, Highly water-selective hybrid membrane by incorporating g-C3N4 nanosheets into polymer matrix, J. Membr. Sci., **2015**, 490, 72-83.
[152] Y. Wang, L. Li, Y. Wei, J. Xue, H. Chen, L. Ding, J. Caro, H. Wang, Water transport with ultralow friction through partially exfoliated g-C3N4 nanosheet membranes with self-supporting spacers, Angew. Chem. Int. Ed., **2017**, 56, 8974-8980.
[153] J. Safaei, N.A. Mohamed, M.F.M. Noh, M.F. Soh, N.A. Ludin, M.A. Ibrahim, W.N.R.W. Isahak, M.A.M. Teridi, Graphitic carbon nitride (gC 3 N 4) electrodes for energy conversion and storage: a review on photoelectrochemical water splitting, solar cells and supercapacitors, J. Mater. Chem. A, **2018**, 6, 22346-22380.
[154] S. Hong, J.K. El-Demellawi, Y. Lei, Z. Liu, F.A. Marzooqi, H.A. Arafat, H.N. Alshareef, Porous Ti3C2T x MXene Membranes for Highly Efficient Salinity Gradient Energy Harvesting, ACS Nano, **2022**, 16, 792–800.
[155] H. Wang, X. Liu, P. Niu, S. Wang, J. Shi, L. Li, Porous two-dimensional materials for photocatalytic and electrocatalytic applications, Matter, **2020**, 2, 1377-1413.
[156] J. Wan, L. Huang, J. Wu, L. Xiong, Z. Hu, H. Yu, T. Li, J. Zhou, Microwave Combustion for Rapidly Synthesizing Pore-Size-Controllable Porous Graphene, Adv. Funct. Mater., **2018**, 28, 1800382.
[157] L. Cao, H. Wu, C. Fan, Z. Zhang, B. Shi, P. Yang, M. Qiu, N.A. Khan, Z. Jiang, Lamellar Porous Vermiculite Membranes for Boosting Nanofluidic Osmotic Energy Conversion, J. Mater. Chem. A, **2021**, 9, 14576-14581.
[158] L. Wang, Z. Wang, S.K. Patel, S. Lin, M. Elimelech, Nanopore-based power generation from salinity gradient: why it is not viable, ACS Nano, **2021**, 15, 4093-4107.
[159] L. Cao, Q. Wen, Y. Feng, D. Ji, H. Li, N. Li, L. Jiang, W. Guo, On the Origin of Ion Selectivity in Ultrathin Nanopores: Insights for Membrane-Scale Osmotic Energy Conversion, Adv. Funct. Mater., **2018**, 28, 1804189.
[160] X. Han, M.R. Funk, F. Shen, Y.-C. Chen, Y. Li, C.J. Campbell, J. Dai, X. Yang, J.-W. Kim, Y. Liao, Scalable holey graphene synthesis and dense electrode fabrication toward high-performance ultracapacitors, ACS Nano, **2014**, 8, 8255-8265.

[161] T. Li, X. Zhang, S.D. Lacey, R. Mi, X. Zhao, F. Jiang, J. Song, Z. Liu, G. Chen, J. Dai, Cellulose ionic conductors with high differential thermal voltage for low-grade heat harvesting, Nat. Mater., **2019**, 18, 608-613.
[162] M. Yang, K. Cao, L. Sui, Y. Qi, J. Zhu, A. Waas, E.M. Arruda, J. Kieffer, M. Thouless, N.A. Kotov, Dispersions of aramid nanofibers: a new nanoscale building block, ACS Nano, **2011**, 5, 6945-6954.
[163] Z. Man, J. Safaei, Z. Zhang, Y. Wang, D. Zhou, P. Li, X. Zhang, L. Jiang, G. Wang, Serosa-Mimetic Nanoarchitecture Membranes for Highly Efficient Osmotic Energy Generation, J. Am. Chem. Soc., **2021**.
[164] C. Zhu, P. Liu, B. Niu, Y. Liu, W. Xin, W. Chen, X.-Y. Kong, Z. Zhang, L. Jiang, L. Wen, Metallic two-dimensional MoS2 composites as high-performance osmotic energy conversion membranes, J. Am. Chem. Soc., **2021**, 143, 1932-1940.
[165] Z. Zhang, S. Yang, P. Zhang, J. Zhang, G. Chen, X. Feng, Mechanically strong MXene/Kevlar nanofiber composite membranes as high-performance nanofluidic osmotic power generators, Nat. Commun., **2019**, 10, 1-9.
[166] Y. Wu, W. Xin, X.-Y. Kong, J. Chen, Y. Qian, Y. Sun, X. Zhao, W. Chen, L. Jiang, L. Wen, Enhanced ion transport by graphene oxide/cellulose nanofibers assembled membranes for high-performance osmotic energy harvesting, Mater. Horizons, **2020**, 7, 2702-2709.
[167] W. Xin, H. Xiao, X.-Y. Kong, J. Chen, L. Yang, B. Niu, Y. Qian, Y. Teng, L. Jiang, L. Wen, Biomimetic nacre-like silk-crosslinked membranes for osmotic energy harvesting, ACS Nano, **2020**, 14, 9701-9710.
[168] C. Chen, D. Liu, L. He, S. Qin, J. Wang, J.M. Razal, N.A. Kotov, W. Lei, Bio-inspired nanocomposite membranes for osmotic energy harvesting, Joule, **2020**, 4, 247-261.
[169] S. Wang, D. Zhang, B. Li, C. Zhang, Z. Du, H. Yin, X. Bi, S. Yang, Ultrastable in-plane 1T–2H MoS2 heterostructures for enhanced hydrogen evolution reaction, Adv. Energy Mater., **2018**, 8, 1801345.
[170] M. Acerce, D. Voiry, M. Chhowalla, Metallic 1T phase MoS 2 nanosheets as supercapacitor electrode materials, Nat. Nanotechnol., **2015**, 10, 313-318.
[171] J.N. Coleman, M. Lotya, A. O'Neill, S.D. Bergin, P.J. King, U. Khan, K. Young, A. Gaucher, S. De, R.J. Smith, Two-dimensional nanosheets produced by liquid exfoliation of layered materials, Science, **2011**, 331, 568-571.
[172] L. Mei, Z. Cao, T. Ying, R. Yang, H. Peng, G. Wang, L. Zheng, Y. Chen, C.Y. Tang, D. Voiry, Simultaneous electrochemical exfoliation and covalent functionalization of MoS2 membrane for ion sieving, Adv. Mater., **2022**, DOI: 10.1002/adma.202201416, 2201416.
[173] R. Yang, L. Mei, Q. Zhang, Y. Fan, H.S. Shin, D. Voiry, Z. Zeng, High-yield production of mono-or few-layer transition metal dichalcogenide nanosheets by an electrochemical lithium ion intercalation-based exfoliation method, Nature protocols, **2022**, 17, 358–377.
[174] M. Chhowalla, H.S. Shin, G. Eda, L.-J. Li, K.P. Loh, H. Zhang, The chemistry of two-dimensional layered transition metal dichalcogenide nanosheets, Nat. Chem., **2013**, 5, 263-275.
[175] D. Voiry, M. Salehi, R. Silva, T. Fujita, M. Chen, T. Asefa, V.B. Shenoy, G. Eda, M. Chhowalla, Conducting MoS2 nanosheets as catalysts for hydrogen evolution reaction, Nano Lett., **2013**, 13, 6222-6227.
[176] P. Sun, R. Ma, W. Ma, J. Wu, K. Wang, T. Sasaki, H. Zhu, Highly selective charge-guided ion transport through a hybrid membrane consisting of anionic graphene oxide

and cationic hydroxide nanosheet superlattice units, NPG Asia Mater., **2016**, 8, e259-e259.
[177] G. Yang, D. Liu, C. Chen, Y. Qian, Y. Su, S. Qin, L. Zhang, X. Wang, L. Sun, W. Lei, Stable Ti3C2T x MXene–Boron Nitride Membranes with Low Internal Resistance for Enhanced Salinity Gradient Energy Harvesting, ACS Nano, **2021**, 15, 6594-6603.
[178] Z. Zhang, P. Zhang, S. Yang, T. Zhang, M. Löffler, H. Shi, M.R. Lohe, X. Feng, Oxidation promoted osmotic energy conversion in black phosphorus membranes, Proc. Natl. Acad. Sci. U. S. A, **2020**, 117, 13959-13966.
[179] S. Qin, D. Liu, G. Wang, D. Portehault, C.J. Garvey, Y. Gogotsi, W. Lei, Y. Chen, High and stable ionic conductivity in 2D nanofluidic ion channels between boron nitride layers, J. Am. Chem. Soc., **2017**, 139, 6314-6320.
[180] S. Qin, D. Liu, Y. Chen, C. Chen, G. Wang, J. Wang, J.M. Razal, W. Lei, Nanofluidic electric generators constructed from boron nitride nanosheet membranes, Nano Energy, **2018**, 47, 368-373.
[181] Z. Zhu, D. Wang, Y. Tian, L. Jiang, Ion/molecule transportation in nanopores and nanochannels: From critical principles to diverse functions, J. Am. Chem. Soc., **2019**, 141, 8658-8669.
[182] S. Wang, G. Wang, T. Wu, Y. Zhang, F. Zhan, Y. Wang, J. Wang, Y. Fu, J. Qiu, BCN nanosheets templated by g-C3N4 for high performance capacitive deionization, J. Mater. Chem. A, **2018**, 6, 14644-14650.
[183] Y.K. Recepoglu, A.Y. Goren, V. Vatanpour, Y. Yoon, A. Khataee, Boron carbon nitride nanosheets in water and wastewater treatment: A critical review, Desalination, **2022**, 533, 115782.
[184] J. Yu, Y. Liu, X. Zhang, R. Liu, Q. Yang, S. Hu, H. Song, P. Li, A. Li, S. Zhang, Enhanced capacitive deionization of a low-concentration brackish water with protonated carbon nitride-decorated graphene oxide electrode, Chemosphere, **2022**, 293, 133580.
[185] T. Zhou, Y. Yu, B. He, Z. Wang, T. Xiong, Z. Wang, Y. Liu, J. Xin, M. Qi, H. Zhang, Ultra-compact MXene fibers by continuous and controllable synergy of interfacial interactions and thermal drawing-induced stresses, Nat. Commun., **2022**, 13, 4564.
[186] P. Srimuk, F. Kaasik, B. Krüner, A. Tolosa, S. Fleischmann, N. Jäckel, M.C. Tekeli, M. Aslan, M.E. Suss, V. Presser, MXene as a novel intercalation-type pseudocapacitive cathode and anode for capacitive deionization, J. Mater. Chem. A, **2016**, 4, 18265-18271.
[187] J. Ma, Y. Cheng, L. Wang, X. Dai, F. Yu, Free-standing Ti3C2Tx MXene film as binder-free electrode in capacitive deionization with an ultrahigh desalination capacity, Chemical Engineering Journal, **2020**, 384, 123329.
[188] A. Amiri, Y. Chen, C.B. Teng, M. Naraghi, Porous nitrogen-doped MXene-based electrodes for capacitive deionization, Energy Storage Materials, **2020**, 25, 731-739.
[189] W. Bao, X. Tang, X. Guo, S. Choi, C. Wang, Y. Gogotsi, G. Wang, Porous cryo-dried MXene for efficient capacitive deionization, Joule, **2018**, 2, 778-787.
[190] F. Xing, T. Li, J. Li, H. Zhu, N. Wang, X. Cao, Chemically exfoliated MoS2 for capacitive deionization of saline water, Nano Energy, **2017**, 31, 590-595.
[191] S. Tian, X. Zhang, Z. Zhang, Capacitive deionization with MoS2/g-C3N4 electrodes, Desalination, **2020**, 479, 114348.
[192] S. Tian, X. Zhang, Z. Zhang, Novel MoS2/NOMC electrodes with enhanced capacitive deionization performances, Chem. Eng. J., **2021**, 409, 128200.
[193] R. Kappera, D. Voiry, S.E. Yalcin, B. Branch, G. Gupta, A.D. Mohite, M. Chhowalla, Phase-engineered low-resistance contacts for ultrathin MoS2 transistors, Nat. Mater., **2014**, 13, 1128-1134.

[194] G. Eda, T. Fujita, H. Yamaguchi, D. Voiry, M. Chen, M. Chhowalla, Coherent atomic and electronic heterostructures of single-layer MoS2, ACS Nano, **2012**, 6, 7311-7317.
[195] B.E. Logan, M. Elimelech, Membrane-based processes for sustainable power generation using water, Nature, **2012**, 488, 313-319.
[196] Z. Zhang, L. He, C. Zhu, Y. Qian, L. Wen, L. Jiang, Improved osmotic energy conversion in heterogeneous membrane boosted by three-dimensional hydrogel interface, Nat. Commun., **2020**, 11, 875.
[197] R. Long, Z. Kuang, Z. Liu, W. Liu, Reverse electrodialysis in bilayer nanochannels: salinity gradient-driven power generation, Phys. Chem. Chem. Phys., **2018**, 20, 7295-7302.
[198] L. Bocquet, E. Charlaix, Nanofluidics, from bulk to interfaces, Chem. Soc. Rev., **2010**, 39, 1073-1095.
[199] Z. Zhang, W. Shen, L. Lin, M. Wang, N. Li, Z. Zheng, F. Liu, L. Cao, Vertically transported graphene oxide for high-performance osmotic energy conversion, Adv. Sci., **2020**, 7, 2000286.
[200] A. Siria, P. Poncharal, A.-L. Biance, R.m. Fulcrand, X. Blase, S.T. Purcell, L.r. Bocquet, Giant osmotic energy conversion measured in a single transmembrane boron nitride nanotube, Nature, **2013**, 494, 455-458.
[201] Z. Zhang, S. Yang, P. Zhang, J. Zhang, G. Chen, X. Feng, Mechanically strong MXene/Kevlar nanofiber composite membranes as high-performance nanofluidic osmotic power generators, Nat. Commun., **2019**, 10, 2920.
[202] X. Cai, Y. Luo, B. Liu, H.-M. Cheng, Preparation of 2D material dispersions and their applications, Chem. Soc. Rev., **2018**, 47, 6224-6266.
[203] T.J. Silhavy, D. Kahne, S. Walker, The bacterial cell envelope, Cold Spring Harb. Perspect Biol., **2010**, 2, a000414.
[204] J. Xu, D.A. Lavan, Designing artificial cells to harness the biological ion concentration gradient, Nat. Nanotechnol., **2008**, 3, 666-670.
[205] Y. Ma, Q. Zheng, Y. Liu, B. Shi, X. Xue, W. Ji, Z. Liu, Y. Jin, Y. Zou, Z. An, W. Zhang, X. Wang, W. Jiang, Z. Xu, Z.L. Wang, Z. Li, H. Zhang, Self-powered, one-stop, and multifunctional implantable triboelectric active sensor for real-time biomedical monitoring, Nano. Lett., **2016**, 16, 6042-6051.
[206] Z. Jia, B. Wang, S. Song, Y. Fan, Blue energy: Current technologies for sustainable power generation from water salinity gradient, Renew. Sustain. Energy Rev., **2014**, 31, 91-100.
[207] B. Delley, From molecules to solids with the $DMol^3$ approach, J. Chem. Phys., **2000**, 113, 7756-7764.
[208] Generalized Gradient Approximation Made Simple, Phys. Rev. Lett., **1996**, 77, 3865-3868.
[209] A. Tkatchenko, M. Scheffler, Accurate molecular van der Waals interactions from ground-state electron density and free-atom reference data, Phys. Rev. Lett., **2009**, 102, 073005.
[210] H.J. Monkhorst, J.D. Pack, Special points for Brillouin-zone integrations, Phys. Review B, **1976**, 13, 5188-5192.
[211] T.A. Halgren, W.N. Lipscomb, The Synchronous-Transit Method for Determining Reaction Pathways and Locating Molecular Transition States, Chem. Phys. Lett., **1977**, 49, 225-232.
[212] A.K. Rappe, C.J. Casewit, K.S. Colwell, W.A. Goddard, W.M. Skiff, UFF, a full periodic table force field for molecular mechanics and molecular dynamics simulations, J. Am. Chem. Soc., **1992**, 114, 10024-10035.

[213] L. Martinez, R. Andrade, E.G. Birgin, J.M. Martinez, PACKMOL: a package for building initial configurations for molecular dynamics simulations, J. Comput. Chem., **2009**, 30, 2157-2164.
[214] M.G. Rabbani, A.K. Sekizkardes, Z. Kahveci, T.E. Reich, R. Ding, H.M. El-Kaderi, A 2D mesoporous imine-linked covalent organic framework for high pressure gas storage applications, Chem., **2013**, 19, 3324-3328.
[215] L. Wen, Y. Sun, T. Dong, C. Lu, W. Xin, L. Yang, P. Liu, Y. Qian, Y. Zhao, X.-Y. Kong, L. Jiang, Tailoring poly(ether sulfone) bipolar membrane for osmotic energy generator with high power density, Angew. Chem. Int. Ed., **2020**, 59, 17423-17428.
[216] Z. Zhang, L. Wen, L. Jiang, Nanofluidics for osmotic energy conversion, Nat. Rev. Mater., **2021**.
[217] D. Zhou, X. Tang, X. Guo, P. Li, D. Shanmukaraj, H. Liu, X. Gao, Y. Wang, T. Rojo, M. Armand, G. Wang, Polyolefin-based janus separator for rechargeable sodium batteries, Angew. Chem. Int. Ed., **2020**, 59, 16725-16734.
[218] K. Goh , W. Jiang , H.E. Karahan, S. Zhai, L. Wei, D. Yu, A.G. Fane, R. Wang, Y. Chen, All-carbon nanoarchitectures as high-performance separation membranes with superior stability, Adv. Funct. Mater., **2015**, 25, 7348–7359.
[219] E.F. Hacopian, Y. Yang, B. Ni, Y. Li, X. Li, Q. Chen, H. Guo, J.M. Tour, H. Gao, J. Lou, Toughening graphene by integrating carbon nanotubes, ACS Nano, **2018**, 12, 7901-7910.
[220] Y. Yang, X. Yang, L. Liang, Y. Gao, H. Cheng, X. Li, M. Zou, A. Cao, M. Renzhi, Q. Yuan, X. Duan, Large-area graphene-nanomesh/ carbon-nanotube hybrid membranes for ionic and molecular nanofiltration, Science, **2019**, 364, 1057–1062.
[221] X. Huang, Z. Zhang, X.-Y. Kong, Y. Sun, C. Zhu, P. Liu, J. Pang, L. Jiang, L. Wen, Engineered PES/SPES nanochannel membrane for salinity gradient power generation, Nano Energy, **2019**, 59, 354-362.
[222] W. Kong, C. Wang, C. Jia, Y. Kuang, G. Pastel, C. Chen, G. Chen, S. He, H. Huang, J. Zhang, S. Wang, L. Hu, Muscle-inspired highly anisotropic, strong, ion-conductive hydrogels, Adv. Mater., **2018**, 30, 1801934.
[223] J. Ji, Q. Kang, Y. Zhou, Y. Feng, X. Chen, J. Yuan, W. Guo, Y. Wei, L. Jiang, Osmotic power generation with positively and negatively charged 2D nanofluidic membrane pairs, Adv. Funct. Mater., **2017**, 27, 1603623.
[224] R. Li, J. Jiang, Q. Liu, Z. Xie, J. Zhai, Hybrid nanochannel membrane based on polymer/MOF for high-performance salinity gradient power generation, Nano Energy, **2018**, 53, 643-649.
[225] D.-K. Kim, C. Duan, Y.-F. Chen, A. Majumdar, Power generation from concentration gradient by reverse electrodialysis in ion-selective nanochannels, Microfluid. Nanofluid., **2010**, 9, 1215-1224.
[226] J. Wan, L. Huang, J. Wu, L. Xiong, Z. Hu, H. Yu, T. Li, J. Zhou, Microwave combustion for rapidly synthesizing pore-size-controllable porous graphene, Adv. Funct. Mater., **2018**, 28, 1800382.
[227] C. Yu, X. Zhu, C. Wang, Y. Zhou, X. Jia, L. Jiang, X. Liu, G.G. Wallace, A smart cyto-compatible asymmetric polypyrrole membrane for salinity power generation, Nano Energy, **2018**, 53, 475-482.
[228] X. Zhu, J. Hao, B. Bao, Y. Zhou, H. Zhang, J. Pang, Z. Jiang, L. Jiang, Unique ion rectification in hypersaline environment: a high-performance and sustainable power generator system, Sci. Adv., **2018**, 4, eaau1665.
[229] C. Chen, D. Liu, G. Yang, J. Wang, L. Wang, W. Lei, Bioinspired ultrastrong nanocomposite membranes for salinity gradient energy harvesting from organic solutions, Adv. Energy Mater., **2020**, 10, 1904098.

[230] J. Chen, W. Xin, X.-Y. Kong, Y. Qian, X. Zhao, W. Chen, Y. Sun, Y. Wu, L. Jiang, L. Wen, Ultrathin and robust silk fibroin membrane for high-performance osmotic energy conversion, ACS Energy Lett., **2019**, 5, 742-748.
[231] L. Fu, J. Jiang, B. Lu, Y. Xu, J. Zhai, Using smart nanochannels as a power switch in salinity gradient batteries, ChemNanoMat., **2019**, 5, 1182-1187.
[232] J. Gao, W. Guo, D. Feng, H. Wang, D. Zhao, L. Jiang, High-performance ionic diode membrane for salinity gradient power generation, J. Am. Chem. Soc., **2014**, 136, 12265-12272.
[233] C. Wang, F.F. Liu, Z. Tan, Y.M. Chen, W.C. Hu, X.H. Xia, Fabrication of bio-inspired 2D MOFs/PAA hybrid membrane for asymmetric ion transport, Adv. Funct. Mater., **2019**, 30, 1908804.
[234] T. Xiao, Q. Zhang, J. Jiang, J. Ma, Q. Liu, B. Lu, Z. Liu, J. Zhai, pH-Resistant Nanofluidic Diode Membrane for High-Performance Conversion of Salinity Gradient into Electric Energy, Energy Technol., **2019**, 7, 1800952.
[235] L. Wen, X. Hou, Y. Tian, F.-Q. Nie, Y. Song, J. Zhai, L. Jiang, Bioinspired smart gating of nanochannels toward photoelectric-conversion systems, Adv. Mater., **2010**, 22, 1021-1024.
[236] D. Stein, M. Kruithof, C. Dekker, Surface-charge-governed ion transport in nanofluidic channels, Phys. Rev. Lett., **2004**, 93, 035901.
[237] J. Safaei, G. Wang, Progress and prospects of two-dimensional materials for membrane-based osmotic power generation, Nano Research Energy, **2022**, 1, e9120008.
[238] S. Chen, C. Zhu, W. Xian, X. Liu, X. Liu, Q. Zhang, S. Ma, Q. Sun, Imparting ion selectivity to covalent organic framework membranes using de novo assembly for blue energy harvesting, J. Am. Chem. Soc., **2021**, 143, 9415-9422.
[239] Z. Zhang, P. Bhauriyal, H. Sahabudeen, Z. Wang, X. Liu, M. Hambsch, S.C. Mannsfeld, R. Dong, T. Heine, X. Feng, Cation-selective two-dimensional polyimine membranes for high-performance osmotic energy conversion, Nat. Commun., **2022**, 13, 1-9.
[240] L. Cao, I.-C. Chen, C. Chen, D.B. Shinde, X. Liu, Z. Li, Z. Zhou, Y. Zhang, Y. Han, Z. Lai, Giant Osmotic Energy Conversion through Vertical-Aligned Ion-Permselective Nanochannels in Covalent Organic Framework Membranes, J. Am. Chem. Soc., **2022**.
[241] J. Xiong, J. Di, J. Xia, W. Zhu, H. Li, Surface defect engineering in 2D nanomaterials for photocatalysis, Adv. Funct. Mater., **2018**, 28, 1801983.
[242] J. Safaei, S.M.H. Mashkani, H. Tian, C. Ye, P. Xiong, G. Wang, Self-Assembled NbOPO4 Nanosheet/Reduced Graphene Oxide Heterostructure for Capacitive Desalination, ACS Applied Nano Materials, **2021**, 4, 12629-12639.
[243] Z. Wu, L. Jiang, W. Tian, Y. Wang, Y. Jiang, Q. Gu, L. Hu, Novel Sub-5 nm Layered Niobium Phosphate Nanosheets for High-Voltage, Cation-Intercalation Typed Electrochemical Energy Storage in Wearable Pseudocapacitors, Adv. Energy Mater., **2019**, 9, 1900111.
[244] G. Kresse, J. Furthmüller, Efficiency of ab-initio total energy calculations for metals and semiconductors using a plane-wave basis set, Computational materials science, **1996**, 6, 15-50.
[245] G. Kresse, J. Hafner, Ab initio molecular dynamics for open-shell transition metals, Physical Review B, **1993**, 48, 13115.
[246] J.P. Perdew, K. Burke, M. Ernzerhof, Generalized gradient approximation made simple, Phys. Rev. Lett., **1996**, 77, 3865.
[247] S. Grimme, Semiempirical GGA-type density functional constructed with a long-range dispersion correction, J. Comput. Chem., **2006**, 27, 1787-1799.

[248] G. Henkelman, B.P. Uberuaga, H. Jónsson, A climbing image nudged elastic band method for finding saddle points and minimum energy paths, The Journal of chemical physics, **2000**, 113, 9901-9904.
[249] C. Bannwarth, E. Caldeweyher, S. Ehlert, A. Hansen, P. Pracht, J. Seibert, S. Spicher, S. Grimme, Extended tight-binding quantum chemistry methods, Wiley Interdisciplinary Reviews: Computational Molecular Science, **2021**, 11, e1493.
[250] C. Bannwarth, S. Ehlert, S. Grimme, GFN2-xTB—An accurate and broadly parametrized self-consistent tight-binding quantum chemical method with multipole electrostatics and density-dependent dispersion contributions, Journal of chemical theory and computation, **2019**, 15, 1652-1671.
[251] T. Lu, F. Chen, Multiwfn: a multifunctional wavefunction analyzer, J. Comput. Chem., **2012**, 33, 580-592.
[252] J. Zhang, T. Lu, Efficient evaluation of electrostatic potential with computerized optimized code, Physical Chemistry Chemical Physics, **2021**, 23, 20323-20328.
[253] J.C. Phillips, R. Braun, W. Wang, J. Gumbart, E. Tajkhorshid, E. Villa, C. Chipot, R.D. Skeel, L. Kale, K. Schulten, Scalable molecular dynamics with NAMD, J. Comput. Chem., **2005**, 26, 1781-1802.
[254] A.K. Rappé, C.J. Casewit, K. Colwell, W.A. Goddard III, W.M. Skiff, UFF, a full periodic table force field for molecular mechanics and molecular dynamics simulations, J. Am. Chem. Soc., **1992**, 114, 10024-10035.
[255] L. Martínez, R. Andrade, E.G. Birgin, J.M. Martínez, PACKMOL: A package for building initial configurations for molecular dynamics simulations, J. Comput. Chem., **2009**, 30, 2157-2164.
[256] W. Humphrey, A. Dalke, K. Schulten, VMD: visual molecular dynamics, Journal of molecular graphics, **1996**, 14, 33-38.
[257] K. Momma, F. Izumi, VESTA: a three-dimensional visualization system for electronic and structural analysis, J. Appl. Crystallogr., **2008**, 41, 653-658.
[258] N. Kinomura, N. Kumada, Preparation of an acid niobium phosphate and alkali-metal niobium phosphates, having NbOPO4. cntdot. H2O layers condensed with the phosphate group, Inorg. Chem., **1990**, 29, 5217-5222.
[259] Z. He, H. Cui, S. Hao, L. Wang, J. Zhou, Electric-field effects on ionic hydration: a molecular dynamics study, The Journal of Physical Chemistry B, **2018**, 122, 5991-5998.
[260] B. Zhang, J. Kang, T. Kang, Effect of water on methane adsorption on the kaolinite (0 0 1) surface based on molecular simulations, Appl. Surf. Sci., **2018**, 439, 792-800.
[261] J. Lao, R. Lv, J. Gao, A. Wang, J. Wu, J. Luo, Aqueous stable Ti3C2 MXene membrane with fast and photoswitchable nanofluidic transport, ACS Nano, **2018**, 12, 12464-12471.
[262] A. Razmjou, M. Asadnia, E. Hosseini, A. Habibnejad Korayem, V. Chen, Design principles of ion selective nanostructured membranes for the extraction of lithium ions, Nat. Commun., **2019**, 10, 1-15.
[263] J.R. Werber, C.O. Osuji, M. Elimelech, Materials for next-generation desalination and water purification membranes, Nat. Rev. Mater., **2016**, 1, 16018.
[264] P. Srimuk, X. Su, J. Yoon, D. Aurbach, V. Presser, Charge-transfer materials for electrochemical water desalination, ion separation and the recovery of elements, Nat. Rev. Mater., **2020**, 5, 517-538.
[265] J. Cao, Y. Wang, L. Wang, F. Yu, J. Ma, Na3V2(PO4)3@C as faradaic electrodes in capacitive deionization for high-performance desalination, Nano Lett., **2019**, 19, 823-828.

[266] S. Huo, Y. Zhao, M. Zong, B. Liang, X. Zhang, I.U. Khan, X. Song, K. Li, Boosting supercapacitor and capacitive deionization performance of hierarchically porous carbon by polar surface and structural engineering, J. Mater. Chem. A, **2020**, 8, 2505-2517.
[267] J.S. Kang, S. Kim, D.Y. Chung, Y.J. Son, K. Jo, X. Su, M.J. Lee, H. Joo, T.A. Hatton, J. Yoon, Rapid Inversion of Surface Charges in Heteroatom-Doped Porous Carbon: A Route to Robust Electrochemical Desalination, Adv. Funct. Mater., **2020**, 30, 1909387.
[268] X. Gong, S. Zhang, W. Luo, N. Guo, L. Wang, D. Jia, Z. Zhao, S. Feng, L. Jia, Enabling a Large Accessible Surface Area of a Pore-Designed Hydrophilic Carbon Nanofiber Fabric for Ultrahigh Capacitive Deionization, ACS Appl. Mater. Inter., **2020**, 12, 49586-49595.
[269] Y. Zhu, G. Zhang, C. Xu, L. Wang, Interconnected Graphene Hollow Shells for High-Performance Capacitive Deionization, ACS Appl. Mater. Inter., **2020**, 12, 29706-29716.
[270] W. Shi, X. Liu, T. Deng, S. Huang, M. Ding, X. Miao, C. Zhu, Y. Zhu, W. Liu, F. Wu, C. Gao, S.-W. Yang, H.Y. Yang, J. Shen, X. Cao, Enabling Superior Sodium Capture for Efficient Water Desalination by a Tubular Polyaniline Decorated with Prussian Blue Nanocrystals, Adv. Mater., **2020**, 32, 1907404.
[271] X. Xu, J. Tang, Y.V. Kaneti, H. Tan, T. Chen, L. Pan, T. Yang, Y. Bando, Y. Yamauchi, Unprecedented capacitive deionization performance of interconnected iron–nitrogen-doped carbon tubes in oxygenated saline water, Mater. Horiz., **2020**, 7, 1404-1412.
[272] H. Wang, L. Edaño, L. Valentino, Y.J. Lin, V.M. Palakkal, D.-L. Hu, B.-H. Chen, D.-J. Liu, Capacitive deionization using carbon derived from an array of zeolitic-imidazolate frameworks, Nano Energy, **2020**, 77, 105304.
[273] X. Xu, T. Yang, Q. Zhang, W. Xia, Z. Ding, K. Eid, A.M. Abdullah, M.S.A. Hossain, S. Zhang, J. Tang, Ultrahigh capacitive deionization performance by 3D interconnected MOF-derived nitrogen-doped carbon tubes, Chem. Eng. J., **2020**, 390, 124493.
[274] X. Xu, A.E. Allah, C. Wang, H. Tan, A.A. Farghali, M.H. Khedr, V. Malgras, T. Yang, Y. Yamauchi, Capacitive deionization using nitrogen-doped mesostructured carbons for highly efficient brackish water desalination, Chem. Eng. J., **2019**, 362, 887-896.
[275] T. Alencherry, A. Naveen, S. Ghosh, J. Daniel, R. Venkataraghavan, Effect of increasing electrical conductivity and hydrophilicity on the electrosorption capacity of activated carbon electrodes for capacitive deionization, Desalination, **2017**, 415, 14-19.
[276] C. Kim, P. Srimuk, J. Lee, S. Fleischmann, M. Aslan, V. Presser, Influence of pore structure and cell voltage of activated carbon cloth as a versatile electrode material for capacitive deionization, Carbon, **2017**, 122, 329-335.
[277] P. Liu, T. Yan, L. Shi, H.S. Park, X. Chen, Z. Zhao, D. Zhang, Graphene-based materials for capacitive deionization, J. Mater. Chem. A, **2017**, 5, 13907-13943.
[278] L. Chang, Y. Fei, Y.H. Hu, Structurally and chemically engineered graphene for capacitive deionization, J. Mater. Chem. A, **2021**, 9, 1429-1455.
[279] R. Kumar, S.S. Gupta, S. Katiyar, V.K. Raman, S.K. Varigala, T. Pradeep, A. Sharma, Carbon aerogels through organo-inorganic co-assembly and their application in water desalination by capacitive deionization, Carbon, **2016**, 99, 375-383.
[280] G. Luo, Y. Wang, L. Gao, D. Zhang, T. Lin, Graphene bonded carbon nanofiber aerogels with high capacitive deionization capability, Electrochim. Acta, **2018**, 260, 656-663.

[281] K. Sharma, Y.-H. Kim, J. Gabitto, R. Mayes, S. Yiacoumi, H. Bilheux, L. Walker, S. Dai, C. Tsouris, Transport of ions in mesoporous carbon electrodes during capacitive deionization of high-salinity solutions, Langmuir, **2015**, 31, 1038-1047.
[282] X. Xu, Y. Liu, M. Wang, C. Zhu, T. Lu, R. Zhao, L. Pan, Hierarchical hybrids with microporous carbon spheres decorated three-dimensional graphene frameworks for capacitive applications in supercapacitor and deionization, Electrochim. Acta, **2016**, 193, 88-95.
[283] W. Shi, X. Zhou, J. Li, E.R. Meshot, A.D. Taylor, S. Hu, J.-H. Kim, M. Elimelech, D.L. Plata, High-performance capacitive deionization via manganese oxide-coated, vertically aligned carbon nanotubes, Environ. Sci. Technol. Lett., **2018**, 5, 692-700.
[284] J. Cao, Y. Wang, C. Chen, F. Yu, J. Ma, A Comparison of graphene hydrogels modified with single-walled/multi-walled carbon nanotubes as electrode materials for capacitive deionization, J. Colloid Interface Sci., **2018**, 518, 69-75.
[285] F. Yu, L. Wang, Y. Wang, X. Shen, Y. Cheng, J. Ma, Faradaic reactions in capacitive deionization for desalination and ion separation, J. Mater. Chem. A, **2019**, 7, 15999-16027.
[286] T. Liu, J. Serrano, J. Elliott, X. Yang, W. Cathcart, Z. Wang, Z. He, G. Liu, Exceptional capacitive deionization rate and capacity by block copolymer–based porous carbon fibers, Sci. Adv., **2020**, 6, eaaz0906.
[287] P. Nie, S. Wang, X. Shang, B. Hu, M. Huang, J. Yang, J. Liu, Self-supporting porous carbon nanofibers with opposite surface charges for high-performance inverted capacitive deionization, Desalination, **2021**, 520, 115340.
[288] S. Vafakhah, L. Guo, D. Sriramulu, S. Huang, M. Saeedikhani, H.Y. Yang, Efficient sodium-ion intercalation into the freestanding Prussian blue/graphene aerogel anode in a hybrid capacitive deionization system, ACS Appl. Mater. Inter., **2019**, 11, 5989-5998.
[289] W. Zhao, L. Guo, M. Ding, Y. Huang, H.Y. Yang, Ultrahigh-desalination-capacity dual-ion electrochemical deionization device based on Na3V2(PO4)3@C–AgCl electrodes, ACS Appl. Mater. Inter., **2018**, 10, 40540-40548.
[290] B. Hu, X. Shang, P. Nie, B. Zhang, K. Xu, J. Yang, J. Qiu, J. Liu, Facile Fabrication of a Highly Porous N-Doped Nanotubular Carbon Aerogel by an In Situ Template-Growth Method for High-Performance Supercapacitors, ACS Appl. Energy Mater., **2021**, 4, 6991-7001.
[291] B. Chen, Y. Wang, Z. Chang, X. Wang, M. Li, X. Liu, L. Zhang, Y. Wu, Enhanced capacitive desalination of MnO 2 by forming composite with multi-walled carbon nanotubes, RSC Adv., **2016**, 6, 6730-6736.
[292] S. Vafakhah, M. Saeedikhani, S. Huang, D. Yan, Z.Y. Leong, Y. Wang, L. Hou, L. Guo, P.V. y Alvarado, H.Y. Yang, Tungsten disulfide-reduced GO/CNT aerogel: a tuned interlayer spacing anode for efficient water desalination, J. Mater. Chem. A, **2021**, 9, 10758-10768.
[293] Y. Zhu, L. Peng, Z. Fang, C. Yan, X. Zhang, G. Yu, Structural engineering of 2D nanomaterials for energy storage and catalysis, Adv. Mater., **2018**, 30, 1706347.
[294] Z. Li, D. Li, H. Wang, P. Chen, L. Pi, X. Zhou, T. Zhai, Intercalation Strategy in 2D Materials for Electronics and Optoelectronics, Small Methods, **2021**, 5, 2100567.
[295] P. Xiong, B. Sun, N. Sakai, R. Ma, T. Sasaki, S. Wang, J. Zhang, G. Wang, 2D superlattices for efficient energy storage and conversion, Adv. Mater., **2020**, 32, 1902654.
[296] S. Wang, S. Zhao, X. Guo, G. Wang, 2D Material-Based Heterostructures for Rechargeable Batteries, Adv. Energy Mater., **2021**, 2100864 (doi.org/2100810.2101002/aenm.202100864).

[297] W. Li, Q. Song, M. Li, Y. Yuan, J. Zhang, N. Wang, Z. Yang, J. Huang, J. Lu, X. Li, Chemical Heterointerface Engineering on Hybrid Electrode Materials for Electrochemical Energy Storage, Small Methods, **2021**, 5, 2100444.
[298] P. Xiong, R. Ma, N. Sakai, T. Sasaki, Genuine unilamellar metal oxide nanosheets confined in a superlattice-like structure for superior energy storage, ACS Nano, **2018**, 12, 1768-1777.
[299] P. Xiong, X. Zhang, F. Zhang, D. Yi, J. Zhang, B. Sun, H. Tian, D. Shanmukaraj, T. Rojo, M. Armand, Two-dimensional unilamellar cation-deficient metal oxide nanosheet superlattices for high-rate sodium ion energy storage, ACS Nano, **2018**, 12, 12337-12346.
[300] P. Xiong, R. Ma, N. Sakai, L. Nurdiwijayanto, T. Sasaki, Unilamellar metallic MoS2/graphene superlattice for efficient sodium storage and hydrogen evolution, ACS Energy Lett., **2018**, 3, 997-1005.
[301] R. Zhao, M. Wang, D. Zhao, H. Li, C. Wang, L. Yin, Molecular-level heterostructures assembled from titanium carbide MXene and Ni–Co–Al layered double-hydroxide nanosheets for all-solid-state flexible asymmetric high-energy supercapacitors, ACS Energy Lett., **2017**, 3, 132-140.
[302] C. Masquelier, L. Croguennec, Polyanionic (phosphates, silicates, sulfates) frameworks as electrode materials for rechargeable Li (or Na) batteries, Chem. Rev., **2013**, 113, 6552-6591.
[303] K. Nanjundaswamy, A. Padhi, J. Goodenough, S. Okada, H. Ohtsuka, H. Arai, J. Yamaki, Synthesis, redox potential evaluation and electrochemical characteristics of NASICON-related-3D framework compounds, Solid State Ionics, **1996**, 92, 1-10.
[304] A. Manthiram, J. Goodenough, Lithium insertion into Fe2(MO4)3 frameworks: comparison of M = W with M = Mo, J. Solid State Chem., **1987**, 71, 349-360.
[305] A. Manthiram, J. Goodenough, Lithium insertion into Fe2(SO4)3 frameworks, J. Power Sources, **1989**, 26, 403-408.
[306] C. Wu, X. Lu, L. Peng, K. Xu, X. Peng, J. Huang, G. Yu, Y. Xie, Two-dimensional vanadyl phosphate ultrathin nanosheets for high energy density and flexible pseudocapacitors, Nat. Commun., **2013**, 4, 1-7.
[307] P. Xiong, F. Zhang, X. Zhang, S. Wang, H. Liu, B. Sun, J. Zhang, Y. Sun, R. Ma, Y. Bando, Strain engineering of two-dimensional multilayered heterostructures for beyond-lithium-based rechargeable batteries, Nat. Commun., **2020**, 11, 1-12.
[308] X. Wang, Q. Li, L. Zhang, Z. Hu, L. Yu, T. Jiang, C. Lu, C. Yan, J. Sun, Z. Liu, Caging Nb2O5 nanowires in PECVD-derived graphene capsules toward bendable sodium-ion hybrid supercapacitors, Adv. Mater., **2018**, 30, 1800963.
[309] V. Augustyn, J. Come, M.A. Lowe, J.W. Kim, P.-L. Taberna, S.H. Tolbert, H.D. Abruña, P. Simon, B. Dunn, High-rate electrochemical energy storage through Li+ intercalation pseudocapacitance, Nat. Mater., **2013**, 12, 518-522.
[310] D. Chen, J.-H. Wang, T.-F. Chou, B. Zhao, M.A. El-Sayed, M. Liu, Unraveling the nature of anomalously fast energy storage in T-Nb2O5, J. Am. Chem. Soc., **2017**, 139, 7071-7081.
[311] D.C. Marcano, D.V. Kosynkin, J.M. Berlin, A. Sinitskii, Z. Sun, A. Slesarev, L.B. Alemany, W. Lu, J.M. Tour, Improved synthesis of graphene oxide, ACS Nano, **2010**, 4, 4806-4814.
[312] G. Kresse, J. Furthmüller, Efficient iterative schemes for ab initio total-energy calculations using a plane-wave basis set, Phys. Rev. B, **1996**, 54, 11169.
[313] H.J. Monkhorst, J.D. Pack, Special points for Brillouin-zone integrations, Physical review B, **1976**, 13, 5188.

[314] S. Porada, R. Zhao, A. Van Der Wal, V. Presser, P. Biesheuvel, Review on the science and technology of water desalination by capacitive deionization, Prog. Mater. Sci., **2013**, 58, 1388-1442.
[315] D. Qu, G. Wang, J. Kafle, J. Harris, L. Crain, Z. Jin, D. Zheng, Electrochemical impedance and its applications in energy-storage systems, Small Methods, **2018**, 2, 1700342.
[316] Y. Liu, X. Gao, K. Wang, X. Dou, H. Zhu, X. Yuan, L. Pan, Rocking-chair capacitive deionization with flow-through electrodes, J. Mater. Chem. A, **2020**, 8, 8476-8484.
[317] P. Xiong, X. Zhang, H. Wan, S. Wang, Y. Zhao, J. Zhang, D. Zhou, W. Gao, R. Ma, T. Sasaki, Interface modulation of two-dimensional superlattices for efficient overall water splitting, Nano Lett., **2019**, 19, 4518-4526.
[318] J. Zhang, J. Fang, J. Han, T. Yan, L. Shi, D. Zhang, N, P, S co-doped hollow carbon polyhedra derived from MOF-based core–shell nanocomposites for capacitive deionization, J. Mater. Chem. A, **2018**, 6, 15245-15252.
[319] S. Choi, B. Chang, S. Kim, J. Lee, J. Yoon, J.W. Choi, Battery Electrode Materials with Omnivalent Cation Storage for Fast and Charge-Efficient Ion Removal of Asymmetric Capacitive Deionization, Adv. Funct. Mater., **2018**, 28, 1802665.
[320] X. Liu, S. Zhang, G. Feng, Z.-G. Wu, D. Wang, M.D. Albaqami, B. Zhong, Y. Chen, X. Guo, X. Xu, Core–Shell MOF@COF Motif Hybridization: Selectively Functionalized Precursors for Titanium Dioxide Nanoparticle-Embedded Nitrogen-Rich Carbon Architectures with Superior Capacitive Deionization Performance, Chem. Mater., **2021**, 33, 1657-1666.
[321] X. Liu, M. He, D. Calvani, H. Qi, K.B.S.S. Gupta, H.J.M. de Groot, G.J.A. Sevink, F. Buda, U. Kaiser, G.F. Schneider, Power generation by reverse electrodialysis in a single-layer nanoporous membrane made from core-rim polycyclic aromatic hydrocarbons, Nat. Nanotechnol., **2020**, 15, 307-312.
[322] X. He, T. Li, Z. Shi, X. Wang, F. Xue, Z. Wu, Q. Chen, Thermal-oxidative aging behavior of nitrile-butadiene rubber/functional LDHs composites, Polym. Degrad. Stab., **2016**, 133, 219-226.
[323] F. Liu, A. Zheng, I. Noshadi, F.-S. Xiao, Design and synthesis of hydrophobic and stable mesoporous polymeric solid acid with ultra strong acid strength and excellent catalytic activities for biomass transformation, Appl. Catal. B: Environ., **2013**, 136-137, 193-201.
[324] W. Xin, Z. Zhang, X. Huang, Y. Hu, T. Zhou, C. Zhu, X.-Y. Kong, L. Jiang, L. Wen, High-performance silk-based hybrid membranes employed for osmotic energy conversion, Nat. Commun., **2019**, 10, 3876.
[325] L. Ding, D. Xiao, Z. Lu, J. Deng, Y. Wei, J. Caro, H. Wang, Oppositely Charged $Ti_3C_2T_x$ MXene Membranes with 2D Nanofluidic Channels for Osmotic Energy Harvesting, Angew. Chem. Int. Ed., **2020**, 59, 8720-8726.
[326] Z. Zhang, X. Sui, P. Li, G. Xie, X.-Y. Kong, K. Xiao, L. Gao, L. Wen, L. Jiang, Ultrathin and ion-selective janus membranes for high-performance osmotic energy conversion, J. Am. Chem. Soc., **2017**, 139, 8905-8914.
[327] A. Sasahara, M. Tomitori, XPS and STM study of Nb-doped TiO2 (110)-(1× 1) surfaces, The Journal of Physical Chemistry C, **2013**, 117, 17680-17686.
[328] S. Wang, G. Wang, X. Che, S. Wang, C. Li, D. Li, Y. Zhang, Q. Dong, J. Qiu, Enhancing the capacitive deionization performance of NaMnO 2 by interface engineering and redox-reaction, Environ. Sci. Nano, **2019**, 6, 2379-2388.